

Hydrogen in V-Fe thin films and Fe/V-Fe multi-layered thin films

Dissertation

zur Erlangung des Doktorgrades

der Mathematisch-Naturwissenschaftlichen Fakultäten

der Georg-August-Universität zu Göttingen

vorgelegt von

Ryota Gemma
aus Kanagawa

Göttingen 2011

D7

Referent : Prof. Dr. A. Pundt

Korreferent : Prof. Dr. R. Kirchheim

Datum der Promotion: 04.05.2011

Index

1. Introduction	1
2. Hydrogen in thin films	7
2.1 Hydrogen in metals	7
2.1.1 Hydrogen induced lattice expansion	8
2.1.2 Solubility of hydrogen in metals	8
2.1.3 Electrochemical hydrogen loading	10
2.1.4 Formation of hydride phase	10
2.1.5 V-H and V-D systems	11
2.1.6 Fe (bcc) -H system	13
2.1.7 Pd-H and Pd-D system	14
2.1.8 W-H system	14
2.1.9 FeV-H system	15
2.2 Hydrogen induced volume expansion in thin films	17
2.2.1 Directional dependence of E and ν	18
2.2.2 Hydrogen induced expansion and stress in (110) films	21
3. Experimental	23
3.1 Sample preparation	23
3.2 X-ray diffraction (XRD) and X-ray reflectivity (XRR)	25
3.2.1 XRD	25
3.2.2 XRR	26
3.2.3 <i>In-situ</i> XRD during hydrogen loading	29
3.3 Electrochemical hydrogen loading	30
3.3.1 Electromotorical Force (EMF) measurement	30
3.3.2 Hydrogen loading cell for <i>in-situ</i> XRD	30
3.3.3 Hydrogen loading cell for <i>in-situ</i> stress measurement	32
3.3.4 Acoustic emission (AE)	33
3.4 Deuterium gas loading	35
3.5 Field ion microscopy (FIM) and Atom probe tomography (APT)	37
3.5.1 Field ion microscopy (FIM)	37
3.5.2 Atom probe tomography (APT)	40
4. Sample characterization of as-prepared films	44
4.1 Initial lattice expansion and in-plane orientation	44
4.1.1 V-Fe films on Al ₂ O ₃ (0001) substrates	45
4.2.1 V-Fe and Fe/V films on Al ₂ O ₃ (11 $\bar{2}$ 0) substrates	45
4.2.2.1 V-Fe single layered films	48
4.2.2.2 Fe/V multi-layered films	51

4.2 Interface roughness	55
4.3 Characterization by FIM and APT	57
4.3.1 Epitaxial growth of V-Fe single layer	58
4.3.2 Layer interdiffusion at high deposition temperature	60
4.3.3 Interface intermixing by sputtering process	62
4.3.4 Combined effect of sputtering and thermal interdiffusion	65
5. Results and discussion	67
5.1 In-plane stress evolution upon hydrogen absorption	67
5.1.1 Impact of deposition temperature	67
5.1.2 Impact of film thickness	73
5.1.2.1 400-nm thick film	73
5.1.2.2 200-nm thick film	74
5.1.2.3 100-nm thick film	75
5.1.2.4 50-nm thick film	76
5.1.2.5 20-nm thick film	77
5.1.2.6 10-nm thick film	78
5.1.2.7 Relationship between initial in-plane stress and film thickness	79
5.1.2.8 Change of phase boundary	81
5.1.2.9 Stress release during unloading of hydrogen	82
5.1.3 H-induced stress in Fe/V-Fe multi-layered film on Al ₂ O ₃ (11 $\bar{2}$ 0) and on Al ₂ O ₃ (0001) substrate	83
5.1.3.1 [Fe 20.31 nm / V 42.84 nm] x 2	84
5.1.3.2 [Fe 10.13 nm / V 21.52 nm] x 4	85
5.1.3.3 [Fe 5.08 nm / V 10.82 nm] x 8	85
5.1.3.4 [Fe 5.95 nm / V 6.04 nm] x 8	86
5.2 <i>In-situ</i> XRD during hydrogen loading	89
5.2.1 V-Fe3at% film on Al ₂ O ₃ (11 $\bar{2}$ 0) deposited at 1073 K	89
5.2.2 [Fe 10 nm / V 21 nm] multi-layered film on Al ₂ O ₃ (11 $\bar{2}$ 0)	95
5.3 Acoustic emission measurements	99
5.3.1 Thickness dependency - Single layered films	99
5.3.2 Thickness dependency - Multi-layered films	102
5.4 Local hydrogen-distribution: Atom probe tomography (APT) analysis	105
5.4.1 Temperature impact on D-concentration in V-Fe single layered film	105
5.4.1.1 Analysis at 60 K : high D-mobility	107
5.4.1.2 Analysis at 45 K : low D-mobility	110
5.4.1.3 Analysis at 30 K : nearly-frozen D-mobility	111
5.4.1.4 Analysis at 22 K : frozen D-mobility	113

5.4.1.5 Overview : Analysis at high temperatures (60 K - 45 K) ·	115
5.4.1.6 Overview : Analysis at low temperatures (30 K - 22 K) ···	116
5.4.2 Artificial D distribution at Pd/V interface ·········	118
5.4.3 Local deuterium concentration at interfaces of VFe single layered films ·········	119
5.4.3.1 Impact of Pd and O atoms at the W substrate ·······	120
5.4.3.2 Artificial interface mixing : analysis problem ·····	121
5.4.3.3 Impact of Fe and O atoms at the W substrate ·····	124
5.4.4 Fe/V-Fe multi-layered film ·········	126
5.4.4.1 Impact of analysis temperature ·········	128
- Analysis at 30 K, D ₂ 0.2 Pa ·········	128
- Analysis at 60 K, D ₂ 0.2 Pa ·········	129
5.4.4.2 Impact of D ₂ pressure, at 30 K ·········	130
- D ₂ 0.05 Pa ·········	130
- D ₂ 0.5 Pa ·········	131
- D ₂ 2 Pa ·········	132
- D ₂ 10 Pa ·········	133
- D ₂ 1000 Pa ·········	134
5.4.4.3 Comparison with EMF curve (pressure-composition isotherm) ·········	135
5.4.4.4 Local chemistry at Fe/V interface ·········	136
6. Global discussion ·········	140
6.1 At $0 < c_H \leq 0.005$ H/V - Interaction of H with vacancy in VFe thin films ·········	140
6.2 At $0.005 < c_H \leq 0.1$ H/V - Quasiplastic response in the elastic regime of VFe thin films upon H uptake ·········	143
6.3 At $c_H \sim 0.1$ H/V ·········	149
6.4 At $0.1 < c_H < 0.3 \sim 0.4$ H/V - Hydride formation in V-Fe thin films ·········	149
6.5 Fe/V multi-layered films ·········	151
6.6 Investigation of local chemistry by APT ·········	155
6.6.1 Impact of oxygen adsorbates on the local D distribution in V-Fe single-layer and Fe/V multi-layered films ·········	155
6.6.2 D distribution in V-layer affected by the presence of the Fe-interface ·········	158
7. Summary and outlook ·········	160
Appendix ·········	163

Bibliography	167
List of publications (since 2004)	178
Danksagung	180
Lebenslauf	182

1. Introduction

Ever since the energy crisis in 1970's, hydrogen (H) has been regarded as one of the carbon-free secondary energy sources. In this context, hydrogen storage materials have been considered as possible candidates of clean energy storage media (see e.g. website of Department of Energy in US [DOE]). Hydrogen is the smallest and the lightest element and thus can be easily absorbed in interstitial sites of metal lattice. A pioneering work in this field is known by Sieverts [Siev29]. In some of metal alloys with tailored composition, considerable amount of hydrogen (several wt%) can be reversibly stored through metal/metal hydride (MH) phase transition, just by controlling pressure or temperature [Vught70]. Practically, some of them (LaNi₅, TiFe) are really easy to handle and have already been utilized for technical applications like in fuel cell system [Iwas03] or in MH refrigerator [Uchi04] after intensive studies and developments in this field. Owing to its extraordinary high volume density and high stability, such metal hydrides still hold advantage to other storage methods like liquid hydrogen or high-pressure H₂ gas tanks. Currently, further research and development is on the way focusing on improvement of gravimetric hydrogen density and reaction kinetics [Orimo07, Dornh07].

In relation to this, nano-structuring has been attracting attention since early 90's to improve total performance including thermodynamics of M-H reaction. In fact, many studies report that metallic nano-clusters and metallic thin films have rather different, as well very interesting hydriding reaction properties from that of massive metals. Such aspects are reviewed in detail by Pundt and Kirchheim [Pundt06]. This new aspect, therefore, calls revisit of fundamental physics on metal-hydrogen system. For this purpose, it is important to choose well-investigated metals like Pd or V, as their properties have been well investigated on bulk scale and thus the discussion can be carried out on robust knowledge.

Based on this, a detailed investigation of H-related behavior at hetero-interfaces of multi-layered thin films can be carried out. Thereby, the local chemistry at the interfaces is strongly modified and, thus stark contrast to bulk-behavior is expected.

Usually, in massive metals, hydrogen absorption in interstitial sites induces lattice expansion in three dimensions. This process rather enables formation of cracks at the surface, through dislocation nucleation, which finally supplies fresh surface for hydrogen to be introduced in the metal or alloy easily.

In case of a metallic thin film, however, the film is deposited usually

on elastically hard substrate. As long as the film is fixed to the substrate, free volume expansion of the film is not allowed and the lattice expands one dimensionally in the film's out-of-plane direction by Poisson response (linear elasticity theory e.g. in [Slaug02]). Consequently, the stress field in the film's in-plane directions becomes highly compressive. Such anisotropy of stress field would induce anisotropic displacement of lattice in x,y and z directions and, thus causes directional dependence of H-H interaction in the film. Such mechanical boundary conditions are suggested to change thermodynamics of MH reaction [Alefeld72]. That is, even the initial displacement (stress) of the lattice in the film modifies the interaction in the same way.

By constituting a multi-layered film, it is possible to tune this initial stress state. In a Fe/V multi-layered epitaxial film, for example, the V lattice as the H absorbing layer feels in-plane compressive stress due to the adjacent Fe layers because lattice constant of Fe is smaller than that of V. Thus the out-of-plane V lattice is expanded already at as-deposited state. In combination of Mo/V, inverse situation can be established, as Mo has larger lattice constant than that of V. Primarily, the H-absorption behavior in V is very sensitive to such lattice strain and, accordingly, hydrogen absorption site is drastically changed [Koike81]. Constitution of the Fe/V strained-multi-layered film would establish anisotropic strain distribution since each V layer is both chemically and mechanically isolated by the adjacent Fe layers. This situation in turn modifies elastic boundary condition. Interestingly, this modification strongly influences different aspects of H-related phenomena.

The group of Hjörvarsson has intensively studied the thermodynamics of the above mentioned Fe/V and Mo/V superlattice systems with (100) orientation on hydrogen absorption for many years. For a review article, see e.g. Ref. [Hjörv97]. They have successfully demonstrated that stronger attractive H-H interaction is present in in-plane direction of Fe/V than that of V, while it is repulsive in out-of-plane direction, which is closely linked with gigantic out-of-plane expansion at low concentrations observed by XRD [Hjörv97]. These observations were finally discussed in terms of site occupation. They concluded that preferential O_z site occupation occurs in tetragonally distorted V lattice of Fe/V system throughout the whole concentration range (< 0.5 H/V). This situation was regarded as polarized elastic dipole formation [Alefeld72, Ander97]. Such particular case cannot be described by the above mentioned linear elasticity theory and remarkable departure from in-plane compressive stress development behavior is expected.

It is also worth to note that they did not observe any trace of hydride

formation for the films with 2 nm V layer thickness. Usually, when the hydrogen concentration exceeds the solubility limit, misfit dislocations are formed in the film. Miceli *et al.* have reported misfit dislocation formation in Nb/Ta epitaxial films by XRD measurement of H-loaded sample [Miceli91]. In extremely reduced dimension, incoherent phase transition may be hindered due to reduced stability of dislocation. In clusters the energy to create dislocation is higher than that in bulk and no dislocation was observed [Zütt00]. The formation of dislocation is always accompanied by acoustic emission (AE) [Mill87]. Such emission of acoustic wave is detected by AE technique, which is widely used to study plasticity of bulk materials. Application of AE to thin films will offer a new access to investigate the plastic behavior of thin films.

For Fe/V, the measured enthalpy change at high c_H was found to be smaller than that of bulk V, meaning the stability of MH solution is lower than that of V. The modification of hydride stability is often observed by alloying in bulk system. In case of hydrogenation of Fe-V alloy, the plateau pressure should increase [Yuka03] and the H-solubility should decrease compared to those of pure V. If intermixing of Fe and V is significant, this alloying effect possibly explains the lower stability. However, the Fe/V sample above showed the interface mixing thickness of only 0.2 ~ 0.3 nm and thus the alloying effect is of minor importance in such case of ideally prepared superlattice.

The most interesting finding concerning the H-solubility has been observed both in Fe/V and Mo/V systems. According to the investigation of H concentration by N^{15} method [Hjörv89], no H was detected in the V layer of 0.45 nm (= 3 ML = 3/2 unit cell of V (100) planar distance) from the Fe(Mo)/V interface. This H-depleted layer is named “dead-layer”, which is most probably caused by electron transfer from the Fe or Mo layer into the V layer [Hjörv91]. Later, Meded *et al.* [Mede05] have proposed that the origin of this dead-layer is purely ascribed to an elastic effect by rigid Fe or Mo layers. Up to now, direct proof of such layer has not been given experimentally yet. But, experimental results by ion beam measurements by different researchers on Mo/V [Hjörv91], on Nb/Fe [Nagen95] and on Nb/Cu [Yamam95] commonly suggest the existence of the dead-layer effect. More importantly, the dead-layer effect cannot ultimately be distinguished from an alloying effect, which may also cause the reduction of H-solubility.

Therefore, it is of particular interest to investigate hydrogen distribution at such heterogeneous interface, as local distribution of hydrogen is actually not known due to limited depth resolution (~ 10 nm typically, depending on the depth) of ion beam-assisted profiling of hydrogen, which is particularly called N^{15} -method. Time-of-Flight Secondary ion mass spec-

troscopy (ToF-SIMS) [Benni94] might be strong for this purpose. However, the surface segregation of H must be completely suppressed by e.g. cryogenic cooling of sample. As discussed later, hydrogen or even deuterium is highly mobile in the metal lattice. When more energetically stable sites as sub-surface and defect sites are available, the H or D immediately diffuses to such sites. This would alter the correct distribution of H or D. Therefore, how to freeze H and D diffusion is of a major consequence concerning an analysis of these light species. This aspect in fact critically concerns in this study. When such segregation is avoided, atom probe tomography (APT) analysis [Al-K03] will open up a new way of hydrogen characterization in metals with sub-nm-resolution.

As it is already introduced above, hydrogen is highly sensitive to stress field present in the host metal lattice [Hjörv97] and, thus to the structural imperfections like dislocation, vacancy and grain boundary since hydrogen favors tensile stress around these open volume defects [Kirch88, Pundt04, Pundt06]. If these defects were present (which is usually the case in reality), hydrogen atom can be “trapped” there. Even in epitaxial thin film this interaction cannot be completely excluded. Such trapping effect then causes deviation from the linear elastic behavior as well. When *in-situ* stress measurement (e.g. cantilever method) during H-absorption [Lauda98, Nikit08] is conducted, this departure possibly is detected.

This study is motivated by the above mentioned background. Both $V_{1-x}Fe_x$ ($x = 0.02 - 0.08$) single layered film and Fe/V multi-layered film are of subjects in this study. To begin with, the $V_{1-x}Fe_x$ single layered films were studied because the hydrogenation properties and the local chemistry of V-H thin film system “at around room temperature” have not been well investigated as well for Fe/V multi-layered system. In particular, following aspects are of major interest in this study.

- (i) Stress response of $V_{1-x}Fe_x$ single layered and Fe/V multi-layered films upon hydrogen uptake (elastic and plastic properties). Departure from the linear elasticity, expected for Fe/V and for defect-H interactions.
- (ii) Local chemistry of these films with hydrogen. Establishment of new characterization method with high-resolution for H-Metal system. Proofs of dead layer.
- (iii) Interaction of hydrogen with defects (vacancies, dislocations) present in the films. New outcome by AE measurements.

To investigate these points systematically, the films were prepared

with different thicknesses. Most of the films were epitaxially grown on sapphire substrates. On these films their crystal structure and interface roughness were characterized by X-ray diffraction (XRD) and X-ray reflectivity (XRR) measurement, respectively. Pole figure measurement was also conducted to investigate in-plane configuration of the films and respective epitaxial relationship was suggested. This information enables correct evaluation of results of stress measurements later on.

Hydrogen absorption behavior was monitored by electrochemical hydrogen loading and resulting equilibrium property was assessed from the shape of electromotive force (EMF) curve, which corresponds to pressure-composition isotherm (p - c - T). The results provide information about phase transition at around room temperature.

This simple H-loading technique was combined with stress measurement set up, so that the hydrogen induced in-plane stress can be simultaneously measured *in-situ*. Likewise, the structure development (H-induced lattice expansion and phase transition) was recorded by *in-situ* XRD at DESY in Hamburg, with using specially designed electrochemical H-loading cell. In corporation with Charles University in Prague, we utilized *in-situ* acoustic emission (AE) measurement during H-loading first in the world, aiming to detect hydrogen-related dislocation propagation behavior in the film. Results of these *in-situ* measurements mutually complement and one can later discuss e.g. on the presence of defect-H interaction, shift of phase boundary and onset of hydride formation.

Local microstructure and local chemistry of V and Fe/V were studied by field ion microscopy (FIM) and atom probe tomography (APT), respectively. For these analyses, films were deposited on W needle-shaped substrate. APT [Al-K03] is a strong tool especially to investigate chemistry in nm-range because of its extremely high spatial resolution (0.1 nm) in analysis direction. As this technique is based on time-of-flight measurement, all of the elements can be in principle detected. But, we used deuterium (D) instead of hydrogen in order to differentiate from residual hydrogen gas in the analysis chamber and also to suppress above addressed diffusion problem. Previous APT study by Kesten [Kest02] has detected D-distribution in V layer of Fe/V stack first in the world. However, the average D concentration was considerably lower than expected concentration. This discrepancy was later on ascribed to be D-desorption caused by exposure to air. In this study, we designed portable D₂ gas loading system to avoid this problem. In this gas loading chamber, D was introduced in the films at a controlled pressure and subsequent analysis was carried out. The evaluated D concentration was compared with that of expected from the results of EMF measurement. Additionally, local D-distribution

at Fe/V interface was investigated in relation to the existence of “dead-layer”.

This thesis consists of 7 chapters. In this chapter 1, the background and motivation of this study is described. Chapter 2 treats theoretical background of metal-hydrogen system. In chapter 3, experimental techniques used in this study are introduced. In chapter 4, results of sample characterization both on V single layer and on Fe/V multi-layer by XRD, XRR, FIM and APT are summarized. Chapter 5 introduces experimental results separately in individual sections, and shortly discusses on the results. In the results of stress measurement, emphasis is put on the influence of initial in-plane stress and initial domain size or film thickness on hydrogen-induced stress and observed deviation from the prediction by linear elasticity theory in some cases. The result of *in-situ* XRD measurement is converted to corresponding in-plane stress and comparison with those of stress measurement is made to determine phase boundaries. Thereby, hydride formation is certainly manifested. In the section of AE measurement result, increasing AE signal with increasing hydrogen concentration is successfully shown. Here, dependence of film thickness on AE is introduced. The APT section firstly introduces the influence of analysis temperature in search of correct determination of D concentration in V single layered film. Then, characterization of local D-distribution detected under proper condition is made. For Fe/V multi-layered film, the impact of D₂ pressure on the distribution as well as the average concentration of D is shown. In the last section, a symptom of dead-layer effect is introduced. In chapter 6, all of these results are globally discussed in a combined way, especially focusing on vacancy-H interaction suggested by stress measurement, plastic deformation, phase transition and occurrence of preferential site occupation. Chapter 7 summarizes this thesis.

2. Hydrogen in thin films

Thin films on rigid substrates are subjected to high in-plane stress upon hydrogen uptake. Such stress is believed to have a marked influence on thermodynamics of metal-hydrogen (MH) system [Pundt06, Wagn08]. Moreover, the microstructure of the film changes solubility of hydrogen and terminal concentration of hydrogen from those of bulk metal, too [Pundt06]. This chapter treats fundamental knowledge on Metal-H system, focusing especially on the H solubility in V, Fe, Pd and W. All of these systems are considered in this study. Discussions on the effect of alloying are found in Chap. 4.3 and in Chap. 5.4. Further information can be obtained from reference [HinMeII].

2.1 Hydrogen in metals

Hydrogen atoms introduced in metal host lattice occupy typically 2 different interstitial sites, denoted as tetragonal site (T site) and octahedral site (O site), respectively. The positions depending on the metal lattice are shown in Fig. 2.1. For example, the bcc lattice contains 3 possible O-sites and 6 T-sites per metal atom, resulting in a maximum theoretical solubility of 3 H/Me and 6 H/Me, respectively. Usually, not all sites are available according to the Westlake-criterion [West83]. Often, the site occupation of H in bcc lattices changes from T-site to O-site as the hydrogen concentration increases (see following sections). Note anisotropic M-H

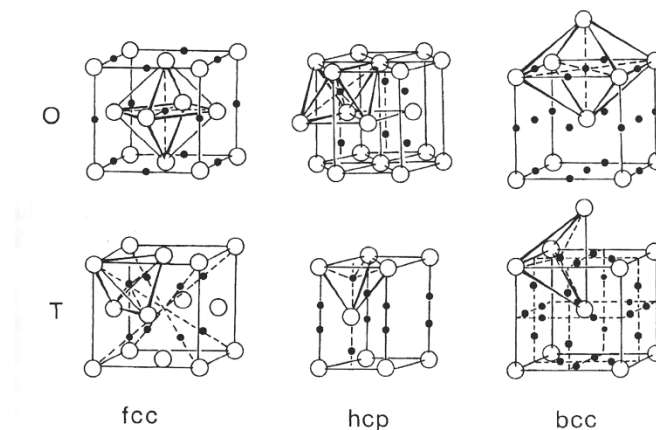


Fig. 2.1 Hydrogen's interstitial sites (T=tetrahedral site, O=octahedral site) in fcc, hcp and bcc metal host lattices [Fukai05]. Full circles mark possible hydrogen atoms positions. Open circles depict metal atom positions.

distance for O-sites in bcc.

2.1.1 Hydrogen induced lattice expansion

The introduction of one hydrogen atom into a metal crystal lattice with lattice constant a induces a volume expansion Δv . For a whole metal volume with a mean atomic volume Ω , the relative volume change $\Delta V/V$ is defined as follows [HinMeI],

$$\frac{\Delta V}{V} \approx 3 \cdot \frac{\Delta a}{a} = c_H \cdot \frac{\Delta v}{\Omega} \quad (2.1)$$

and, thus, yields a linear relationship with hydrogen concentration c_H (H/M) in the ideal case. The linear increase of the lattice parameter is experimentally verified for most metals.[HinMeI] Using Eq. (2.1), the relative sample volume change $\Delta V/V$ can be determined by XRD-lattice parameter measurement or by dilatometric measurement at several c_H .

For a V single crystal, the experimental value determined by dilatometry is $\Delta V/V = 0.189 \cdot c_H$ ($\Delta a/a = 0.063 \cdot c_H$) [Mage76] at room temperature up to concentrations at the solubility limit $\sim \text{VH}_{0.03}$.

For Pd, the expansion coefficient is $\Delta V/V = 0.19$ [HinMeI]. For W and Fe, data were not found.

2.1.2 Solubility of hydrogen in metals

Solution of hydrogen atom from gas phase into metal can be expressed by following reaction [HinMeI].



Under equilibrium condition, the chemical potential of hydrogen atom in gas phase is the same as that of solved hydrogen in the host metal.

$$\frac{1}{2} \mu_{\text{H}_2} = \mu_H \quad (2.3)$$

By Gibb's function of reaction, the change of chemical potential of a H atom μ_H is then expressed as,

$$\Delta \mu_H = \Delta \bar{H} - T \Delta \bar{S} \quad (2.4)$$

as regarded as

$$\Delta G = \Delta \bar{H} - T \Delta \bar{S} \text{ per mol} \quad (2.5)$$

where $\Delta \bar{H}$ and $\Delta \bar{S}$ are called as partial molar enthalpy and partial molar entropy, respectively. At a given temperature, equilibrium constant K_p has a known relationship with ΔG as follows.

$$\Delta G = -RT \ln K_p \quad (2.6)$$

Considering on the basis of 0.5 mol H_2 , the equilibrium condition $\Delta G = 0$

yields,

$$\begin{aligned}
\Delta G &= \mu_H - \frac{1}{2}\mu_{H_2} \\
&= \left(\mu_H^0 + RT \ln a_H\right) - \left(\frac{1}{2}\mu_{H_2}^0 + \frac{1}{2}RT \ln f_{H_2}\right) \\
&= \mu_H^0 - \frac{1}{2}\mu_{H_2}^0 + RT \ln a_H - \frac{1}{2}RT \ln f_{H_2} \\
&= \Delta G_0 + RT \ln \frac{a_H}{\sqrt{f_{H_2}}} = 0
\end{aligned} \tag{2.7}$$

where ΔG_0 is the standard free energy change of hydrogen solution reaction per mol H, a_H is activity of solved H, and f_{H_2} is the fugacity of H_2 gas. If $c_H \sim 0$, and the pressure of hydrogen p_{H_2} is below several MPa, one can approximate the activity coefficient γ_H and the fugacity coefficient β_{H_2} as ~ 1 and thus $a_H \sim c_H$ (defined as $c/(1-c) = H/Me$) and $f_{H_2} \sim p_{H_2}$.

By this, the logarithmic term in Eq. (2.7) becomes

$$\frac{a_H}{\sqrt{f_{H_2}}} = \frac{c_H \cdot \gamma_H}{\sqrt{p_{H_2} \cdot \beta_{H_2}}} \cong \frac{c_H}{\sqrt{p_{H_2}}} \tag{2.8}$$

Combining Eqs. (2.7) and (2.8) results in

$$\Delta G^0 = -RT \ln \frac{c_H}{\sqrt{p_{H_2}}} \tag{2.9}$$

Eq. (2.6) and Eq. (2.9) gives a relationship between $\sqrt{p_{H_2}}$ and c_H as follows.

$$\begin{aligned}
K_p &= \frac{c_H}{\sqrt{p_{H_2}}} \\
c_H &= K_p \cdot \sqrt{p_{H_2}}
\end{aligned} \tag{2.10}$$

This indicates that the hydrogen concentration c_H is proportional to $\sqrt{p_{H_2}}$. This relationship was firstly found by Sieverts [Siev29] and is called Sieverts' law and the equilibrium constant K_p is called as Sieverts' constant often noted as K_s or S .

From Eqs. (2.5) and (2.9), c_H can readily be calculated at given p_{H_2} and T as follows, if ΔH^0 and ΔS^0 or ΔG^0 are known.

$$c_H = \frac{-\Delta G^0}{RT} \cdot \sqrt{p_{H_2}} = \exp\left(\frac{\Delta H^0 - T\Delta S^0}{RT}\right) \cdot \sqrt{p_{H_2}} \tag{2.11}$$

2.1.3 Electrochemical hydrogen loading

In case of electrochemical hydrogen loading and corresponding electromotive force (EMF) measurement, the same treatment of thermodynamics as in the case of gas phase loading is possible through Eq. (2.12) (see also Chap 3.3.1). Here, n is the number of electrons in the reaction, E is the chemical potential and F is the Faraday constant. Detailed process of electrochemical hydrogen absorption is found e.g. in [Dornh02].

$$\Delta G = -n \cdot E \cdot F \quad (2.12)$$

2.1.4 Formation of hydride phase

At low concentrations hydrogen is introduced in the metal host lattice by forming a solid solution (MH^∞). With increasing c_H (i.e. p_{H_2}), the pair interaction of H-H (W_{HH}) usually becomes significant compared to the entropy contribution. Pair interaction originates from elastic and electronic terms. This consequently induces nucleation of a hydride phase (M_xH_y) and a change of the chemical potential of hydrogen $-\Delta\mu$ becomes 0 until the system is fully hydrided. That is, Gibb's phase rule suggests an existence of constant pressure region in pressure-composition-isotherm (p - c - T), as exemplarily shown for V-H in Fig. 2.2.

The formation enthalpy ΔH^0 and formation entropy ΔS^0 can be estimated from such p - c - T at different temperatures according to the following relationship.

$$\frac{1}{2} \ln p = \frac{\Delta H^0}{RT} - \frac{\Delta S^0}{R} \quad (2.13)$$

By plotting $\log p_{H_2}$ vs. $1/T$ as exemplary shown in Fig. 2.3 (Van't Hoff plot), ΔH^0 and ΔS^0 can thus be derived from its slope and the intersection.

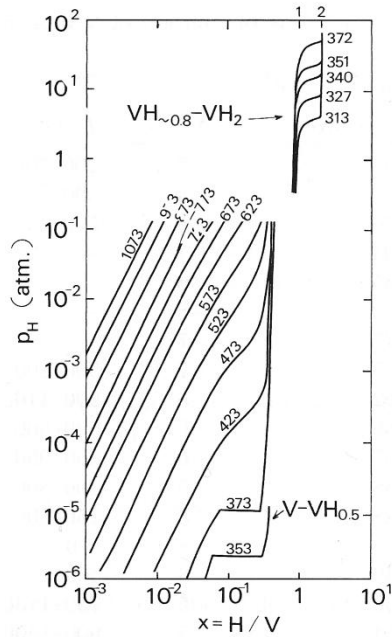


Fig. 2.2 Pressure-composition-isotherms (p - c - T) of V-H system at different temperatures (K) [Fukai05].

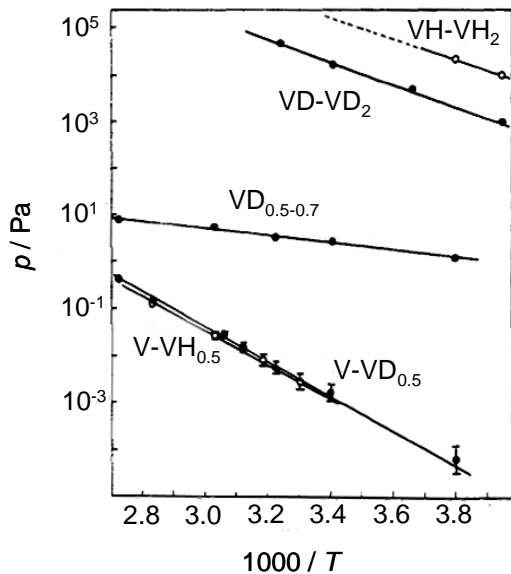


Fig. 2.3 Van't Hoff plot of the plateau pressure p against inverse temperature $1/T$ taken from [Papat82].

The enthalpy change (J/mol-H) and entropy change (J/Kmol-H) of the hydride formation can approximately be deduced from this plot by the Van't Hoff relationship, Eq. (2.13).

2.1.5 V-H and V-D systems

Phase diagrams of vanadium-hydrogen (V-H) and vanadium-deuterium (V-D) systems have been intensively investigated via XRD, DSC and DTA studies by Maeland and Schober [Mael64, Schob77] as summarized in ref. [HinMeII]. Asano *et al.* [Asano76] and Fukai *et al.* [Fukai75] have studied the same system in parallel around the same time. The agreement with the results by Schober was qualitatively good, except for some discussions on low temperature phases. Modified phase diagrams reproduced from Pesch [Pesc81] are shown in Fig. 2.4. The α -phase has V bcc lattice structure with random T site occupation.

The β_1 and β_2 -phases have tetragonally distorted bct lattices with a

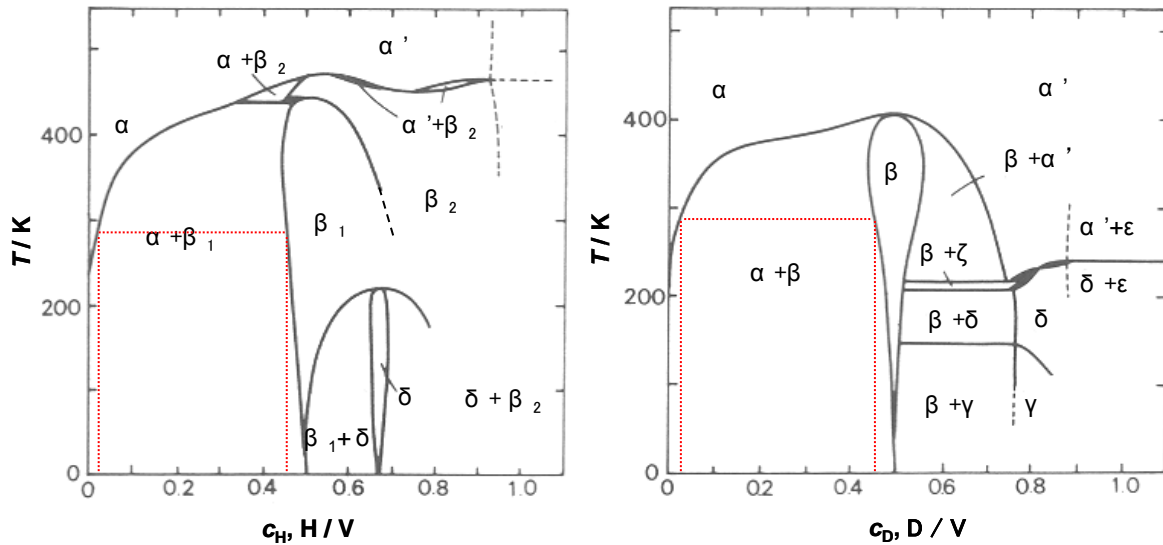


Fig. 2.4 V-H and V-D binary phase diagrams reproduced from [Pesc81]. Phase boundaries at 298 K (indicated by red dotted lines) are as follows.
 H-V: α -solubility = 0.03 H/V, $\alpha + \beta_1 = 0.03 - 0.47$ H/V, $\beta_1 = 0.47 - 0.67$ H/V
 D-V: α -solubility = 0.04 D/V, $\alpha + \beta = 0.04 - 0.47$ D/V, $\beta = 0.47 - 0.56$ H/V

length ratio $cla \sim 1.1$. Here, preferential O_z -site occupancy is reported [Wana72, Camb74, Takano74, Noda86, Marsh87]. The β -phase was assigned as a monoclinic structure with only a slight tilt of $\beta = 91^\circ$. Although, the difference between this structure and bct was not clearly confirmed due to experimental resolution of XRD [Asano76], the order \rightarrow disorder transition from $\beta_1 \rightarrow \beta_2$ -phase is proposed. In the (ordered) β_1 phase half of O_z sites are statistically occupied, while in the β_2 phase O_z sites are occupied with equal probability [Asano76]. Interestingly, the shift of the site occupancy from the T-site to the O_z -site occurs through a unique re-configuration of four the T-sites to a laterally distorted 4T-site [Sugi84]. This geometrical location is schematically shown in Fig. 2.5. Here, the $4T_{xy}$ -site has the same symmetry as the O_z -site occupancy. The other $4T_{yz}$ - or $4T_{zx}$ -sites have a 2-fold symmetry. The origin of this occupation is discussed to originate from a change of the self-trapping energy with lattice strain ε [Sugi84]. Hjorvarsson *et al*, [Olsson03] suggested that this site occupation of H in V is highly sensitive to stress state of the lattice. This property is indeed important for thin films, as they are usually subjected to large in-plane stress.

The phase boundaries of V-H and V-D, at room temperature (298 K), are indicated in Fig. 2.4. Except for the α -phase solubility, the miscibility gap of $\alpha + \beta$ agrees well for both of H-V and D-V (see red dotted lines). Details on the α -phase solvus-line are summarized by Schober [Schob77, Schob78] on pure V with impurity levels of C < 16, N < 10, O < 70 ppm.

The isotope effect on equilibrium pressures of the V-H and V-D systems, as determined for polycrystalline V-films of 500 nm thickness, is shown in Fig. 2.3. For the di-hydride formation an isotope effect is visible, but for the V_2H -hydride formation, it is not detectable: Both hydrides, the $VH_{0.5}$ and $VD_{0.5}$ are formed at 0.001 Pa at 298 K. The absence of an isotope effect on the plateau pressure of $V-VH(D)_{0.5}$ is consistent with a calorimetric study of Luo *et al.* [Luo90]. In this study, this feature is of highly importance because such almost identical property within $VH(D)_{0.5}$ allows direct comparison of H and D concentration and to alternatively use D for atom probe studies. The consequence on using D instead of H for atom probe analysis is described e.g. in Chap. 3.4.

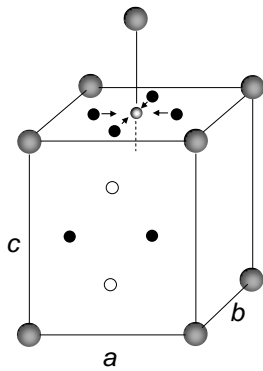


Fig. 2.5 Schematic drawing of $4T_{xy}$ site and $4T_{zy}$ or $4T_{zx}$ sites in a bct lattice ($a, b, c = x, y, z$). (after [Fukai05])

2.1.6 Fe (bcc) -H system

There is no study published on the equilibrium concentration of hydrogen in α -Fe at around room temperature up to now. Previously published data at $T = 473 \text{ K} - 1193 \text{ K}$ gives the hydrogen concentration c_H by following formula [FG76], which is based on Eq. (2.9).

$$\log_{10} c = \frac{1}{2} \log_{10} p - 2.25 - \frac{1268}{T} \quad (2.14)$$

Here, c is in wt%, p in Torr (= mmHg) and T in K. Provided that the H_2 pressure is at 0.001 Pa, the hydrogen concentration c_H in α -Fe will be $c_{H,\alpha} = 4.74 \times 10^{-8} \text{ H/Fe}$, assuming that Eq.(2.14) holds at 298 K. At the same pressure and temperature, V_2H ($H/V = 0.5$) starts to form. This suggests that the H atoms will be exclusively absorbed in V, and c_H in Fe is theoretically negligible when hydrogen is introduced in e.g. a multi-layered system of Fe and V.

Under the condition of ideal H solution, the difference of solubility defined as $k (= c_{H \text{ in Fe}} / c_{H \text{ in V}})$ calculated by following equation

$$k = \frac{c_{H\text{ in Fe}}}{c_{H\text{ in V}}} = \exp\left(\frac{\Delta G_V^0 - \Delta G_{Fe}^0}{RT}\right) \quad (2.15)$$

amounts to $\sim 10^{-10}$. Experimental solubility data of D in Fe at room temperature are currently not found. Some important thermodynamic parameters for different MH systems are tabulated in Table 2.1 by using different sources [FG76, Fukai05, Blei87, Papat82, Gries88, Schob77, Wick64, Läss84].

2.1.7 Pd-H and Pd-D system

The α -Pd phase solves hydrogen up to $c_H = 0.01$ H/Pd at 298 K, according to the phase diagram [Fries73]. Further hydrogen uptake gives an α' -phase with a plateau pressure of about 2×10^3 Pa at this temperature, which is at a much higher pressure than that of the formation of V_2H (0.001 Pa). At 0.001 Pa and at 298 K, the c_H and c_D are similarly calculated as shown in Eq.(2.11) and yield $c_H = 1.3 \times 10^{-5}$ H/Pd and $c_D = 4.9 \times 10^{-6}$ D/Pd, respectively. Similar estimation as Eq.(2.15) gives $k (= c_{H\text{ in Pd}}/c_{H\text{ in V}}) \sim 10^{-4}$. Thus, at 0.001 Pa, the hydrogen concentration c_H in Pd can be neglected compared to c_H in V for a layered stack of Pd and V.

In this study thin Pd film is deposited as capping layer to avoid oxidation of underlying V layer and to promote H absorption reaction. Details on the H adsorption on Pd surface can be found in Ref.[Chris88].

2.1.8 W-H system

W was used as one of the substrates for V and Fe/V films because H practically cannot solve in W. In fact, the H solubility extrapolated from high temperatures (1173 K – 2023 K) [FG76] to 298 K gives only $c_H = 2 \times 10^{-24}$ H/W. No hydride is reported. Phase diagrams of the binary W-H system are not available.

Table 2.1 Enthalpy change, entropy change and free energy change of Me-H reaction. Note that the values are for molH¹, but not molH₂⁻¹. The estimated H-solubility difference k is shown together.

	ΔH [kJ/mol H]	ΔS [J/Kmol H]	ΔG_{298K} [kJ/mol H]	Ref.	T [K]	k_{Me} (c_{Me}/c_V)
V-H	-32	-61	-14	[FG76]	373 - 773	1
	-27	-67	-7	[Fukai05]	423 - 773	
	-21.6	-52	-6	[Blei87]	316	
	-26	-47	-12	[Papat82]	253 - 373	
	-33	-	-	[Gries88]	293 - 328	
	-27	-	-	[Schob77]	200 - 473	
V-D	-27.5	-64	-8	[Blei87]	316	
	-28	-50	-13	[Papat82]	253 - 373	
	-26	-	-	[Schob78]	200 - 473	
V ₂ H	-35.6	-54	-20	[Fukai05]	273 - 373	
	-35	-42	-22	[Papat82]	253 - 373	
V ₂ D	-36	-46	-22	[Papat82]	253 - 373	
Pd-H	-10	-	-	[Gries88]	273 - 420	
	-9.7	-54	6	[Wick64]	323	
	-9.2	-53	7	[Läss84]	413	
Pd-D	-7.9	-53	8	[Wick64]	323	$\sim 10^{-4}$
	-7.5	-52	8	[Läss84]	413	
α Fe-H	29	-49	39	[Fukai05]	280 - 1184	$\sim 10^{-10}$
W-H	96	-42	118	[Fukai05]	1100 - 3070	$\sim 10^{-24}$

2.1.9 FeV-H system

In Fig. 2.6, binary phase diagram of FeV system is shown [Land08]. At room temperature (298 K), the solubility of Fe in V and V in Fe is 12 at% and 25 at%, respectively (indicated by red dot line). At 35at% Fe, the tetragonal σ phase (α -FeCr-type) exists. The lattice parameter of σ phase changes with Fe concentration and, is extremely larger ($a \sim 0.89$ nm, $c \sim 0.46$ nm at 35at% Fe) [Smith93] than that of Fe ($a = 0.286$ nm) or V ($a = 0.300$ nm).

It has been reported that the addition of Fe (up to 10at%) in V reduces H-solubility [Egu74]. According to the difference of lattice parameter

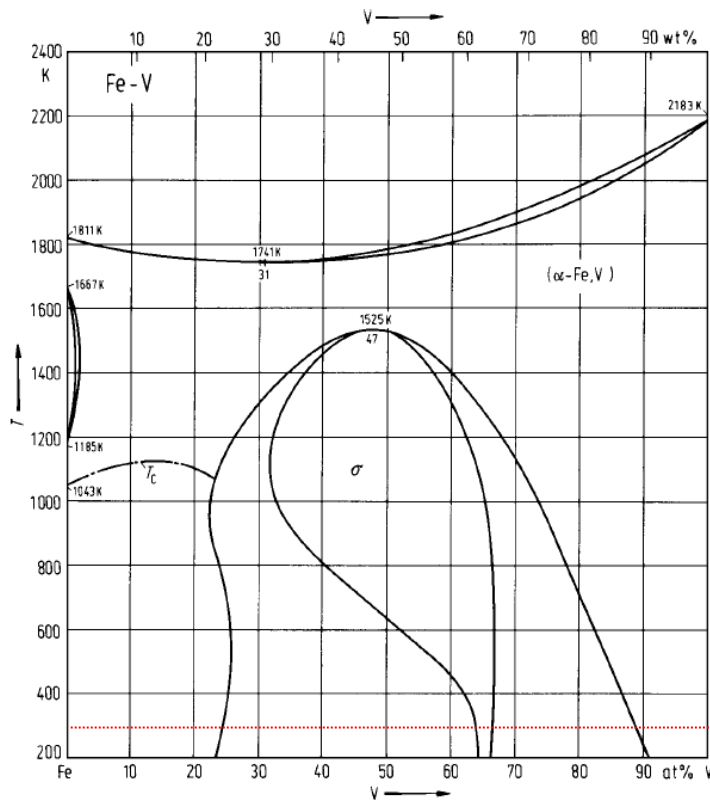


Fig. 2.6 Binary phase diagram of Fe-V [Land08]. Red dot line is drawn at 298 K, at which the solubility of Fe in V and V in Fe is 12 at% and 25 at%, respectively

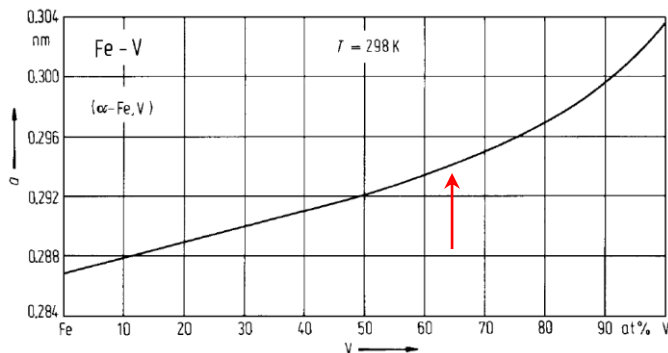


Fig. 2.7 Lattice parameter change of Fe-V solid solution phase at 298 K [Land08]. A strong deviation from the Vegard's law was reported at around 35at% Fe (65at% V) [Shiga78], as indicated by the red arrow.

between Fe and V, the lattice size decreases with increasing Fe concentration. This is exemplarily shown in Fig. 2.7 for FeV solid solution phase [Land08]. The deviation from Vegard's law is obviously observed at around 35at% Fe. Shiga *et al.* [Shiga78] have suggested that the localized magnetic moment of Fe atom breaks down at this concentration, with increasing V content. Change of the lattice parameter is believed to change available volume for H atom. Lebon *et al.* [Lebon10] demonstrated by Density Functional Theory (DFT) calculation that alloying of V with Fe, Mn and Cr decreases the volume for H. The result is consistent with the experimentally observed reduction of H-solubility by alloying.

2.2 Hydrogen induced volume expansion in thin films

For bulk M-H system without any mechanical restriction, the hydrogen induced volume expansion ε_0 (see Chap. 2.1.1) takes place homogeneously in 3 directions x, y and z and thus the hydrogen induced stress can be accommodated by such free expansion (Fig. 2.8 (a)). For thin films deposited on elastically hard substrates like Si or Al₂O₃, the expansion cannot occur in x and y directions (in-plane directions) as the films are mechanically clamped on the substrates (Fig. 2.8 (b)). In order to conserve the strain energy (a), additional expansion in the film normal direction (z) is necessary ($\Delta\varepsilon_{zz}$ in b). Here, corresponding biaxial compressive stress should also be accompanied (Fig. 2.8 (c)). It is known that this compressive stress can be as huge as several GPa [Lauda99] and that the underlying substrate shows even measurable curvature of substrate, when it is thin [Nörth06].

According to Hook's law ($\sigma = -M \cdot \varepsilon$) [Popov68], such compressive biaxial stress induced by hydrogen can be calculated simply from Young's modulus E and Poisson's ratio ν by Eq. (2.16), if

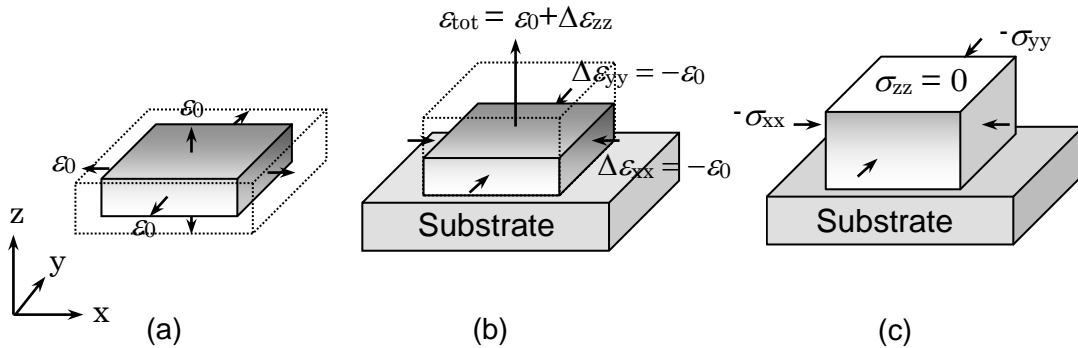


Fig. 2.8 Schematic drawing of hydrogen induced volume expansion. (a) Isotropic expansion of bulk metal or free-standing film (b) 1-dimensional expansion of a thin film on substrate (c) Biaxial stress in the film and corresponding expansion in out-of-plane direction

- (i) the film material is elastically isotropic (i.e. the stiffness anisotropy factor $m_{ani} = C_{11} - C_{12} - 2C_{44} = 0$, like for W, for example [Sand99]) and
- (ii) the in-plane configuration of the grain is homogeneous (i.e. isotropic in-plane texture with isotropic in-plane strain) [Lauda98].

$$\langle \sigma_{xx=yy} \rangle = -\frac{E}{(1-\nu)} \cdot \Delta \varepsilon_0 \quad (2.16)$$

By assuming that these conditions (i) and (ii) are fulfilled, the average in-plane stress $\langle \sigma \rangle$ in V film is calculated as $-12.8 \cdot c_H$ [GPa·H/V]. In this calculation, $\varepsilon_0 = 0.063 \cdot c_H$ [Mage76] is assumed and $E = 128$ GPa, $\nu = 0.37$. Corresponding total expansion in z direction ε_{tot} is expressed as follows.

$$\varepsilon_{tot} = \varepsilon_0 + \Delta \varepsilon_{zz} = \left(1 + \frac{2\nu}{1-\nu} \right) \cdot \varepsilon_0 \quad (2.17)$$

For V, $\varepsilon_{tot} = 0.137 \cdot c_H$.

However, the condition (i) cannot be established for most of metals [Sand99, Zhan07]. Since this study treats epitaxial V (110) films, elastic anisotropy and the corresponding stress are examined in the following section.

2.2.1 Directional dependence of E and ν

The relationship between strain and stress is given by Hook's law [Popov68]. For a cubic structure with isotropic symmetry, actual tensor components of stiffness and compliance can be reduced from 81 to 36 because only C_{11} , C_{12} and C_{44} are independent. Thus, the matrix of the elastic modulus is expressed as [Sand99, Dornh02, Nörth06],

$$\sigma = C_{ij} \cdot \varepsilon, \quad \varepsilon = S_{ij} \cdot \sigma \quad (2.18)$$

$$C_{ij} = \begin{pmatrix} C_{11} & C_{12} & C_{12} & 0 & 0 & 0 \\ C_{12} & C_{11} & C_{12} & 0 & 0 & 0 \\ C_{12} & C_{12} & C_{11} & 0 & 0 & 0 \\ 0 & 0 & 0 & C_{44} & 0 & 0 \\ 0 & 0 & 0 & 0 & C_{44} & 0 \\ 0 & 0 & 0 & 0 & 0 & C_{44} \end{pmatrix}, \quad S_{ij} = \begin{pmatrix} S_{11} & S_{12} & S_{12} & 0 & 0 & 0 \\ S_{12} & S_{11} & S_{12} & 0 & 0 & 0 \\ S_{12} & S_{12} & S_{11} & 0 & 0 & 0 \\ 0 & 0 & 0 & S_{44} & 0 & 0 \\ 0 & 0 & 0 & 0 & S_{44} & 0 \\ 0 & 0 & 0 & 0 & 0 & S_{44} \end{pmatrix} \quad (2.18)$$

For convenience, Voigt notation is usually used rather than the matrix notation if we consider stress-strain relationship on crystal directions as, 1=xx, 2=yy, 3=zz, 4=xy (yx), 5=xz (zx), 6=yz (zy). Specifically, if there is no shear strain assumed to occur (Fig. 2.6), $\varepsilon_4 = \varepsilon_5 = \varepsilon_6 = 0$.

In order to calculate the directional dependence of the elastic constants, the matrix notation is used. The elastic stiffness constants C_{ijkl} or the elastic compliance constants S_{ijkl} must be transformed by introducing a rotation matrix a .

$$S'_{ijkl} = {}^t a_{im} \cdot a_{jn} \cdot {}^t a_{ko} \cdot a_{lp} \cdot S_{mnop} \quad i, j, \dots, p = 1, 2, 3 \quad (2.20)$$

The transposed matrix ${}^t a_{ij}$ gives now the rotation of x, y and z axes as follows.

$${}^t a_{ij} = \begin{pmatrix} a_{11} & a_{21} & a_{31} \\ a_{12} & a_{22} & a_{32} \\ a_{13} & a_{23} & a_{33} \end{pmatrix} = \begin{pmatrix} \sin \theta \cos \phi & \cos \theta \cos \phi & -\sin \phi \\ \sin \theta \sin \phi & \cos \theta \sin \phi & \cos \phi \\ \cos \theta & -\sin \theta & 0 \end{pmatrix} \quad (2.21)$$

The definitions of θ and ϕ with respect to the crystal axes are drawn in Fig. 2.9 ($0^\circ \leq \theta < 180^\circ$ and $0^\circ \leq \phi < 360^\circ$).

The directional dependence of E and ν can then be calculated by Eq. (2.22) and by Eq. (2.23), respectively.

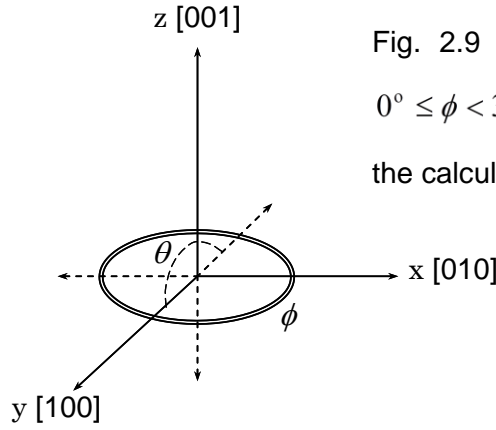


Fig. 2.9 Rotation of θ $0^\circ \leq \theta < 180^\circ$ and ϕ $0^\circ \leq \phi < 360^\circ$ respect to the crystal axes for the calculation of directional dependence of E .

$$\frac{1}{E'} = S'_{11} = S'_{1111} = a_{1m} a_{1n} a_{1o} a_{1p} S_{mnop}, \quad (2.22)$$

$$\frac{1}{E'} = S_{11} - 2 \left(S_{11} - S_{12} - \frac{1}{2} S_{44} \right) (a_{11}^2 a_{12}^2 + a_{11}^2 a_{13}^2 + a_{12}^2 a_{13}^2)$$

$$\nu' = -\frac{S'_{12}}{S'_{11}},$$

$$\nu' = -\frac{S_{12} + 2 \left(S_{11} - S_{12} - \frac{1}{2} S_{44} \right) (a_{11}^2 a_{12}^2 + a_{12}^2 a_{22}^2 + a_{13}^2 a_{23}^2)}{S_{11} - 2 \left(S_{11} - S_{12} - \frac{1}{2} S_{44} \right) (a_{11}^2 a_{12}^2 + a_{11}^2 a_{13}^2 + a_{12}^2 a_{13}^2)} \quad (2.23)$$

The elastic compliances S_{ij} are summarized e.g. by Gray [Gray72] and Hirth [Hirth68] for various metals. For V, $S_{11} = 6.83$ (TPa) $^{-1}$, $S_{12} = -2.34$ (TPa) $^{-1}$, $S_{44} = 23.48$ (TPa) $^{-1}$. For Fe, $S_{11} = 7.72$ (TPa) $^{-1}$, $S_{12} = -2.85$ (TPa) $^{-1}$, $S_{44} = 9.02$ (TPa) $^{-1}$. The results of these calculations on V and Fe using S in Ref. [Hirth68] are shown in Fig. 2.10 (a) and (b).

A completely opposite directional dependence of the elastic modulus E is visible for V and Fe. In the directions from $[-1-10]$ to $[001]$, E varies

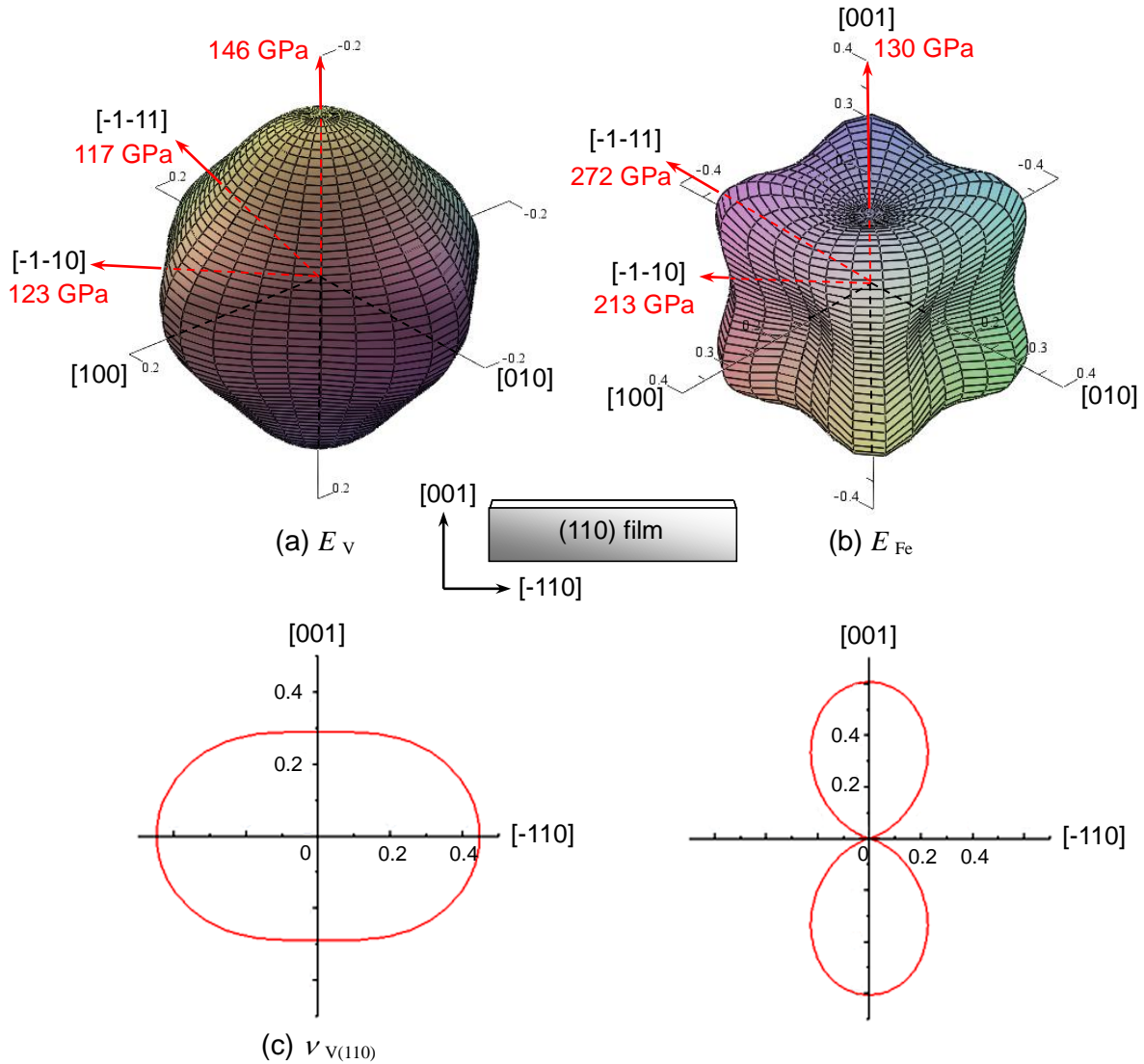


Fig. 2.10 Directional dependence of E and ν of V and Fe calculated by Eqs. (2.22) and (2.23). (a) E_V (b) E_{Fe} (c) $\nu_{V(110)}$ (d) $\nu_{Fe(110)}$. Respective sample geometry of (110) film applied for stress measurement in this study is shown together. Completely opposite directional dependence of E between V and Fe is confirmed. Poisson's ratio shows strong anisotropy in (110) plane, while those in (100) and (111) planes show isotropic distribution (not shown).

between 123 GPa and 146 GPa for V and, for Fe, it varies between 213 GPa and 130 GPa. The Poisson's ratios which are plotted in Fig. 2.10 (c) and (d) for V and Fe, respectively, show a strong anisotropy in (110) plane. This is also reported in the work of Zhang [Zhan07]. Poisson's ratios of V and Fe in (100) and (111) planes (not shown) show isotropic distribution.

2.2.2 Hydrogen induced expansion and stress in (110) films

The stress σ is the partial derivative by strain $d\varepsilon$ of the strain energy density f . For an isotropic linear elastic body, f_{el} is

$$\begin{aligned} f_{el} &= \int_0^{\varepsilon_{ij}} \sum_{ij} \sigma_{ij} d\varepsilon_{ij} \\ & \left(ij \leftrightarrow kl \therefore C_{ijkl} = C_{klij} \right) \\ &= \frac{1}{2} C_{ijkl} \varepsilon_{ij} \varepsilon_{kl} + const. \end{aligned} \quad (2.24).$$

Here, introduction of the Voigt notation, for convenience, yields

$$f_{el} = \frac{1}{2} C_{11} (\varepsilon_1^2 + \varepsilon_2^2 + \varepsilon_3^2) + C_{12} (\varepsilon_1 \varepsilon_2 + \varepsilon_1 \varepsilon_3 + \varepsilon_2 \varepsilon_3) + \frac{1}{2} C_{44} (\varepsilon_4^2 + \varepsilon_5^2 + \varepsilon_6^2) \quad (2.25).$$

To calculate f_{el} for the (110) plane, a rotation versus z and xy axes with -90° and 135° is needed. From Eq. (2.21) this rotation manipulation gives

$$a_{ij} = \begin{pmatrix} \frac{-1}{\sqrt{2}} & 0 & \frac{1}{\sqrt{2}} \\ \frac{1}{\sqrt{2}} & 0 & \frac{1}{\sqrt{2}} \\ 0 & 1 & 0 \end{pmatrix}. \quad (2.26).$$

By tensor transformation for strain the corresponding strain components are now expressed as follows (shear strain is neglected).

$$\varepsilon_{ij} = \begin{pmatrix} \frac{1}{2}(\varepsilon_1 + \varepsilon_3) & \frac{1}{2}(\varepsilon_3 - \varepsilon_1) & 0 \\ \frac{1}{2}(\varepsilon_3 - \varepsilon_1) & \frac{1}{2}(\varepsilon_1 + \varepsilon_3) & 0 \\ 0 & 0 & \varepsilon_2 \end{pmatrix} \quad (2.27)$$

By combining Eq. (2.25) and Eq. (2.27), the strain energy density f_{el} is obtained by the following equation.

$$f_{el} = \frac{1}{4} C_{11} (\varepsilon_1^2 + 2\varepsilon_2^2 + 2\varepsilon_1 \varepsilon_3 + \varepsilon_3^2) + \frac{1}{4} C_{12} (\varepsilon_1^2 + 4\varepsilon_1 \varepsilon_3 + 4\varepsilon_2 \varepsilon_3 + \varepsilon_3^2) + \frac{1}{2} C_{44} (\varepsilon_3 - \varepsilon_1)^2 \quad (2.28)$$

The condition of the free expansion ε_3 is assumed (Fig. 2.8) and thus the stress in z direction is 0 ($\partial f_{el} / \partial \varepsilon_3 = \sigma_3 = 0$).

For V (110) film, the hydrogen induced expansion ε_3 is then given by

$$\varepsilon_3 = \varepsilon_{tot} = \varepsilon_0 + \Delta \varepsilon_{zz} = \left(1 + \frac{C_{11} + 3C_{12} - 2C_{44}}{C_{11} + C_{12} + 2C_{44}} \right) \cdot \varepsilon_0, \quad \varepsilon_0 = 0.063 \cdot c_{H(H/V)} \quad (2.29).$$

$$\varepsilon_3 = \varepsilon_{tot} = 0.135 \cdot c_{H(H/V)}$$

The biaxial stress σ_1 ([1-10] as longitudinal direction of sample) and σ_2 ([001] as transversal direction of sample) can separately be given by

substitution of Eq. (2.29) in Eq. (2.28).

$$\sigma_{1=[110]} = \frac{\partial f_{el(110)}}{\partial \varepsilon_1} = \frac{4C_{44}(C_{11} + C_{12})\varepsilon_1 + 4C_{12}C_{44}\varepsilon_2}{C_{11} + C_{12} + 2C_{44}}, \quad (2.30)$$

$$\sigma_{2=[001]} = \frac{\partial f_{el(110)}}{\partial \varepsilon_2} = \frac{4C_{12}C_{44}\varepsilon_1 + \{C_{11}^2 - 2C_{12}^2 - C_{11}(C_{12} + 2C_{44})\}\varepsilon_2}{C_{11} + C_{12} + 2C_{44}} \quad (2.31)$$

For the same biaxial expansion, $\varepsilon_1 = \varepsilon_2 = -\varepsilon_0 = -0.063c_H$, the biaxial stress in V (110) film is calculated by following equations, with published stiffness values of $C_{11} = 229$ GPa, $C_{12} = 119$ GPa, and $C_{44} = 43$ GPa for bulk V [Bolef61].

$$\begin{aligned} \sigma_{1=[110]}[\text{GPa}/c_H] &= \frac{\partial f_{el(110)}}{\partial \varepsilon_1} = -4 \cdot \left(\frac{C_{44}(C_{11} + 2C_{12})}{C_{11} + C_{12} + 2C_{44}} \right) \cdot \varepsilon_0 \\ &= -11.7 \cdot c_H \end{aligned} \quad (2.32)$$

$$\begin{aligned} \sigma_{2=[001]}[\text{GPa}/c_H] &= \frac{\partial f_{el(110)}}{\partial \varepsilon_2} = - \left(\frac{2C_{44}(C_{11} + 2C_{12}) + C_{11}^2 + C_{11}C_{12} - 2C_{12}^2}{C_{11} + C_{12} + 2C_{44}} \right) \cdot \varepsilon_0 \\ &= -13.3 \cdot c_H \end{aligned} \quad (2.33)$$

The negative sign means compressive stress. In a σ - c_H curve, the linear elastic region is characterized by the slope of $-11.7 \sim -13.3$ GPa/ c_H depending on the direction of bending.

3. Experimental

3.1 Sample preparation

The thin film samples were prepared by UHV sputter deposition system. The base pressure of the vacuum chamber can hold the order of 10^{-8} Pa when no heating of the sample is applied. In order to prepare coarse-grained or epitaxial samples it is mostly necessary to heat the substrate. In this system, it is possible to heat the substrate up to 1073 K. While heating the substrate at this temperature the base pressure increases typically up to 10^{-5} Pa due to degas and gradually stabilizes down to 10^{-6} Pa. Subsequent deposition was carried out only after the pressure stabilized. The Al_2O_3 substrates were cleaned by acetone and isopropanol before introduction to pre-evacuation chamber. After reaching at 10^{-5} Pa the sample was transferred to the sputtering chamber. The target holder in the system is rotational and can mount four targets at maximum. The

Table 3.1 Conditions for sputter deposition

Sputtering gas	Ar (purity: 99.9999%)	
Sputtering gas pressure [Pa]	$5 \times 10^{-3} \sim 1 \times 10^{-2}$	
Substrate-target distance [cm]	15	
Target purity (Fe, V, Pd) [%]	> 99.9	
Energy of Ar^+ [eV]	880	
RF power [W]	76	
Substrate, size	For flat films : Al_2O_3 (0001) or (11-20)	
	<i>In-situ</i> XRD : 10 mm x 10 mm x 0.5 mm	
	Stress measurement : 30 mm x 7 mm x 0.2 mm	
	Acoustic emission : 10 mm x 7 mm x 0.2 mm	
Deposition rate [nm / min.]	Pd	0.95
	V	0.35
	Fe	0.70
Substrate temperature [K]	297 ~ 1073	

Fe/V multi-layered samples were prepared by alternative rotation of the target holder manually. This system is ideally so designed for nm-order

thin film preparation that the low ion current density can be applied and therefore the sputtering rate is approximately 10 times smaller (less than 1 nm min^{-1} .) than that of the other systems operated with hot cathode. Additionally, the UHV-STM system is equipped directly to the sputter chamber, as illustrated in Fig. 3.1.

The orientation of the substrate, deposition temperature and the thickness were varied on purposes of experiments. Typical sputtering parameters are summarized in Table 3.1. Two different orientations of sapphire substrate, (0001) and (11-20) supplied by Crystec GmbH were used to investigate probability of different growth orientation. Some specified conditions will be described on each result. Preparation of Fe/V multi-layered film was carried out typically at 343 K after deposition of V 21 nm buffer layer at 1073 K to ensure epitaxial growth of Fe/V. For atom probe analysis, sharpened W tip was used as substrate for V and Fe/V films because the lattice mismatch between them is relatively small (~

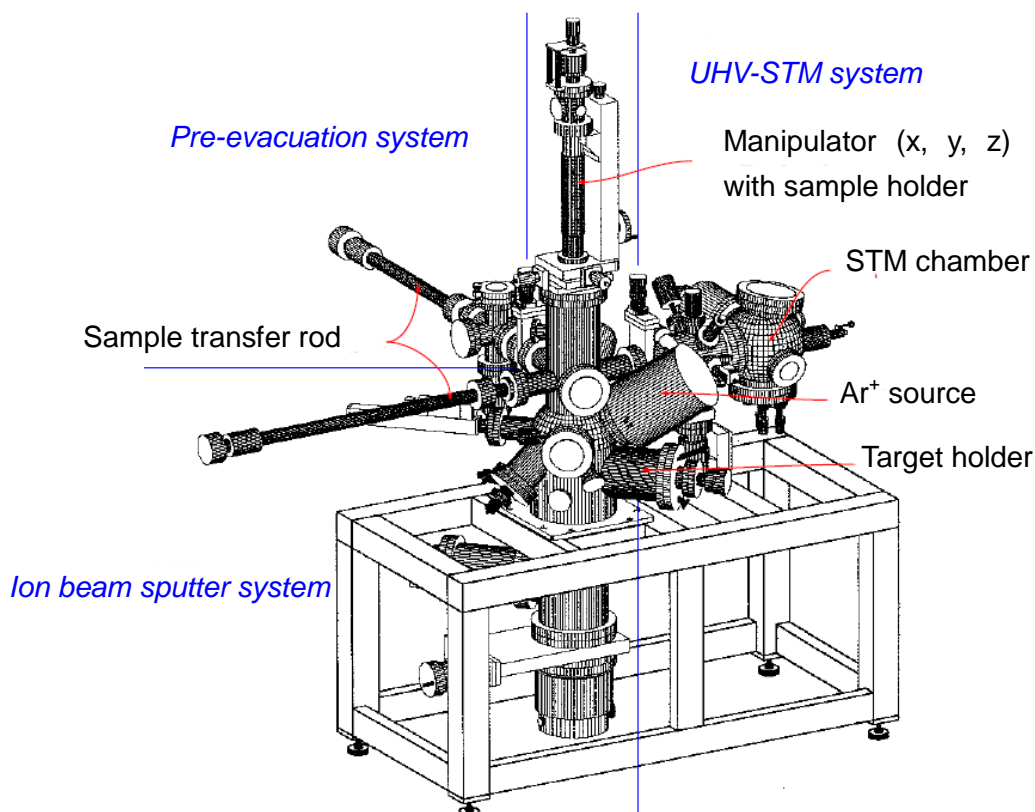


Fig. 3.1 Ar ion beam sputtering system used in this study (The picture was taken from Ref. [Nörth06]). The system consists of 3 parts; pre-evacuation chamber, sputter chamber and STM chamber as divided by blue lines. The manipulator is capable of translational motion in x, y and z directions. The target holder is a cube-shaped Cu block with water cooling tube. Pd, V and Fe targets were mounted on this cube so as to enable multi-layered film fabrication.

5%) and W is one of the suitable element for atom probing owing to its high mechanical strength. In case of deposition on W substrate, the substrate temperature was kept at 298 K. A detailed description about W substrate preparation is found in Chap. 3.5.1.

All of the samples prepared were followed by capping of Pd over-layer in order to prevent oxidation and to facilitate subsequent hydrogen absorption.

3.2 X-ray diffraction (XRD) and X-ray reflectivity (XRR)

3.2.1 XRD

The microstructure, initial strain state, texture and lattice expansion upon hydrogen uptake have been investigated by X-ray diffraction (XRD). For the samples without hydrogen loading the diffraction measurement was carried out with X'pert MRD (Philips, Co K α). Additionally to normal 2θ - θ scans, rocking curves for some films were recorded to determine the crystal quality of the films. By Bragg's law, the peak position in 2θ gives the corresponding interplanar distance d . For cubic structure, lattice parameter a can be calculated by following relationship with $(h\ k\ l)$ and its measured interplanar distance d [Culli78].

$$a = d\sqrt{h^2 + k^2 + l^2} \quad (3.1)$$

Additionally, the full width at half maximum (FWHM) of the peak gives information about the domain size or about the lattice coherency in the out-of-plane direction of the film [Culli78]. For the determination of this XRD domain size, Scherrer's formula was applied where;

$$t = \frac{0.9\lambda}{B \cos \theta_B} \quad (3.2)$$

t : domain size, λ : wavelength, B : FWHM and θ : peak position.

Unfortunately, initial in-plane stress contribution has to be neglected because of the thin film condition where only one diffraction peak typically is found. The calculated domain sizes are, therefore, usually lower limits for the true domain size.

In case of the multi-layered film, the total X-ray scattering intensity is a sum of that in the individual multi-layer constituents (Fe and V, in this study) and thus the XRD patterns are different from that of single layered film. These patterns can be calculated in a simple way by step model

[McWhan83, Full92] by assuming an average lattice spacing d_0 as

$$d_0 = \frac{n_{Fe}d_{Fe} + n_Vd_V}{n_{Fe} + n_V} = \frac{\Lambda}{n} \quad (3.3)$$

Here, n is the number of lattice planes with d and Λ is the double layer thickness. Through the following equations, the total scattering intensity can be calculated,

$$\begin{aligned} I &= I_N(I_{Fe} + I_V + I_{FeV}) \\ &= \frac{\sin^2(\pi n N)}{\sin^2(\pi n)} \left[f_{Fe}^2 \frac{\sin^2\left(\pi n_{Fe} \frac{d_{Fe}}{d_0}\right)}{\sin^2\left(\pi \frac{d_{Fe}}{d_0}\right)} + f_V^2 \frac{\sin^2\left(\pi n_V \frac{d_V}{d_0}\right)}{\sin^2\left(\pi \frac{d_V}{d_0}\right)} \right. \\ &\quad \left. + 2f_{Fe}f_V \cos(\pi n) \frac{\sin\left(\pi n_{Fe} \frac{d_{Fe}}{d_0}\right) \sin\left(\pi n_V \frac{d_V}{d_0}\right)}{\sin\left(\pi \frac{d_{Fe}}{d_0}\right) \sin\left(\pi \frac{d_V}{d_0}\right)} \right] \end{aligned} \quad (3.4)$$

where N is the repetition number of the double layer, f is the atomic scattering factor, which can be approximated by the atomic number. The continuous variable l is defined as following for given 2θ , with X-ray wave length λ .

$$l = \frac{2d \sin \theta}{\lambda} \quad (3.5)$$

By these equations, XRD patterns can be simulated with arbitrary given n_{Fe} , n_V , d_{Fe} and d_V . Thus, fitting of an experimentally given XRD pattern of multi-layered film by Eq. (3.4) allows a structure refinement,

Texture measurement enables to determine in-plane structure. The epitaxial relationship between the film and the substrate can also be investigated. For stress measurement it is of crucial information in order to calculate stress value correctly.

3.2.2 XRR

The film density, single layer thickness l and surface or interface roughness σ of the samples were determined by X-ray reflectivity (XRR) measurements [Parra54, Tolan99]. XRR method is a non-destructive and non-contact technique for thickness determination between 2 - 200 nm with a precision of about 0.1 – 0.3 nm. This can be carried out by using

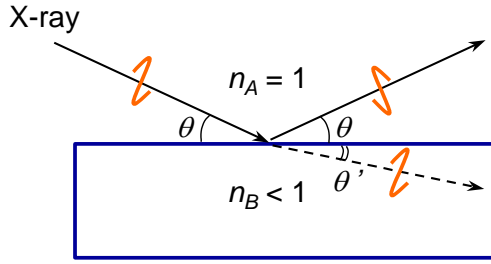


Fig.3.2 Schematic illustration of reflecting and refracting x-ray

normal 2θ geometry but with well-collimated optical condition at glazing angle in X'pert MRD.

Below the so-called as critical angle θ_c where the reflected intensity abruptly drops, total reflection of x-ray occurs ($n_A=1$ in Fig.3.2). At θ_c the refraction of x-ray in the material starts to take place. The refraction index n of x-rays is slightly smaller than 1 ($n_B < 1$) and expressed as;

$$n = 1 - \delta - i\beta < 1 \quad (3.6)$$

where δ as real part indicates dispersion and β as imaginary part shows absorbance, respectively. The δ and the β have following relationship between the density ρ [Walla95].

$$\delta = \left(\frac{r_e}{2\pi} \right) \rho_i N_A \lambda^2 \left(\frac{Z_i + f_i'}{M_i} \right) \quad (3.7)$$

$$\beta = \left(\frac{r_e}{2\pi} \right) \rho_i N_A \lambda^2 \left(\frac{f_i''}{M_i} \right) \quad (3.8)$$

Here, N_A is Avogadro's number, λ is the wavelength of the x-rays, r_e is the classical electron radius, Z_i is the number of electrons per atom, M_i is the atomic weight and f_i' , f_i'' are the atomic scattering factors.

By Snell's law, the refraction angle θ of x-ray can be expressed as

$$\cos \theta = n_B \cos \theta' \quad (3.9)$$

At the proximity of θ_c the absorbance can be neglected as a first approximation and $\theta_c = \theta$.

$$\cos \theta = n = 1 - \delta - i\beta \cong 1 - \delta \quad (3.10)$$

$$\theta = \cos^{-1}(1 - \delta) [\text{rad}] \quad (3.11)$$

$$\approx \sqrt{2\delta} [\text{deg.}]$$

From (3.7) and (3.11) the density of the material can be calculated by measuring θ_c .

At angles θ greater than θ_c , the x-ray penetrates in the material. If the

optical density of the material varies in vertical direction i.e. metal film layers are on a substrate, the interference of refracted x-ray from the films and substrate can be recorded as phase difference at each interface, which is analogous to Bragg's condition.

The m -th interference maximum for a path difference $\Delta = m\lambda$, is located at

$$m\lambda = \Delta = 2l\sqrt{\sin^2 \theta_m - \sin^2 \theta_c} \quad (3.12)$$

where m is an integer. From the difference of 2 neighboring maxima, the thickness l can be derived by Eq. (3.12).

The surface roughness, interface roughness or composition diffuseness in 2 different layers can also be evaluated as these also change the electron density (diffuseness changes δ/β). With help of different interface profile functions developed by Stearns [Stear98], the interface imperfections can be evaluated. Details of the formalism are found in [Parra54].

In Fig.3.3 a simulated example of XRR curve of a V 100-nm thick film on a Al_2O_3 (11-20) substrate capped by Pd 20-nm thick film is shown. The simulation was done by IMD developed by Windt [Windt98]. The information included in XRR curve is schematically illustrated therein. There are 2 type of fringes found in the figure. The finer fringe represents 100-nm thick V, while the wider fringe is for Pd 20 nm. By fitting experimentally obtained XRR curve with that of simulated by IMD software the parameters shown above can be refined.

Additionally, the interface roughness can be compared with that obtained in atom probe measurement.

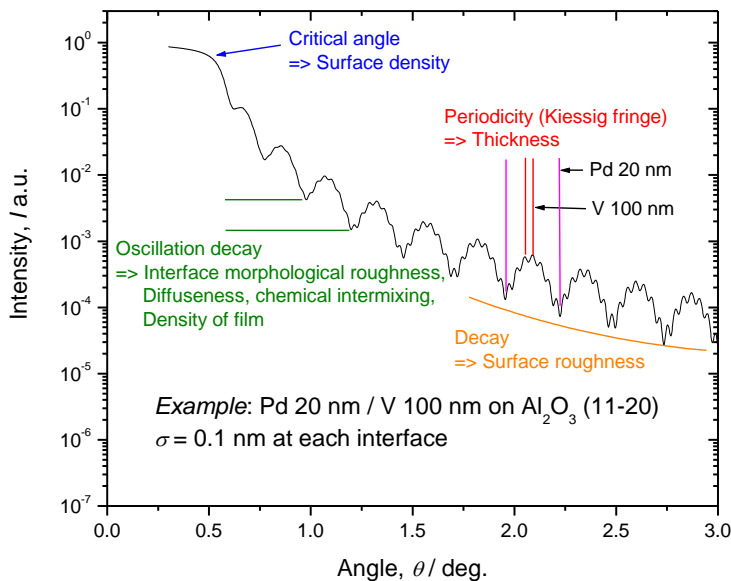


Fig.3.3 An example of simulated XRR curve by IMD [Windt98] on Pd 20 nm / V 100 nm on Al_2O_3 (11-20) substrate and different information drawn out of it.

3.2.3 *In-situ* XRD during hydrogen loading

In-situ XRD measurement during electrochemical hydrogen loading is one of the main scopes of this study. At B2 beam line of HASYLAB, DESY in Hamburg these *in-situ* XRD data were collected using a specially designed electrochemical loading cell developed by “Hydrogen in Metals group” in Göttingen University (described in Chap. 3.3.2). The sample in this cell is mounted on Euler cradle so that the rotation and tilt of the sample can be adjusted (see Fig. 3.4). In each loading cycle a known amount of hydrogen is loaded step-by-step in the sample and at each step the diffractogram is recorded. Fig. 3.5 shows an example of result showing the whole diffractograms recorded for V-Fe3at% 100 nm single layered film capped with Pd 20 nm at each hydrogen concentration. The shift of V peak

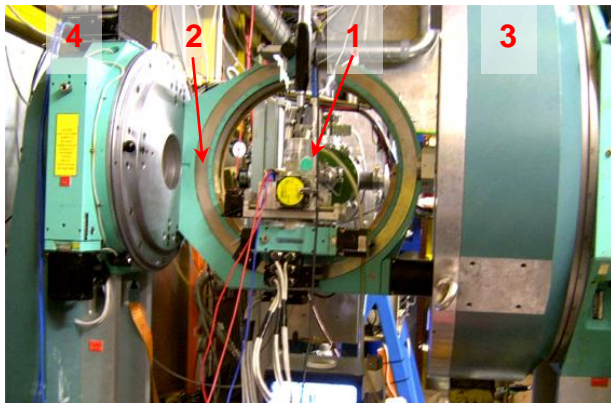


Fig. 3.4 The experimental station at HASYLAB B2.

- 1: Electrochemical loading cell,
- 2: Euler cradle,
- 3: Goniometer for detector,
- 4: Goniometer for sample

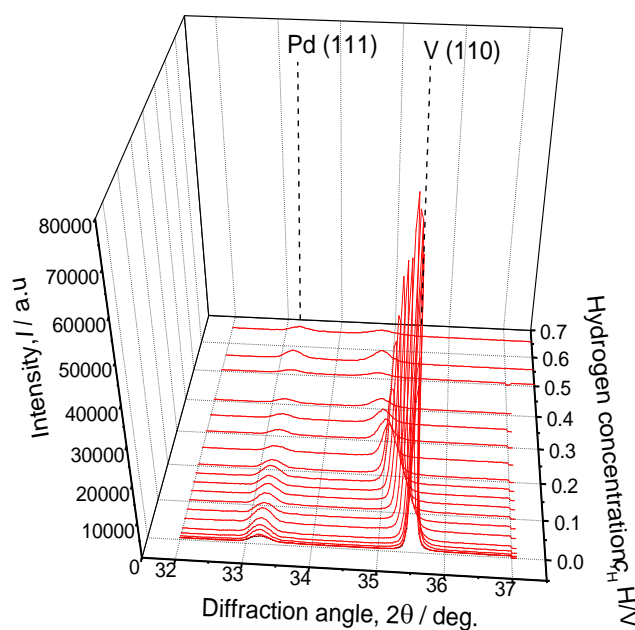


Fig. 3.5 Diffractograms of V-Fe3at% 100 nm single layer capped with Pd 20 nm at each hydrogen concentration recorded at HASYLAB B2 ($\lambda = 0.119$ nm) The V(110) peak shifting to the left means the lattice expansion upon H uptake.

position induced by hydrogen absorption, indicating lattice expansion can be clearly seen. The x-ray wavelength used in this experiment was 0.119 or 0.129 nm, depending on the mirror setting.

3.3 Electrochemical hydrogen loading

3.3.1 Electromotorical Force (EMF) measurement

The hydrogen loading treatment for the films deposited on Al₂O₃ substrates were carried out electrochemically, by using a house-made current pulse source in the Institut für Materialphysik, Göttingen University. The simplest loading set up composed of this current source, impedance converter, a reference electrode (Ag/AgCl_{sat.}), a counter electrode (Pt or Pd) and electrolyte as 1 : 2 (vol.) mixture of H₃PO₄ (85%) and Glycerin (85%).

A known amount of hydrogen can be charged step-by-step in the sample according to Faraday's law. At each loading step, hydrogen ion produced at the sample surface diffuses in and the process is observed as a change of electromotorical force (EMF) curve until it equilibrates. The EMF value at equilibrium as a measure of the chemical potential of hydrogen is directly translated into hydrogen partial pressure by Nernst equation [Atkins82].

$$p_{H_2} = \exp\left(\frac{(E - E_0)nF}{RT}\right) \quad (3.13)$$

Here, E is the measured EMF value, E_0 is the standard potential of reference electrode (0.2223 V for the Ag/AgCl saturated electrode at 298 K), n is the number of electrons related to the reaction ($n = 1$ for hydrogen), F is the Faraday constant, R is the gas constant and T is absolute temperature.

Consequently, a pressure-composition isotherm (p - c - T) can be drawn from one measurement. A schematic picture of hydrogen loading flow is illustrated in Fig. 3.6.

On purposes of *in-situ* measurement in this study, the basic H loading set up was combined with an induction gauge for film stress measurements, with AE sensor for AE measurements and with XRD at HASYLAB, respectively. Some special H loading cells used for these measurements are shown in the next section.

3.3.2 Hydrogen loading cell for *in-situ* XRD

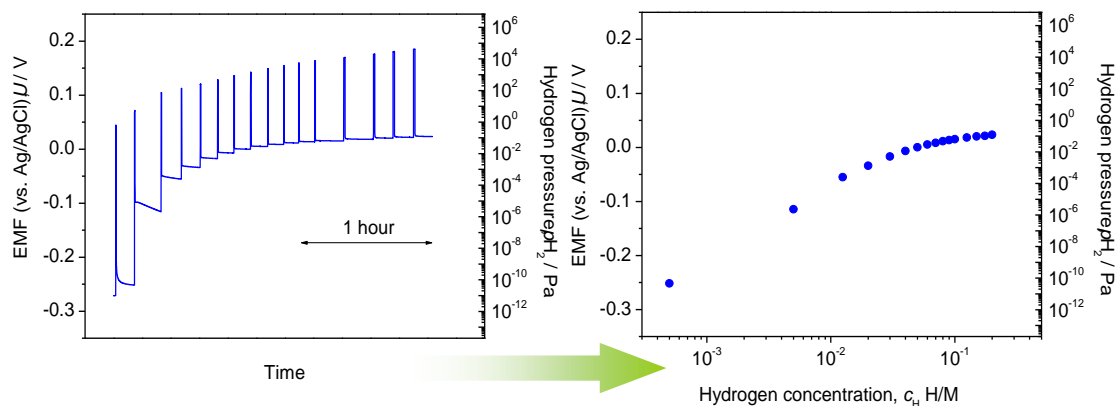


Fig. 3.6 A schematic picture showing H loading pulses (left) and a p - c - T curve derived from a series of the equilibrium values of EMF (right) via Eq. 3.13.

In Fig. 3.7, the loading cell for *in-situ* XRD measurements at HASYLAB is shown. Original cell design was developed by N.M. Jisrawi from Brookhaven National Laboratory (BNL) and further optimization was done by M. Dornheim [Dornh02]. The level of electrolyte in the cell can be controlled by the injector. During the XRD scan the electrolyte is removed by this injector and for the next loading step it again covers the sample surface.

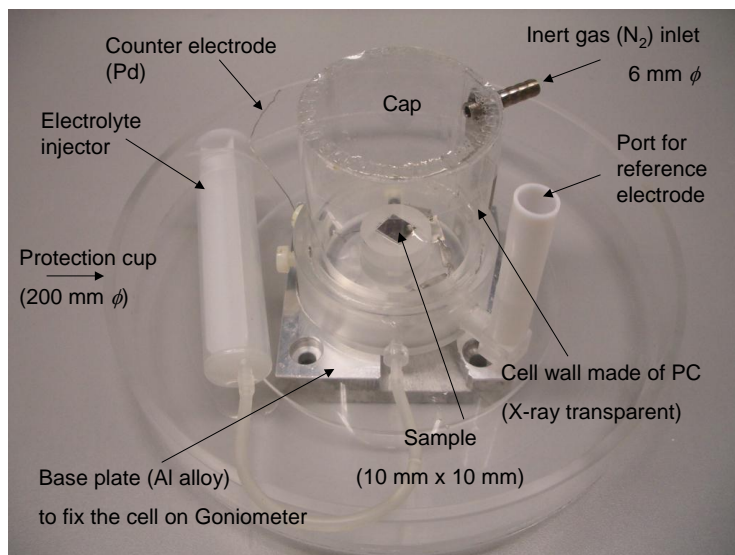


Fig. 3.7 The H loading cell used for *in-situ* XRD at HASYLAB. Original design was made by N.M. Jisrawi.

The N_2 port is important to prevent H-loss from the sample. During the scan the sample surface is exposed to atmosphere and thus any oxygen at the surface can form H_2O . To avoid this, N_2 gas was continuously flown into the cell during the whole measurement and kept under inert atmosphere.

3.3.3 Hydrogen loading cell for *in-situ* stress measurement

The stress measurement was conducted in order to investigate in-plane stress response upon hydrogen absorption in the film. According to the linear elasticity theory the compressive stress development should have a known slope in the elastic range and deviates when any plastic deformation occurs. The obtained results are discussed from this point of view.

For the stress measurement, a set up schematically shown in Fig. 3.8 was used. This set up was developed in the study of Nikitin [Nikit08]. The cell itself, shown as blue line, has the holder to grab the sample as to be a cantilever. One side of the sample is now fixed and is adjusted so that the backside of the sample connected with a small Pd plate comes close to the induction gauge mounted at the bottom of the cell. The distance between the metal plate i.e. the sample and the gauge can be measured as voltage in a certain range, where the voltage has linear relationship with the distance.

According to the calibration of the sensor used in this study, this linear sensibility τ was $7.6 \text{ mV}/\mu\text{m}$ (for Pd plate). The hydrogen absorption will cause in-plane stress in the film and the entire sample bends and the curvature radius varies as a result of elastic response as shown in the figure. The resulting change of sample-gauge distance z is detected as change of capacitance ΔU . Therefore,

$$z = \frac{\Delta U}{\tau} \quad (3.14)$$

The radius of curvature R is therefore calculated from z and length of the

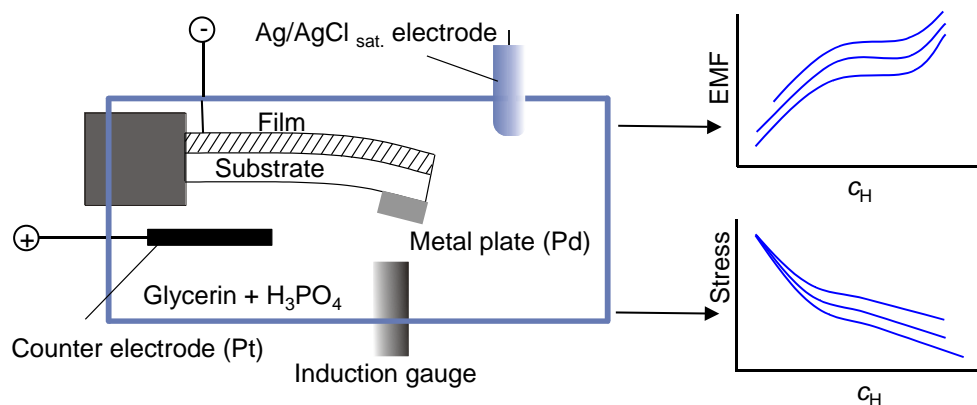


Fig. 3.8 Schematic picture of *in-situ* stress measurement set up during EMF measurement. EMF data and stress data can be obtained simultaneously.

sample L as

$$R \approx \frac{L^2}{2z} \quad (3.15)$$

From the curvature radius obtained, the in-plane stress in the film can be calculated by Stoney's formula [Ston09].

$$\sigma = \frac{E_s \cdot t_s^2}{6t_f(1-\nu_s)} \cdot \frac{1}{R} \quad (3.16)$$

Here, E_s is Young's modulus of substrate, ν_s is Poisson's ratio of the substrate, t_s and t_f is thickness of the substrate and of the film, respectively.

Only the total thickness of V was taken into consideration for t_f in this study, as the hydrogen is absorbed practically only in the V layer. Hydrogen absorption in Pd cap and Fe layers is negligible (see H solubility data in Chap. 2).

3.3.4 Acoustic emission (AE)

AE technique has been applied only for bulk samples. In this study, this application was extended to thin film samples. In the frame of joint research project with P. Dobron and J. Cizek in Charles University in Prague of the Czech Republic, acoustic emission (AE) measurement was carried out. The objective was to focus on mechanical response of thin films during hydrogen absorption e.g. dislocation's motion, creation of film bucking and subsequent detachment. Detailed description on this method

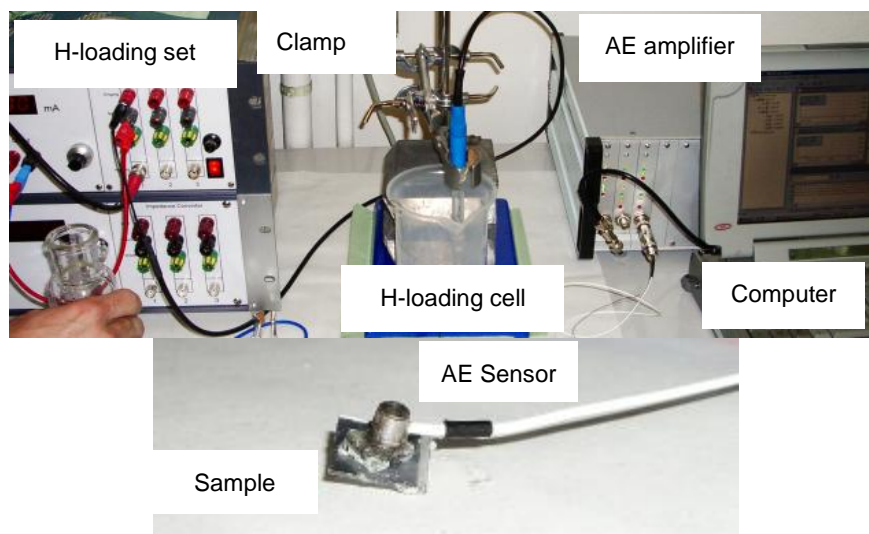


Fig. 3.9 An overview of AE measurement set up. The sensor is mounted by glue on the back side of the substrate so that only the film plane is in contact with the electrolyte. Actual sample holder is illustrated in Fig. 3.10.

is found for instance in Ref. [Mill87].

An overview of the experimental set up is shown in Fig. 3.9 and in Fig. 3.10. The AE measurements were performed *in-situ* during the electrochemical hydrogen loading with a computer-controlled DAKEL-XEDO-3 AE system. Threshold voltage for the AE count was set at 480 mV (full scale was ± 2.4 V). The signal sampling rate was 4 MHz. A piezoelectric sensor MST8S (3 mm diameter, a frequency band from 100 to 600 kHz) was

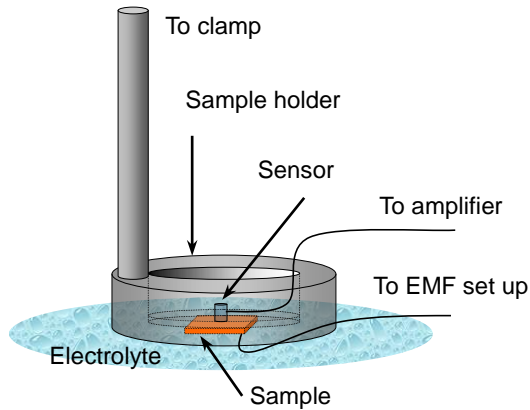


Fig. 3.10 A schematic illustration of the sample holder made of PVC with the sensor. The holder has a wide opening on one side. Another side (electrolyte side) has a small (3 mm) hole to connect the sensor to the sample.

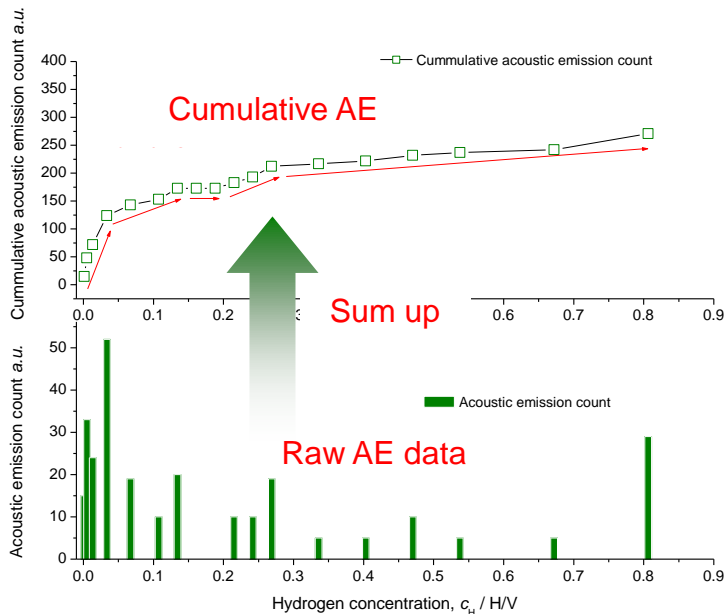


Fig. 3.11 An example of AE data treatment to obtain a cumulative AE curve from a series of raw AE data.

attached to the backside on the substrate of the loaded film. Only the front side of the film sample was immersed into the electrolyte to protect the sensor from corrosion.

The collected raw AE counts are summed up in relation to each H concentration step and plotted against c_H as a cumulative AE curve. This treatment is schematically shown in Fig. 3.11.

3.4 Deuterium gas loading

For the samples subjected to atom probe tomography (APT) analysis, gas-loading procedure was applied.

The reason why to use D_2 gas but not H_2 can be summarized as follows. As introduced later in the coming section, the APT technique is based on time-of-flight technique and, therefore H can also be detected. However, the loaded H must be ultimately distinguished from residual hydrogen in the chamber atmosphere. Besides, even at cryogenic temperatures as low as 50 K, which is a typical analysis temperature for APT, interstitial hydrogen is highly mobile and has a diffusion coefficient of about $10^{-9} \text{ cm}^2 \text{ s}^{-1}$ e.g. in V [Fukai05]. During the APT analysis the surface of the sample is removed continuously and the absorbed H will immediately diffuse towards the newly created surface because such fresh surface is energetically favorable for H. Finally, the hydrogen will be lost by recombining into H_2 or by forming H_2O in the chamber atmosphere. To avoid this, use of heavier isotopes like D instead of H is thus strongly recommended for APT.

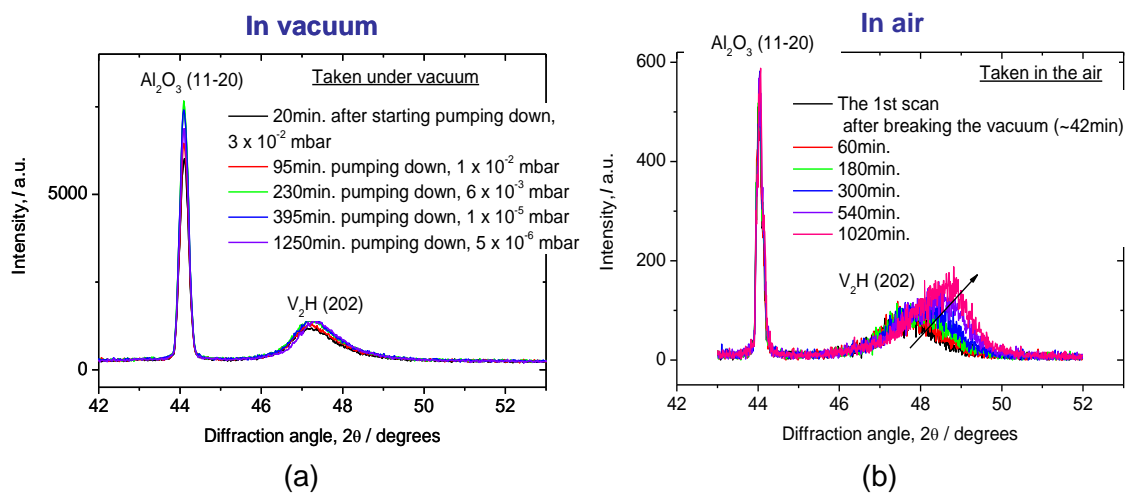


Fig. 3.12 XRD profiles of H-loaded V 100 nm film on Al_2O_3 (11-20) substrate (Co $K\alpha$). The film surface was capped with 20 nm Pd film. The Pd peak is not seen due to peak overlap. Under vacuum condition (a) there is no peak shift of V-hydride observed in the course of repeated scan. However, similar scans in air (b) indicate clear peak shift to higher angles as the time elapses, which indicates clear trace of H-loss from the V layer. The scans in vacuum were carried out using a house-made XRD machine in Institut für Materialphysik, Göttingen University, under operation by D. Plischke.

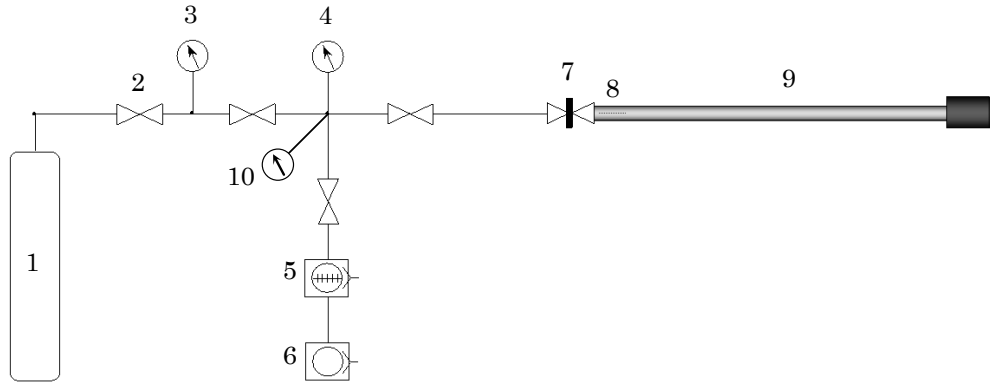


Fig.3.13 Deuterium gas loading set up. 1: D₂ gas bottle (99.98%), 2: Variable leak valve, 3: Capacitance manometer 10⁵ Pa max., 4: Capacitance manometer 100 Pa max., 5: Turbo molecular pump, 6: Oil rotary pump, 7: Gate valve, 8: Sample mounted on transfer rod, 9: Magnetic transfer rod with sample, 10: Vacuum gauge

In the pioneering work performed by Kesten [Kest02], indeed, D was used. Nevertheless, the observed D concentration was significantly lower than that of expected from corresponding p - c - T curve. This study also encountered the same problem. Later, the origin of this problem was identified by performing XRD investigation of H-loaded film in air and in vacuum.

In Fig. 3.12, the results of these XRD scans are shown [Gemma09]. It is obviously seen that the peak of V hydride phase shifts to higher angle when the scan is performed under atmospheric air condition, while the same scan under vacuum shows no peak shift. This result clearly indicates hydrogen-loss from the V layer by H₂O formation at the film surface, namely at the Pd capping layer.

Unless an O₂-free condition is established, no successful analysis is possible. This topic was studied in this thesis and the D₂ loading chamber was newly designed and built with technical help by T. Schulz. The set up is schematically shown in Fig.3.13. This system is equipped with a magnetic sample transfer rod, which is coupled with a gate valve so that the D₂-loaded sample can be transferred from the loading chamber to APT chamber without breaking D₂ atmosphere.

Actual D₂-loading procedure typically starts as follows. At first, the whole system was evacuated until the pressure reaches better than 1×10^{-5} Pa after bake-out of the transfer rod at 383 K for 12 hours. After this bake-out, the pressure typically showed 10^{-6} Pa. Thereafter, deuterium gas (purity: 99.98%) was leaked into the system. The pressure of the D₂ gas can be measured by capacitance manometer and is kept at a desired pressure by adjusting the leak valve's opening. As soon as the D₂ gas was

introduced at a desired pressure, the gate valve for the transfer rod was closed and the sample was loaded with deuterium for 24 ~ 48 hours.

After loading, the transfer rod was removed from the set up and connected to a pre-evacuation chamber on the APT (Fig.3.14). Before introducing the sample into the main chamber, the pre-evacuation chamber was evacuated to a pressure of better than 6×10^{-6} Pa (to minimize oxygen partial pressure). Then, the gate valve was opened to evacuate also the D_2 gas remaining in the transfer rod. After breaking D_2 atmosphere the introduction of sample into the main chamber was done within 10 min. Upon mounting the sample on cooling stage, the sample was rapidly cooled down to 130 K and thereafter, to desired temperature for analysis.

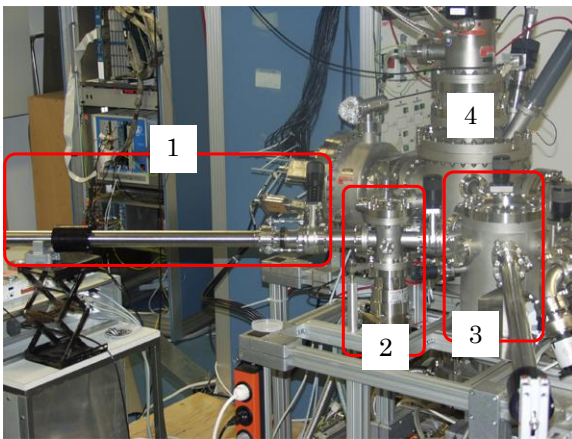


Fig.3.14 Transfer rod mounted at atom probe analysis system.

- 1: Transfer rod with D_2 loaded sample
- 2: Pre-evacuation chamber
- 3: Sample parking chamber
- 4: Main analysis chamber

3.5 Field ion microscopy (FIM) and Atom probe tomography (APT)

3.5.1 Field ion microscopy (FIM)

The FIM enables to investigate the surface of a conductive sample with a magnification of about 10^7 with help of an imaging gas and its field ionization. In 1951 E. W. Müller has firstly developed FIM and this invention has later been developed to Atom Probe Tomography (APT). A detailed history on the development of FIM and APT technique can be found e.g. in a review article by Kelly [Kell07]. An absolute demand for the FIM and APT is the sample to be in a shape of sharp needle because a high electrical field must be applied in order to field-evaporate atoms.

The sample tip for APT in this study was prepared by electropolishing of W ($0.1 \text{ mm-}\phi$) wire as shown in Fig. 3.15. First, the W wire was cut into

about 15-mm-length and clamped in a Cu tube (15 mm). Then the sample was placed into a cuvet filled with 2N- NaOH_{aq} . The sample was moved upwards and downwards alternatively while the AC voltage (1-5 V) was applied. Finally the bottom part of the W drops off due to thinning and the rest part was used as W substrate.

In Fig.3.16 a schematic picture of the FIM and APT system used in

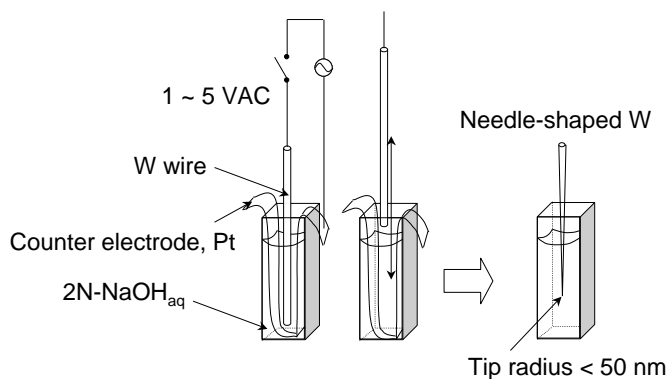


Fig. 3.15 Electro polishing of W wire. The wire is moved downwards and upwards alternatively while electro polishing is carried out. Finally, a sharp needle-shape is obtained.

this study is sketched. The image is produced by applying high DC voltage to the sample placed in a ultra high vacuum chamber, but filled with some amount of imaging gas as He, Ne, Ar etc. at a pressure around 10^{-3} Pa. For the imaging the sample tip must be cooled down to cryogenic tempera-

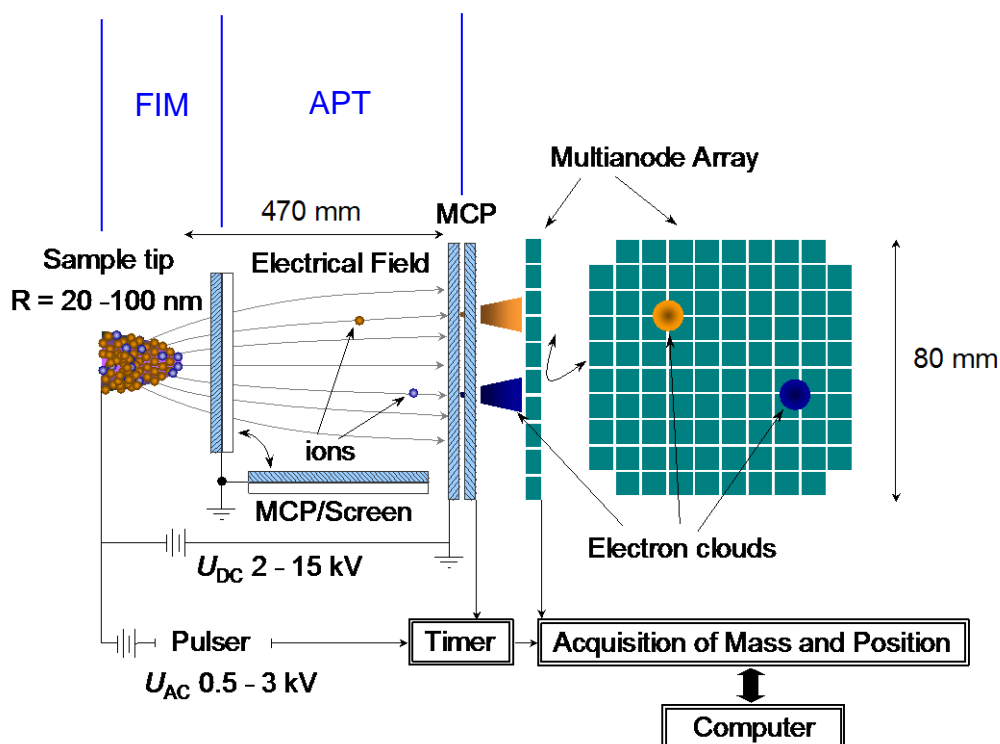


Fig.3.16 Schematic drawing of FIM and APT. For FIM operation the MCP/Screen stands in front of the sample tip, while for APT mode this screen is removed. The sample is connected with He cryogenerator. The minimum temperature achieved in the system is 20 K.

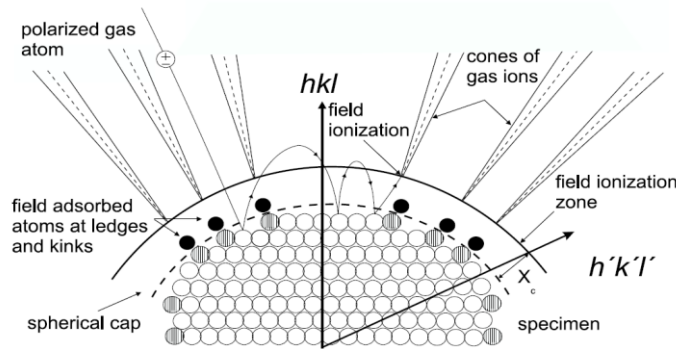


Fig.3.17 Schematic illustration of the field ionization process of gas atoms. (Taken from Ref. [Mill00].)

tures of 100 - 20 K to suppress lattice vibration and to induce quantum tunneling for the imaging gas. The imaging gas atoms are first polarized at the proximity of tip surface due to the high electric field and attracted to the surface (Fig.3.17). The collided gas atom loses its kinetic energy at the surface and trapped in the ionization zone. This is called as field induced adsorption, which occurs at about 0.5 nm above the tip surface. If the electric field is high enough as e.g. 44 V/nm for He, the quantum mechanical tunneling process induces the ionization of the accommodated atoms and, as a result, the ionized gas atoms are repelled to the MCP/phosphor screen.

The ions hitting the screen produce prominent spots as a consequence of electron multiplication at MCP as seen in Fig. 3.18 (W tip). These spots

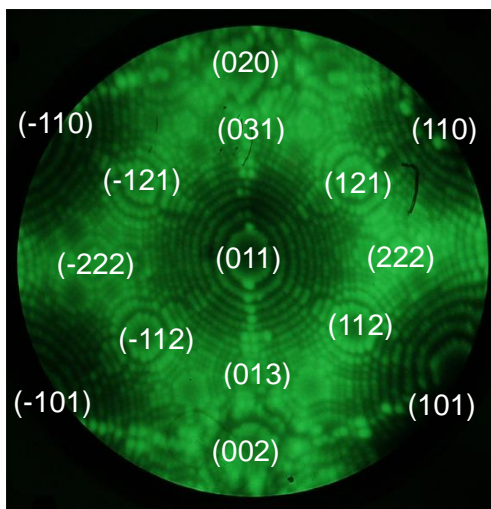


Fig. 3.18 FIM image of W tip (76 K, 7.6 kV, He gas 5×10^{-3} Pa). I

are interpreted as atomic terraces and one series of spots produce a concentric ring, representing each crystallographic plane. Their geographical relationship each other can be considered approximately by stereographic projection.

If the applied voltage is high enough to exceed field evaporation strength E_F , the surface atoms will be ionized and evaporated layer-by-layer. With increasing the voltage, the curvature radius of the tip

increases in the meanwhile. This process can, therefore, be used to “clean” the surface of an already prepared W substrate before the film deposition process. The increase of the tip radius will require further electric field to keep evaporation to occur as can be imagined from Eq. (3.17).

$$R = \frac{U_0}{E \cdot \beta} \quad (3.17)$$

R is the curvature radius of tip, U_0 is the applied voltage, E_F is the evaporation field (ca. 30 ~ 40 V/nm for transition metals) and β is called geometry factor, which is to consider the deviation from the ideal hemispherical shape of tip and ranges usually from 5 to 7 [Mill00].

All of the W substrates used in this study were developed by field evaporation until voltage of about 10 ~ 12 kV and thus the curvature radius of 30 ~ 50 nm.

The developed tips were then mounted on a specially designed sample holder shown in Fig. 3.19 and subjected to sputter deposition.

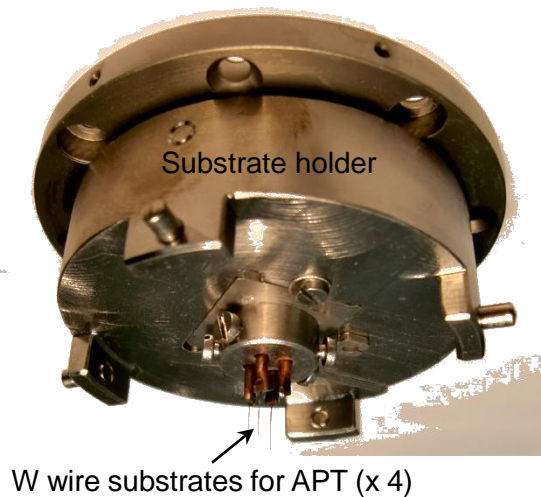


Fig. 3.19 A special holder for the sputter deposition on W substrates for APT. 4 tip-samples can be prepared at once. Targets are lying below this picture, so that the sputtered particles are deposited from the bottom side onto the substrates.

3.5.2 Atom probe tomography (APT)

The beauty of atom probe lies on the ability of detecting all elements as it is based on the time-of-flight principle. The atom probe tomography (APT) enables us to look even into the 3-dimensional distribution of atoms through the position sensitive detector and development of computational method. Under optimized reconstruction condition and at low temperatures (10 ~ 30 K), the spatial resolution in analysis direction is about 0.1 nm. The APT technique itself and the system used in this study were developed by Blavette *et al.* in Rouen. Detailed information can be found in

Ref. [Al-K03].

The APT analysis is after all based on field evaporation process. By the superposition of pulse voltage (U_p) on the standing voltage (U_0), the atoms can be removed layer-by-layer in a controlled way with assistance of computer program. The value of U_p and also the analysis temperature must be carefully chosen to avoid any preferential evaporation when multi-component system is measured, as the evaporation field E_F for each element sometimes significantly differs. In this study, U_p was typically 20.0 % of U_0 and, the pulse repetition rate f of 2 kHz were applied.

Again in Fig.3.16, the screen for FIM is now removed from the axis for APT analysis and the imaging gas is evacuated until base pressure in the range of 10^{-7} Pa is established. When a pulse voltage is applied i.e. at the onset of the evaporation, the “clock” for flight time measurement starts. On the impingement of ion at the position sensitive detector, the clock stops and thus, the flight time is measured. Simultaneously, the x and y coordinates of the ion at the detector will also be recorded in the computer. This evaporation sequence is repeated until the voltage reaches its limit or until the sample tip ruptures due to mechanical stress induced by high voltage.

Using the principle of energy conservation, the flight time can be converted by mass-to-charge ratio as in Eq. (3.18),

$$\frac{m}{n} = 2e \cdot (U_0 + U_p) \left(\frac{t}{L} \right)^2 \quad (3.18)$$

where m is the mass, n is the ionization state, e is the elementary charge, t is the flight time and L is the flight distance. The ion hitting the MCP produces charge cloud covering usually more than 2 anodes. The x and y coordinates are determined by interpolation of charge cloud distribution on these anodes to the center of gravity and the magnification of the image η which must be previously determined from image compression factor. The initial positions of atoms are therefore obtained as,

$$\left(x = \frac{x_a}{\eta}, y = \frac{y_a}{\eta}, z \right) \quad (3.19).$$

In principle the increment of depth z can be calculated from the number of atoms removed from the surface by taking the atomic volume, the detection efficiency of the detector (0.5 ~ 0.6) and the detector surface. However, as expected also from Eq. (3.17), the change of curvature radius must be taken into account, too.

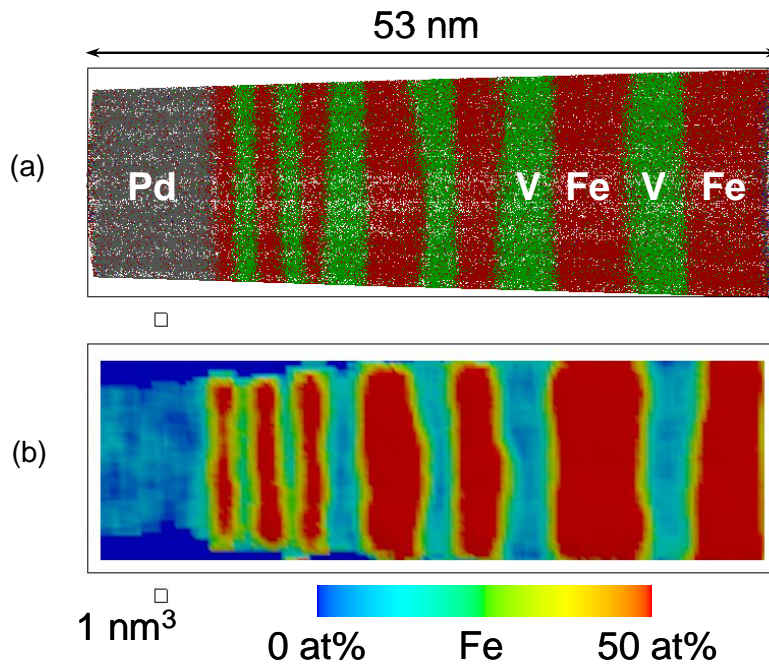


Fig. 3.20 (a) An example of volume reconstruction of Fe/V multi-layered film analyzed by APT. (b) The same volume represented by 2D Fe iso-concentration map (0 - 50 at%).

The requirement of consideration on the sample geometry is especially strict for multi-layered sample, as the product $E \cdot \beta$ cannot be regarded as constant in this case and application of Eq. (3.17) causes severe distortion of the reconstruction volume. G. Schmitz [Schm01] has developed a different reconstruction algorithm to solve this problem by introducing the factors on the specimen's initial radius and shaft angle. In this study his algorithm was employed and successful reconstruction was obtained.

By using the raw data obtained, reconstruction was carried out on AVS [AVS]. The depth concentration profile is one of the basic representations of the data, and especially suitable to investigate localized information at materials interface. In order to calculate this concentration profile, a cylinder volume of 5 nm diameters along the analysis direction was placed along the analysis direction. In this cylinder the volume was sliced into 0.3-nm thick disks where more than 120 atoms were included in each, and the number of atoms therein was calculated. Thereafter, these slices were overlapped together by 0.1 nm and plotted as a depth concentration profile.

Because of evaporation aberration and, also because the detection efficiency of APT is not 100 % (typically ~ 60 %), the volume along a pole should not be used for concentration profiling from reliability point of view [Hono98, Hono99].

From visualization point of view, 2D iso-concentration color mapping is also useful to have an overview of chemical modulation in the entire sample (see Fig. 3.20). Likely in 1D profile, the volume was divided into a selected size and spaced at certain mesh size for overlap. In this work the representation was carried out typically with the box size of 3 nm x 3 nm x 0.5 nm in which more than 100 atoms are included, and with the spacing of 0.3 nm.

4. Sample characterization of as-prepared films

The chemical composition of the films was determined by Energy Dispersion X-ray spectroscopy (EDX) and by APT. These analysis results revealed that V single layered films contain several at% Fe, which could be brought from sputter source. Alloying of V with Fe is known to logarithmically increase dissociation pressure of V hydride and its relationship is found e.g in Ref. [Yuka03]. Estimation of the dissociation pressure is, therefore, accessible when Fe concentration is known. It should be notified that 2 - 8at% Fe is originally contained in V layer depending on sputter condition prepared in this study. Upon D₂ gas loading, this alloying effect rather helps to control the D₂ pressure at desired value because pure V shows significantly low dissociation pressure of 10⁻³ Pa at room temperature [Velec69, Papat82].

Thin film growth is always governed by substrate material and its orientation, which induces different film orientation and in-plane stress. Such impact is reported to influence on *p-c-T* property of the film [Tal-G10]. In this study, two different substrates, namely (0001) sapphire, (11-20) sapphire were used as plane substrates. For FIM and AP, W substrate with (110) wire texture was used. Two different orientations of sapphire substrate were chosen to investigate influence on film orientation in view of epitaxial growth and on H absorption behavior. For the evaluation of stress measurement it is necessary to investigate film orientation and its relationship with substrate orientation.

Moreover, initial stress state of as-prepared film is considered to influence on its H absorption behavior and corresponding stress response (see Chap. 2.2). Those kinds of information are given by XRD and pole figure measurement. FIM imaging enables to check the orientation relationship between the film and the W substrate.

Additionally, roughness and chemical environment at Fe/V interfaces should be characterized in order to discuss about H-related phenomena. XRR and APT measurements complementary supply information about this question.

This chapter discusses on the above mentioned aspects.

4.1 Initial lattice expansion and in-plane orientation

4.1.1 V-Fe films on Al_2O_3 (0001) substrates

V-Fe single layered films were deposited on Al_2O_3 (0001) substrate at various temperatures. The composition of V was determined to be V-Fe8(1) at.% regardless of deposition temperature according to EDX elemental analysis for these films. An APT analysis conducted on a similar film deduced homogeneous distribution of Fe in V layer.

In Fig.4.1, the results of $2\theta/\theta$ XRD scans of the samples are shown together with their rocking scans in the inset. The reference 2θ position of bulky V-Fe8 \pm 1 at% alloy was obtained by using experimental data summarized by Shiga [Shiga78]. The obtained parameters for V-Fe8 \pm 1at% alloy are $d(110) = 0.2124(2)$ nm and $a = 0.3003(2)$ nm. Each film shows preferential growth in [110] direction regardless of substrate temperature. However, the peak position shifts towards higher 2θ angle with the temperature, which implies that a higher deposition temperature is correlated to a larger out-of-plane contraction i.e. smaller lattice parameter. This trend can be explained by considering the difference in thermal expansion coefficients α_{th} of V ($\alpha_{\text{th}} = 2.5 \times 10^{-5}$ at 1073 K [Nase69]) and Al_2O_3 ($\alpha_{\text{th}} = 7-8 \times 10^{-6}$ at 1073 K [Yim74]). During cooling down, the difference in α_{th} makes the film to shrink more than the substrate does. Since shrinking is not possible when the film is clamped to the substrate, this leads to in-plane tensile stress between film and substrate. This tensile stress increases with increasing temperature difference. Because of converse-contraction, in-plane tensile stress is accompanied by out-of-plane lattice contraction showing the described temperature dependence. The obtained (110) lattice plane distance and corresponding degree of expan-

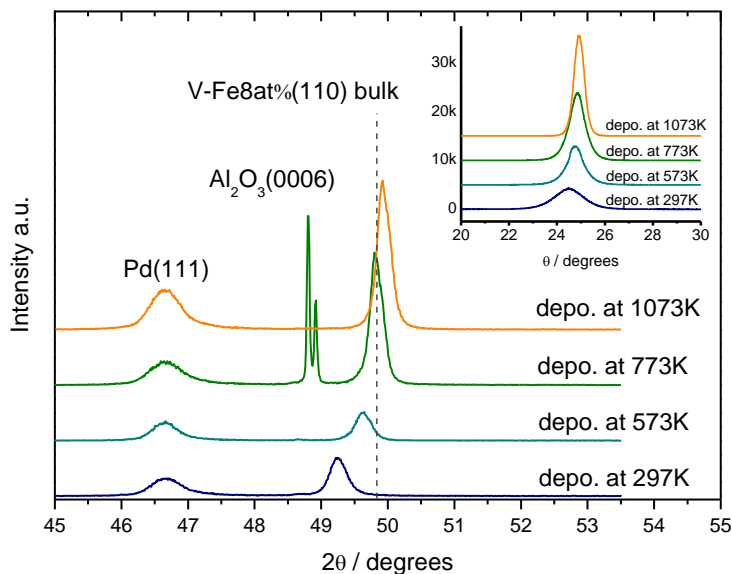


Fig.4.1 $2\theta/\theta$ XRD profiles of V-Fe8 at% films deposited on Al_2O_3 (0001) at 297, 573, 773 and 1073 K. The 2θ position of V-Fe8 at% bulk taken from Ref. [Shiga78] is also shown together. Inset shows the rocking curve of each sample.

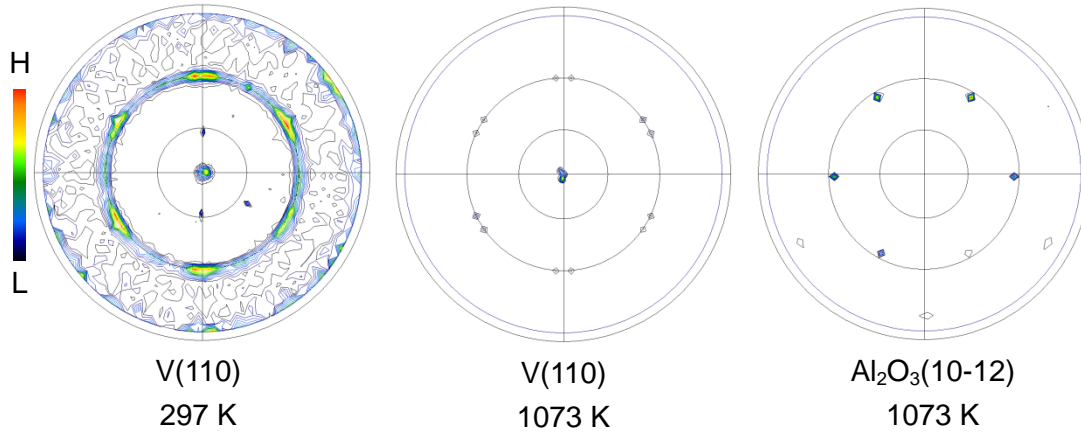


Fig. 4.2 Pole figures of V(110) and $\text{Al}_2\text{O}_3(10-12)$. Due to the 3-fold symmetry of basal plane (0001), V (110) oriented domains are rotated 60° each other.

Table. 4.1 The out-of-plane interplanar distance $d(110)$ and domain size of V-Fe8 at% films at different deposition temperatures. Reference value of V-Fe8 at% bulk [Shiga78] is also shown together.

	$d(110) / \text{nm}$	$d-d_{ref.} / d_{ref.} (\%)$	Domain size, t / nm
Ref. V-Fe8at% alloy	0.2124(2)	0	-
297K	0.2147	1.13	37.4(3)
573K	0.2133	0.46	40.6(3)
773K	0.2125	0.05	50.5(5)
1073K	0.2119	-0.23	50.5(5)

sion (+) and compression (-) in out-of-plane (110) lattice plane distance calculated by using reference data of $d(110)$ are shown in Table. 4.1 together with domain size of the samples calculated by Scherrer's formula [Culli78]. The rocking curves show a FWHM of the peak decreasing from 1.7° to 0.4° with increasing temperature. Thus, the domain size actually increases with increasing temperature.

Texture measurements on these films were also carried out to study the in-plane relationship of the film and the substrate orientation and the film quality. The pole figures shown in Fig. 4.2 are those of V (110) deposited at 297 K and 1073 K and that of the substrate $\text{Al}_2\text{O}_3(10-12)$ (Note that (0001) pole figure does not give any information concerning in-plane orientation.). From these results, one can see an epitaxial growth of V (110) is established on $\text{Al}_2\text{O}_3(0001)$ even at room temperature.

However, the pictures do not indicate growth of one domain. Considering the 3-fold symmetry of the substrate, at least 3 different domains can be deduced in the V-Fe8at% layer, in approximately 60° in-plane rota-

tion.

From the results of pole figures, the orientation relationship can be shown as in Fig. 4.3. For V (110) pole figure, three different lines indicat-

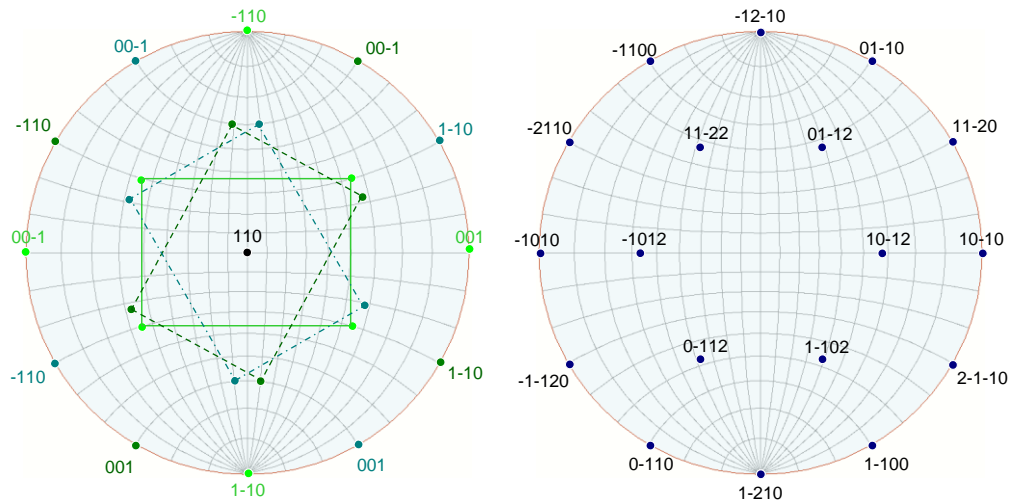


Fig. 4.3 Interpretation of the pole figures (Wulff net) in Fig. 4.2 (left: V, right Al_2O_3) The 3 domains (I, II, III) of V (110) fill the following orientation relationship; V (110) // Al_2O_3 (0001), V $\langle 001 \rangle$ // $\text{Al}_2\text{O}_3 \langle 10-10 \rangle$.

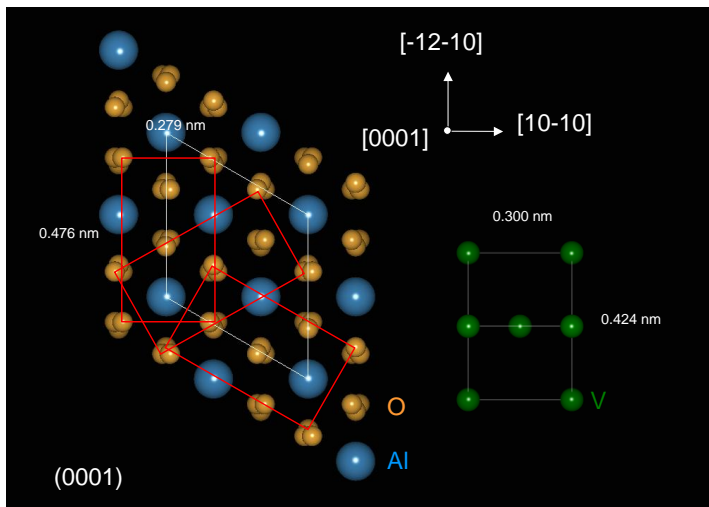


Fig. 4.4 Possible arrangement of V (110) on Al_2O_3 (0001) implied by lattice matching and in-plane domain rotation of 60° (—). Drawn by VICS by F. Izumi [Izumi05].

ing each (110) domain are assigned to differentiate them. According to this, the orientation relationship can be summarized as

$$\text{V (110)} // \text{Al}_2\text{O}_3 (0001), \text{V} \langle 001 \rangle // \text{Al}_2\text{O}_3 \langle 10-10 \rangle$$

Similar epitaxy was reported by Ikuhara *et al.* [Ikuha98]. Thus, the V (110) films on Al_2O_3 (0001) were grown epitaxially with equal probability for each domain orientation.

From the results obtained, a possible arrangement of V (110) on Al_2O_3

(0001) is illustrated in Fig. 4.4. On this assumption, the lattice mismatch between V and Al₂O₃ amounts as large as 10 %. Moreover, on this atom-on-atom assumption, the lattice contracts in [10-10] direction, while it expands in [-12-10] direction and thus a tetragonal distortion is finally required. This will in reality implement dislocations with high density at the interface.

As a first approximation, the 3-domain in-plane arrangement is regarded as random arrangement. In such case, the in-plane stress, σ , in the V layer can be roughly estimated by using out-of-plane lattice parameters as [Culli78];

$$\sigma = -\left(\frac{E}{2\nu}\right) \cdot \left(\frac{a - a_0}{a_0}\right) \quad (4.1)$$

where, E is Young's modulus (128 GPa for pure V), ν is Poisson's ratio (0.37 for pure V), a is measured out-of-plane lattice parameter and a_0 is reference lattice parameter. This estimation is based on an assumption that the film exhibits Poisson type response. According to the data shown in Table. 4.1, the resulting in-plane stress can be summarized as in Table 4.2. These values are then taken into account for results of stress measurement on hydrogen absorption.

Table 4.2 Initial in-plane stress the V-Fe8at% films deposited at different temperatures

	Initial in-plane stress, σ / GPa
Ref. V-Fe8at% alloy	0
297K	-1.97
573K	-0.79
773K	-0.10
1073K	+0.18

It has been shown that single domain structure cannot be established on (0001) substrate. Therefore, another orientation (11-20) was employed aiming for epitaxial growth of one domain. This is described in the next section.

4.1.2 V-Fe and Fe/V films on Al₂O₃ (11-20) substrate

4.1.2.1 V-Fe single layered films

On the substrate of Al_2O_3 (11-20), V-Fe films and Fe/V multi-layered films were deposited likewise those on (0001). Fig.4.5 shows $2\theta/\theta$ XRD profile of V-Fe8 at% 100 nm-thick film deposited on Al_2O_3 (11-20) at 1073 K. The calculated d of V(110) was 0.2121 nm, which is slightly smaller the reference value, $d_{\text{V-Fe8at\%}(110)} = 0.2157$ nm.

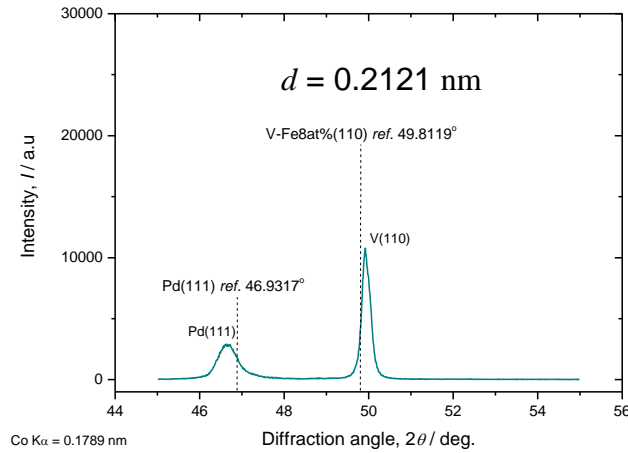


Fig.4.5 $2\theta/\theta$ XRD profile of V-Fe8 at% film deposited on Al_2O_3 (11-20) at 1073 K. The 2θ positions of Pd and V-Fe8 at% bulk taken from Ref. [Shiga78] are also shown together.

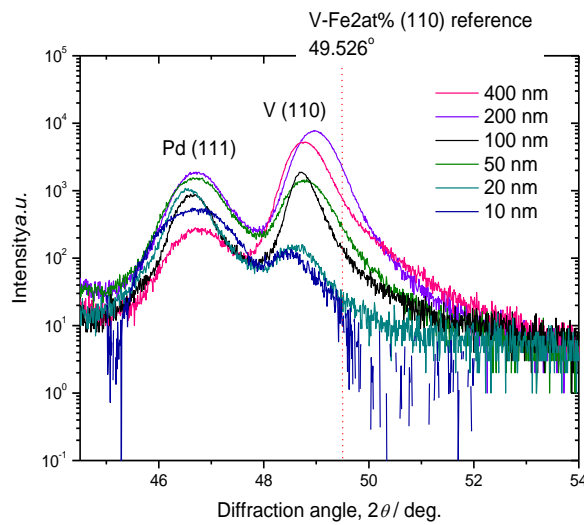


Fig. 4.6 XRD patterns of V-Fe2at% films deposited on Al_2O_3 (11-20) at room temperature with different film thickness. The in-plane stress in [1-10] direction was calculated by Eq. (4.2)

The state of initial lattice expansion is altered by changing film thickness. Fig. 4.6 shows XRD patterns of V-Fe2at% (110) films with different thickness ranging from 10 - 400 nm in log-scale. These films were deposited at room temperature. Contrary to the case of the film deposited at high temperature (Fig.4.5), these films are expanded out-of-plane, implying that they are under in-plane compressive stress. This trend is the same as in the case of the films deposited on (0001) (see Fig.4.1). For (110)-oriented film, an estimation of this in-plane compressive stress along [1-10] is accessible through the modification of Eq. (2.31) as follows.

$$\sigma_{[110]} = -4\varepsilon \left(\frac{(C_{11} + 2C_{12})C_{44}}{C_{11} + C_{12} + 2C_{44}} \right) \quad (4.2)$$

Here, the initial strain ε of the films is approximated via deviation of $d(110)$ from the reference value of bulk V-Fe2at% ($d_0(110) = 0.2135$ nm), which is derived from Ref. [Shiga78]. The estimated initial in-plane stress

Table 4.3 Initial in-plane stress calculated from out-of-plane $d(110)$ of the V-Fe2at% films (Fig. 4.6) deposited on $\text{Al}_2\text{O}_3(11-20)$ at 297 K.

Thickness l [nm], Domain size t [nm]	Initial in-plane stress σ_0 [GPa]
$l = 10, t = 10$	-2.70
$l = 20, t = 14$	-2.51
$l = 50, t = 17$	-1.94
$l = 100, t = 25$	-2.09
$l = 200, t = 20$	-1.45
$l = 400, t = 21$	-1.94

σ_0 and calculated domain size t for each film are summarized in Table 4.3. The minus sign means compressive stress. The compressive stress tends to be larger for thinner films. Note that the estimated domain size t registered in the table is underestimated because strain effect of the film is not taken into account.

These films deposited at room temperature showed multi-domain in-plane structure. The (110) pole figure of 200-nm thick VFe single layered film is shown in Fig. 4.7 as an example (Compare with that of single domain structure shown in e.g. Fig. 4.10 (a)).

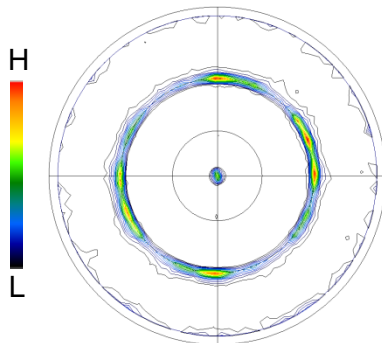


Fig. 4.7 (110) Pole figure of 200-nm thick VFe single layered film. At least two different in-plane domains are suggested.

4.1.2.2 Fe/V multi-layered films

The Fe/V multi-layered films were also deposited on (11-20) oriented substrates with different nominal stacking sequence. First, a result of Fe/V with the following stacking will be shown; Pd 20 nm / [Fe 10.2 nm / V 21.4 nm] x 4 / V 21.4 nm buffer layer. This means, in detail, the following order from the surface; the Pd cap layer 20 nm, stack of [V 21.4 nm / Fe 10.2 nm / V 21.4 nm / Fe 10.2 nm / V 21.4 nm / Fe 10.2 nm / V 21.4 nm / Fe 10.2 nm] and V 21.4 nm as the buffer layer on the substrate. This multi-layered film will be abbreviated as [(Fe 10.2 / V 21.4) x 4]. The substrate temperature for the deposition of the buffer layer was kept at 1073 K aiming for epitaxial growth. After this buffer V deposition, the substrate temperature was reduced to 353 K and following Fe and V layers were deposited at this temperature in order to suppress alloy formation (see Fe-V phase diagram in Fig. 2.6). Pd capping was carried out at room temperature after the Fe/V stacks have been completed.

In Fig.4.8, an example of $2\theta/\theta$ XRD profile of [(Fe 10.2 / V 21.4) x 4 / V_{buff} 21.4] is shown. The 2θ position of V(110) is found at 49.12° , which is slightly smaller than that of V-Fe8at% single layered film deposited at 297 K on (0001) substrate, found at $2\theta = 49.25^\circ$ (Fig.4.1). An interesting fea-

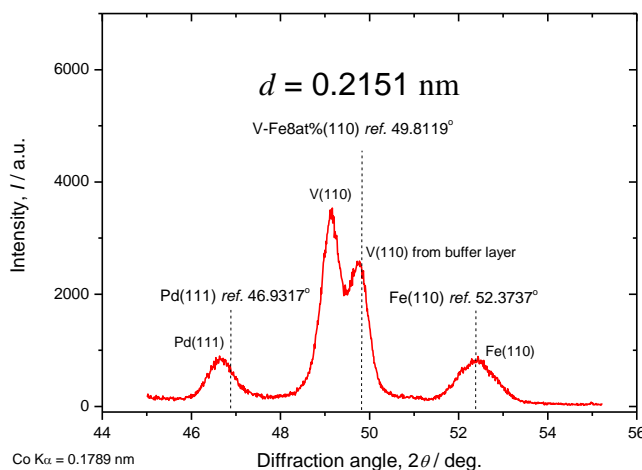


Fig.4.8 An example of $2\theta/\theta$ XRD profile of [(Fe 10.2 / V 21.4) x 4] film deposited on Al_2O_3 (11-20). The double peaks of V (110) apparently seen in the figure arises because of different deposition temperature between V in Fe/V and V buffer layer (see text).

ture is the splitting of the V (110) peak. As the V buffer layer was deposited at 1073 K, while the Fe/V stack was at 353 K, there is a large difference of the initial out-of-plane expansion. According to the XRD results in Fig.4.1 and Fig.4.5, the (110) peak at higher angle can be assigned as that of V buffer layer and another one at lower angle is that of V in Fe/V stack.

Contrary to the result on V-Fe8at% film on (11-20) substrate, the V lattice in this Fe/V stack is expanded out-of-plane with $d = 0.2151$ nm, which implies the film is under compressive in-plane stress state. Due to

the large lattice mismatch (4.6%) between Fe ($a = 0.287$ nm) and V, ($a = 0.300$ nm), the Fe layer between the V layers is subjected to expand in in-plane direction. In fact, the 2θ position of Fe (110) was at 52.39° , which is slightly shifted to a higher angle compared to the reference position of 52.3737° . The V (110) lattice accordingly contracts in in-plane direction, which is in agreement with the XRD picture.

When the double layer thickness Λ of Fe/V is reduced, the diffractograms become more complicated, typically showing satellite peaks. The measured XRD patterns of Fe/V multi-layered films with different double layer thickness Λ and their simulated XRD patterns via Eqs. (3.4) and

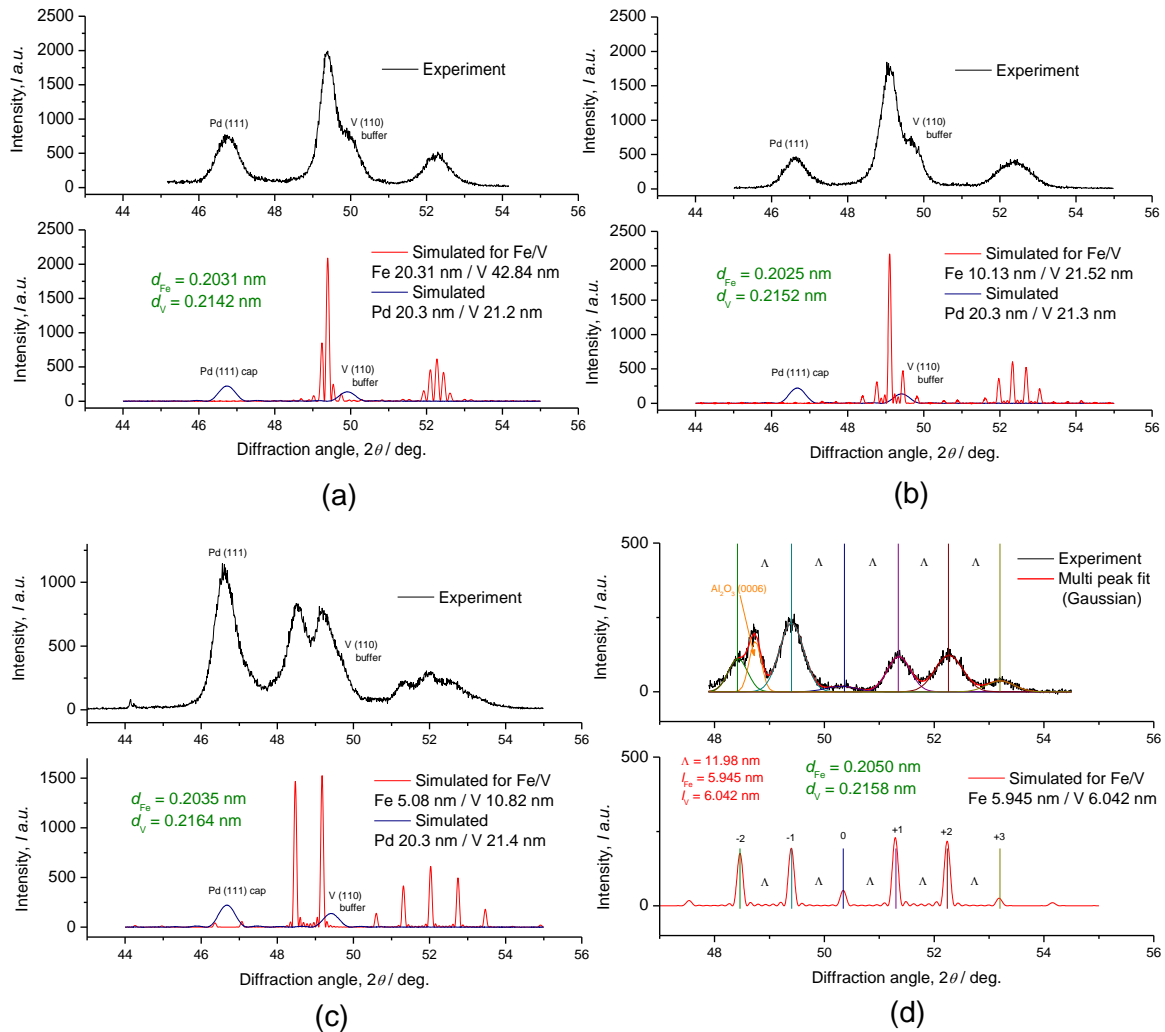


Fig. 4.9 Experimental and simulated XRD patterns of (a) [(Fe 20.3 nm / V 42.8 nm) x 2], (b) [(Fe 10.1 nm / V 21.5 nm) x 4], (c) [(Fe 5.1 nm / V 10.8 nm) x 8], (d) [(Fe 5.9 nm / V 6.0 nm) x 8]. The films (a) ~ (c) were deposited on Al_2O_3 (11-20) with V 21 nm buffer layer. The film (d) was deposited on Al_2O_3 (0001), thus exhibit 3-domain in-plane structure. Satellite peaks are successfully assigned in case of (d), where 0^{th} peak corresponds to d_0 .

(3.5) are shown in Fig. 4.9. In the simulation, the n_{Fe} , n_{V} , d_{Fe} and d_{V} were varied until the peak positions and their intensities fit to the experimental peaks. The peaks of simulated patterns are sharper than those of experimental because interface mixing and roughness were not taken into account and thus no convolution of maxima was made. Nevertheless, the simulated diffractograms reasonably describe the experimental patterns and thus the resulting d_{Fe} and d_{V} are readily accessible, as indicated together in the figures.

Note that d_{V} increases as the Λ decreases, though the total thickness of V is constant for (a) ~ (c). This trend intuitively implies a counter-acting

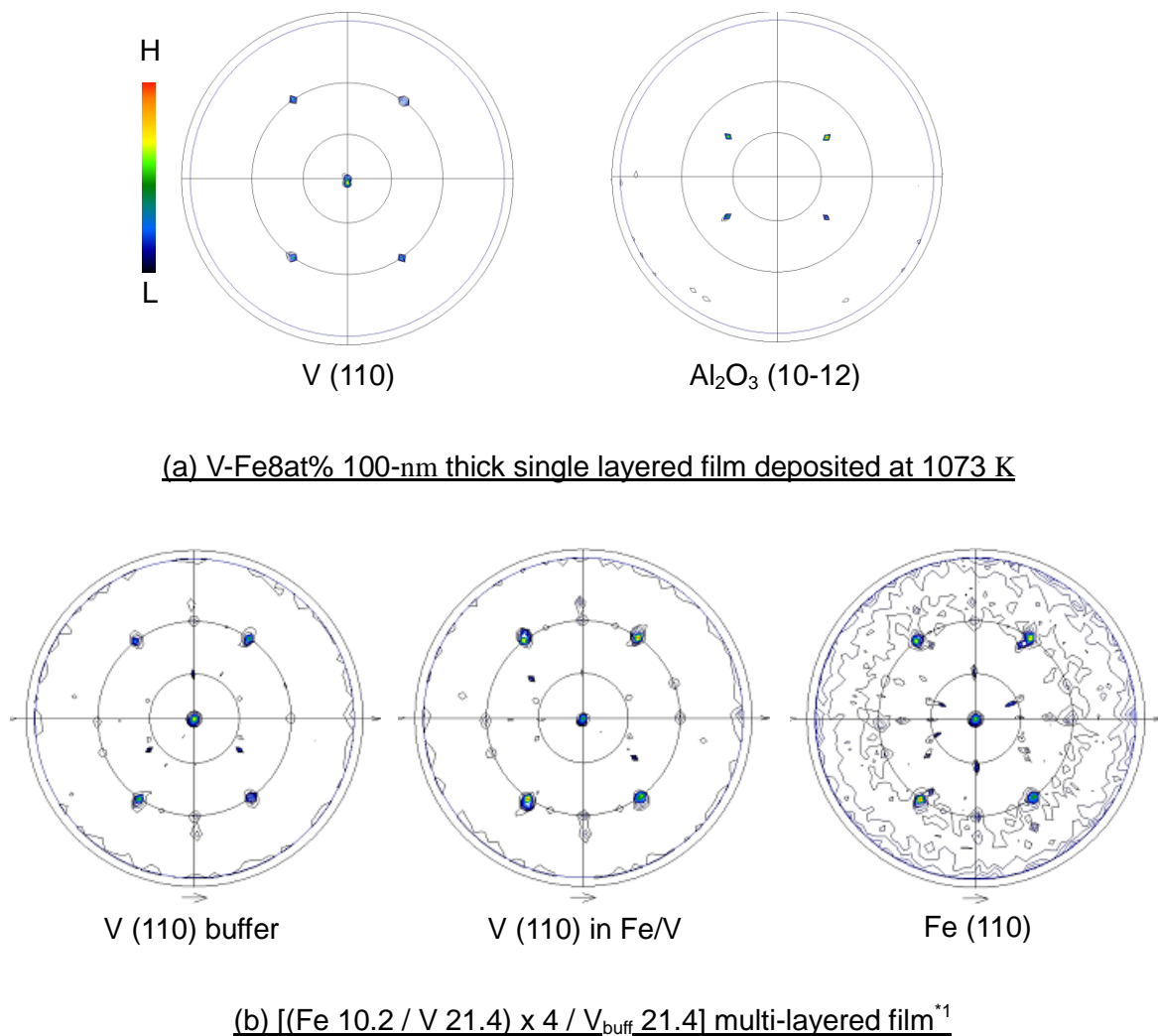


Fig. 4.10 (a) Pole figures of V (110) and Al₂O₃ (10-12) taken for V-Fe8at% 100 nm-thick film on Al₂O₃ (11-20) deposited at 1073 K. (b) Pole figures of V (110) from V buffer layer and from Fe/V layer and Fe (110) taken for [(Fe 10.2 nm / V 21.4 nm) x 4 / V_{buff} 21.4 nm] multi-layer on Al₂O₃ (11-20). For both, epitaxial growth with single domain type is found. *1These 3 pole figures are rotated 90° clockwise because the measured geometry was originally 90° rotated to that of (a).

elastic response of the V layer by the adjacent Fe layers owing to $d_{\text{Fe}} < d_{\text{V}}$. According to the spacing of satellite peaks, Λ is successfully determined for (d).

According to pole figures of both V and Fe/V films, epitaxial growth similar to that of Fig. 4.2 was confirmed.

Concerning in-plane orientation, some representative pole figures of V and Fe/V films on Al_2O_3 (11-20) substrates are summarized in Fig. 4.10.

Judging from Fig. 4.10, the in-plane orientation relationship in this

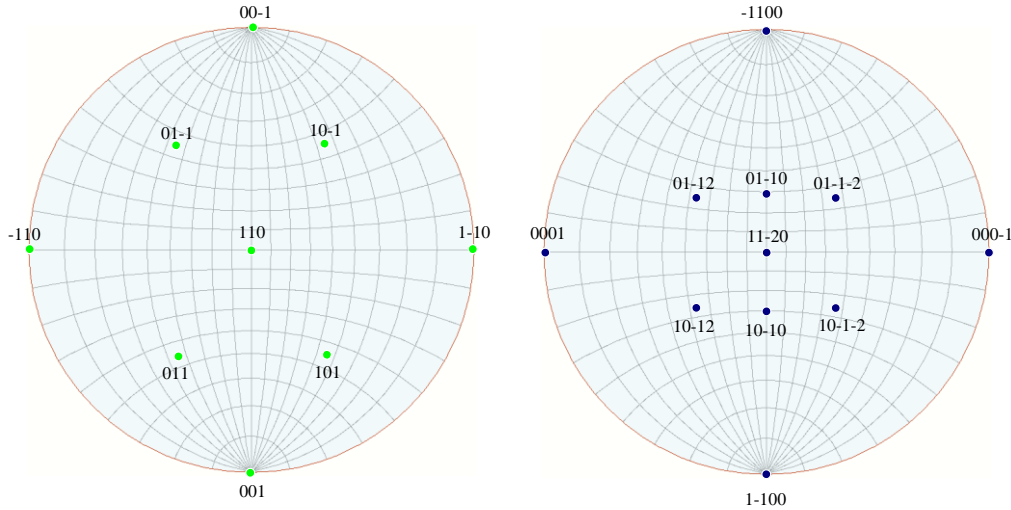


Fig. 4.11 Indication of the pole figures (Wulff net) in Fig.4.7 (left: V, right: Al_2O_3).

V (110) fills the following orientation relationship;

$$\text{V (110)} // \text{Al}_2\text{O}_3 (11-20), \text{V } \langle 001 \rangle // \text{Al}_2\text{O}_3 \langle 1-100 \rangle$$

case can be considered as in Fig. 4.11. Accordingly, the epitaxial relationship of V on Al_2O_3 (11-20) is as follows.

$$\text{V (110)} // \text{Al}_2\text{O}_3 (11-20), \text{V } \langle 001 \rangle // \text{Al}_2\text{O}_3 \langle 1-100 \rangle$$

Direct growth of V (110) layer on Al_2O_3 (11-20) is not reported in detail so far, and thus comparison of this relationship with other studies is not possible.

Based on this relationship, a possible picture of lattice arrangement is drawn in Fig. 4.12. There are two possible arrangements indicated. For further details other observations by e.g. TEM is necessary. However, it seems clear that the both assignments induce tetragonal distortion similarly as in the case of (0001). Similar epitaxy can be established also for the growth of Nb film [Wild01, Nörth06], which has ca. 10 % larger lattice constant ($a = 0.330$ nm) than that of V. According to the STM imaging of this Nb epitaxial film, a large number of misfit dislocation was imple-

mented with the density of approximately $10^{11} / \text{cm}^2$. The same order of high density of dislocation can be considered also for the V and the Fe/V films prepared in this study.

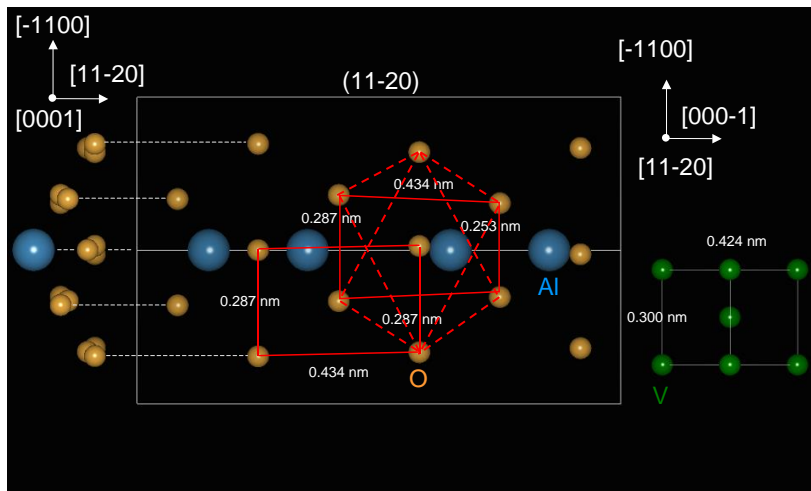


Fig. 4.12 Possible arrangements of V (110) on Al_2O_3 (11-20) implied by lattice matching point of view (—). On the left side of the picture (0001) plane is also shown. Only top-half plane is shown for better visualization's sake. The red dot lines are for multiple-domains (---).

4.2 Interface roughness

For some of the films deposited on Al_2O_3 (11-20), XRR measurement was conducted to investigate film thickness, surface roughness and interface roughness. The measured data were fitted by IMD fitting program

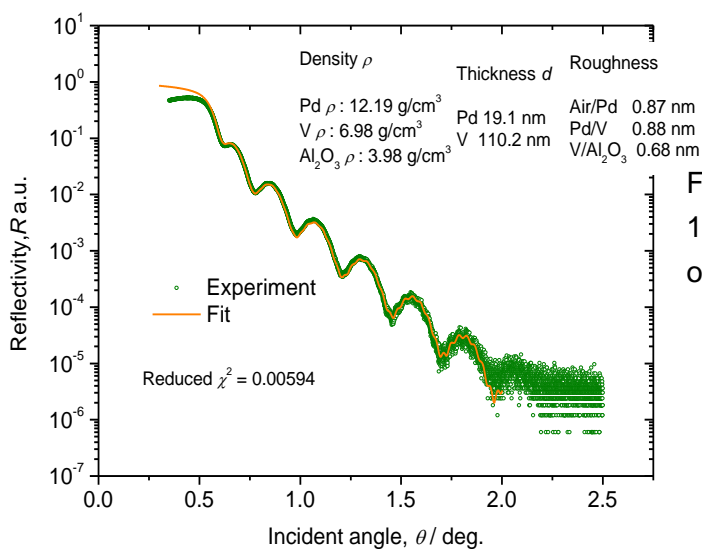


Fig.4.13 XRR curve of Pd 19 nm / V 110 nm deposited on Al_2O_3 (11-20) at 1073 K.

[Windt98].

In Fig.4.13 the XRR curve of V single layer is plotted. The nominal thickness of Pd and V was 20 nm and 100 nm, respectively. After fitting the curve, these values were refined as 19 nm and 110 nm, respectively. The roughness of the films was in the range of 0.7 ~ 0.9 nm. The density value of V film obtained by fitting, 6.98 g/cm³, is different to the density of bulk V, 6.11 g/cm³ (14 % difference). Fe has bulk density of 7.84 g/cm³. Considering that the V is alloyed with 8at% Fe thus with 8.77 wt%Fe, the resulting density would be 6.26 g/cm³. This value is still too small. Usually, sputter deposited thin film has lower density than that of bulk, since Ar impingement into the film cannot be completely avoided and, because the lattice coherency is not as perfect as that of bulk due to high density of defect. The determination of density is highly dependent on accuracy of the measurement. For correct XRR measurements the rotational center of the sample and that of the goniometer must absolutely match each other. Unless this condition is conserved, there will be an error of incident angle and thus it generates a wrong density value. The most crucial factor affecting this matter is the bending of sample. The height difference of the sample Δz causes error in incident angle $\Delta\theta$ as

$$\Delta\theta = \frac{\Delta z \cos^2 \theta}{L} \quad (4.2).$$

L is the goniometer radius (300 mm in this study). In order to explain 14 % difference of density, the Δz must be in the order of > 0.1 mm which is not reasonable considering the substrate thickness of 0.2 mm. The origin of the huge error on V film density is still unclear.

In Fig.4.14, the XRR curve of [(Fe 10.2 nm / V 21.4 nm) x 4 / V_{buff} 21.4 nm] multi-layer is exemplarily shown. In this measurement, density values were almost reasonably determined as those of Pd, V and Fe showed smaller or comparable values as those of bulk. The thickness of each layer was determined individually and the resulting expression of this Fe/V stack was [Fe 10 nm / V 20 nm].

The initial roughness due to substrate surface condition was about 0.9 nm. However, upon the deposition of the 1st Fe layer the roughness increased to 2.9 nm. The origin of this drastic change can be considered as follows. After the deposition of V buffer the heating of the substrate was ceased and the sample was cooled down to 353 K. This cooling takes usually ca. 2 hours in total, but the initial cooling rate is quick. While the cooling was carried out, the surface modification of the V buffer occurred due to further grain growth by residual heating and also by adsorption of residual gas in the chamber. As a result, the surface roughness has in-

creased to 2.9 nm before the deposition of the 1st Fe layer is initiated.

An interesting feature is the smoothing of this roughness in the course of further deposition. As shown in the figure, the roughness of the interface decreased along the sequence from the first double layer stack to Pd capping layer. The reason of this smoothing effect is not clear, as the change of roughness was not observed by other techniques. But, most

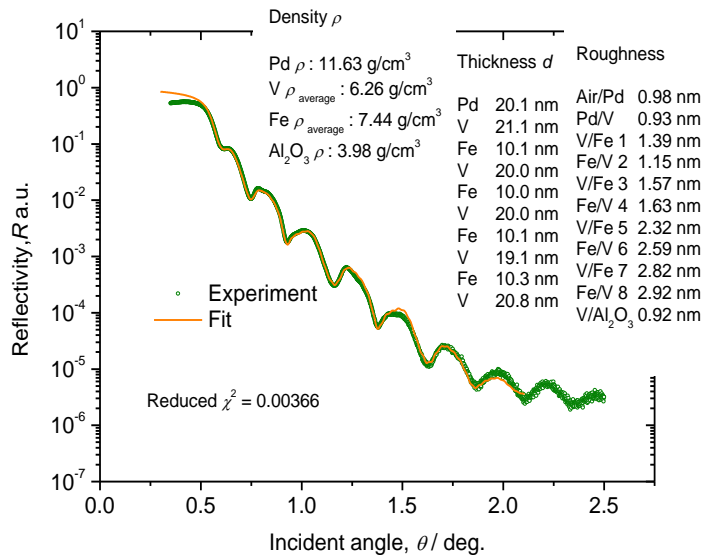


Fig.4.14 XRR curve [(Fe 10 nm / V 20 nm) x 4] deposited on Al₂O₃ (11-20) deposited at 353 K on V buffer layer of 21 nm deposited at 1073 K.

probably it was brought by diffusion process of deposited atoms from hills to valleys of roughened surface. Recent study by Röder [Röder09] has revealed similar thickness dependent smoothing effect by polymers and ZrO₂ on wavy patterned Si substrate.

According to the result in Fig.4.14, the saturating Fe/V interface roughness lied in the order of 1.2 ~ 1.4 nm as a morphological roughness.

The local chemical roughness is believed to be smaller than this value. Additionally, the interface roughness of Fe/V sequence was larger than that of V/Fe sequence. These points will be discussed further in detail by examination of Fe/V interface profile given by APT on as-prepared Fe/V films in the following section.

4.3 Characterization by FIM and APT

In this section, results of FIM image of as-deposited V single layer on W and APT analysis of V and Fe/V as-deposited films will be discussed mainly from a view point of Fe distribution in V layer and Fe/V interface mixing.

4.3.1 Epitaxial growth of V-Fe single layer

FIM imaging provides qualitative information about the microstructure, namely orientation and defects like grain boundaries. In order to determine the lattice matching between film and substrate, FIM imaging is a useful method. In Fig. 4.15, FIM image of a V-Fe single layer 25 nm and the image of the W substrate after the removal of the V-Fe layer by field evaporation are shown together. On the W substrate, a grain boundary (GB) indicated by white dot line is visible. On the V-Fe layer, some

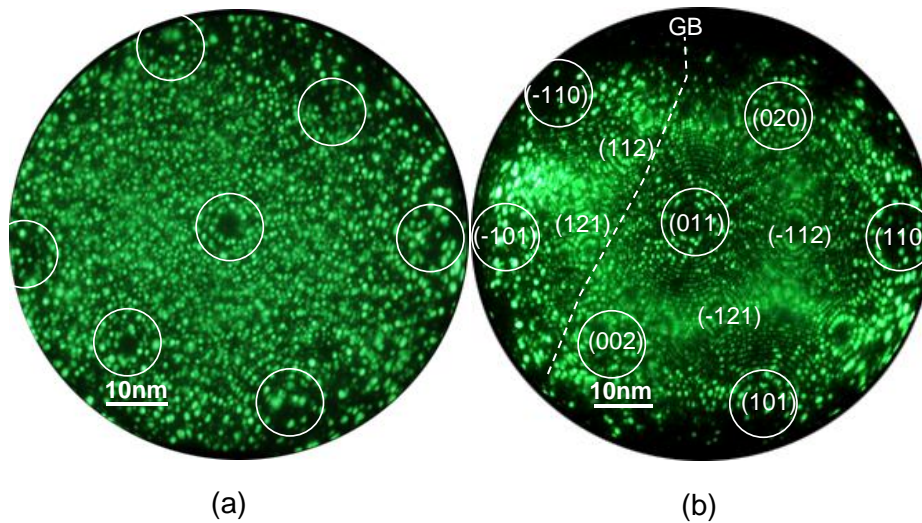


Fig. 4.15 FIM images taken at 35 K, with Ne gas (a) V-Fe single layer at 9.0 kV (b) W substrate after removal of V layer, at 9.0 kV. The positions of concentric rings of V agree with those of W $\{110\}$ and $\{001\}$ as indicated by circles, implying epitaxial growth of V $\{110\}$. Relatively random distribution of bright spot in (a) is due to alloying with Fe. A grain boundary (GB) is seen on W, as indicated by dot line in (b).

concentric rings are visible. When these positions marked by white circles are compared with those of W $\{110\}$, they agree well each other. This implies epitaxial growth of V-Fe $\{110\}$ on W $\{110\}$. Somewhat random distribution of lattice steps seen in (a), is a typical indication of alloying [Mill96]. Particularly, it is due to alloying with Fe in this case.

In

Fig. 4.16 the mass spectra given by APT analysis of the similarly structured V-Fe film is shown in log scale. As described in the beginning of this chapter, the origin of Fe content is due to anode cylinder in the sputter source, which is typical for the films studied in this work. The mass spectra support this assumption, since there are Cr, Ni and Mn peaks that are most probably derived from stainless steel. The peaks of V, Pd and W were successfully detected with reasonable isotope ratio. The small peak

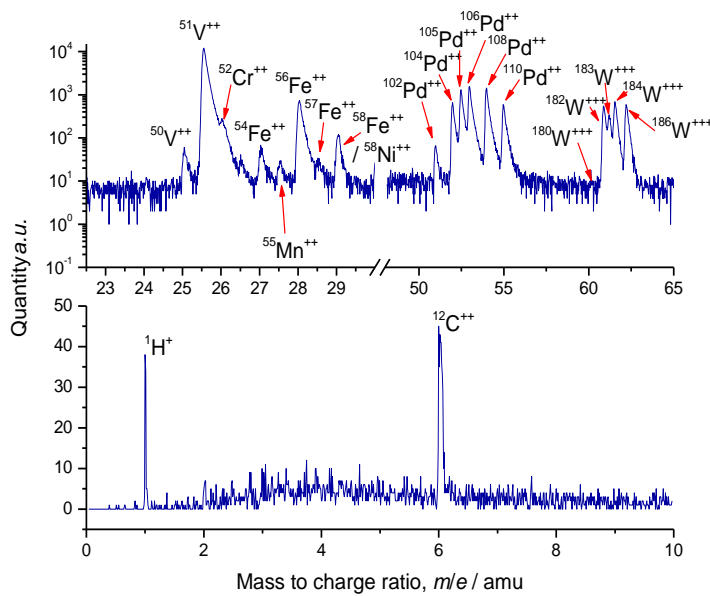


Fig. 4.16 Mass spectra of an as-deposited VFe single layered sample obtained by APT analysis at 30 K.

Only H^+ is found at low m/e , while no H_2^+ exists. This enables ultimate detection of D^+ .

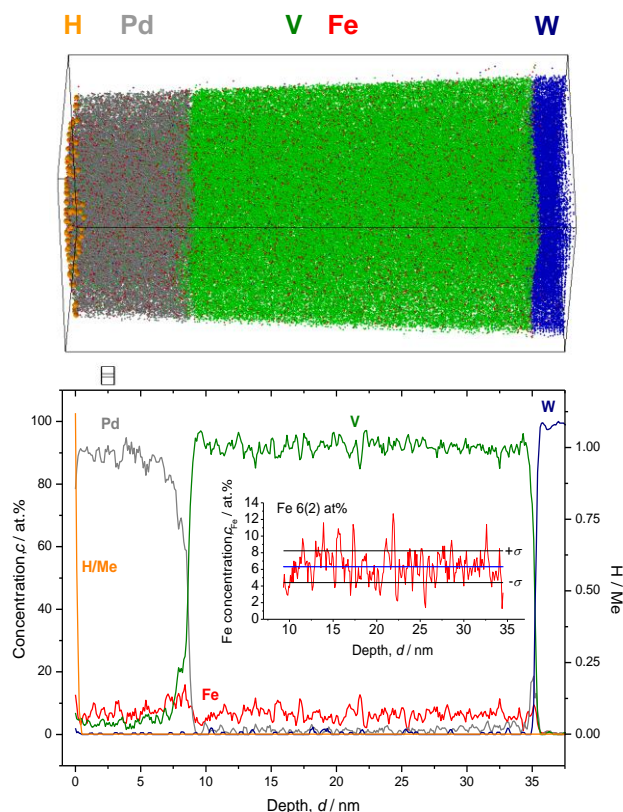


Fig. 4.17 3D reconstruction volume (16 nm x 16 nm x 37 nm) of V 25 nm on W and 1D concentration profile. Analysis was carried out at 30 K. A large number of H atoms (yellow) are found only at the surface of Pd layer, indicating adsorption at surface sites. The Fe concentration is found to be in the range of 6(2) at%, though there is a slight inhomogeneity.

of H^+ originates from the sample surface, and is thus adsorbed hydrogen. Note that no H_2^+ peak visible, also meaning clean vacuum environment in APT chamber used in this study, allowing use of deuterium instead of hydrogen for the APT analysis.

The 3D reconstruction and corresponding depth concentration profile of this film is represented in Fig. 4.17. The H atoms were adsorbed on Pd

surface and no H was observed in the V-Fe layer. Such a clean analysis atmosphere enables ultimate detection of deuterium. In the following discussions on APT, any suspicion about H pre-absorption in the V-Fe layer is therefore disregarded.

As the lattice parameter of W, $a_W = 0.316$ nm is larger than that of V-Fe, $a_{V-Fe8at\%} = 0.300$ nm in this case, V-Fe lattice is expanded in-plane direction and contracted in out-of-plane direction just above at the V-Fe/W interface.

4.3.2 Layer interdiffusion at high deposition temperature

The local chemistry at the Fe/V interface is one of the interests in this study. For epitaxial growth of hetero-structure, deposition at high temperature is often conducted to get smooth interface [Birch90]. In this study, deposition of Fe/V multi-layer was carried out also at 603 K as a trial. An

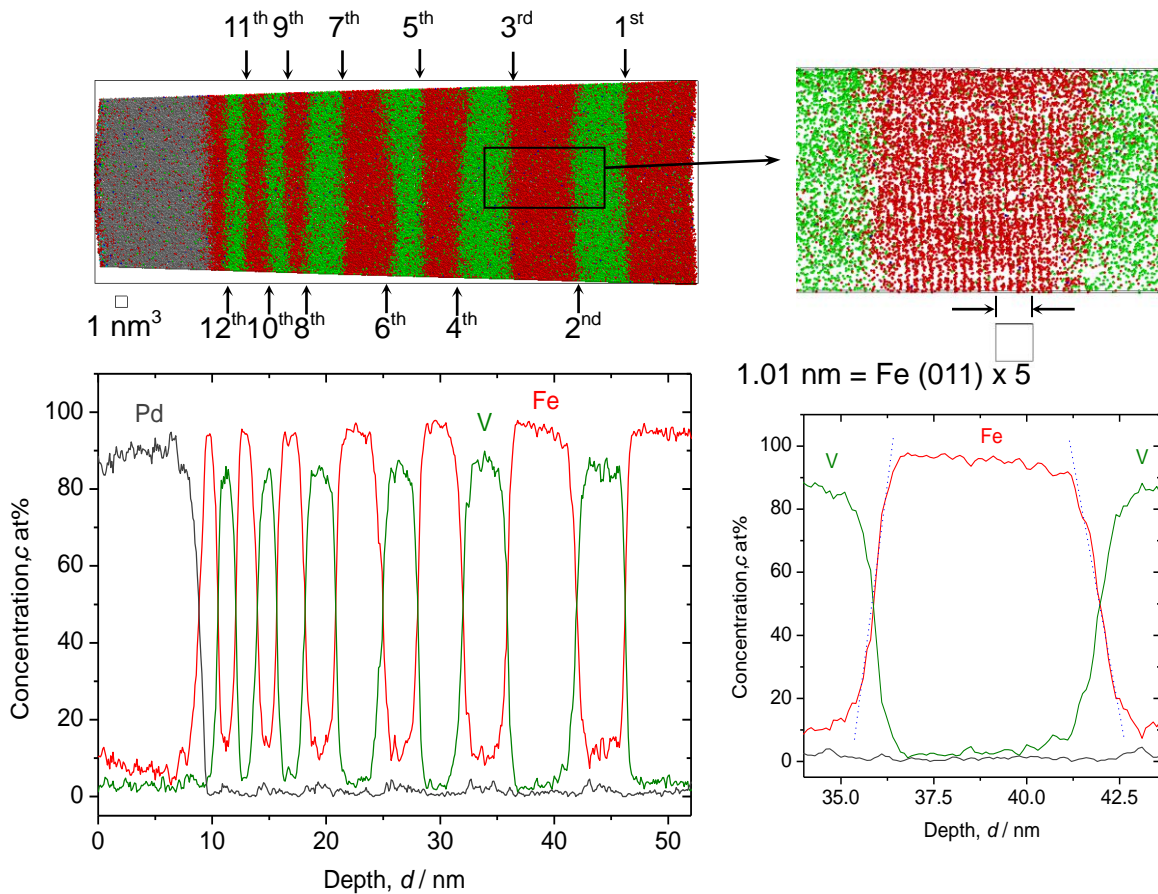


Fig. 4.18 3D reconstruction volume (18 nm x 18 nm x 53 nm) and 1D concentration profile of Fe/V multi-layered film on W deposited at 603 K, with a magnified V/Fe/V interface (right hand side). The number of Fe/V interface (12 in total) is indicated as the order number.

APT reconstruction result of a thickness-modulated Fe/V multi-layered stack deposited at 603 K is shown in Fig. 4.18, together with the depth concentration profile taken from a 5 nm- ϕ cylinder volume. Clearly resolved parallel Fe (011) planes prove a result of successful APT reconstruction.

The Fe content found in the V layers was more than 10 at%. This value is larger than that expected from the experimental set up, which is in the range of 2 ~ 8 at%. Therefore, other processes, like interdiffusion due to high temperature deposition or intermixing by sputtering are re-

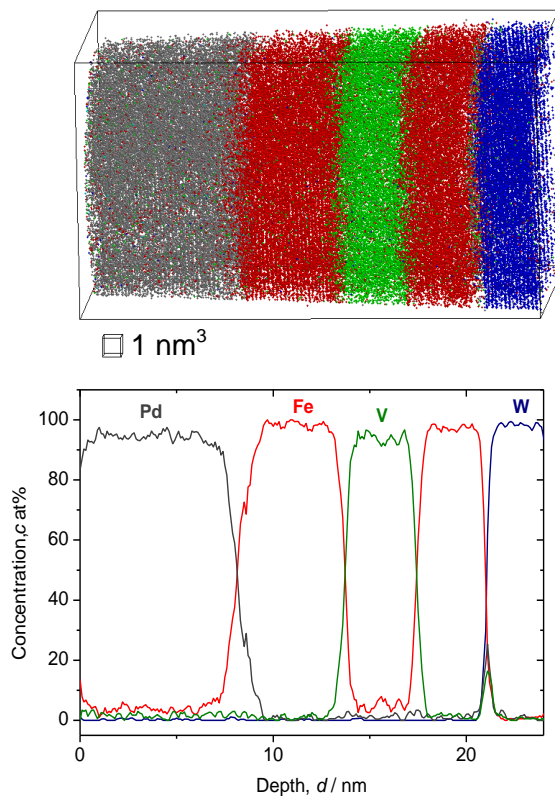


Fig. 4.19 3D reconstruction volume (13 nm x 13 nm x 26 nm) and 1D concentration profile of Fe/V multi-layered film on W deposited at 297 K. The slope for deposition sequence of V on Fe is slightly steeper than that of Fe on V.

sponsible to increase the Fe content. It should also be noted that the alloying of V with Fe becomes significant towards the surface.

When Fe/V multi-layered film is deposited at room temperature, both Fe concentration in V and V concentration in Fe are rather low. The APT analysis result of this film deposited at 297 K is shown in Fig. 4.19. The Fe concentration in V layer is in this case 5(2) at% and V concentration in Fe is nearly zero. The Fe concentration is high (10 at%) at the top surface of Pd, which is found also for the film deposited at 603 K. The slope of the Fe/V interfaces is sharper than in the case of 603 K.

Fe and V concentration in the layers must be considered from Fe-V phase diagram. The Low temperature part of the Fe-V binary phase diagram [Land08] is shown in Fig.4.20. The solubility of Fe in V and V in Fe

at 603 K is 17 at% and 26 at%, respectively. At 297 K, they reduce to 12

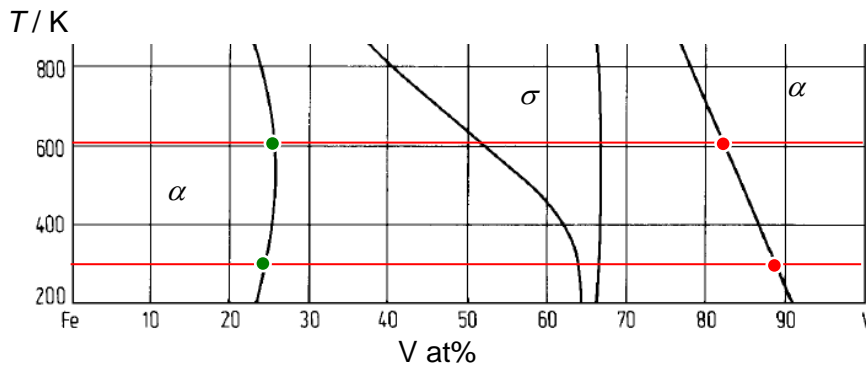


Fig.4.20 Low temperature part of Fe-V binary phase diagram [Land08]. 603 K and 297 K are shown by red lines. Fe solubility limit (red) and V solubility limit (green) at each temperature are indicated by circles.

at% and to 25 at%, respectively. Further excess causes the precipitation of σ phase. The detected Fe and V concentrations were after all below the solubility limits and therefore only the α solid solution phase is considered.

Consequently, the observed high Fe content in the V layers could be caused by thermal interdiffusion at 603 K, while it is suppressed at 297 K. However, there are following points left to be discussed.

- (i) Origin of asymmetric Fe/V interface profile
- (ii) Increasing alloying degree towards the surface

These matters are discussed in the next section.

4.3.3 Interface intermixing by sputtering process

In Fig. 4.21 and in Fig. 4.22, the magnified V/Fe/V region is shown for the films deposited at 603 K and at 297 K, respectively. According to these profiles, the intermixing depth can be estimated as wide as 2 nm when deposited at 603 K. This value is almost twice of the mixing thickness at 297 K, which is 1.0 ~ 1.1 nm. By XRR measurement, the saturated interface roughness at Fe/V interface was determined as 1.2 ~ 1.4 nm. This implies that the chemical intermixing is of the major factor.

At the 2nd and 6th Fe/V interface some relaxation of slope can be seen. But, there is no systematic change in the slope of profiles in the course of deposition even at high temperature of 603 K. Therefore, interdiffusion process only cannot be convincingly attributed for explanation. When the

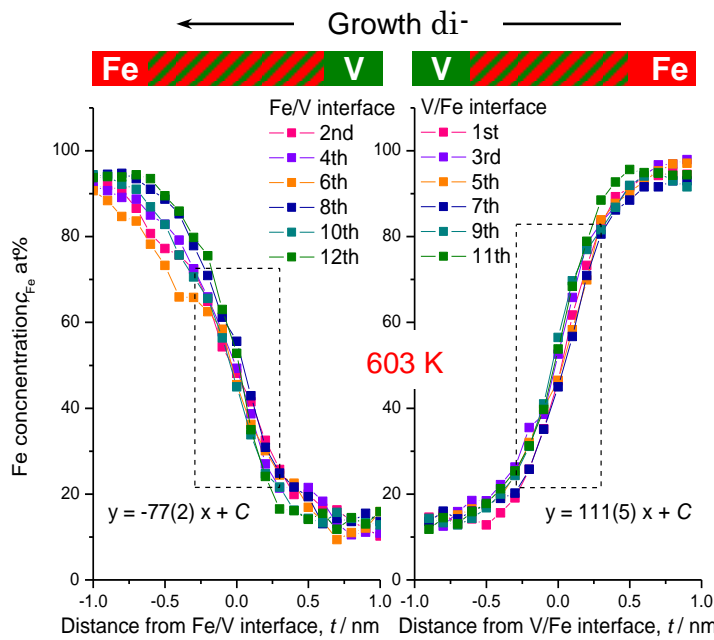


Fig. 4.21 Fe concentration profiles at Fe/V and V/Fe interfaces in Fig. 4.18.

Deposition $T = 603$ K.

The numbers are assigned as for the interfaces indicated in Fig. 4.18.

The concentration slope at each in the same series is almost identical. But the average slope for deposition sequence of V on Fe is steeper than that of Fe on V.

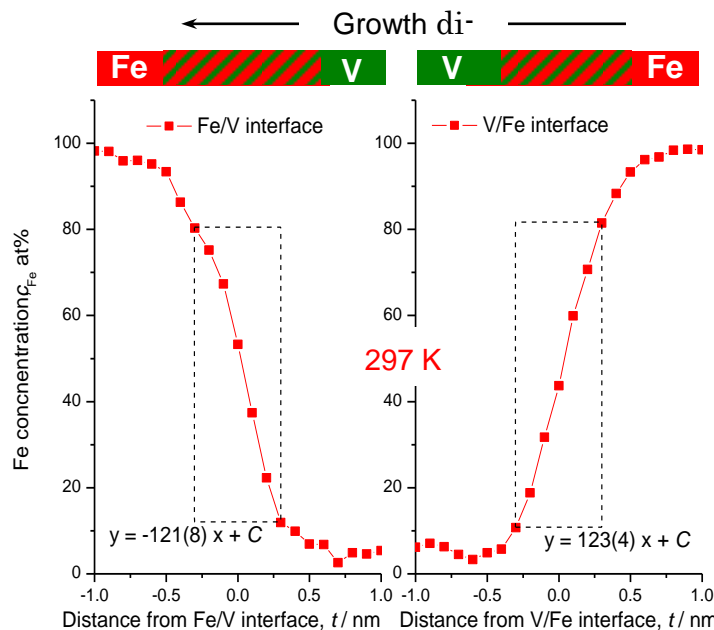


Fig. 4.22 Fe concentration profiles at Fe/V and V/Fe interfaces in Fig. 4.19.

Deposition $T = 297$ K.

The concentration slope for deposition sequence of V on Fe is steeper than that of Fe on V.

both of interface profiles at V/Fe and Fe/V are compared, one can see a slight asymmetry of the concentration slope for both at 603 K and 297 K; the intermixing at V/Fe sequence is less pronounced than that at Fe/V. The same trend was confirmed also by XRR measurement of Fe/V multi-layer. The origin of this asymmetry may be associated with sputter induced implantation and recoil phenomena.

In order to investigate the collision detail of sputtering, simulations were carried out with SRIM 2008 developed by Ziegler [Zieg85]. At first, simulations of the Ar ion (800 eV) bombardment into V and Fe were carried out to set the kinetic energy of the sputtered V and Fe ions as $E_V = 33.01$ eV and $E_{Fe} = 24.81$ eV, respectively. For each collision calculation, a displacement energy (Wigner energy) of 24 eV for target materials was

assumed, as it is reasonable for metals [Haas78]. These parameters were then applied in the simulation.

In Fig.4.23, simulated ion implantation depth profile and target atom recoil profile for Fe ion in V target and V ion in Fe target are shown, re-

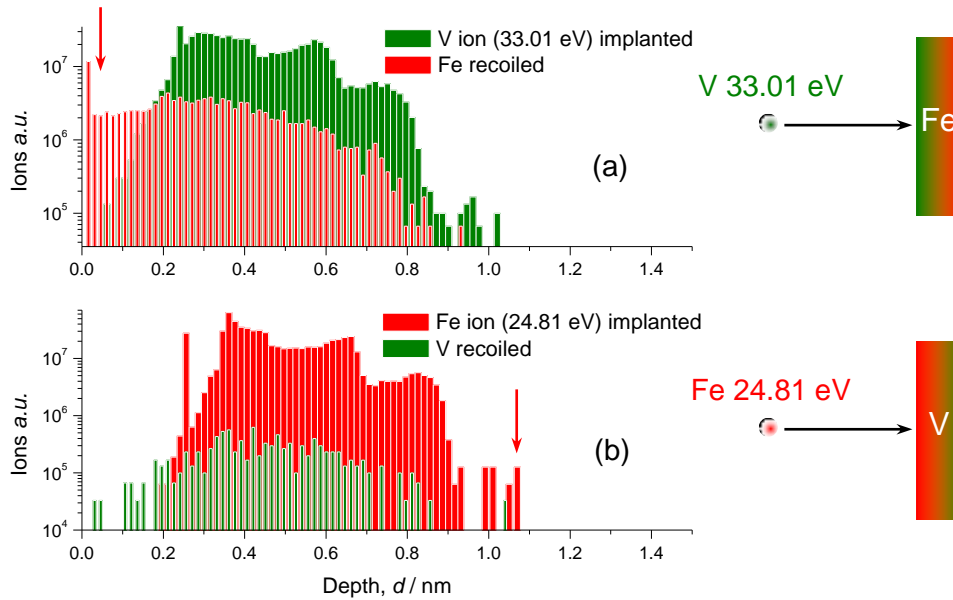


Fig.4.23 SRIM simulation results of implantation depth and recoil distribution, for V in Fe (a) and Fe in V (b). To increase statistics, the process was repeated 20000 times. Note significant recoil of Fe and deeper penetration depth of Fe than that of V (indicated by red arrows).

spectively. According to these results, 3 main insights can be extracted.

- (1) The maximum implantation depth of Fe is slightly deeper than that of V ion.
- (2) The intensive recoil events of Fe indicate (first 0.1 nm in (a)) floating Fe at the deposition front.
- (3) The recoil of V is much less pronounced than that of Fe (recoiled V ion count is one order of magnitude smaller). If we take the displacement energy of 25 eV for V, the recoil events of V do not even happen.

(1) explains slightly wider interface of Fe/V than that of V/Fe, regardless of temperature. (2) and (3) suggest continuous motion of Fe or V atoms towards the deposition front, which may increase the intermixing layer thickness than the values simulated here. This process might

change also the layer composition if the temperature is high and solubility is ensured to certain extent.

4.3.4 Combined effect of sputtering and thermal interdiffusion

The layer composition of the sample deposited at 603 K is also affected by the sputtering process. In Fig.4.24, the in-layer compositions are plotted for the film deposited at 603 K, together with the solubility limit (SS limit) at the same temperature. Very gradual slopes of c_{Fe} and c_{V} along the deposition direction suggest the trace of recoiled atoms and high degree of

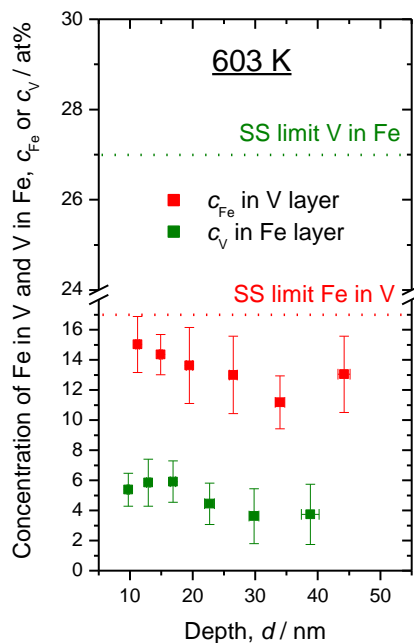


Fig.4.24 In-layer composition of Fe and V plotted against depth at 603 K. Each solubility limit (SS limit) for bulk system is shown, too.

alloying at 603 K.

From the results obtained, a schema of Fe/V multi-layer deposition can be drawn as follows. The primary knocked-on Fe or V atoms are deposited not only onto the surface, but also in a sample depth. A series of this process, i.e. sputter deposition, creates new intermixed surface. Consequently, the actual intermixing width becomes slightly wider than the values calculated on single process like shown in Fig.4.23.

Moreover, especially on the sequence of V on Fe, Fe atoms propagate always towards the deposition front due to the recoil and substantially alloyed with V if the deposition temperature is high. The same process is possible also for the deposition of Fe onto V, but very suppressed due to small kinetic energy of Fe ion to recoil V. A continuous propagation of the floating Fe atoms finally stops at the Pd surface, where it is terminated

with high amount of Fe (see Fig. 4.18 and Fig. 4.19).

As a conclusion, the interdiffusion process was incorporated with floating phenomenon of atoms at high deposition temperature and thus resulted in higher extent of alloying than at room temperature.

Hetero-epitaxy of multi-layered film with high crystal quality is established often at certain high deposition temperatures at given deposition rate and atmosphere. For Fe/V superlattice growth by magnetron sputtering, which has 10 times higher deposition rate than here, it is reported e.g. at 453 K [Isbe98]. But, this was not the case for Fe/V prepared in this study. In this study, therefore, the sputter deposition of Fe/V multi-layer was not carried out at high temperatures, except for the V buffer layer.

5. Results and discussion

5.1 In-plane stress evolution upon hydrogen absorption

In this section, the results of in-plane stress evolution upon hydrogen absorption measured simultaneously with EMF measurement will be presented. The hydrogen induced lattice expansion and its relationship with the observed stress development can be influenced by defect-hydrogen interaction and also by initial state of lattice expansion in the film. Some peculiar features in stress curves reflecting such consideration are of special interest in this section.

5.1.1 Impact of deposition temperature

The hydrogen induced stress developments of the V-Fe8at% (110) 100-nm thick films deposited on Al₂O₃ (0001) at 297 K, 773 K and 1073 K are plotted against hydrogen concentration (c_H) in Fig. 5.1.1 (a), together with their EMF curves recorded simultaneously (b).

In (a), all films exhibit in-plane compressive stress, showing some inflection points that are marked by arrows. These inflection points are found typically at around $c_H = 0.10$ H/V and at around $c_H = 0.35 \sim 0.40$ H/V.

In (b), low c_H regions are magnified in the inset. At low c_H , a straight line is drawn as RT/F . This line is deduced from the Sieverts' law, which is regarded as ideal relationship between chemical potential of H and c_H . All of the actual EMF curves lie below this straight line, usually indicating a trapping of H at defects like dislocations and vacancies. At around $c_H = 0.04$ H/V (circled with red line in the inset), the curves start to follow the Sieverts' law (RT/F). The deviation from the Sieverts' law in the low concentration region is thereafter observed at $c_H = 0.06 \sim 0.10$ H/V, where α -phase region is most probably terminated. After passing the plateau region between 0.10 and 0.40 H/V, the EMF starts to increase again. This means, further hydrogen absorption in β -phase (hydride phase) occurs at $c_H = 0.40$ H/V.

According to linear elasticity theory of bcc crystal, the expected compressive stress of vanadium in directions of $\langle 1\cdot10 \rangle$ (x), and $\langle 001 \rangle$ (y) are calculated as $\sigma \cdot c_H = -11.7$ GPa·H/V and $\sigma \cdot c_H = -13.3$ GP·H/V, respectively. The average product of these compressive stresses thus gives $\langle \sigma \rangle \cdot c_H = -12.5$ GPa·H/V. This average value was applied to verify the linear elastic

behavior of the films deposited on Al_2O_3 (0001) substrate, as the domains for these films were confirmed to orient isotropically in in-plane direction (Fig. 4.2 and Fig. 4.3). The red dot line in Fig. 5.1.1 (a) shows this linear elasticity prediction based on the above assumption. The elastic modulus of Al_2O_3 (0001) basal plane can be treated as isotropic as well (Fig. 4.4). The stress values were, therefore, calculated by using the biaxial elastic modulus published in [Thok95], where $E / (1 - \nu) = 697.7 \text{ GPa}$ ($E = 540 \text{ Pa}$, $\nu = 0.226$).

As a general trend of Fig. 5.1.1 (a), the films deposited at high temperatures show totally different shapes of curve compared to that deposited at 297 K. While the film prepared at 297 K shows distinct change of

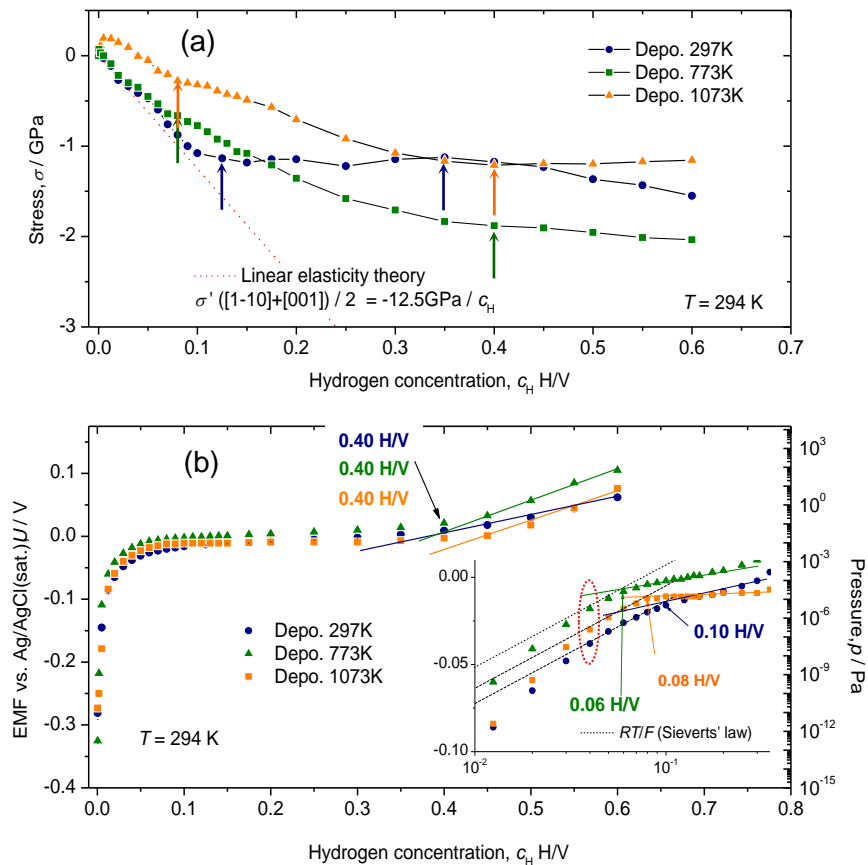


Fig. 5.1.1 (a) In-plane stress development of the V-Fe8at% (110) 100 nm-thick films deposited on Al_2O_3 (0001) at different temperature. The straight line (red dot) with the slope of $-12.5 \text{ GPa}/c_H$ is the predicted behavior by linear elasticity theory. Arrows indicated are inflection points in the curves. (b) The EMF curves recorded simultaneously. The inset shows magnification of low c_H range. The black dot line shows Sieverts' law. Arrows show inflection points in the curves. Colored lines are guide for eyes.

its slope in the curve with showing a plateau-like region at high concentrations ($c_H = 0.10 \sim 0.40$ H/V), the films prepared at 773 K and 1073 K show continuous stress release without showing plateau until around $c_H = 0.40$ H/V. In the α -phase region (for low concentrations between $c_H = 5 \times 10^{-3}$ H/V and 0.10 H/V, the linear increase of compressive stress with a slope of -12 (1) GPa/H/V was confirmed for the film deposited at 297 K. However, the other 2 films show less pronounced stress release. Interestingly, the film deposited at 1073 K initially shows an upward-curvature up to $c_H = 0.005$ H/V, meaning a tensile stress occurred.

At concentrations higher than 0.40 H/V, the in-plane stress again starts to increase for the film of 297 K. However, the films deposited at high temperatures do not show further drastic stress release, but remain relaxed. For thin films on rigid substrates, the stress relaxation is often associated to film buckling and subsequent peeling off, which is usually visible even with eyes. However, any buckling of the films was not observed in this case until 0.40 H/V. This implies strong adhesion at film/substrate interface and, thus the stress relaxation can be established through plastic deformation within the film, with a surface morphology change.

For more detailed examination of initial stress release, the region of $c_H = 0 \sim 0.2$ H/V was magnified and shown in Fig. 5.1.2. In the low concentration region, the interaction of hydrogen atoms and defects are expected to be rather significant. Therefore, different defect density in the sample may reflect different behavior in the stress release curve.

In fact, there are some interesting differences visible. As already observed, the tensile stress of the film deposited at 1073 K reached $\Delta\sigma = 0.19$ GPa. Moreover, the film deposited at 773 K also shows the tensile stress, which is not as much as that of 1073 K though, up to $\Delta\sigma = 0.07$ GPa. The film deposited at room temperature does not show such deviation at all. This tensile stress release was observed only at extremely low concentrations between $c_H = 0$ and 0.005 H/V. At such a low c_H , defect-H interaction is usually present.

The slope of the stress development m also shows the deposition temperature dependence, showing smaller slope for the films deposited at higher temperatures.

It should also be stressed that the critical stress $\sigma_{\alpha, \text{lim}}$, where the last deviation from the linear behavior occurs (indicated by thick red arrows), decreases with increasing the deposition temperature from -1.13 GPa to -0.28 GPa. Until this deviation is observed, a relatively good agreement of the compressive stress with that of prediction by linear elastic theory was confirmed only in a selected low concentrations between 0 and 0.04 H/V

and between 0.06 and 0.125 H/V, for the film deposited at 297 K. In case of the film deposited at 773 K, this ideally elastic behavior was observed only between 5×10^{-4} and 0.03 H/V. The film at 1073 K does not show any agreement with the predicted linear elastic slope. At the concentration of 0.04 H/V, a small relaxation of the stress occurs for the films of 297 and 773 K, as denoted by c_1 . Surprisingly, this concentration corresponds to the point where the EMF curve shows Sieverts' behavior. It is within the α -phase. The slope thereafter becomes more gentle in case of 773 K and the 2nd deviation ($c_{\alpha, \text{lim}}$) appears at 0.125 and at 0.08 H/V for 297 K and 773 K, respectively. The last deviation point before plateau-like region is denoted as $\sigma_{\alpha, \text{lim}}$. According to the EMF curve recorded simultaneously, these concentrations nearly correspond to α -phase boundary, i.e. the solute hydrogen starts to form hydride phase, where plastic deformation is usually incorporated.

The observed dependence of $c_{\alpha, \text{lim}}$ on the deposition temperature is roughly consistent with general prediction from the viewpoint of the Hall-Petch relationship, as the domains are larger for the films deposited at high temperatures. It is usually predicted that the film consists of

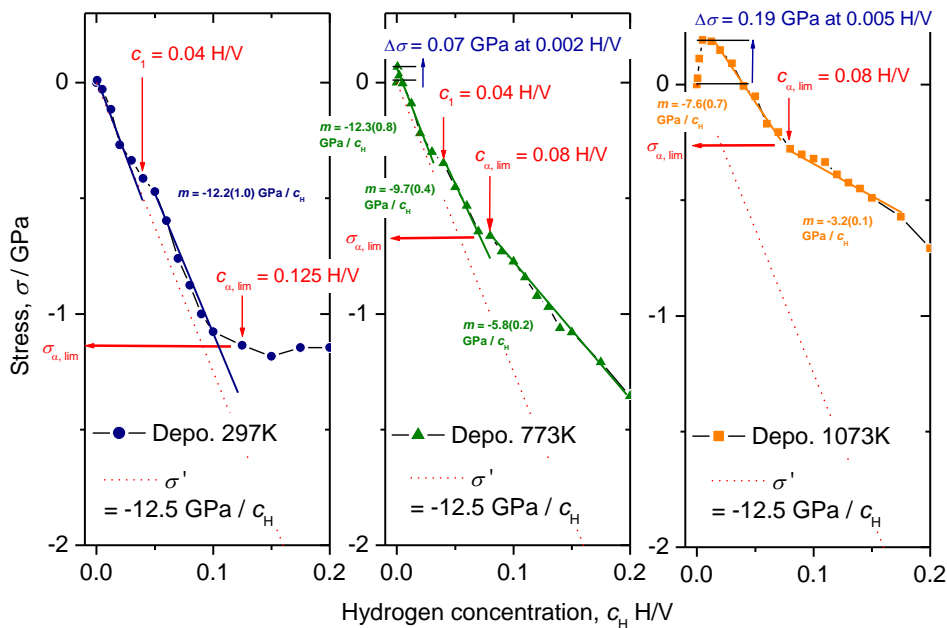


Fig. 5.1.2 Magnified plots of Fig. 5.1.1 shown separately for the samples deposited at different temperatures. The straight line with the slope of $-12.5 \text{ GPa} / c_H$ is the predicted behavior by linear elastic theory assuming one dimensional lattice expansion upon H absorption. Several deviations from the linear elastic behavior are indicated by red arrows. Note $\sigma_{\alpha, \text{lim}}$ decreases as the deposition temperature increases (see text).

larger grains will release the stress more efficiently than that with smaller grains does, as the pile-up of the dislocations upon plastic deformation is significant in small grains and thus results in mechanical hardening [Haas78+]. The observed decrease of $\sigma_{\alpha,lim}$ with increasing deposition temperature confirms this general consideration. However, the total stress release observed for the film deposited at 297 K is smaller than that of 773 K.

It was shown that the initial out-of-plane interplanar distance d decreased with increasing the deposition temperature (see Chap. 4.1, Table. 4.1). That is, the films deposited at high temperatures are under larger in-plane tensile stress than that of the films at lower temperatures, if the linear elastic response is valid. Additionally to the microstructural feature or to the vacancy concentration, the influence of initial in-plane stress on stress release upon hydrogen absorption should also be considered to compare the total stress release of different thin film samples.

Based on the assumption above, the intrinsic in-plane stress estimated from interplanar distance measured by XRD (Table. 4.2) was taken into account and the stress value was recalculated. This treatment only shifts the whole stress curve upwards or downwards depending on if the

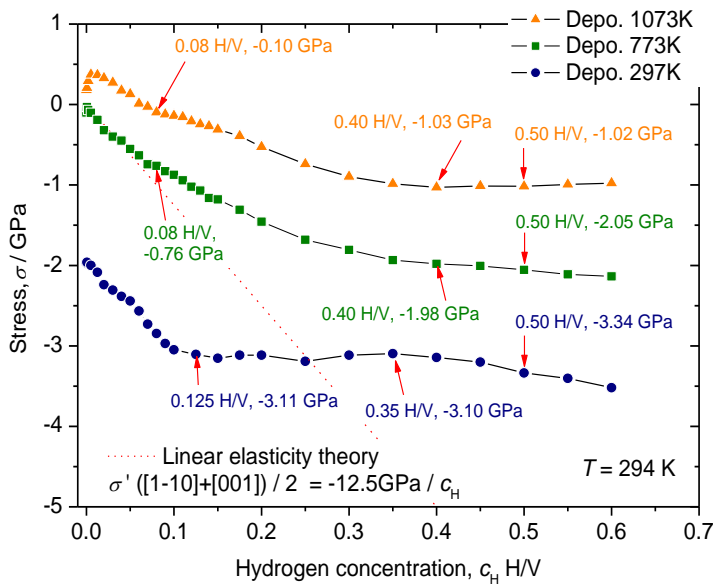


Fig. 5.1.3 (a) Corrected stress curve of V-Fe8at% (110) 100-nm thick films deposited on Al_2O_3 (0001) at different temperature, according to the initial lattice distortion (see text).

film is under tensile or compressive in-plane stress, respectively. For these films, -1.97 GPa, -0.10 GPa and +0.18 GPa was added on each measured stress curve of 297 K, 773 K and 1073 K, respectively. After this treatment the stress curves are replotted in Fig. 5.1.3. The resulting curves show clean order of the total stress release.

Table 5.1 H-induced critical stress σ_c including residual stress and critical hydrogen concentration c_c of V-Fe8at% (110) films deposited on Al_2O_3 (0001) at different deposition temperatures and domain sizes. $\sigma_{\alpha,\text{lim}}$ and $c_{\alpha,\text{lim}}$ are at α -solubility limit. c_1 denotes within α -solubility limit.

Substrate temperature T [K] and X-ray domain size t [nm]	Critical stress σ_c [GPa]		Critical concentration c_c [H/V]	
	$\sigma_{\alpha,\text{lim}}$		$c_{\alpha,\text{lim}}$	c_1
$T = 297, t = 37$	-3.11		0.125	0.04
$T = 773, t = 51$	-0.76		0.08	0.04
$T = 1073, t = 51$	-0.10		0.08	-

The corrected $\sigma_{\alpha,\text{lim}}$ and corresponding hydrogen concentration $c_{\alpha,\text{lim}}$ and c_1 are shown in Table 5.1. The c_1 corresponds to the small relaxation observed in the α -phase. The domain sizes t calculated by Scherrer's formula are indicated together. When considered that these domain sizes are not representative for the true domain sizes e.g. in-plane domain size, the obtained relationship between the expected domain size and the critical and total stress implies Hall-Petch type relationship.

Concerning the phase boundary, the comparison was made for c_H , where inflections were observed both in the stress curves and EMF curves, and summarized in Table 5.2. The both inflection points in stress and

Table 5.2 Phase boundaries determined from stress and EMF curves' inflection points of V-Fe8at% (110) 100-nm thick films deposited on Al_2O_3 (0001) substrates.

Substrate temperature T [K]	Inflection point in stress curve [H/V]		Inflection point in EMF curve [H/V]	
	α -phase limit	End of $\alpha+\beta$ -phase	α -phase limit	End of $\alpha+\beta$ -phase
297	0.125	0.35	0.10	0.40
773	0.08	0.40	0.06	0.40
1073	0.08	0.40	0.08	0.40

EMF curves are in good agreement. According to the phase boundaries bulk pure V-H system [Pesc81], $\alpha+\beta$ -two-phase region at room temperature lies between $c_H = 0.03$ and 0.5 H/V. The observed values of c_H correspond well to these terminal concentrations, but with extended α solubility and narrower miscibility gap (compare with Fig. 2.4).

As a conclusion, the experimental findings can be summarized as follows.

- (i) The phase boundaries of metallic thin film-H system can be determined by the combined method of stress and EMF measurement.
- (ii) The in-plane compressive stress is larger for the films with larger domain size and with larger initial compressive stress.
- (iii) Deviation from the linear elasticity theory at low concentration needs consideration of defect-H interaction.

5.1.2 Impact of film thickness

In the last section, Hall-Petch type relationship was inferred. However, the trend was not verified. Therefore, similar experiments were carried out by changing film thicknesses between 400 ~ 10 nm for the films V-Fe2at% on Al₂O₃ (11-20). The critical thickness for misfit dislocation formation is in this case ~ 1 nm. Thus, the films prepared contain certain amount of dislocation. The deposition temperature was at 297 K. The in-plane orientation of the film investigated by texture measurement revealed multi-domain. Contrary to the case of Al₂O₃ (0001), the biaxial modulus of the substrates must be considered as anisotropic. The longitudinal direction Al₂O₃<000-1>, thus the bending direction of the substrate is parallel to V<1-10> (Fig. 4.11). Therefore, the linear elastic stress of -11.7 GPa/c_H for V<1-10> is expected in the elastic regime. The calculation of stress was carried out by using the biaxial elastic modulus of Al₂O₃ published in [Thok95], where $E / (1 - \nu) = 516.5$ GPa ($E = 516.5$ GPa, $\nu = 0$).

5.1.2.1 400-nm thick film

In Fig.5.1.4 the stress curve of 400-nm thick film is shown together with corresponding EMF curve. The inflection points in both curves are indicated by arrows. At low c_H, the agreement with the predicted linear elastic behavior is established up to 0.07 H/V. We call the stress value at this deviation point just before the plateau as $\sigma_{\alpha,lim}$, and corresponding c_H as c _{α,lim} unless otherwise stated. In this film, the $\sigma_{\alpha,lim}$ at the end of linear elastic region showed -0.79 GPa. Unlikely to the 100-nm thick films on Al₂O₃ (0001), no deviation below c _{α,lim} was observed. Further hydrogen absorption leads to drastic relaxation of compressive stress until the c_H reaches 0.35 H/V, showing positive slope of +0.5 GPa/c_H. Above this concentration the slope again turns to negative. The linear fit in this concen-

tration region shows $-1.1 \text{ GPa}/c_{\text{H}}$. The total stress released at 0.5 H/V was estimated to be -0.81 GPa .

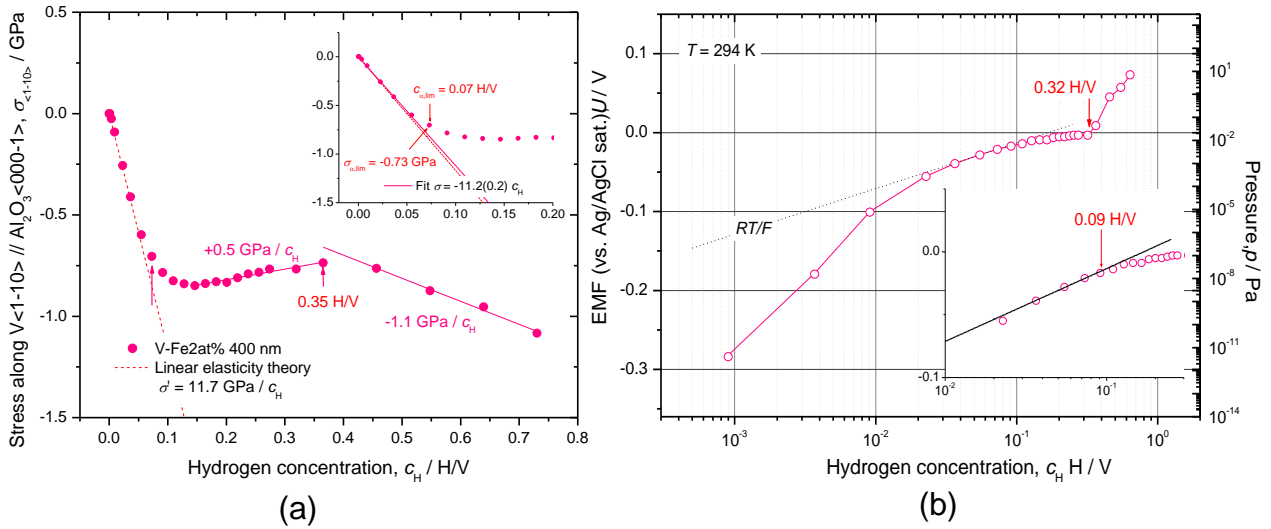


Fig.5.1.4 (a) Stress curve of 400-nm thick film on Al_2O_3 (11-20) deposited at 297 K. Fitting curve of linear elastic region is shown in the inset. Arrows indicate inflection points, where the slope changes. (b) EMF curve measured simultaneously during stress measurement. Low c_{H} region is magnified in the inset. Deviation from the Sieverts' law and the end of plateau-like region are found at 0.09 H/V and at 0.32 H/V , respectively.

The observed inflection points in the stress curve correspond to those in the EMF curve, at 0.09 H/V and at 0.32 H/V , respectively. However, the plateau-like region is considerably narrow, when compared to those of 100-nm thick films shown in Fig. 5.1.1 (b). Assuming that these inflection points are associated with phase boundaries, the difference of microstructure between the films should be taken into account.

5.1.2.2 200-nm thick film

Fig. 5.1.5 shows results of the same experiment on a 200-nm thick film. Again, a good agreement with the linear elasticity theory was observed. The first inflection in the stress curve occurs at 0.04 H/V , where the $\sigma_{\alpha,\text{lim}}$ shows only -0.34 GPa , which is almost a half of that in 400-nm thick film. The EMF curve also shows a deviation at a similar concentration, $c_{\text{H}} = 0.05 \text{ H/V}$. After showing moderate compressive stress increase with a slope of $-0.4 \text{ GPa}/c_{\text{H}}$, the slope starts to increase at $c_{\text{H}} = 0.21 \text{ H/V}$. At exactly the same concentration the EMF curve shows positive sloping as well. The

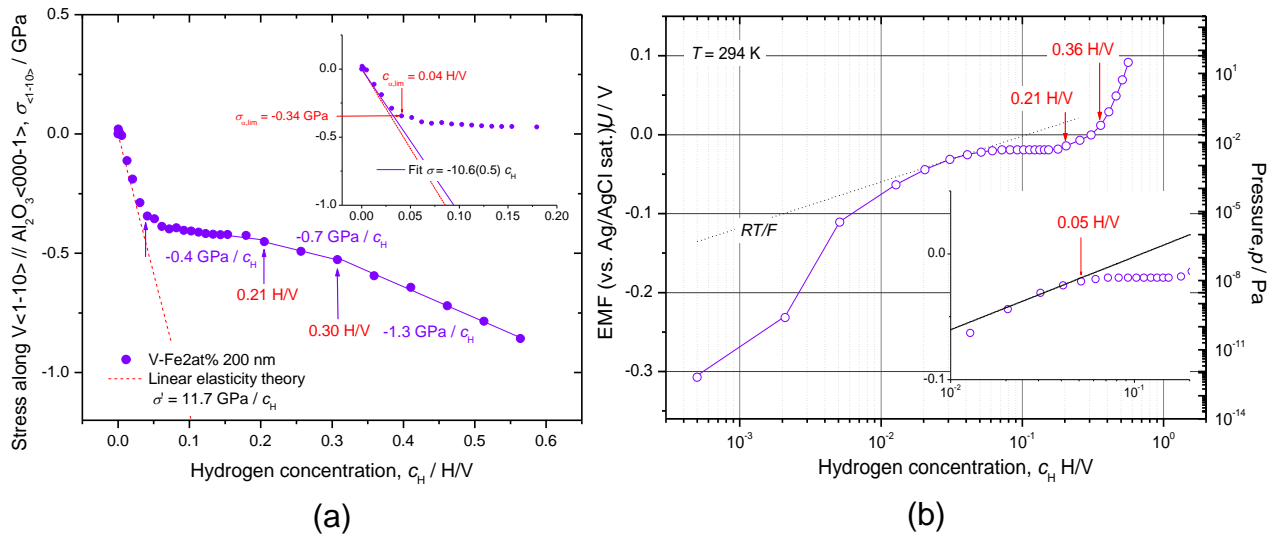


Fig. 5.1.5 (a) Stress curve of 200-nm thick film on Al_2O_3 (11-20) deposited at 297 K. Fitting curve of linear elastic region is shown in the inset. Arrows indicate inflection points, where the slope changes. (b) EMF curve measured simultaneously during stress measurement. Low c_H region is magnified in the inset. Deviation from the Sieverts' law and the end of plateau-like region are found at 0.05 H/V and at 0.30 H/V, respectively.

final slope of the stress curve was with $-1.3 \text{ GPa}/c_H$, starting at 0.30 H/V, while the EMF increases at higher concentration, 0.36 H/V.

Unlike to 400-nm thick film, the relaxation of stress within the 2 phase region is not pronounced. No tensile stress occurred. The total stress released at 0.5 H/V was -0.77 GPa . This is comparable to that of 400-nm thick film, -0.81 GPa .

5.1.2.3 100-nm thick film

The result of 100-nm thick film is shown in Fig. 5.1.6. At this thickness a slight deviation of the initial stress curve from the linear elastic behavior is observed. Similar behavior was also confirmed in the 100-nm thick film on Al_2O_3 (0001) deposited at room temperature as well. At the concentration of 0.04 H/V the 1st deviation of the curve ($\sigma_1 = -0.28 \text{ GPa}$) occurs. As already observed in the films on (0001), this concentration corresponds to where the curve starts to follow the Sieverts' law in the EMF curve. The linear elastic behavior ends at $c_H = 0.1 \text{ H/V}$. The stress value remains constant until c_H reaches 0.40 H/V. The slope afterwards shows $-1.3 \text{ GPa}/c_H$. The total stress release at $c_H = 0.5 \text{ H/V}$ indicates -0.87 GPa . The EMF curve

shows termination of plateau-like region at 0.35 H/V.

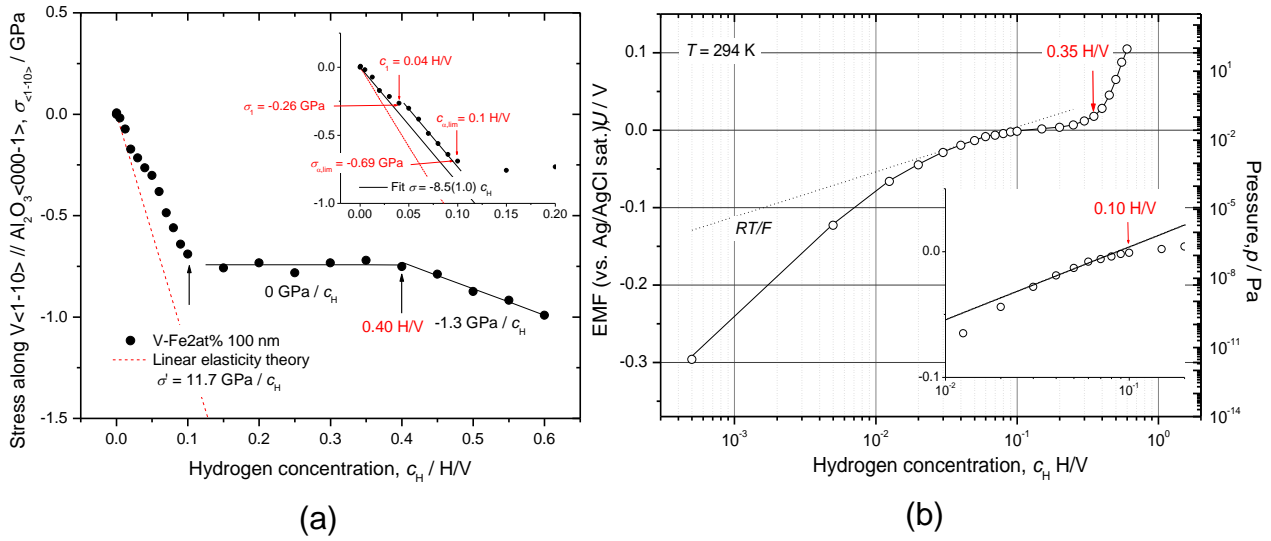


Fig. 5.1.6 (a) Stress curve of 100-nm thick film on Al_2O_3 (11-20) deposited at 297 K. Fitting curve of linear elastic region is shown in the inset. Arrows indicate inflection points, where the slope changes. (b) EMF curve measured simultaneously during stress measurement. Low c_H region is magnified in the inset. Deviation from the Sieverts' law and the end of plateau-like region are found at 0.10 H/V and at 0.35 H/V, respectively.

5.1.2.4 50-nm thick film

Similar to the case of films deposited at 773 K or 1073 K, positive deviation $\Delta\sigma = +0.04(2)$ GPa at the very beginning of hydrogen loading is observed, as indicated by a blue arrow in Fig. 5.1.7. Several deviations from the linear elastic behavior below $c_{\alpha, \text{lim}}$ are visible also in this film, as denoted c_2 and c_1 at 0.03 H/V and at 0.09 H/V, respectively. Though it was not observed in thicker films with 200 nm or 400 nm, these deviations tend to become more visible as the thickness decreases. At $c_H = 0.03$ H/V there is no distinctive change in the EMF curve. However, the onset of Sieverts' law behavior can be estimated at $c_H = 0.07$ H/V, which is close to the $c_1 = 0.09$ H/V in the stress curve.

At $c_H = 0.12$ H/V the curve starts to bend and shows gentle slope of -0.7 GPa/ c_H . The next bending occurs at $c_H = 0.25$ H/V, with steeper slope of -1.5 GPa/ c_H . The slope of plateau-like region in the EMF curve is more considerable than that of the thicker films. It is clearly seen in the inset of EMF curve, where the overlap of Sieverts' law line and the measured curve is

rather pronounced. The final stress value at $c_H = 0.50$ H/V reaches at -1.2 GPa.

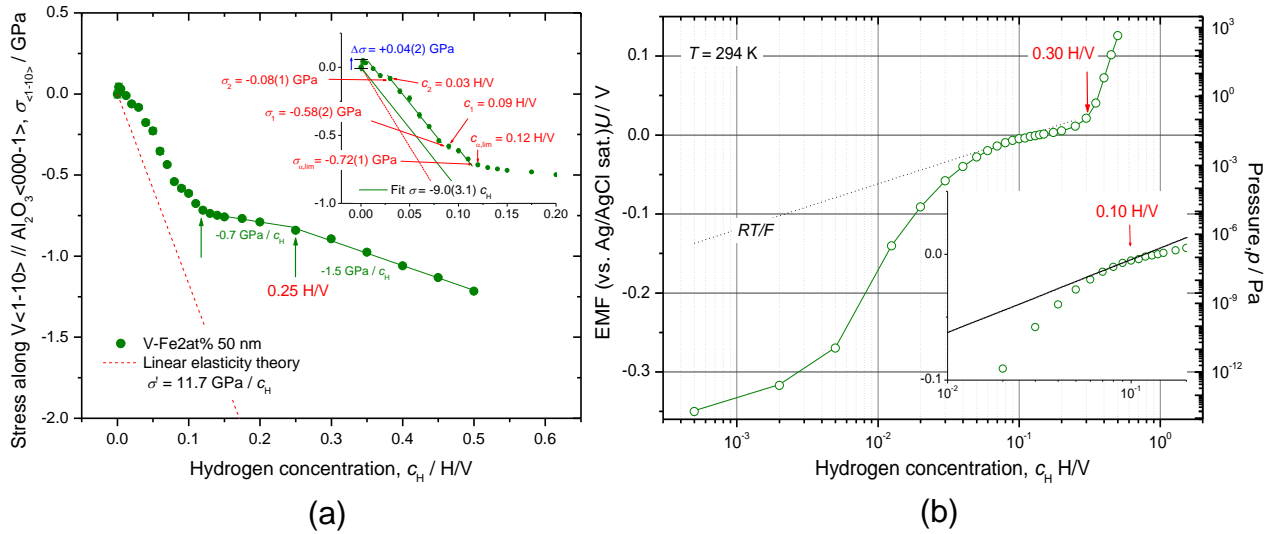


Fig. 5.1.7 (a) Stress curve of 50-nm thick film on Al_2O_3 (11-20) deposited at 297 K. Fitting curve of linear elastic region is shown in the inset. Arrows indicate inflection points, where the slope changes. (b) EMF curve measured simultaneously during stress measurement. Low c_H region is magnified in the inset. Deviation from the Sieverts' law and the end of plateau-like region are found at 0.10 H/V and at 0.30 H/V, respectively.

5.1.2.5 20-nm thick film

The impact of decreasing the film thickness on stress release behavior becomes more significant. The results of 20-nm thick film is shown in Fig. 5.1.8. It is clearly seen that the total stress and the slope of the curve is significantly larger than those seen in the thicker films.

At the first loading step of 5×10^{-4} H/V, there is an abrupt increase of stress. Thereafter the compressive stress increases linearly with a slope of -12.8(1.3) GPa/ c_H . Although this is larger than the ideal slope -11.7 GPa/ c_H , it is still in the range of error. The already observed several inflections in this linear elastic region are again observed also in this sample, at 0.03 H/V and at 0.07 H/V. At the concentrations above 0.13 H/V the intermediate region shows still large slope of -3.6 GPa/ c_H up to 0.30 H/V. Further loading then induces even smaller slope, -1.7 GPa/ c_H , followed by final stress value of -2.2 GPa at $c_H = 0.5$ H/V.

The corresponding EMF curve as well shows considerable slope as a whole. Only the onset of the overlap at 0.10 H/V can barely be confirmed.

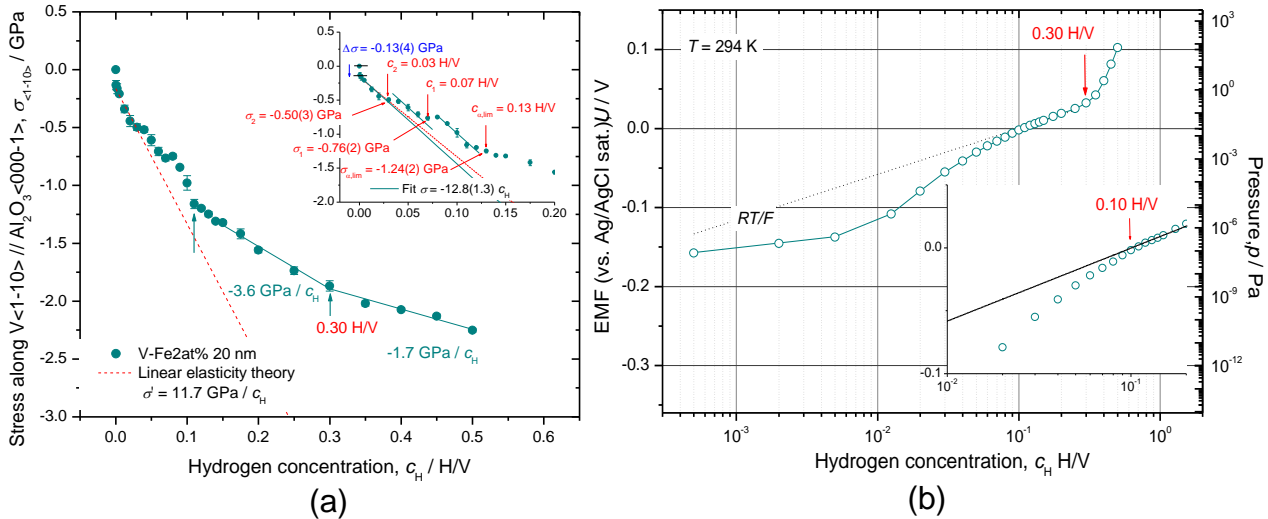


Fig. 5.1.8 (a) Stress curve of 20 nm-thick film on Al_2O_3 (11-20) deposited at 297 K. Fitting curve of linear elastic region is shown in the inset. Arrows indicate inflection points, where the slope changes. (b) EMF curve measured simultaneously during stress measurement. Low c_H region is magnified in the inset. Deviation from the Sieverts' law as a sign of solubility limit cannot be confirmed.

The comparison with Sieverts' law does not make usual sense anymore, as the both overlap each other until 0.30 H/V, at which the end of two phase field is suggested. The Sieverts' law does not take stress effect into account. In case of this 20-nm thick film, large compressive biaxial stress as depicted in Fig. 5.1.8 (a) might play a significant role for the considerable slope of EMF curve in (b).

5.1.2.6 10-nm thick film

Results on the thinnest film in the series, namely 10-nm thick film are shown in Fig. 5.1.9. The stress release is linear showing good agreement with ideal slope up to $c_H = 0.12$ H/V, with including a slight relaxation at $c_H = 0.05$ H/V. The slope in the intermediate region shows -2.1 GPa/ c_H , which is smaller than that of 20-nm thick film. However, the slope after $c_H = 0.25$ H/V shows considerably large value of -6.5 GPa/ c_H . The largest final stress of -3.0 GPa is established at $c_H = 0.50$ H/V.

The corresponding EMF curve shows the same trend as that of 20-nm thick film. The slope of intermediate region is almost the same as that of Sieverts' law and, therefore, only the onset of overlap can be confirmed at 0.06 H/V. The end of the intermediate region is found at 0.25 H/V, which agrees well with the bending point in the stress curve.

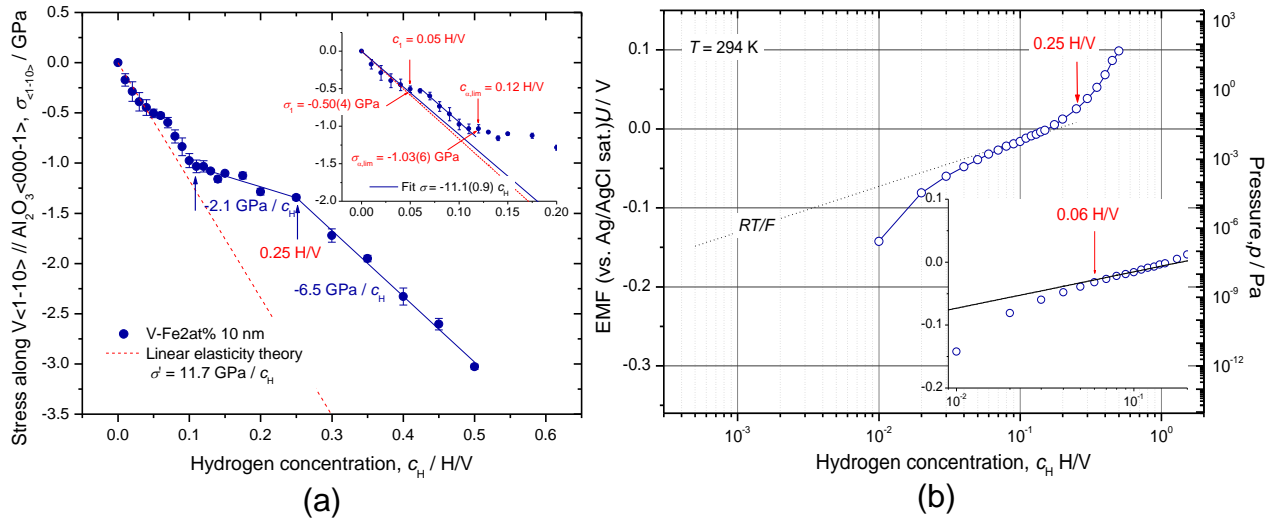


Fig. 5.1.9 (a) Stress curve of 10-nm thick film on Al_2O_3 (11-20) deposited at 297 K. Fitting curve of linear elastic region is shown in the inset. Arrows indicate inflection points, where the slope changes. (b) EMF curve measured simultaneously during stress measurement. Low c_H region is magnified in the inset. Deviation from the Sieverts' law as a sign of solubility limit cannot be confirmed.

5.1.2.7 Relationship between initial in-plane stress and film thickness

In Table 5.3, some specific σ values at each inflection point and the resulting slope changes are summarized. The observed slopes m_{lin} were in good agreement with the theoretical prediction ($\sigma' = -11.7 \text{ GPa}/c_H$) within error. Concerning the critical stress value, $\sigma_{\alpha,\text{lim}}$ and the maximum stress at $c_H = 0.5 \text{ H/V}$, σ_{max} seems to increase with reducing the thickness.

According to the XRD results of as-prepared films, huge compressive in-plane stress σ_0 of $-1 \sim -3 \text{ GPa}$ was confirmed (see Table 4.3). These residual stress values were added to H-induced stress, $\sigma_{\alpha,\text{lim}}$ and to σ_{max} for an accurate evaluation. The corrected stresses $\sigma_{\alpha,\text{lim}}'$ and σ_{max}' were tabulated together in Table 5.4 (in high lightened columns).

In XRD profiles of these films (Fig. 4.6), significant broadening of the (110) peak was observed. Under such a large stress, simple estimation of domain size by utilizing Scherrer's formula would fail. Thus, the tabulated t values in Table 5.4 are, unfortunately, not true in a strict meaning. Therefore, the dependence of stress on sample dimension is plotted against reciprocal of squared film thickness, $1/l^{0.5}$, as shown in Fig. 5.1.10.

Expected linear relationship can be seen for critical stress $\sigma_{\alpha,\text{lim}}$, but with large scatter (note e.g. the small R value as correlation coefficient of

Table 5.3 Summary of stress measurement on V-Fe 2at% (110) 10-nm ~ 400-nm thick films deposited on Al₂O₃ (11-20)

Characteristic values in stress curve	Thickness, <i>l</i> [nm]					
	400	200	100	50	20	10
$\sigma_{\alpha, \text{lim}}$ [GPa]	-0.73	-0.34	-0.69	-0.72(1)	-1.24(2)	-1.03(6)
σ_1 [GPa]	-	-	-0.26	-0.58(2)	-0.76(2)	-0.50(4)
σ_2 [GPa]				-0.08(1)	-0.50(3)	
Slope in linear elastic region, $m_{\text{lin.}}$ [GPa / (H/V)] Theoretical value $\sigma' = 11.7$ [GPa / (H/V)]	-11.2 (0.2)	-10.6 (0.5)	-8.5 (1.0)	-9.0 (3.1)	-12.8 (1.3)	-11.1 (0.9)
Maximum stress at 0.5 H/V, $\sigma_{\text{max.}}$ [GPa]	-0.81	-0.77	-0.87	-1.20	-2.24	-3.03

0.84). An extrapolation of critical stress (black line in Fig. 5.1.10) to infinitely large grain (zero at x axis) leads -1.97(0.35) GPa. This, as an absolute value, is reasonably close to $0.03G = 1.4$ GPa ($G = 46.7$ GPa [Bolef61]), when error is considered.

Considering the huge initial in-plane stress in the film, it is useful to examine its relationship with the hydrogen induced stress. The result is shown in Fig. 5.1.11. Both of the corrected critical stress $\sigma_{\alpha, \text{lim}}'$ and the corrected maximum stress at $c_H = 0.5$ H/V $\sigma_{\text{max.}}'$ showed clear dependence on the initial in-plane stress σ_0 in the examined stress region, i.e. the more compressive the initial in-plane stress is, the larger is the hydrogen induced stress.

Table 5.4 Intrinsic in-plane stress and domain size measured by XRD and corrected values of hydrogen induced stress in V-Fe2at% (110) 10-nm ~ 400-nm thick films deposited on Al₂O₃ (11-20)

Thickness <i>l</i> [nm], Out-of-plane domain size <i>t</i> [nm]	$1/l^{0.5}$ [1/nm ^{0.5}]	Initial in-plane stress σ_0 [GPa]	$\sigma_{\alpha, \text{lim}}$ [GPa]	$\sigma_{\alpha, \text{lim}}' = \sigma_0 + \sigma_{\alpha, \text{lim}}$ [GPa]	$\sigma_{\text{max.}}$ [GPa]	$\sigma_{\text{max.}}' = \sigma_0 + \sigma_{\text{max.}}$ [GPa]
<i>l</i> = 10, <i>t</i> = 10	0.316	-2.70	-1.03	-3.73	-3.03	-5.73
<i>l</i> = 20, <i>t</i> = 14	0.224	-2.51	-1.24	-3.75	-2.24	-4.75
<i>l</i> = 50, <i>t</i> = 17	0.141	-1.94	-0.72	-2.66	-1.2	-3.14
<i>l</i> = 100, <i>t</i> = 25	0.100	-2.09	-0.69	-2.78	-0.87	-2.96
<i>l</i> = 200, <i>t</i> = 20	0.071	-1.45	-0.34	-1.79	-0.77	-2.22
<i>l</i> = 400, <i>t</i> = 21	0.050	-1.94	-0.73	-2.67	-0.81	-2.75

Thus, both the initial in-plane stress and the film thickness are considered to have similar impact on the development of hydrogen induced stress.

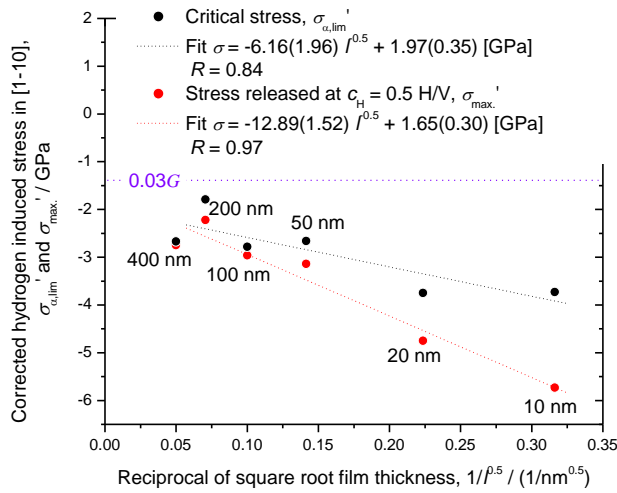


Fig. 5.1.10 Hall-Petch type plot of hydrogen induced stress and stress at 0.5 H/V for V-Fe2at% (110) films of various thickness deposited on Al_2O_3 (11-20) at room temperature. The black and red lines are linear fits, showing that the hydrogen induced stress is larger for thinner films. The Peierl's stress $0.03G$ of V is indicated by the purple dot line at 1.4 GPa. R is the correlation coefficient.

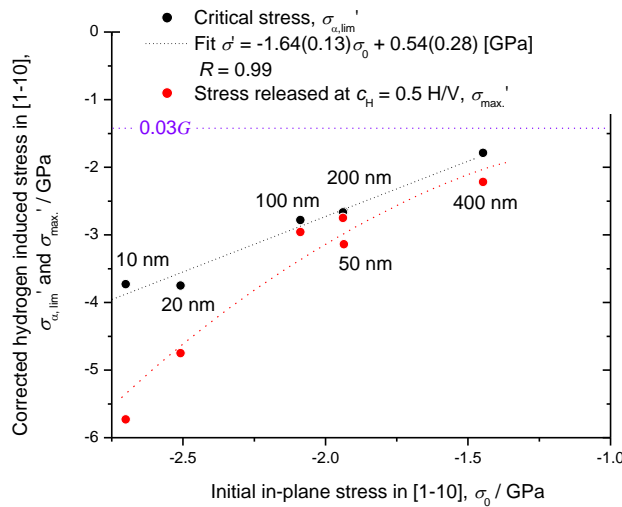


Fig. 5.1.11 Relationship of hydrogen induced critical stress and stress at 0.5 H/V vs. initial in-plane stress for V-Fe2at% (110) films of various thickness deposited on Al_2O_3 (11-20) at room temperature. The red trend line is drawn to guide eyes, showing that the hydrogen induced stress is larger for films with larger compressive in-plane stress. R is the correlation coefficient.

5.1.2.8 Change of phase boundary

The inflection points in the stress curves are compared to those in the EMF curves and summarized in

Table 5.5. Narrower miscibility gap than that of V bulk ($c_{\text{H}} = 0.03$ H/V ~ 0.47 H/V) was found. Better agreement can be seen for thicker films than in case of thinner films. The concentration width of plateau like region does not agree well each other, showing difference of typically 0.05 H/V. As

the hydrogen loading was carried out with rough concentration steps (typically 0.05 H/V) at high concentrations, this deviation cannot be avoided easily.

The observed values qualitatively hint on a shift of the phase boundaries; larger α -phase solubility and narrower miscibility gap width occurs.

However, it should also be noted that the relaxation of stress (at low c_H) occurs always before the inflection in the EMF shows up for thicker films (V 400 nm and V 200 nm), while the difference disappears when the thickness reaches at 100 nm. For the 50 nm film the order changes and the relaxation occurs even after the inflection in the EMF curve. This calls an intimate attention in relation to the fact that some small deviations (relaxation) have been observed already in the elastic regime for the films thinner than 100 nm.

Table 5.5 Observed inflection points of c_H and resulted concentration width in the stress and EMF curves of V-Fe2at% (110) films deposited on Al_2O_3 (0001) with different thickness ($c_{\alpha, \text{lim}}$ values are used for low c_H of stress curve)

Film thickness l [nm], Out-of-plane domain size t [nm]	Inflection point in stress curve [H/V]		Inflection point in EMF curve [H/V]	
	Low c_H	High c_H	Low c_H	High c_H
$l = 10, t = 10$	0.12(1)	0.25	-	0.25
$l = 20, t = 14$	0.13	0.30	-	0.30
$l = 50, t = 17$	0.12	0.25	0.10	0.30
$l = 100, t = 25$	0.10	0.40(5)	0.10	0.35
$l = 200, t = 20$	0.04	0.30	0.05	0.36
$l = 400, t = 21$	0.07	0.35	0.09	0.32

Additionally to the origin of the observed small deviations of the elastic regime, a question arises if the relaxation in the intermediate region is caused truly by the phase transition and resulting plastic deformation or not. This is in connection to the question on the behavior of hydrogen unloading curve because plastic deformation is irreversible and, thus leaves a trace of non-identical stress curve.

5.1.2.9 Stress release during unloading of hydrogen

The films with thicknesses of 200 nm and 20 nm that were fully loaded with hydrogen were examined for possibility of hydrogen unloading elec-

trochemically by applying similar process as hydrogen loading, but with inverse polarity. Simultaneously, the resulting stress release behavior was recorded against EMF value.

The results are shown in Fig. 5.1.12 (a) and (b). Correction of stress value by initial in-plane stress is already applied for each curve. A remarkable difference of the unloading behavior between these two films is observed. The 200-nm thick film shows tensile in-plane stress after un-

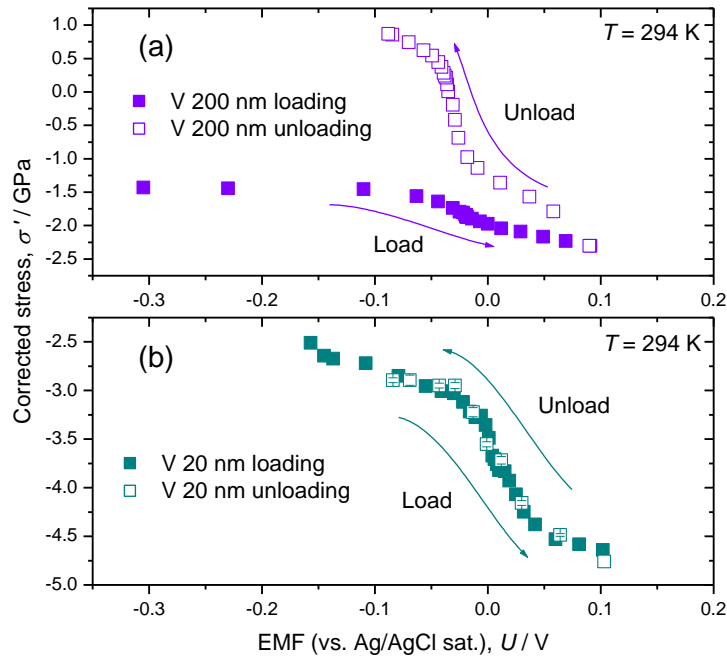


Fig. 5.1.12 (a) Stress curve against EMF of V 200 nm on Al_2O_3 (11-20) deposited at 297 K. Tensile in-plane stress is observed after H unloading (The stress in the film is relaxed). (b) Stress curve against EMF of V 20 nm on Al_2O_3 (11-20) deposited at 297 K. Both the loading and unloading curves follow the same trace. The resulting stress state after unloading is still compressive.

loading, showing more flat plateau than that of loading curve. On the other hand, the unloading curve of 20 nm-thick film exhibits completely the same trace as that of loading curve, and the final stress state is still compressive. That is, plastic deformation in a usual sense is missing between the film and the substrate, in the course of hydrogen uptake in the 20-nm thick film.

5.1.3 H-induced stress in Fe/V-Fe multi-layered film on Al_2O_3 (11-20) and on Al_2O_3 (0001) substrate

In the last section, it was manifested that the critical stress value σ_c and the total stress development σ_{\max} are strongly dependent both on films' initial stress and on film thickness. Similar consideration will be given in this section as well using the XRD data shown in Chap. 4.2.2.2 (Fig. 4.9).

5.1.3.1 [Fe 20.3 nm / V 42.8 nm] x 2

The stress release curve of [Fe 20.3 nm / V 42.8 nm] x 2 and the EMF curve are shown in Fig. 5.1.13. Well defined inflection points both in the stress and EMF curves at $c_H = 0.06$ H/V and $c_H = 0.07$ H/V, and at $c_H = 0.475$ H/V and at $c_H = 0.50$ H/V are evidently found, respectively. In the

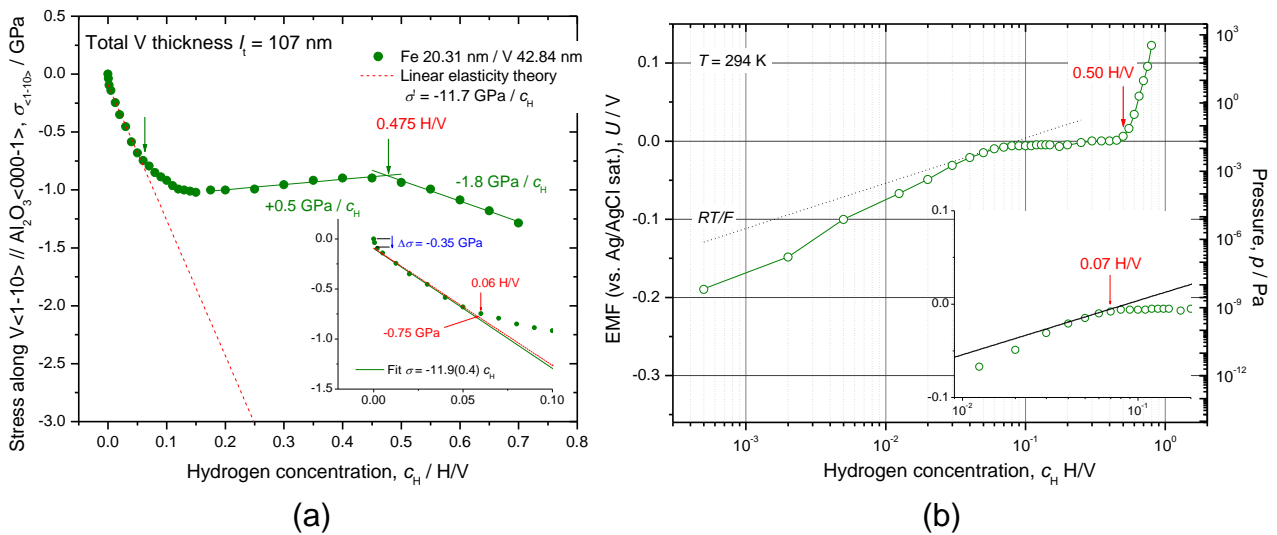


Fig. 5.1.13 (a) Stress curve of [Fe 20.3 nm / V 42.8 nm] x 2 on Al_2O_3 (11-20) deposited at 297 K. Fitting curve of linear elastic region is shown in the inset. Arrows indicate inflection points, where the slope changes. (b) EMF curve measured simultaneously during stress measurement. Low c_H region is magnified in the inset.

very beginning of stress curve up to $c_H = 5 \times 10^{-4}$ H/V an abrupt compressive stress of $\Delta\sigma = -0.35$ GPa was observed. Then the curve follows linear elasticity with a reasonable slope of -11.9 GPa/ c_H . At concentrations above $c_H = 0.06$ H/V the relaxation of film stress occurs. In this intermediate region the positive slope of $+0.5$ GPa/ c_H was observed, which is similar to the case of V 400 nm film. Note that no additional small deviation is found in the elastic regime.

5.1.3.2 [Fe 10.1 nm / V 21.5 nm] x 4

Fig. 5.1.14 shows the results on [Fe 10.1 nm / V 21.5 nm] x 4. The 1st inflection point found at $c_H = 0.04$ H/V in the stress curve agrees well with that in the EMF curve. Contrary to the results of [Fe 20.3 nm / V 42.8 nm] x 2, a significant slope in the EMF curves is observed in the intermediate region. The corresponding slope in the stress curve shows slightly com-

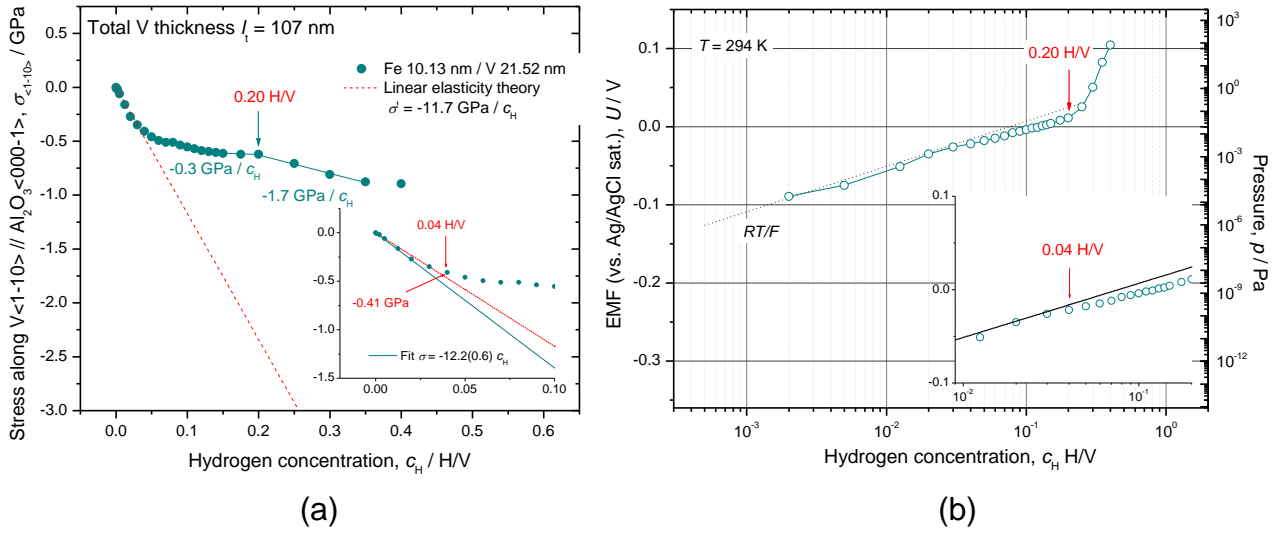


Fig. 5.1.14 (a) Stress curve of [Fe 10.1 nm / V 21.5 nm] x 4 on Al_2O_3 (11-20) deposited at 297 K. Fitting curve of linear elastic region is shown in the inset. Arrows indicate inflection points, where the slope changes. (b) EMF curve measured simultaneously during stress measurement. Low c_H region is magnified in the inset.

pressive trend (-0.3 GPa/ c_H) until $c_H = 0.20$ H/V. Above this concentration the stress curve shows, again, strong compressive stress as well as that of [Fe 20.3 nm / V 42.8 nm] x 2, with a slope of -1.7 GPa/ c_H .

5.1.3.3 [Fe 5.1 nm / V 10.8 nm] x 8

In Fig. 5.1.15 the result on [Fe 5.1 nm / V 10.8 nm] x 8 is shown. This film shows even more pronounced slope of EMF than that of [Fe 10.1 nm / V 21.5 nm] x 4. After the 1st inflection point at $c_H = 0.05$ H/V, the stress curve shows a smaller slope, meaning a stress relaxation. However, further stress increase in the whole curve is not observed anymore, even though the EMF shows significant increase again at above $c_H = 0.30$ H/V.

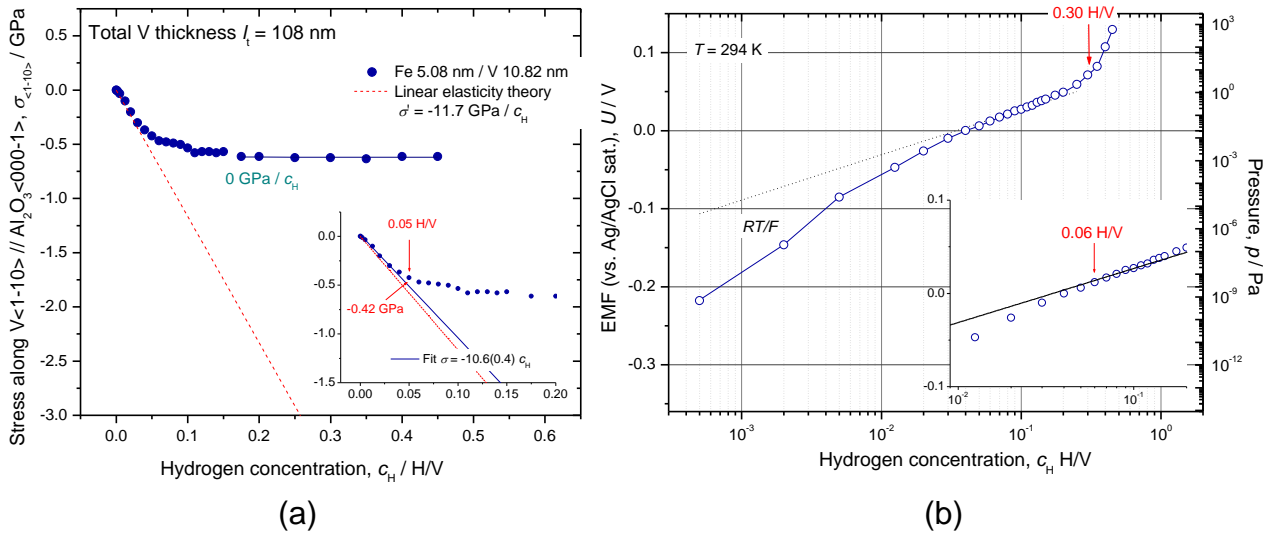


Fig. 5.1.15 (a) Stress curve of [Fe 5.08 nm / V 10.82 nm] x 8 on Al_2O_3 (11-20) deposited at 297 K. Fitting curve of linear elastic region is shown in the inset. Arrows indicate inflection points, where the slope changes. (b) EMF curve measured simultaneously during stress measurement. Low c_H region is magnified in the inset. Note the flat region in the stress curve.

5.1.3.4 [Fe 5.9 nm / V 6.0 nm] x 8

A completely different stress release behavior is observed in case of this film as shown in Fig. 5.1.16. It is notable that the stress value shows positive value i.e. tensile in-plane stress release with increasing hydrogen concentration. This behavior is opposite to general idea and experimental findings of the other films, where in-plane compressive stress is usually accompanied upon hydrogen uptake.

Two films (sample 1 and sample 2) of this same stacking type were measured and the stress values are plotted against c_H and shown in Fig. 5.1.16 (a) and (c) with corresponding EMF curves in (b) and (d), respectively. Between these two measurements, the waiting time for equilibrium is different; for sample 2 the total waiting time is about two times longer than that of sample 1. The error bars are implemented as the scattering of the stress values is large. Nevertheless, the same trend of tensile stress development is obvious for both samples, revealing certain reproducibility of this strange behavior. The observed tensile stress was in the range of 3 GPa. Such a huge tensile stress cannot be explained by conventional theory.

The shape of stress curve for both films is not identical, which could be

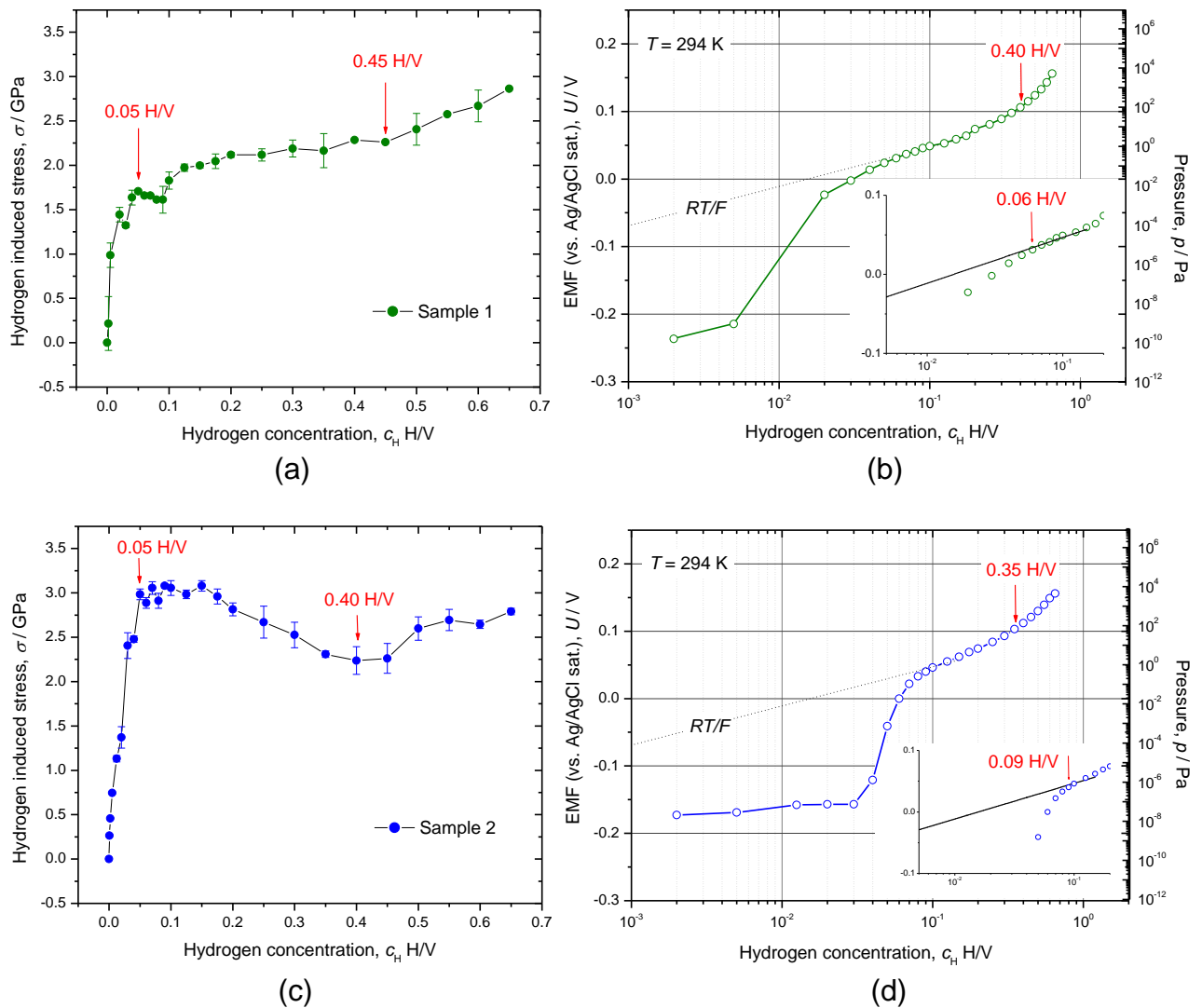


Fig. 5.1.16 Stress curves and EMF curves of [Fe 5.9 nm / V 6.0 nm] x 8 on Al₂O₃ (0001) deposited at 297 K. Sample 1 and 2 are identical, but the sample 2 was measured with longer waiting time for equilibrium. (a) stress curve of sample 1 (b) EMF curve of sample 1 (c) stress curve of sample 2 (d) EMF curve of sample 2. Note that tensile stress release is observed in the both cases.

an influence of different waiting time for equilibrium. This could also be a reason of compressive stress release in the intermediate region for the sample 2, while the sample 1 continuously shows tensile stress increase (transient mechanical response). But the inflection points agree well each other, showing the 1st inflection at $c_H = 0.05$ H/V and the 2nd one at $c_H = 0.45$ H/V or at $c_H = 0.40$ H/V. The EMF curves of these two films are not identical either, especially in the low c_H region, but, the values at high c_H region (after the 1st inflection) fit almost perfectly each other.

Any film detachment in the very beginning of the measurement might explain the observed behavior, as the initial in-plane film stress is compressive. But, no detachment or film buckling was observed at least by eyes, until the film was loaded up to around $c_H = 0.30$ H/V. The origin of this tensile stress is unknown. However, it may be explained by change of site occupation of H in the V layers, since the stress has a large impact on the site occupation in V ([Yagi86], [Koike93], [Hjörv97+]) In general consideration, random distribution of H occupation sites is always assumed to explain H-induced linear elastic volume expansion of a clamped film. In case of [Fe 5.9 nm / V 6.0 nm] x 8 multi-layered film, this obviously is not the case.

The impact of initial in-plane stress demonstrated for V single layered film is not valid for Fe/V multi-layered system, as indicated in Table 5.6

Table 5.6 Intrinsic in-plane stress and V layer thickness determined by XRD and corrected values of hydrogen induced stress in Fe/V-Fe2at% multi-layered films deposited on Al_2O_3 (11-20)

V layer thickness, l [nm]	Initial in-plane stress σ_0 [GPa]	$\sigma_{\alpha, \text{lim}}$ [GPa]	$\sigma_{\alpha, \text{lim}}' = \sigma_0 + \sigma_{\alpha, \text{lim}}$ [GPa]	σ_{max} [GPa]	$\sigma_{\text{max}}' = \sigma_0 + \sigma_{\text{max}}$ [GPa]
$l = 6.04$	-1.92	+1.88	-0.04	+2.59	+0.67
$l = 10.82$	-2.31	-0.42	-2.73	-0.62	-2.93
$l = 21.52$	-1.53	-0.41	-1.94	-0.89	-2.42
$l = 42.84$	-0.88	-0.75	-1.63	-0.89	-1.77

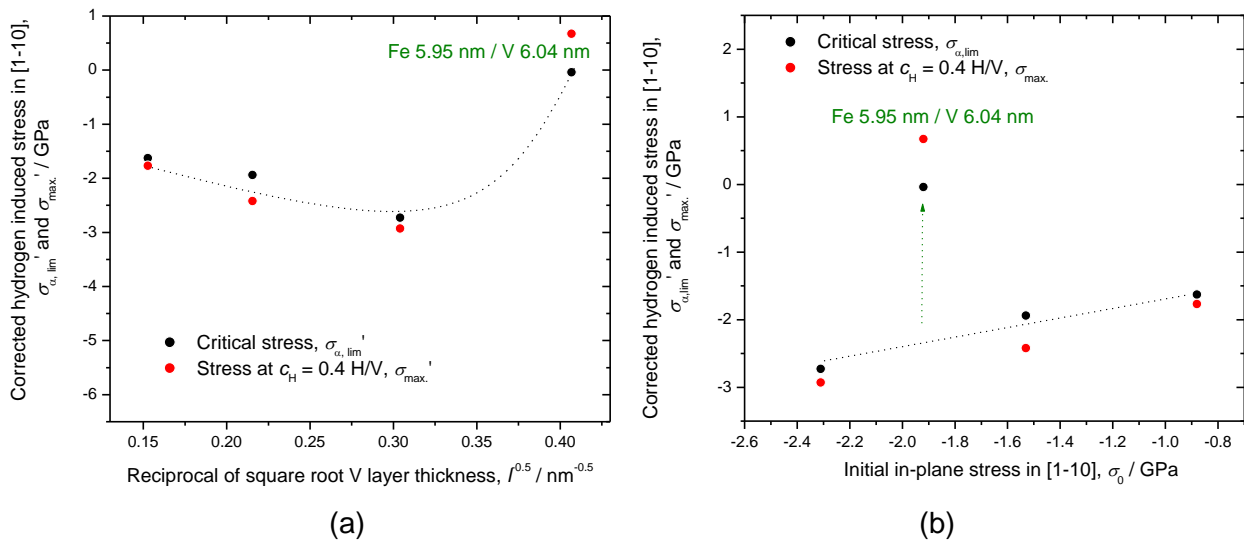


Fig. 5.1.17 (a) Impact of V layer thickness and (b) initial in-plane stress on stress release for Fe/V-Fe2at% multi-layered (110) films with various V layer thickness deposited on Al_2O_3 (11-20). The dot line is drawn to guide eyes. Note the remarkable deviation from the global trend in case of Fe 5.9 nm / V 6.0 nm multi-layer.

and in Fig. 5.1.17. Despite that the in-plane compressive stress is the largest for the [Fe 5.1 nm / V 10.8 nm] x 8 film, only the [Fe 5.9 nm / V 6.0 nm] x 8 film, which has the minimum V layer thickness, shows remarkable tensile stress.

Consequently, it seems to be more reasonable to take intrinsic size effect into account to consider the observed peculiarity, i.e. development of two-dimensional feature of the layered structure may play a significant role as suggested from the works of Hjörvarsson [Hjörv97+] and Andersson [Ander02].

5.2 *In-situ* XRD during hydrogen loading

Hydrogen-induced lattice expansion both in out-of-plane and in-plane direction was monitored by *in-situ* XRD at HASYLAB, DESY in Hamburg. The films are expected to follow linear elastic behavior in the α -phase region. Additionally, the clamping nature of the film should induce 1 dimensional lattice expansion in the film normal direction. This theoretical description and the proofs are given in Chap. 2 and in Chap. 5.1, respectively. The deviation from this behavior is discussed in relation to vacancy-hydrogen interaction, plastic deformation as well as O_z occupation and β -phase (hydride phase) formation.

The hydrogen induced stress release, which is derived from the result of out-of-plane expansion, is compared with the results of stress measurements.

5.2.1 V-Fe3at% film on Al₂O₃ (11-20) deposited at 1073 K

The out-of-plane lattice expansion of V-Fe3at% 100-nm thick film epitaxially grown on Al₂O₃ (11-20) deposited at 1073 K at different hydrogen concentrations ($c_H = 0$ H/V \sim 0.60 H/V) was carried out and the results are summarized in Fig. 5.2.1. It is clearly shown that V (110) peak shifts towards low angles with hydrogen uptake, while the Pd (111) capping layer shows no peak shift. This indicates that the hydrogen is absorbed successfully in the V layer. However, even though the intensity of V (110) peak drops significantly (this means loss of coherency or loss of volume fraction), no β -phase peak was found at high concentrations. Moreover, the α -phase peak V (110) remains visible even though the c_H exceeds 0.5 H/V, where V₂H β -phase formation is usually expected according to V-H phase diagram at room temperature. Also, it is known that the EMF values at

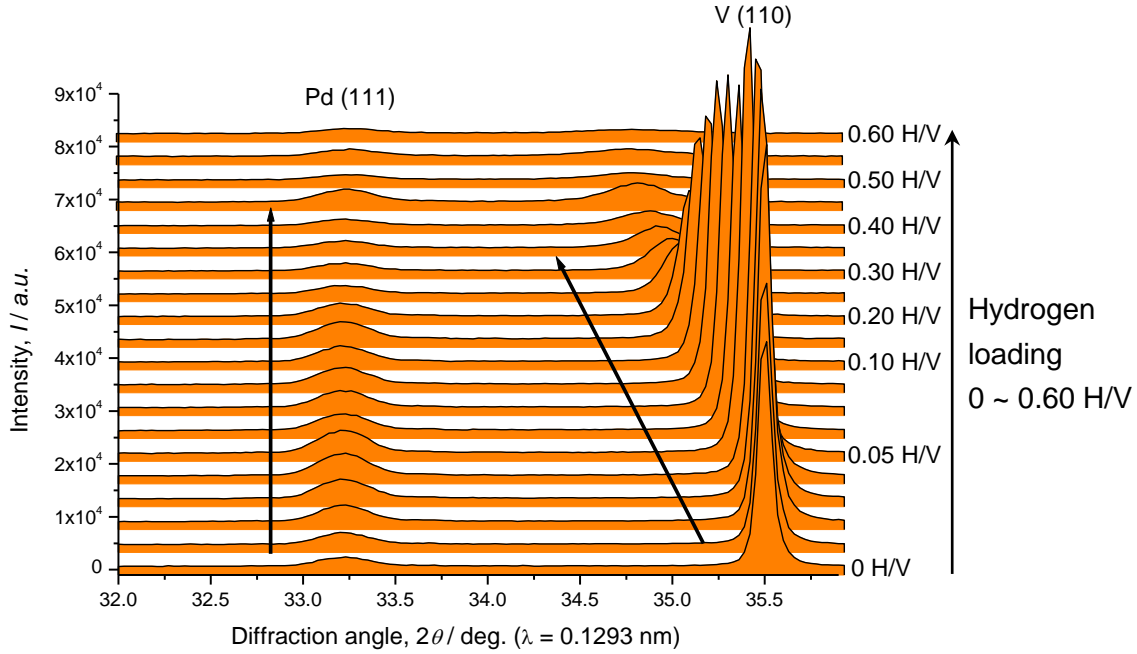


Fig. 5.2.1 *In-situ* XRD patterns during electrochemical hydrogen absorption of V-Fe3at% 100 nm (110) epitaxial film on Al_2O_3 (11-20) deposited at 1073 K. $\lambda = 0.1293$ nm. Hydrogen induced lattice expansion of V layer is clearly observed. But, no β -phase peak is found.

above $c_H = 0.5$ H/V shows steep increase.

As this film is epitaxially grown, the β -phase might not grow isotropically. Therefore, the diffraction patterns were recorded also at tilt angle (ψ) of 60° . Some examples of these patterns are shown in Fig. 5.2.2. It is clearly confirmed that there is an additional peak arising at concentrations above $c_H = 0.40$ H/V, which is considered to be that of V_2H (101). We should note that this peak has sharper width than that of V (110), implying somewhat larger domain size of hydride phase than that of matrix.

The results of d (110) measurement in the series of scans at $\psi = 0^\circ$ and at $\psi = 60^\circ$ enable to estimate in-plane interplanar distance $d_{\text{in-plane}}$, via following equation [Dornh02].

$$d_{\text{in-plane}} = \sqrt{\frac{d_\psi^2 - \cos^2 \psi \cdot d_{\text{out-of-plane}}^2}{\sin^2 \psi}} \quad (5.1)$$

In Fig. 5.2.3 (a), $d_{\text{out-of-plane}}$, $d_{(110)60^\circ}$ and $d_{\text{in-plane}}$ are plotted together against c_H . By applying modified Eq. (5.1), the d values of the β -hydride phase, $d_\beta(101)$ are inversely estimated by assuming $d_{\text{in-plane}} = 0.2134$ nm and plotted for comparison. A remarkable feature of this film is that the initial lattice is both in in-plane and out-of-plane directions contracted compared to that of bulk. This simply implies high vacancy concentration in the film.

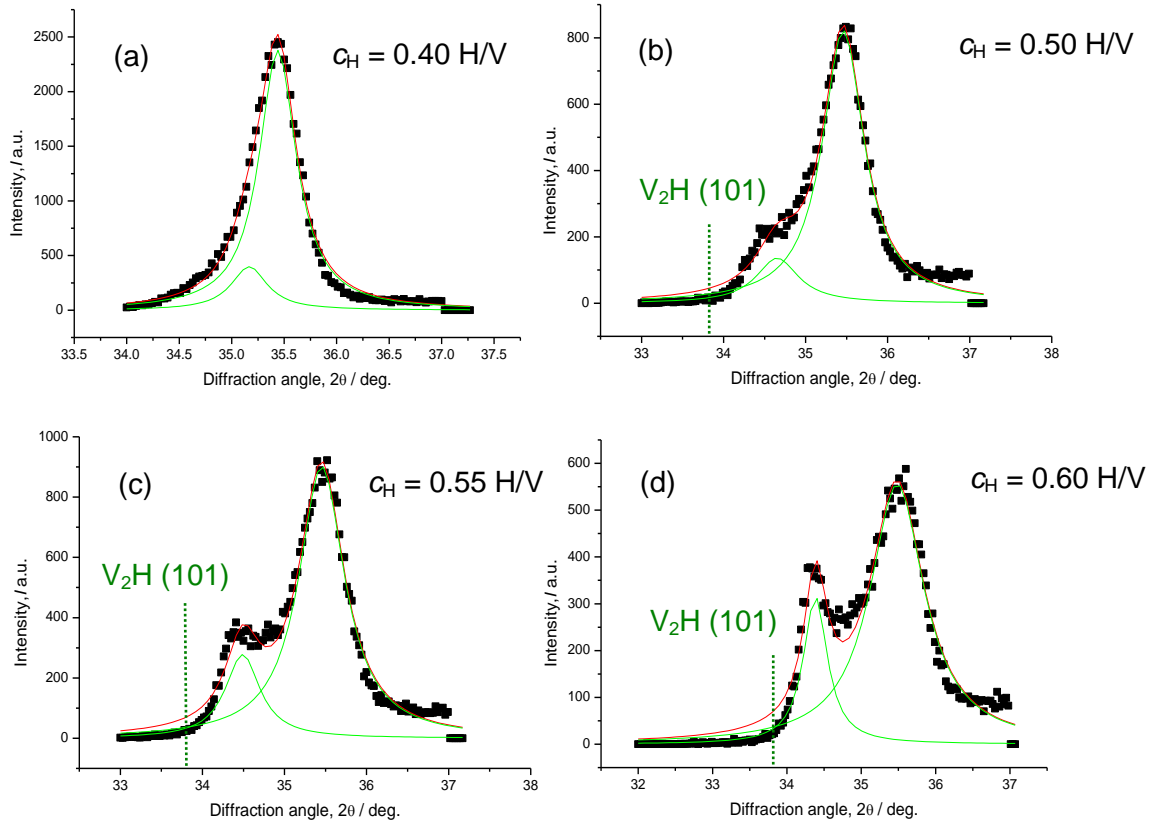


Fig. 5.2.2 *In-situ* XRD patterns V-Fe3at% 100-nm thick epitaxial film on Al_2O_3 (11-20) deposited at 1073 K at $c_{\text{H}} = 0.40 \sim 0.60$ H/V (a) ~ (d), taken at $\psi = 60^\circ$. $\lambda = 0.1293$ nm. Red and green lines are fitting curves. Each fitting was carried out with Lorentzian. Note that the β -phase peak V_2H (101) gradually appears with increasing c_{H} . Dot line (green) indicates the position of bulk V_2H (101).

The reference unit cell volume of V-Fe3at% bulk is $2.757 \times 10^{-2} \text{ nm}^3$, while that of film deposited at 1073 K has 1.7% smaller volume, $2.709 \times 10^{-2} \text{ nm}^3$. Until the c_{H} reaches at 0.005 H/V, there was no expansion observed (see the inset in (b)). Thereafter, the curve shows linear increase with a slope of $\Delta d = 0.058(1) \cdot c_{\text{H}}$, which is close to 3-dim. expansion. However, $d_{\text{in-plane}}$ shows almost constant value until $c_{\text{H}} = 0.15$ H/V. This is consistent with the expectation that the film is not allowed to expand in lateral direction in the elastic regime. But, it is then consistent with the expected 1-dim. expansion. Thus, some sort of relaxation process is inferred even in the linear expansion regime.

Further hydrogen uptake then induces lattice contraction in in-plane direction and deviation from the linear behavior in out-of-plane as well, which means an onset of formation of hydride phase (hydrogen atoms introduced in the matrix are simultaneously consumed for nucleation of hydride phase) and resulting stress relaxation process, although the onset

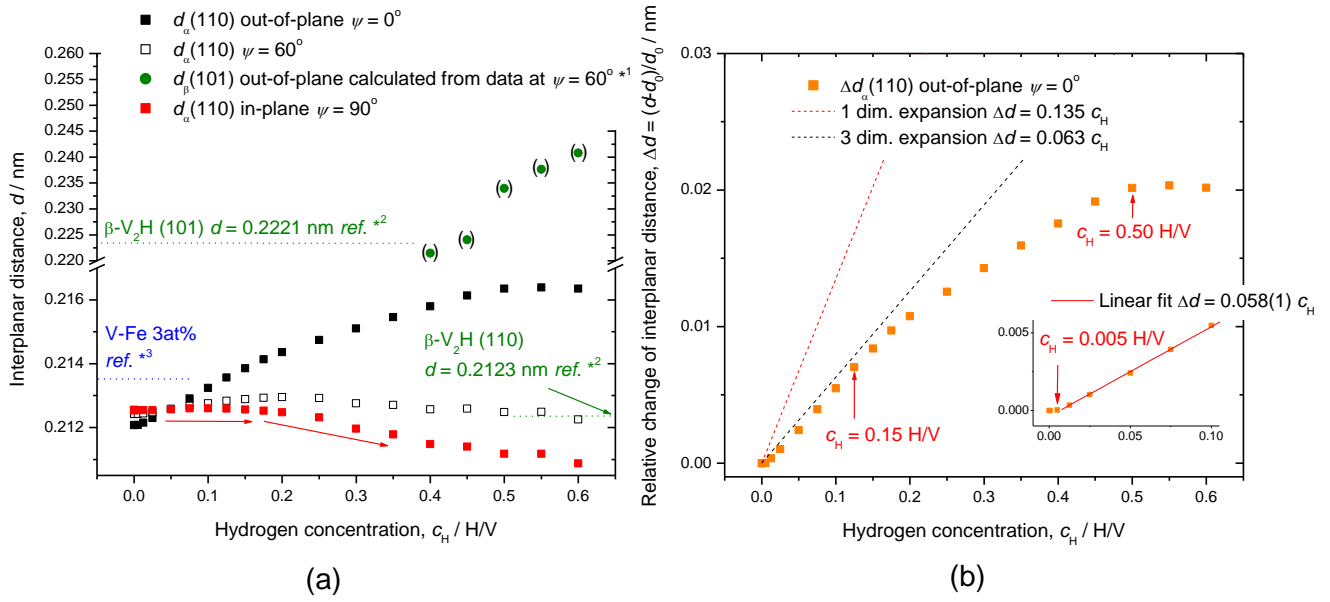


Fig. 5.2.3 (a) Change of interplanar distance d as a function of hydrogen concentration c_H . It can be confirmed that the initial lattice is contracted both in film normal and film parallel direction compared to that of bulk V-Fe3at%, implying high vacancy concentration. (b) Relative change of $d_{\text{out-of-plane}}$ against c_H . The film does not follow 1-dim. expansion model, but with a smaller slope of 0.058(1) as shown in the inset. Note that no expansion found until 0.005 H/V.

^{*1} Attention must be paid, since the values are calculated on a crude assumption that $d_{\text{in-plane}} = 0.2134$ nm, which is the average of $d(110)_{\text{in-plane}}$ between $c_H = 0.4 \sim 0.6$ H/V as the only available value for the estimation of $d_{\text{out-of-plane}}$.

^{*2} Tetragonal, space group $I4_1/amd$, $a = 0.60012$ nm, $c = 0.66188$ nm, where $a = 2a_0$, $c = 2c_0$ ($a_0 = 0.30006$ nm, $c_0 = 0.33094$ nm) [Noda86].

^{*3} Calculated from data presented in [Shiga78], with a_{FeV} [nm] = $-0.00247c_{\text{Fe}} + 0.303$, where c_{Fe} is in at%.

of β -phase formation was not immediately observed in the XRD patterns until $c_H = 0.40$ H/V. Here, we should remember that too small precipitates of several nm (or coherent precipitates) cannot ultimately be detected by XRD technique [Micha95]. At $c_H = 0.5$ H/V, the expansion of $d_{\text{out-of-plane}}$ ceases and additional hydrogen uptake in the β -phase takes place.

For the (110) oriented film, biaxial strain $\varepsilon_0 = \varepsilon_1 = \varepsilon_2$ in the film can be estimated by applying out-of-plane expansion data ε_3 of (110) plane and assuming elastic constants of pure V. Modification of Eq. (2.28) gives the following relationship,

$$\varepsilon_0 = \frac{\varepsilon_3}{1 + \frac{C_{11} + 3C_{12} - 2C_{44}}{C_{11} + C_{12} + 2C_{44}}} \quad (5.2)$$

where, ε_3 is the relative change of $d_{(110)\text{out-of-plane}}$, Δd . Corresponding biaxial stress is then calculated by Eqs. (2.31) and (2.32) for [1-10] and [001] directions, respectively. Since the in-plane orientation of the film for the *in-situ* XRD was unknown, the average product of Eqs. (2.31) and (2.32) was approximated as the biaxial stress. The same consideration on the ideal behavior predicts 1-dim. expansion with a slope of $\sigma' = -12.5 \text{ GPa}/c_{\text{H}}$. Modification of the biaxial modulus of the film due to hydrogen absorption is not taken into account.

The hydrogen induced stress σ is then plotted against c_{H} in Fig. 5.2.4. For comparison, the σ of similar film measured by stress measurement is plotted together. Even though the sample for stress measurement was deposited on Al_2O_3 (0001), the agreement is reasonable, showing similar slope of compressive stress. An interesting feature is clearly observed in the beginning of hydrogen loading, as shown in the inset. The stress measurement indicates at first tensile stress release up to $c_{\text{H}} = 0.005 \text{ H/V}$. Below this concentration, any lattice expansion was not observed, according to the XRD data.

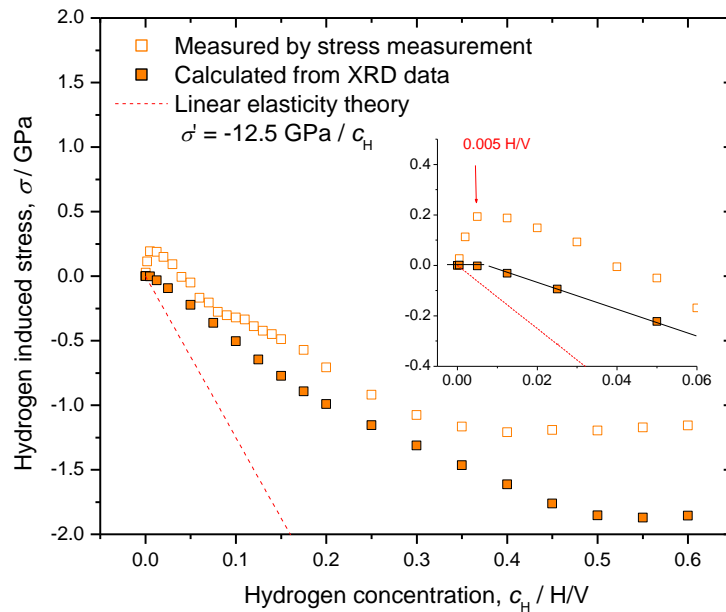


Fig. 5.2.4 Hydrogen induced biaxial stress calculated from *in-situ* XRD data through Eqs. (2.31) and (2.32) compared with the results of stress measurement. In the inset the vacancy-hydrogen interaction up to $c_{\text{H}} = 0.005 \text{ H/V}$ is demonstrated.

These two behaviors tell us that the hydrogen could be trapped at vacancies: A trapped hydrogen atom as protium interacts with the negative electrostatic field around a vacancy and thus tensile stress can be introduced in the film. The stress measurement technique is sensitive enough to detect this tensile stress because the substrate is thin and can deflect. In the XRD measurement, however, such an interaction cannot be monitored because (i) the substrate is thick and completely fixed on the holder and, thus bending of the substrate is not allowed. Therefore, any shift of 2θ peak induced by change of sample height does not occur. Moreover, (ii) high aspect ratio the film (quasi 2 dimensional) induces pronounced hydrogen trapping at vacancies in lateral direction. But, clamping of the film on rigid substrate will not allow lateral contraction of the film. Thus, the film shows apparently no change of d both in in-plane and out-of-plane directions while the vacancy-hydrogen interaction is dominant.

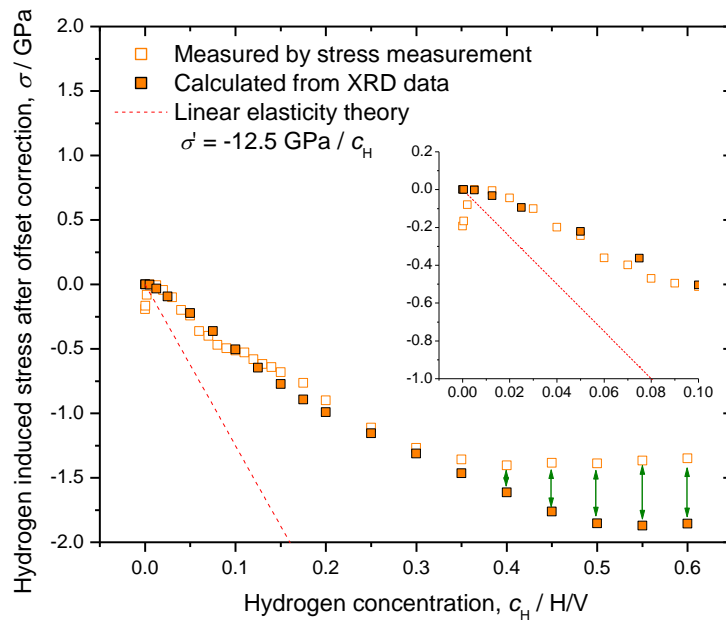


Fig. 5.2.5 The offset ($\Delta\sigma = +0.19$ GPa at $c_H = 0.005$ H/V) subtraction of Fig. 5.2.4. A good agreement is established until $c_H = 0.35 \sim 0.40$ H/V.

This interaction as an offset ($\Delta\sigma = +0.19$ GPa at $c_H = 0.005$ H/V) was subtracted and plotted again with the data of stress measurement in Fig. 5.2.5 in order to make the difference in between more clear. Except for some small deviations, the both curves exhibit a good agreement up to $c_H = 0.35 \sim 0.40$ H/V. Above this concentration, the stress calculated by XRD data shows compressive stress until $c_H = 0.50$ H/V, while the stress curve shows significant stress relaxation. This discrepancy is indicated by green

arrows in the figure. It should be noted that distinct β -phase formation was detected at $c_H = 0.40$ H/V (Fig. 5.2.2). At the same concentration, a remarkable relaxation was found in the stress curve (see also Fig. 5.1.1). This means, the observed stress relaxation is associated with β -phase formation.

Concerning above mentioned experimental findings, a principal difference between these two measurement-techniques should be now addressed, that is, the stress measurement by bending method manifests “macroscopic behavior” of the film including any trace of second phase formation, while the XRD results applied here as shown in Fig. 5.2.5 demonstrates only the behavior of “V (110) expansion”. Therefore, a comparison of these two measurements conclusively shows phase transformation phenomena accompanied by stress relaxation process. Inversely, any process of phase transformation without significant stress relaxation, like a formation of semi-coherent phase can be implied by the results of XRD measurement shown here. This could be in relation to a question on the presence of V (110) peak even at high c_H .

5.2.2 [Fe 10 nm / V 21 nm] multi-layered film on Al_2O_3 (11-20)

In-situ XRD measurements on epitaxial Fe/V multi-layered film with a double layer thickness of [Fe 10 nm / V 21 nm] were carried out. The overview of XRD patterns is shown in Fig. 5.2.6. Successful absorption of hydrogen only in the V layer can be confirmed, as the Pd (111) and the Fe (110) peaks do not show any peak shift. Likewise in the case of single layered film, any clear trace of hydride phase was not detected. The $2\theta/\theta$ scan at $\psi = 60^\circ$, as conducted on single layered film was recorded as well to detect hydride peak. But, significant intensity drop due to tilting of $\{110\}$ scattering vector was caused and the peak disappeared in the end at above $c_H = 0.20$ H/V. Therefore, detailed discussion on the hydride phase formation is unfortunately impossible for this sample.

Nevertheless, the lattice expansion behavior against c_H is plotted in Fig. 5.2.7. A considerable expansion of $d_{\text{out-of-plane}}$ and contraction of $d_{\text{in-plane}}$ at as-deposited state of this film can be seen, when compared to d value of bulk V-Fe3at%. That is, the film is under anisotropic distortion in the as-deposited state, which corresponds to $d_{\text{out-of-plane}}/d_{\text{in-plane}} = 1.014$.

Hydrogen absorption up to $c_H = 0.05$ H/V induces linear lattice expansion in agreement with the 1-dimensional expansion model (Fig. 5.2.7 (b)). The $d_{\text{in-plane}}$ shows constant value until the same c_H . Further hydrogen in-

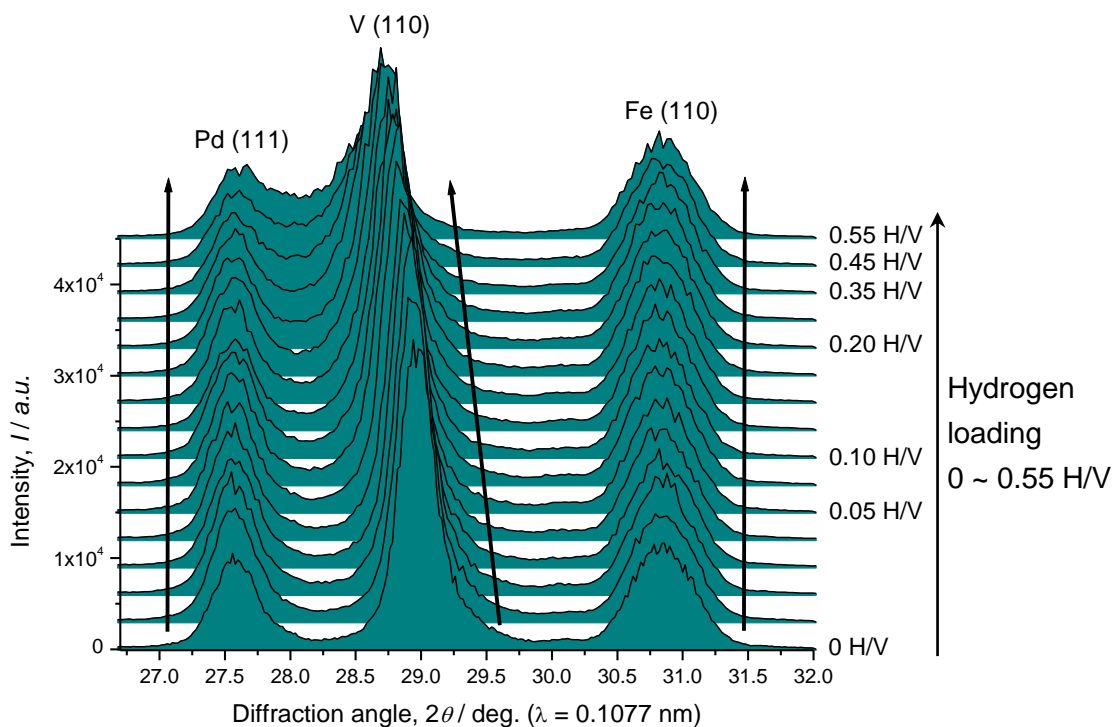


Fig. 5.2.6 *In-situ* XRD patterns during electrochemical hydrogen absorption of [Fe 10 nm / V 21 nm] (110) epitaxial film on Al_2O_3 (11-20) deposited at 297 K. Hydrogen induced lattice expansion of V layer is clearly observed. But, no β -phase peak is found, likewise in the case of V single layered film.

roduction causes 1 lattice relaxation (departure from the 3-dim. expansion behavior). At above $c_H = 0.35$ H/V the film seems to be more relaxed, showing smaller slope.

In bulk V-H system, the V_2H -hydride phase (0.50 H/V) has $c/a = 1.1$ with octahedral site (O_z -site) occupation of H (see Chap.2.1.5). According to the measured anisotropic distortion 1.014 of this film, almost 10% of the hydrogen absorption site in this film could be O_z -sites as an average. Considering already reported results of preferential site occupation in O_z -site for tetragonally distorted Fe/V film [Olsson03], the observed lattice expansion up to $c_H = 0.05$ H/V, which is exactly 10 % of 0.50 H/V, coincidentally implies similar preferential O_z -site occupation. Obviously, this is not consistent with the 1-dimensional model, which is actually deduced from an assumption of random site occupation of H atoms. However, the observed behavior of linear elastic expansion in fact follows this model. Hence, above considered O_z -site occupation alone is not sufficient to explain the experimental results of this Fe/V multi-layered film. That is, this multi-layered film with [Fe 20 nm / V 21 nm] stacking behaves more in the

way of 1-dimensional expansion due to random site occupation.

As demonstrated in the section of V single layered film, the biaxial

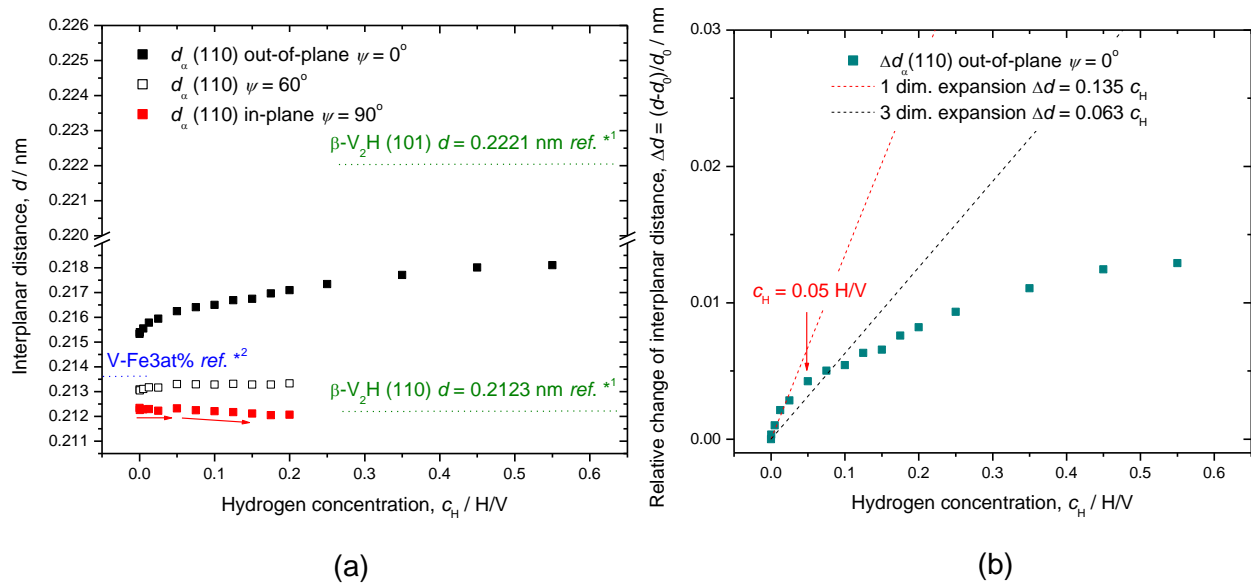


Fig. 5.2.7 (a) Change of interplanar distance d as a function of hydrogen concentration c_H of [Fe 10 nm / V 21 nm] multi-layered film. Huge intrinsic lattice expansion in out-of-plane direction and contraction in in-plane direction (i.e. rhombohedral distortion) compared to that of bulk V-Fe3at% [Shiga78] is confirmed. The in-plane lattice keeps constant until $c_H = 0.05$ H/V. (b) Relative change of $d_{\text{out-of-plane}}$ against c_H . The film follows 1-dim. expansion model up to around $c_H = 0.05$ H/V.

^{*1} Tetragonal, space group $I4_1/amd$, $a = 0.60012$ nm, $c = 0.66188$ nm, where $a = 2a_0$, $c = 2c_0$ ($a_0 = 0.30006$ nm, $c_0 = 0.33094$ nm) [Noda86].

^{*2} Calculated from data presented in [Shiga78], with a_{FeV} [nm] = $-0.00247c_{\text{Fe}} + 0.303$, where c_{Fe} is in at%.

stress was calculated again using Eqs. (2.31) and (2.32) also for this film. The result is shown in Fig. 5.2.8. Again, the agreement is very well each other concerning low c_H region with following the linear elastic model up to $c_H = 0.04 \sim 0.05$ H/V. At above $c_H = 0.15 \sim 0.20$ H/V this agreement is lost, indicating most probably semi-coherent hydride phase formation as demonstrated in V single layered film, which would be associated with misfit dislocation formation.

This phase transition-related plastic behavior of the films will be discussed in the next chapter of AE measurement (Chap. 5.3).

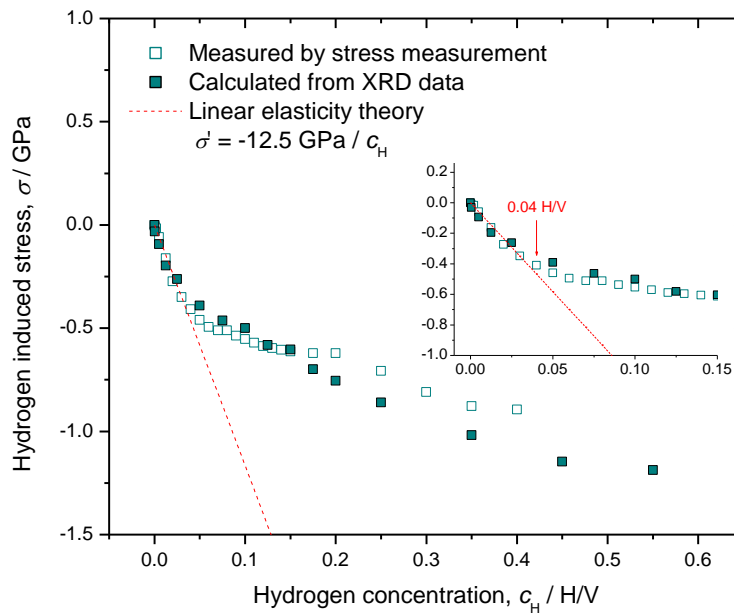


Fig. 5.2.8 Hydrogen induced biaxial stress calculated from *in-situ* XRD data through Eqs. (2.31) and (2.32) compared with the results of stress measurement. Loss of agreement between the two data at above $c_H = 0.15 \sim 0.20$ H/V implies occurrence of incoherent phase formation.

5.3 Acoustic emission measurements

Dislocation related phenomena and corresponding plastic deformation can be qualitatively investigated by measuring the acoustic emission (AE) of samples. Conventionally, this technique is applied for studying bulk samples. In this section, the AE technique will be applied for metallic thin films to investigate their mechanical response during hydrogen uptake. These studies are done in collaboration with J. Cizek and P. Dobron in Prague University, Czech Republic. The observed AE events will be discussed by focusing on plastic and “quasi-plastic” deformation of the film.

5.3.1 Thickness dependency - Single layered films

The measurement was carried out in the way so that the AE at each hydrogen-loading step was detected. The recorded AE counts are then summed up and plotted as a function of the hydrogen concentration c_H , as described in Chap. 3.3.4. For the 1st AE measurement three V-Fe5at% films with thickness of 120 nm, 210 nm and 400 nm were prepared on Al_2O_3

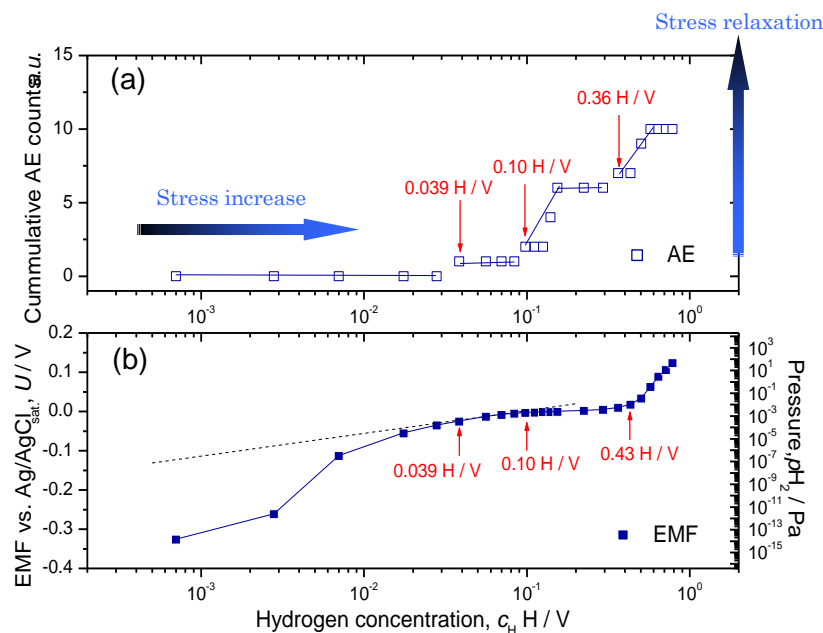


Fig. 5.3.1 (a) Cumulative acoustic emission curve of V-Fe5at% 120 nm on Al_2O_3 (11-20) and (b) EMF curve measured simultaneously at 298 K. Inflection points showing event bursts, are marked in the AE curve (red arrows). The straight lines in AE curve are just guides for eyes. The onset of and the deviation from Sieverts' law (black dotted line), and the end of two-phase region are shown by arrows in the EMF-curve, respectively.

(11-20) at room temperature. In the following figures, the cumulative acoustic emission events from these films are plotted against hydrogen concentration, together with their EMF curves that are measured simultaneously.

Fig. 5.3.1 shows the AE of a 120-nm thick V-Fe5at% film during H-loading. There are some notable changes of the slope in the cumulative AE curve. In case of 120-nm thick film the first AE event was observed at $c_H = 0.039$ H/V. At this concentration the EMF curve starts to follow the Sieverts' law (dotted line in the figure), meaning the trapping of hydrogen atoms at defects are terminated and the introduced H atoms start to mainly occupy interstitial sites in the lattice.

Judging from the EMF curve, this interstitial H occupation seems to occur already at around $c_H = 0.0175$ H/V. That is, in-plane compressive stress contribution becomes significant at this concentration. This stress increases further as the c_H increases, inducing most probably rearrangement of pre-existing dislocation. The observed first acoustic emission at 0.039 H/V may be ascribed to the first slip of the film. This is consistent with the observed stress relaxation at the same concentration in the stress measurement (Fig. 5.1.6 (a)). When the concentration reaches at $c_H = 0.10$ H/V, the AE events start to increase significantly. At the same concentration, the EMF curve shows a deviation from the Sieverts' law, indicating

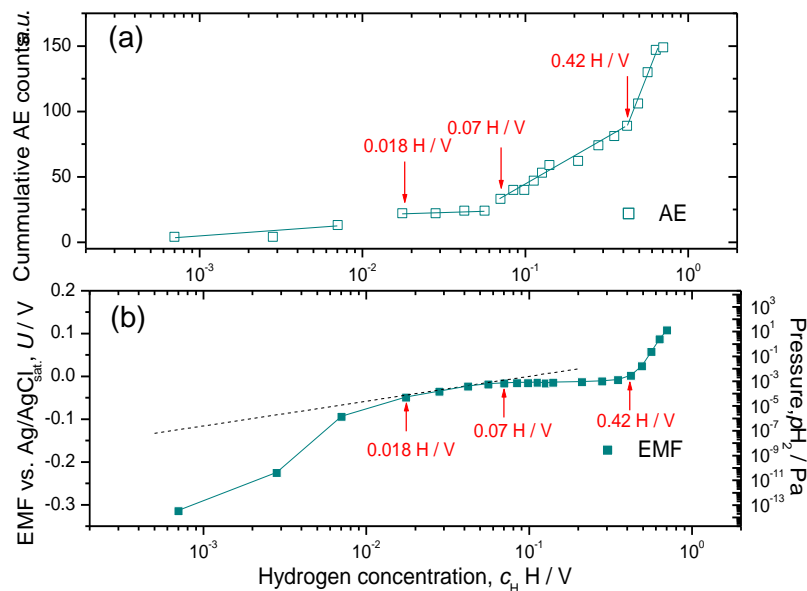


Fig. 5.3.2 (a) Cumulative acoustic emission curve of V-Fe5at% 210 nm on Al_2O_3 (11-20) and (b) EMF curve measured simultaneously at 298 K. Note some inflection points seen in the AE curve (shown by red arrows). The lines in the AE curve are drawn to guide eyes. The onset of and the deviation from Sieverts' law (black dotted line), and the end of the two-phase region are shown by arrows, respectively.

the plateau region where the hydride phase starts to form. The next inflection point of cumulative AE curve is observed at $c_H = 0.36$ H/V. Here, the corresponding EMF curve still verifies the two-phase region. An inflection of the EMF is visible at a little higher concentration of $c_H = 0.43$ H/V.

In Fig. 5.3.2, AE- and EMF-results during H-loading of a V-Fe5at% film with 210 nm thickness are shown. At $c_H = 0.018$ H/V, a distinct onset of acoustic emission is observed and no further signal is detected until the concentration reaches at $c_H = 0.07$ H/V. This concentration corresponds to the onset of the plateau region. Further increase of the c_H causes almost constant increase of AE until $c_H = 0.42$ H/V where the slope again increases.

Fig. 5.3.3 shows the AE curve of a V-Fe5at% film with 400 nm thickness, during H-loading. In case of this film, the coincidence of c_H between AE and EMF is not as pronounced as that for the two other films. The onset at $c_H = 0.018$ H/V where an abrupt AE increase is detected, coincides with that of the 210 nm thick film. However, at the onset of the plateau region (see EMF at $c_H = 0.084$ H/V), the AE shows a continuous increase. If a closer look at the AE curve is taken, a change of the AE-curve slope is

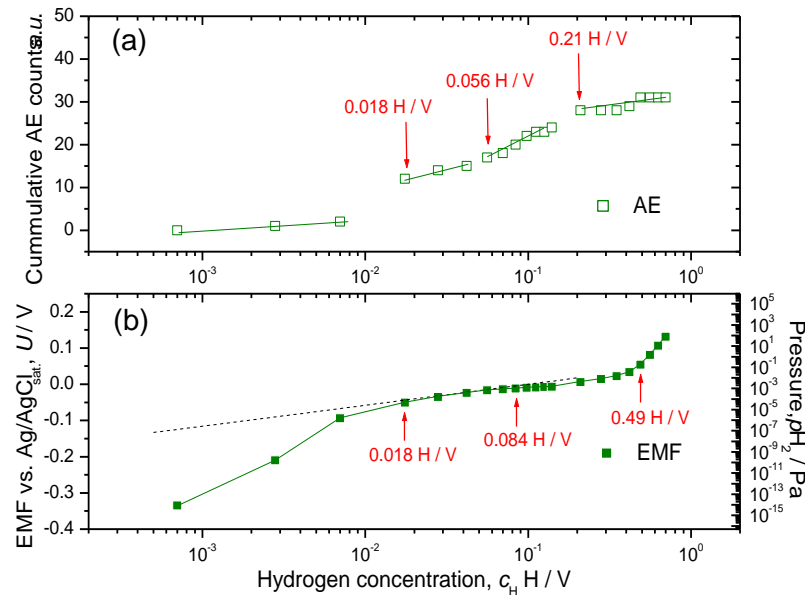


Fig. 5.3.3 (a) Cumulative acoustic emission curve of V-Fe5at% 400 nm on Al_2O_3 (11-20) and (b) EMF curve measured simultaneously at 298 K. Note some inflection points seen in the AE curve (shown by red arrows). The lines in the AE curve are drawn to guide eyes. The onset of and the deviation from Sieverts' law (black dotted line), and the end of the two-phase region are shown by arrows, respectively.

already found at $c_H = 0.056$ H/V. Further increase of c_H causes a smaller slope in the AE curve starting at $c_H = 0.21$ H/V, while the termination of plateau region is found at $c_H = 0.49$ H/V in the EMF curve. In the case of 400-nm thick film, the change of slope in the AE curve is not as pronounced as those of thinner films. This means that, above 0.018 H/V, AE events happen permanent. Corresponding stress release was, however, not observed in the stress curve. In fact, Nb-H thin film system, for instance, does not show any stress release in the α -phase [Lauda99, Nikit08]. This means that the acoustic emission does not necessarily manifest stress relaxation process concerning for instance, above mentioned rearrangement of pre-existing dislocation. This is related with film thickness because H-induced in-plane stress to induce dislocation nucleation is dependent on the film thickness.

General findings in the AE behavior of V-Fe5at% single layered films are summarized as follows.

- (i) AE increase at the onset of Sieverts' type behavior
- (ii) AE increase at the deviation from the Sieverts' type behavior
- (iii) Change of AE behavior near the end of plateau region with increase or decrease of the slope (except for the case of 400-nm thick film).
- (iv) Permanent AE-signals for thicker films above 0.018 H/V

5.3.2 Thickness dependency - Multi-layered films

Similar measurements have been carried out for Fe/V multi-layered films of different double layer thickness deposited on Al_2O_3 (11-20). The results of [Fe 5 nm / V 10 nm] x 8, [Fe 10 nm / V 21 nm] x 4 and [Fe 20 nm / V 42 nm] x 2 with nominal thicknesses, are summarized below.

In Fig. 5.3.4, the AE curve and corresponding EMF curve of [Fe 5 nm / V 10 nm] x 8 are shown. A distinctive change of the slope in the AE curve is observed at $c_H = 0.06$ H/V. In the EMF curve, however, the slope in the concentration-range of the two-phase region cannot be differentiated from that of Sieverts' law. The 2nd inflection point in the AE curve at $c_H = 0.15$ H/V is close to the concentration $c_H = 0.175$ H/V at the terminating point of the plateau region in the EMF curve. At this concentration, the slope of AE curve decreases.

Contrary to the case of single layered films, no significant change of the slope in the AE curve can be found at low concentrations.

Fig. 5.3.5 shows the results of a similarly structured Fe/V film that has a double layer thickness of [Fe 10 nm / V 21 nm] x 4, each single layer

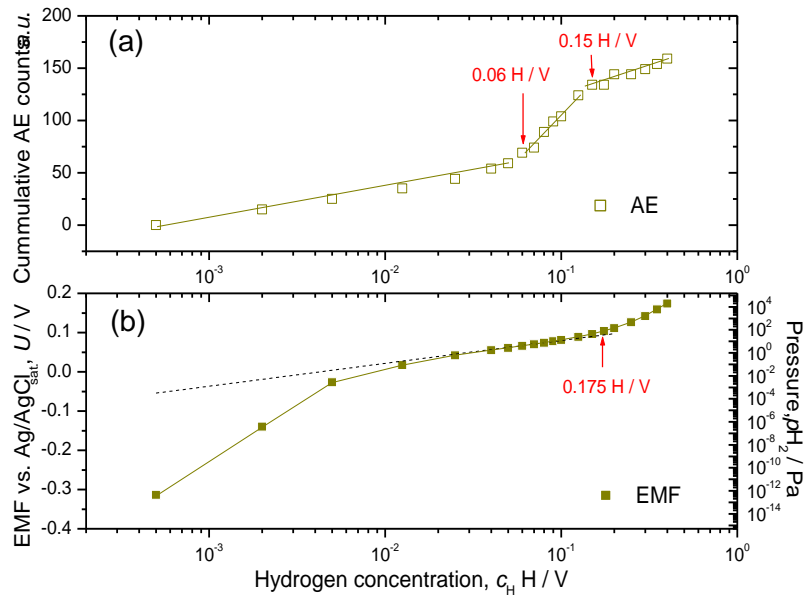


Fig. 5.3.4 (a) Cumulative acoustic emission curve of [Fe 5 nm / V 10 nm] x 8 on Al₂O₃ (11-20) and (b) EMF curve measured simultaneously. Note some inflection points seen in the AE curve (shown by red arrows). The lines in the AE curve are drawn to guide eyes. In the expected plateau-region, deviations from Sieverts' law (black dotted line) are not clear due to a significantly sloped EMF curve.

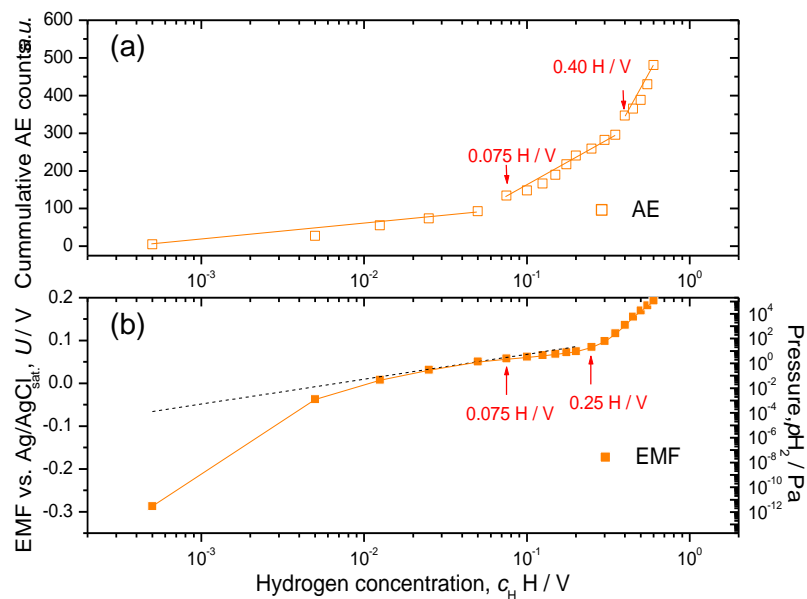


Fig. 5.3.5 (a) Cumulative acoustic emission of [Fe 10 nm / V 21 nm] x 4 on Al₂O₃ (11-20) and (b) EMF measured simultaneously. The onset and the deviation from Sieverts' law (black dotted line), and the end of the two-phase region are shown by arrows, respectively.

being twice as thick as [Fe 5 nm / V 10 nm] x 8. The total film thickness is kept constant. The inclination of the plateau region in this EMF curve is

not as pronounced as that of [Fe 5 nm / V 10 nm] x 8 and, therefore, the onset of the two-phase region can be obviously determined, at $c_H = 0.075$ H/V. The slope of AE curve also shows explicit increase at the same concentration. A further increase of the slope is found at $c_H = 0.40$ H/V, while the EMF curve shows a distinct increase already at $c_H = 0.25$ H/V.

In case of a [Fe 20 nm / V 42 nm] x 2 multi-layered film, the slope changes of the AE curve is not as clear as the last two cases, as shown in Fig. 5.3.6. The first discontinuity of the curve is found as a step-like increase of the AE signals at $c_H = 0.034$ H/V. The next change of the slope is found at $c_H = 0.10$ H/V and at $c_H = 0.15$ H/V, that corresponds to the two-phase region in the EMF curve. The termination of the two-phase region was found at $c_H = 0.40$ H/V in the EMF curve. The inflection points found in the AE curve do not coincide with those of EMF curve, which is analogous to the results of thick V single layered film (Fig. 5.3.3). Also, the observation of poor change in the AE slope similarly found both in this Fe/V multi-layer with thick single layers and in the thick V single layered film, should be noticed.

The basic features of the cumulative AE curve of multi-layered films are identical to that of single layered film. But there are also some clear differences between single layered and multi-layered films:

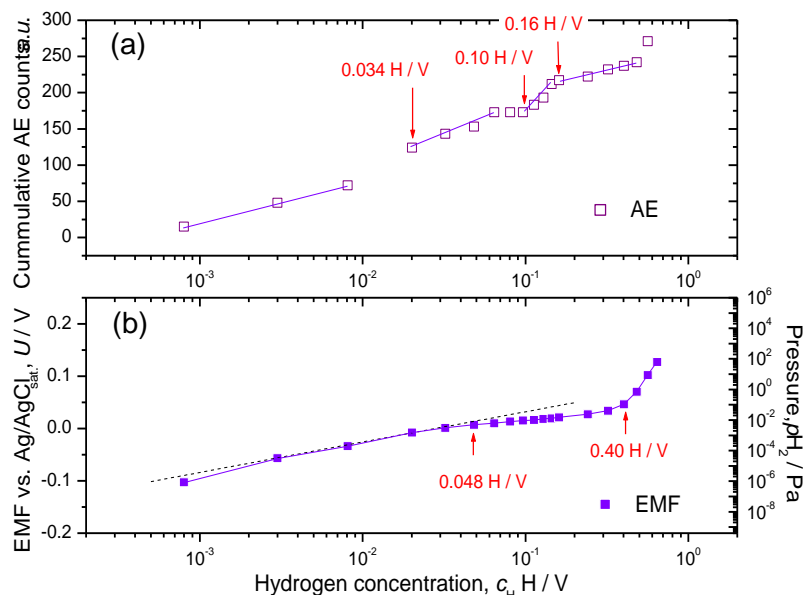


Fig. 5.3.6 (a) Cumulative acoustic emission curve of [Fe 20 nm / V 42 nm] x 2 on Al_2O_3 (11-20) and (b) EMF curve measured simultaneously. Note some inflection points seen in the AE curve (shown by red arrows). The lines in the AE curve are drawn to guide eyes. The onset and the deviation from Sieverts' law (black dotted line), and the end of the two-phase region are shown by arrows, respectively.

- (i) Poor coincidence of inflection points between AE and EMF curve
- (ii) Lack of AE signal increase at the onset of Sieverts' type behavior
- (iii) AE signals over the whole concentration range, also at very small concentration

5.4 Local hydrogen-distribution: Atom probe tomography (APT) analysis

In this section we focus on lateral and vertical hydrogen distribution in V and Fe/V films studied by atom probe analyses on the isotope deuterium at different temperatures. Before the analyses, V single layer alloyed with Fe and Fe/V specimens have been loaded with deuterium in the external vacuum chamber as described in Chap. 3.4. It will be shown that the analysis temperature has a drastic influence on the hydrogen distribution in the layer in connection to diffusion behavior of hydrogen atoms.

As described in Fig. 2.3 in Chap. 2.1.4, the isotope effect is almost negligible as long as within $c_H = \text{VH}_{0.5}$ is concerned. Therefore, the expected D concentration determined by EMF on H concentration can directly be correlated with that of D within the concentration range of this study.

Table.5.7 The expected D concentration, c_0 (D/Me) at each D_2 pressure and analysis temperature, T (K). The subscript means respective phase at a given concentration suggested by Fig. 5.4.1. D-loading was done at RT.

D ₂ pressure / Pa	Analysis temperature, T / K			
	60	45	30	22
0.02	-	0.07 _(α) / 0.28 _(β)	-	0.07 _(α) / 0.28 _(β)
0.2	0.31 _(β)	-	0.31 _(β)	-

5.4.1 Temperature impact on D-concentration in V-Fe single layered film

For V single layered films, analyses at 60 K, 45 K, 30 K and 22 K have been carried out to assess the impact of temperature on deuterium con-

centration. The samples were loaded with deuterium at a D_2 pressure of 0.2 Pa at room temperature for 24 hours, for the cases of 30 K and 60 K, in order to check over both of the temperature and pressure impacts. Although the impact of temperature between 20 K and 60 K has been reported by Kesten [Kest02], it was tested again in this study more in detail. Therefore, for the analyses at 30 K and at 45 K, the D_2 pressure of 0.02 Pa was applied. The details on the expected concentration of D in the film are summarized in Table.5.7. These expected concentrations of D were determined by EMF curve of a similarly structured specimen measured beforehand. Since there is no significant isotope effect of hydrogen within this concentration range, D concentration determined by APT can be directly compared with that of H.

In this section, some interesting variation of D distribution observed at different analysis temperatures will be introduced. The findings will be discussed in Chap. 6.

Fig. 5.4.1 shows the EMF curve of a V-Fe6(1)at% 10-nm thick film on Al_2O_3 (0001) at 294 K. The same film was deposited also on Al_2O_3 (11-20) and, the EMF curve showed completely the same shape. Therefore, impact of substrate orientation on EMF is neglected. Together with the EMF curve, average D concentrations determined by APT at 22 K and at 30 K are plotted, respectively (filled circles with orange color). Phase boundaries are also indicated in the figure with green lines. Presumably, the

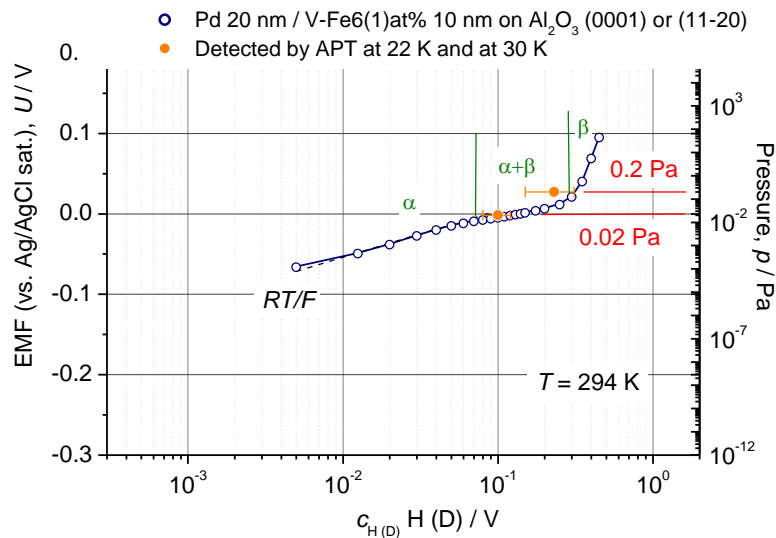


Fig. 5.4.1 EMF curve of V-Fe6(1)at% 10 nm deposited on Al_2O_3 substrate (10 mm x 10 mm x 0.5 mm) at room temperature. The EMF at 0.02 Pa and 0.2 Pa H_2 pressure indicates expected H concentration of 0.13 H/V and 0.31 H/V, respectively. The average c_D detected by APT at 22 K and at 30 K shows good agreement with the curve. The black dot line RT/F shows the ideal solubility known as Sieverts' law.

phase boundaries can be determined by the change of slope in the EMF curve (see stress measurement result Fig. 5.1.1 and *in-situ* XRD result of a similar sample, Fig. 5.2.2).

According to Fig. 5.4.1, the α -solubility limit and the $\alpha+\beta$ limit for this 10-nm thick film can be set at 0.07 H/V and at 0.28 H/V, respectively. Interestingly, the concentrations measured by APT at low temperatures match well with those determined at room temperature. Thus, the loaded D concentration seemed to be quenched by cooling process in the APT chamber.

When compared to bulk vanadium, extended solubility and narrowed 2-phase region are found, as already mentioned in Chap.5.1.2.8 (see e.g.

Table 5.5). Such modification of phase boundary is often observed since the volume fraction of defect increases with decreasing the film thickness [Lauda98]. The films stress exerts a similar impact, also inducing pressure sloping of plateau region [Dornh02, Wagn08]. The observed inflection points and sloped plateau seen in Fig. 5.4.1 agree with this expectation.

However, any deep trapping of D at defects was practically not observed. This is different from the EMF result obtained during stress measurement of a similar 10-nm thick film on Al_2O_3 (11-20) (see Fig. 5.1.9 (b)). Since the substrate geometry is rather different (see Table 3.1) between the stress measurement (0.2-mm thick) and the normal EMF measurement (0.5-mm thick), the stress impact could be different. According to this EMF curve, $\alpha+\beta$ phase is expected with concentration of 0.13 D/Me at 0.02 Pa. At 0.2 Pa D_2 pressure, hydride phase (β) of vanadium with deuterium concentration $c_D = 0.31$ D/Me is expected.

In APT, therefore, only β -phase concentration (0.31 H/V) is expected at 0.2 Pa, while two separated phases (α and β) are expected (α -phase with 0.07 H/V and β -phase 0.28 H/V) according to Table.5.7. But, two phases were not observed probably due to limited analysis volume,

Details of the obtained results will be given separately for different loading pressures and analysis temperatures in the following sections.

5.4.1.1 Analysis at 60 K : high D-mobility

In Fig. 5.4.2 (a) and (b) the APT analysis results of V-Fe6(1)at% loaded in D_2 gas at 0.2 Pa are shown. According to Fig. 5.4.1, at 0.2 Pa the thin film sample is expected to be in the β -phase. The experimental mean concentration is 0.31 H/V. In (a), the circled area corresponds to the (011) pole of the film. Due to the aberration of field evaporation, the density of atoms in this region is apparently found to be low. The big spheres in (b) represent D atoms (light blue colored). It is clearly found that almost all of

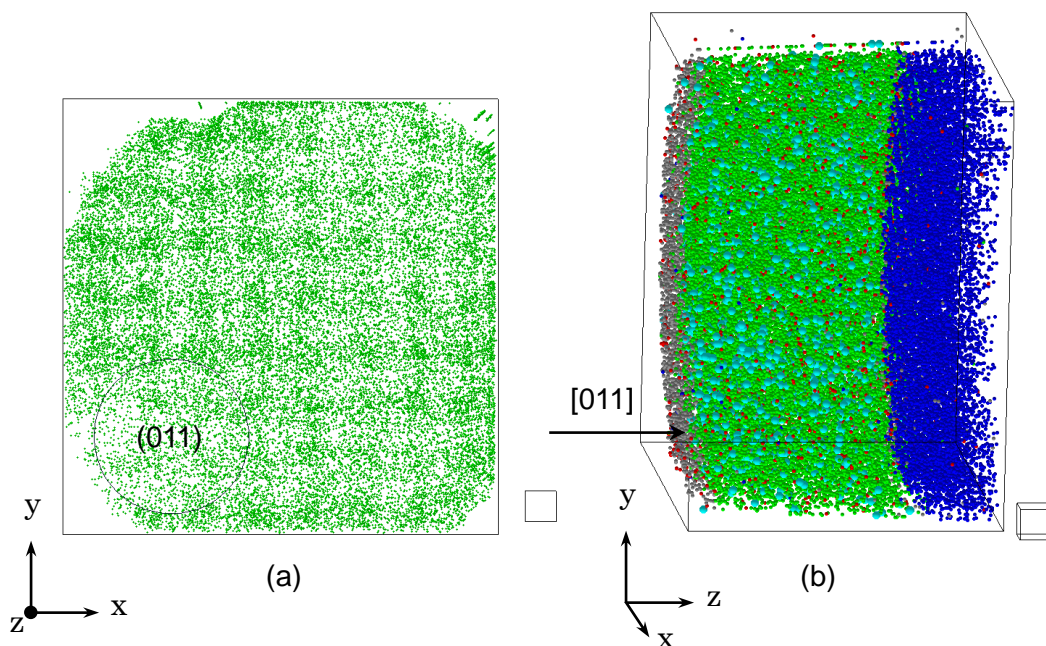


Fig. 5.4.2 The reconstructed volume (14 nm x 14 nm x 10 nm) of V-Fe6(1)at% loaded with D (0.2 Pa), analyzed at 60 K. Small cube represents 1 nm³. (a) Top view only with V, showing the region near the (011) pole (indicated as circle), where the V atoms are depleted. (b) Transversal view (grey: Pd, green: V, red: Fe, blue: W, light blue: D). Accumulation of D atoms at around (011) is slightly visible.

the D atoms are found only in the V layer, which is in accordance with the expectation that V has the largest solubility ($k_{\text{Me}} = 1$) among that of W ($k_{\text{Me}} = 10^{-24}$) and of Pd ($k_{\text{Me}} = 10^{-4}$). The solubility difference factor k_{Me} is summarized in Table 2.1. However, the D distribution in the V layer seems not to be homogeneous, but some accumulation of D atoms at the (011) pole can be ambiguously seen.

In Fig. 5.4.3 (a), the iso-concentration map of D from the same reconstruction as Fig. 5.4.2 (b) is shown. Here, the accumulation is simply visible, but only in the first 3 ~ 4 nm of the V layer. Additionally, 2 concentration depth profiles of different positions are shown in (b) and (c). The cylinders (5 nm diameter) b and c have been chosen for depth profiling as indicated in (a). Obviously, the D concentration near the (011) pole is considerably higher compared to other areas, yet the average D concentration $c_{\text{D}} = 0.06(2)$ D/Me indicated in (b) is much lower than the expected value of $c_{\text{D}} = 0.31$ D/Me. Moreover, the D concentration profile is sloped with showing “tail” towards the W substrate direction as can be seen in (c).

It is worth to see how the depth distribution of D atoms along the [011] is, because the slope of D concentration found in (c) could be a trace of

surface segregation of D atoms, as reported by Kesten *et al.* [Kest02].

By counting the number of D atoms against the number of V and Fe atoms in ladder diagram (not shown), it is possible to estimate the total D concentration in the V layer. According to this estimation, the total c_D was 0.05(1) D/Me, which amounts to only 20 % of the targeted concentration of $c_D = 0.31$ D/Me, suggesting that almost 80 % of loaded D atoms has been lost as gas at the analysis surface by e.g. D_2 formation from surface segregated D atoms, and/or HD formation through H/D exchange reaction from residual H_2 and D.

Another fingerprint of D-loss can be found in the depth profile. At the

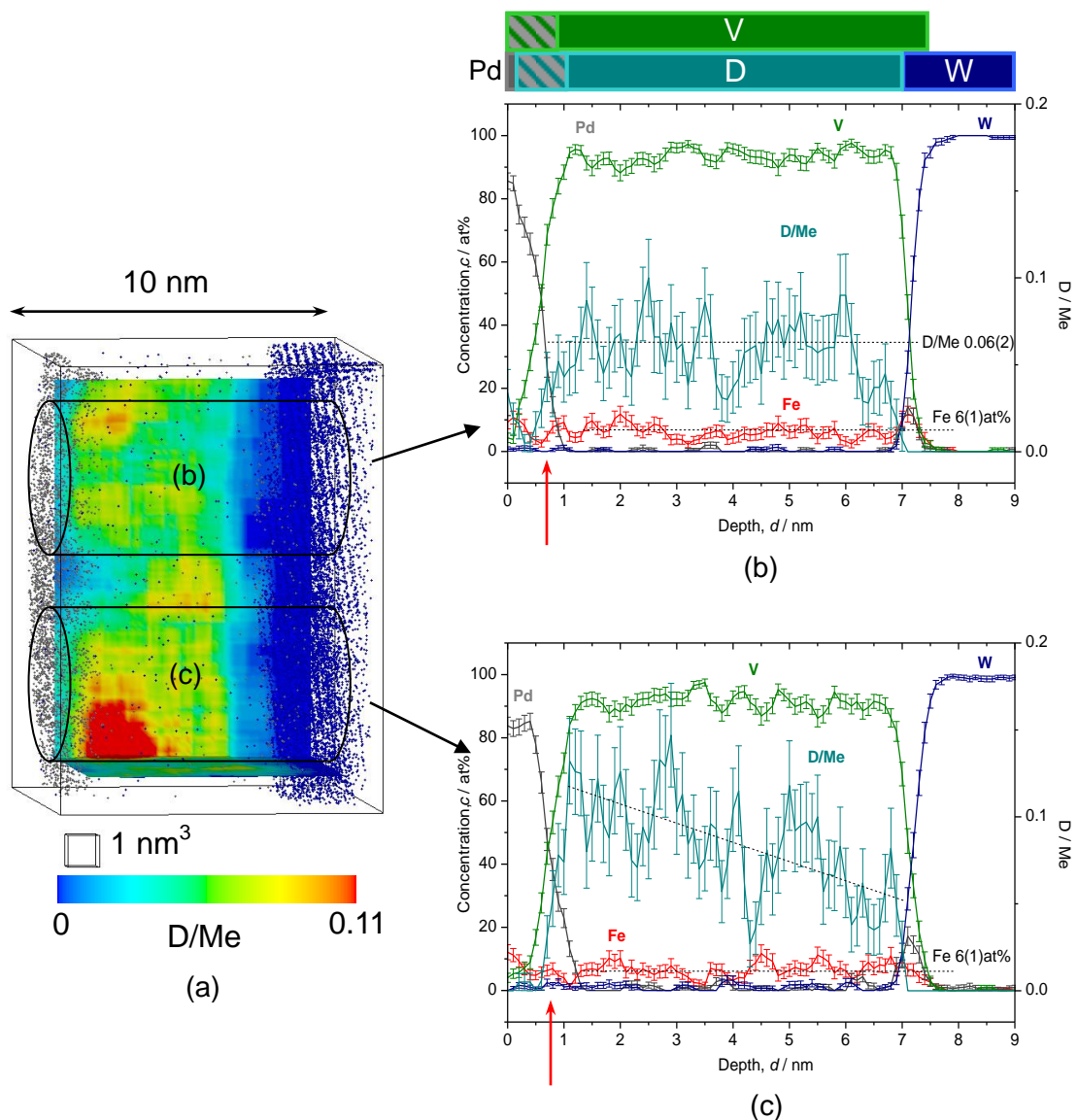


Fig. 5.4.3 (a) Iso-concentration map of D concentration from the same reconstruction in Fig. 5.4.2. (b) Depth profile taken from the cylinder b, far from the (011) pole, showing even profile of D. (c) Depth profile taken from the cylinder c, near the (011) pole. D distribution is sloped along the analysis direction. Red arrows indicate high c_D at the Pd/V.

Pd/V interface, a high amount of D ranging from 0.03 ~ 0.05 D/Me was apparently detected (indicated by red arrows in Fig. 5.4.3 (b) and (c)). The D concentration seems to mirror the V concentration profile, as marked with stripe areas in color bars above Fig. 5.4.3 (b). The observed c_D at Pd/V is, however, not true D concentration here, if we assume D atoms are also absorbed in a PdV alloy. Even in case of a Pd_{0.11}V alloy, hydrogen (thus deuterium) cannot be absorbed more than 6×10^{-6} H/Me at the pressure as low as 0.2 Pa [Saka89]. In order to quantify any light atoms as H or D by atom probe, one should carefully check the D concentration at interfaces that are situated in front of interested region of analysis.

Consequently, the analysis temperature of 60 K is too high to “freeze” D atoms in V. The sample must be cooled down to lower temperatures in order to observe homogeneous D distributions.

5.4.1.2 Analysis at 45 K : low D-mobility

The specimen was cooled down to 45 K and analyzed as described in Chap. 5.4.1.1. The D₂ loading pressure was in this case 0.02 Pa. This pressure corresponds to the two-phase region, where two phases with 0.07 D/Me and with 0.28 D/Me are expected, respectively. The results are shown in Fig. 5.4.4 (a) and (b). Color assignments are same as those of 60 K. The 2 slices for iso-concentration maps are placed in such a way that they cross

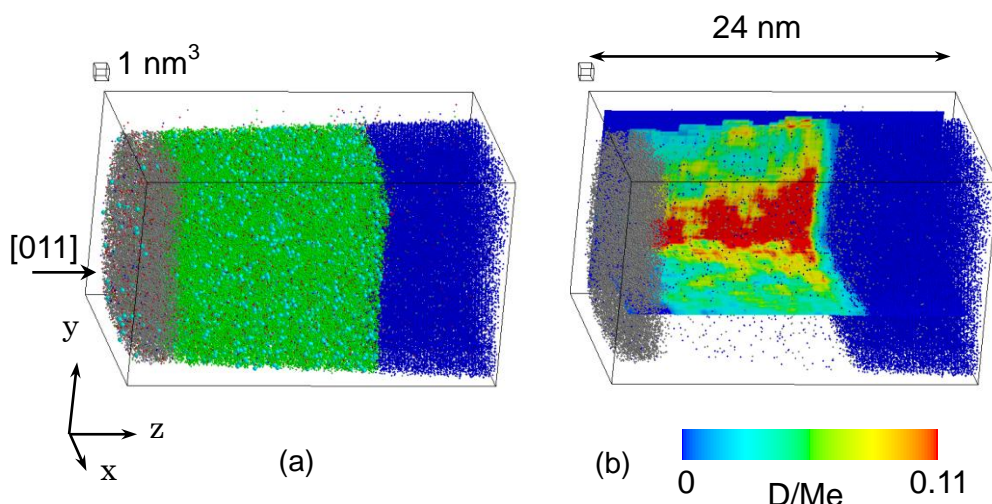


Fig. 5.4.4 Reconstructed volume from the analysis at 45 K (16 nm x 16 nm x 24 nm), loaded with D₂ 0.02 Pa. Small cube represents 1 nm³. (a) The whole volume of reconstruction (grey: Pd, green: V, red: Fe, blue: W, light blue: D). (b) Iso-concentration map of D concentration from the same reconstruction in (a). Accumulation of D atoms is visible at the (011) pole, as same as in the case of 60 K (Fig. 5.4.3). In (b), note a lateral spread of D concentrated region at V/W interface.

each other with 90° exactly at (011) pole. Judging from Fig. 5.4.4 (b), the same trend of the D distribution as found in case of 60 K still appears; (i) lower D concentration than expected, and (ii) apparently high c_D at the (011) pole. In addition to these, some lateral spread of the D concentration along the xy direction at the V/W interface is clearly visible, which implies the trace of D diffusion in the vicinity of the (011) pole.

The depth concentration profile taken from far from (011) is shown in Fig. 5.4.5. Contrary to the case of 60 K, the slope of D concentration is positive towards V/W interface.

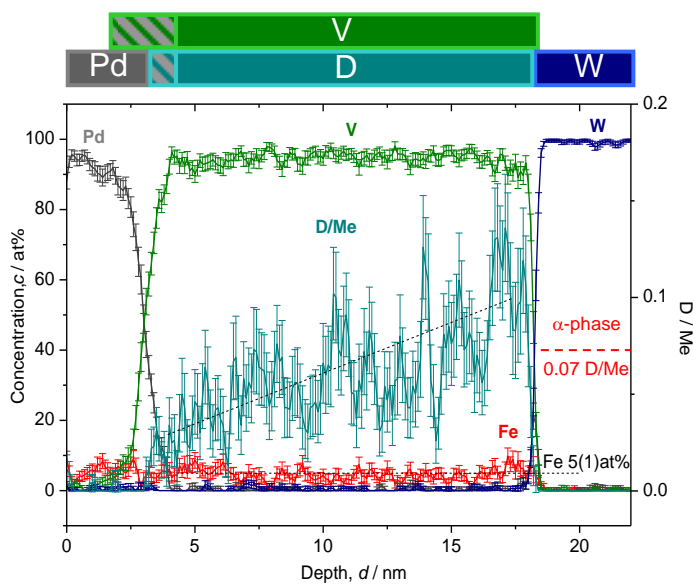


Fig. 5.4.5 Depth profile taken from a cylinder volume of 5 nm diameters put away from (011) pole. D distribution is sloped towards the V/W interface, which is contrary to the case of 60 K. The average c_D was 0.05(2) D/Me, which is close to the expected c_D for the α -phase, 0.07 D/Me (indicated by red dotted line).

The average c_D estimated by ladder diagrams of D and V+Fe (not shown) was 0.05(2) D/Me, which is close to the α -phase concentration, $c_D = 0.07$ D/Me. However, a close examination at the Pd/V interface still gives questionable result, i.e. the c_D at the Pd/V is too high. This was observed also in case of 60 K, implying D-loss through the Pd/V interface. Conclusively, even lower analysis temperature has to be applied.

5.4.1.3 Analysis at 30 K : nearly-frozen D-mobility

At an analysis temperature of 30 K, the D distribution is rather different from the last two cases. In Fig. 5.4.3 - Fig. 5.4.5, clear trace of D-diffusion was visible. Fig. 5.4.6 shows the reconstructed volume and iso-concentration map of D. The iso-concentration slices are set to cross at (011). Note that the color bar for this iso-concentration map has 0.25 D/Me at the maximum.

Not likely to the D distribution at 60 K or at 45 K, the D distribution is more homogeneous and its concentration is approaching to the expected

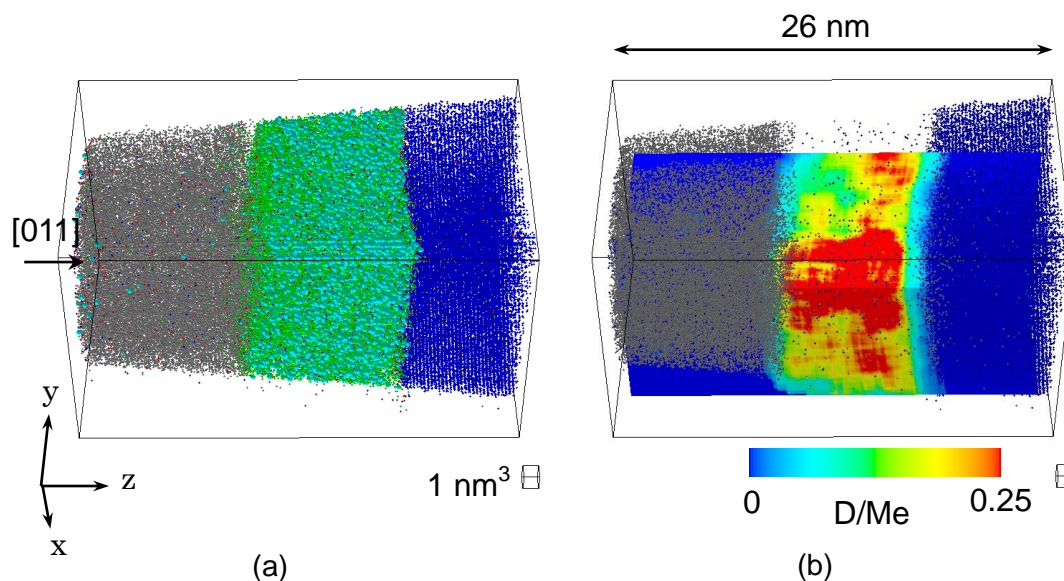


Fig. 5.4.6 Reconstructed volume from the analysis at 30 K (13 nm x 13 nm x 26 nm), loaded with D_2 0.2 Pa. The small cube represents 1 nm^3 box. (a) The whole volume of reconstruction (grey: Pd, green: V, red: Fe, blue: W, light blue: D). (b) Iso-concentration map of D concentration from the same reconstruction in (a). Note that the color bar has different scale from that of 60 K and 45 K. A better homogeneity and high D concentration was found.

value of $c_D = 0.31 \text{ D/Me}$. This hints on that the D atoms have started to become frozen at around this temperature. Albeit, the wide spread and concentration of D atoms in lateral direction can be seen. Interestingly, it appears within a few nano meters away from the V/W interface (Fig.5.4.6 (b)).

In Fig. 5.4.7, depth concentration profile taken from Fig. 5.4.6 is shown. The average D concentration in V layer, c_D was calculated as $0.23(8) \text{ D/Me}$, which amounts to $74(26)\%$ of loaded D atoms. Although it is smaller than the expected concentration, the agreement is good with considering the error.

An important feature in this profile is the nearly depleted D atoms at the Pd/V interface. As expected for ideal, there is less than 0.01 D/Me . Such a low D concentration at Pd/V interface cannot be established at the temperatures above 30 K. Further, at this temperature the sample tips remain mechanically stable and can be measured successfully. The D atoms can be successfully preserved in the V layer concerning the analysis direction for the first time at this temperature.

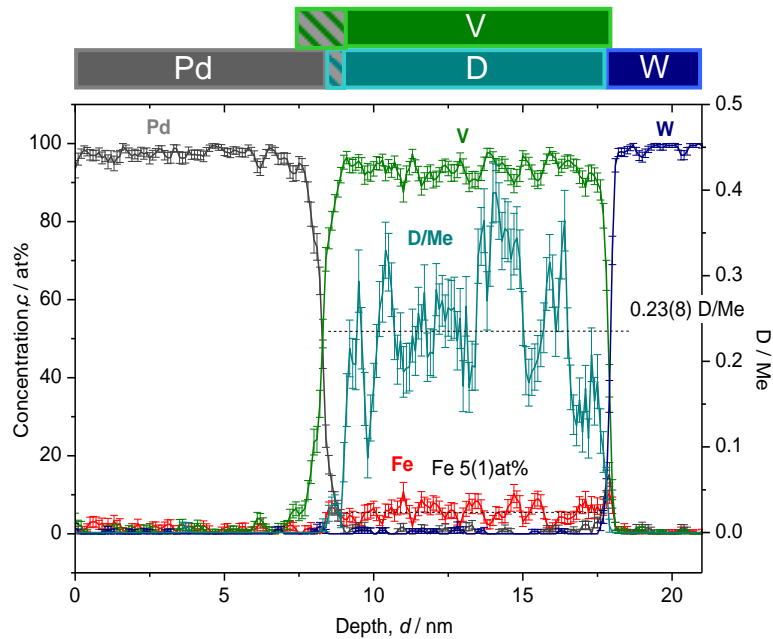


Fig. 5.4.7 Depth concentration profile taken from Fig. 5.6 (30 K). The D depth profile is not sloped any more.

5.4.1.4 Analysis at 22 K : frozen D-mobility

The analysis temperature of 22 K is close to the lowest adjustable temperature for an APT analysis in the system used in this study. At such cryogenic temperatures, the yield of successful analysis drastically de-

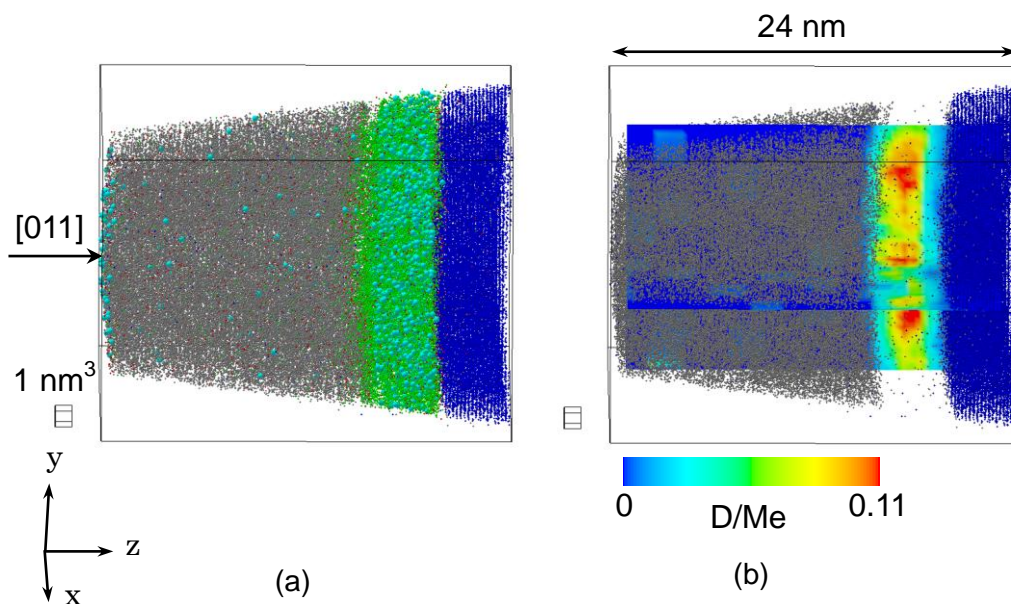


Fig. 5.4.8 The reconstructed volume from the analysis at 22 K (17 nm x 17 nm x 24 nm), loaded with D₂ 0.02 Pa., analyzed at 22 K. (a) The whole volume of reconstruction (grey: Pd, green: V, red: Fe, blue: W, light blue: D). (b) Iso-concentration map of D concentration from the same reconstruction in (a).

creases since the material becomes extremely brittle and sample rupture happens very often. Here, only several successful analyses on very thin V layered samples taken at lower than 22 K could be carried out. An example taken at 22 K is presented in Fig. 5.4.8.

Compared to the similar 3D map of 45 K and 30 K, a better homogeneity of D distribution is clearly seen at least in lateral directions.

The vertical distribution of D atoms in V layer has been checked by the depth profiling and the ladder diagram as shown in Fig. 5.4.9 and in Fig. 5.4.10, respectively. In Fig. 5.4.9 it should be noticed that there is no D atom detected at the Pd/V interface. The depletion of D atoms due to alloying of Pd with V is more pronounced than in the case of 30 K, indicating

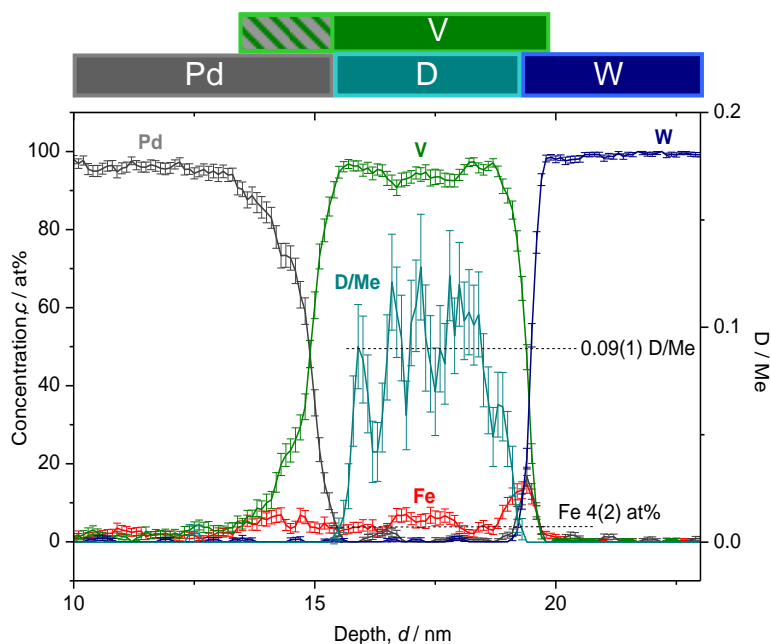


Fig. 5.4.9 Depth concentration profile taken from Fig. 5.4.8 (22 K). The D depth profile is not sloped any more. Note that no D atom is found at Pd/V.

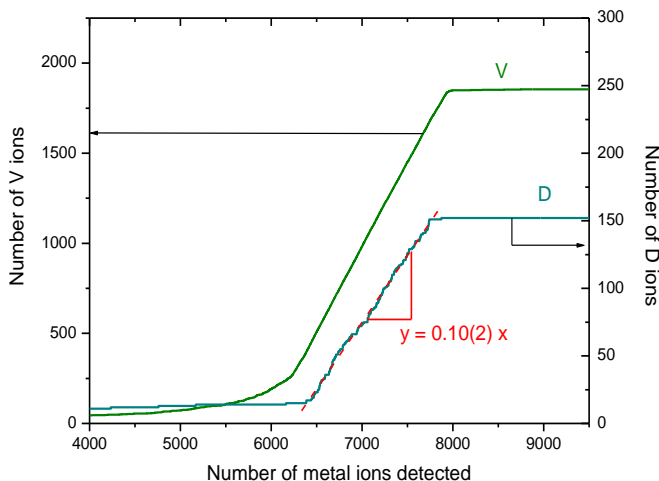


Fig. 5.4.10 Ladder diagram of V and D against the number of metal ions detected, showing $c_D = 0.10(2)$ D/Me.

The sampling was carried out from the same cylinder as for Fig. 5.4.9. The red dotted line shows least square fit.

that there is no detectable loss of D through the Pd/V interface.

According to Fig. 5.4.9, the average D concentration in V layer was found to be 0.09(1) D/Me, which is in good agreement with the expected value of 0.07 D/Me. The D concentration was checked also by plotting ladder diagram (Fig. 5.4.10). From the slope of D accumulation curve, the D concentration in the V layer can be unambiguously determined. The slope tells us the D distribution is homogeneous as there is no distinct step within the slope. The average concentration in the V layer was found to be $c_D = 0.10(2)$ D/Me. Relatively higher concentration than that of expected could be due to reduction of thickness. Meanwhile, the small difference of D preservation degree between 30 K and 22 K indicates that improvement cannot be achieved unless better statistics and smaller errors of D concentrations are established. But, at this low temperature, films tend to fracture in a brittle way and tip rupture often occurs.

5.4.1.5 Overview : Analysis at high temperatures (60 K - 45 K)

Essentially, atom probe analysis is destructive and new surfaces are continuously created during analysis. This surface and the subsurface underneath are energetically attractive for solute species in the matrix [Chris89]. As deuterium is one of the lightest elements and has large diffusion coefficient D , at high temperatures of more than 45 K, the D atoms tend to diffuse towards the sample surface and might evaporate from there. This is regarded as the reason why the D depth profile found was inhomogeneous. Hence, as long as the analysis speed is slow enough (= V layer is thick enough) only a "tail" of the D concentration profile can be observed at temperatures where D atoms are not frozen in.

It can also be considered from a geometrical point of view, that the surface segregation was visible only at around (011) pole since this area is exactly in the middle position of the needle-shaped specimen. Due to its original off-set of tilt of specimen against the detector, the (011) is not seen in the middle but shifted to the edge the reconstructed volume in Fig. 5.4.2 and Fig. 5.4.3. However, the (011) pole is situated actually in the middle of the tip specimen and, therefore is the thickest part of the specimen. The other regions are thinner than here because the film is deposited on a curved geometry. Therefore, D atoms in thinner parts at the shank of the tip can segregate faster than in the middle (011) as the diffusion distance there is shorter. As a result, the D atoms are lost by recombination or/and by formation of DO preferentially at the shank of tip, while the remaining

D atoms around the (011) pole show sloped and relatively higher concentration profile than that of other regions.

Additionally, the aberration effect of APT analysis [Waugh76] is ascribed to the observed artifact at the (011) pole.

This observation again implies how the D atoms are desorbed from the specimen. As the layer thickness of circumferential is thinner, the D atoms are more intensively lost from the shank of specimen than from the analysis direction. In other words, the desorption thorough the shank of specimen has been drastically suppressed at 45 K compared to that at 60 K, as this diffusion trace has become visible at 45 K.

Concerning the D concentration at Pd/V interface, the D found there amounts less than 0.05 D/Me and therefore the D segregation in the analysis direction is drastically suppressed than the case of 60 K, though it is not yet acceptable.

5.4.1.6 Overview : Analysis at low temperatures (30 K - 22 K)

The data points given below 30 K are in very good agreement with the p - c - T , specifically the one measured at 22 K, at 0.10 D/Me in the curve. This was shown in Fig. 5.4.7 and in Fig. 5.4.9, respectively.

However, even though the corresponding EMF curve suggests that, at the concentration of 0.10 D/Me, the sample might already be in the 2-phase region, the peak of the c_D histogram was single (not shown) likely as shown in Fig. 5.4.21. If phase separation occurs, there are at least 2 peaks visible in a histogram. This was not the case. Thus no co-existing phase is implied. This origin can be considered as follows.

- (i) The D solubility is extended :
The V layer thickness is 4 nm for APT analysis and is smaller than that of corresponding EMF curve for V 10 nm. If the defect density in 4-nm thick V is higher than that of 10-nm thick film, D atoms are trapped at defect sites and thus the solubility can apparently increase.
- (ii) The analyzed volume did not contain hydride phase by chance:
The analysis volume is, in fact, limited to only in the middle part of the tip and the film thickness of V is so thin as 4 nm.
- (iii) Semi-coherent hydride precipitate [Nörth08] is present in the whole volume (If it were totally incoherent hydride, the analysis itself would cause tip rupture).

Taking the both (i) and (ii) into consideration is also possible. The assumption (i) means that the α -phase limit is extended from 0.07 D/Me for 10-nm thick V to between 0.08 D/Me and 0.12 D/Me (0.10 \pm 2) for 4-nm thick V. In order to confirm D trapping at defects e.g. vacancy in this case, it is necessary to have some data points of APT at the α -phase region so that we can compare with corresponding EMF curve. However, we did not

Table. 5.8 Mean concentration of deuterium at various analysis temperatures.

Error is indicated in the bracket.

Analysis temperature, T / K	Mean D concentration, c_D (D/Me)	
	Expected, c_0	Found, c_{DF}
60	0.31	0.06 (2)
45	0.13	0.06 (2)
30	0.31	0.23 (4)
22	0.13	0.10 (2)

succeed in it. The assumption (ii) can be supported because the average D concentration found by APT (0.10 D/Me) was actually smaller than the expected mean concentration of 0.13 D/Me, hinting on that some solute D atoms have been consumed by hydride phase formation out side the analysis volume. This picture would be more reasonable. The assumption (iii) might be also valuable to consider, taking the error of c_D into account.

To summarize the results obtained so far, important features are listed as follows.

- (i) Relatively homogeneous D distribution can be observed below 30 K.
- (ii) High D concentration at the V/W interface (Fig. 5.4.6).
- (iii) High D concentration found at the Pd/V interface, when D-diffusion is not suppressed enough at $T > 30$ K.

In Table. 5.8, the expected “mean” D concentration (c_0) and the observed “mean” D concentration (c_{DF}) by APT analyses are summarized.

As the analysis temperature decreases, the mean D concentration increases. This means, in other words, the diffusion length of D atom below 30 K is much shorter than the analyzed length and, consequently the D atoms are “frozen” relative to analysis speed.

The impact of the analysis temperature can be considered from the temperature dependence of diffusion coefficient of D in V. In order to clarify this argument it is useful to run over the diffusion coefficient and its corresponding diffusion rate of D in V against $1/T$. By postulating that D

diffusion coefficient in V containing 4~6 at% Fe alloy is close to that in pure V bulk metal, the diffusion coefficient of D in the samples studied can be written as follows and plotted in Fig. 5.4.11.

$$D = D_0 \exp\left(\frac{E_D}{RT}\right) \quad (5.4.1)$$

Here, D_0 is the pre-exponential factor, $3.70 \times 10^{-4} \text{ cm}^2\text{s}^{-1}$ and E_D is the activation energy for diffusion of D in V bulk, 7.733 kJmol^{-1} [Qi83].

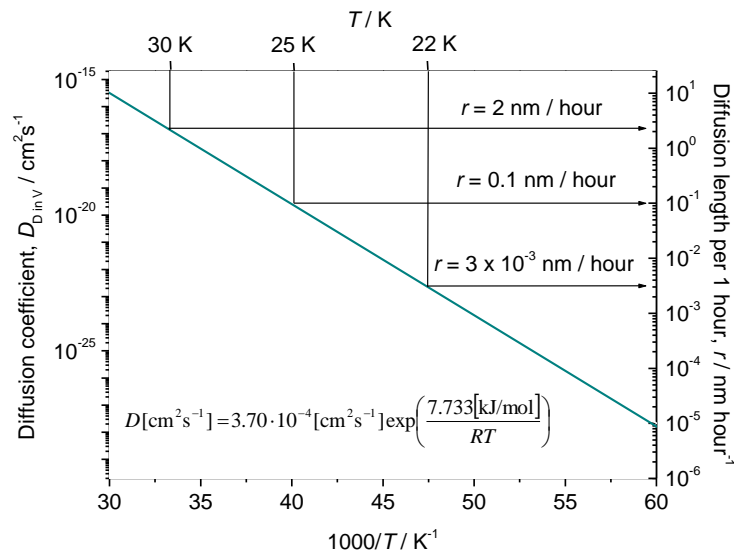


Fig. 5.4.11 The diffusion coefficient of D in bulk V extrapolated from high temperature data from [Qi83], and corresponding diffusion length within 1 hour. At temperatures below 25 K, a reasonable analysis becomes possible.

As the analysis time by APT is in the order of hours for some tens of nanometers, the diffusion rate r must be at least $< 0.1 \text{ nm hour}^{-1}$. Under the conditions given above, the quantification of D concentration by APT will be possible at temperatures below 25 K at which temperature the surface segregation should be totally suppressed and thus the loss of D atoms by recombination and/or by the formation of HD at the analysis surface can be avoided.

5.4.2 Artificial D distribution at Pd/V interface

It has been shown that the lack of D atoms at the Pd/V interface is one of the important criteria for correct analysis. This argument is indirectly supported by the H-solubility data of PdV alloy.

In Fig. 5.4.12, H solubility against V concentration in Pd is shown by using numerical data independently provided by Artman [Artman76] and Sakamoto [Saka89]. Data for high V concentration side are currently not published. Nevertheless, a monotonic decrease of H solubility with increasing V concentration in Pd is obviously seen.

At analysis temperature of 60 K, at 0.2 Pa D_2 pressure, the observed c_D at the Pd/V interface corresponding to $Pd_{0.89}V_{0.11}$ was about 0.01 D/Me (Fig. 5.4.3 (b)). This concentration is extraordinary larger than the expected $c_D = 7 \times 10^{-5}$ H(D)/Me from the alloying effect or isotope effect. On the contrary, the data taken at < 30 K did not show any detectable D atoms at the concentration of $Pd_{0.89}V_{0.11}$. This difference was ascribed whether D segrega-

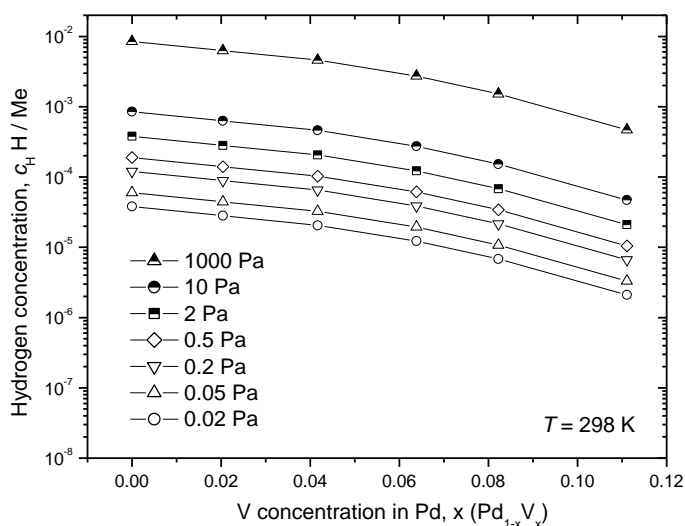


Fig. 5.4.12 Representation of H solubility data of $Pd_{1-x}V_x$ alloy at different H_2 pressures at 298 K. Numerical data were taken from Artman [Artman76] and Sakamoto [Saka89].

tion occurs or not, depending on the analysis temperature. It is thus useful and rather important to verify and run over the solubility data of bulk alloy system to investigate “true” solubility in such a small scale analyzed by APT. Segregation phenomena of light elements like D are practically very sensitive to the analysis temperature even at cryogenic temperatures.

5.4.3 Local deuterium concentration at interfaces of VFe single layered films

It was shown with the expected segregation mechanism that at the analysis temperature lower than 30 K gives good agreement. Besides, in the result of analysis at 30 K with high c_D , a lateral spread of D distribution at V/W interface was observed. As this analysis temperature lies almost at the threshold where the surface segregation of D occurs, a detailed confirmation with data taken at lower temperatures is required.

Two analyses at 20 K have been successfully carried out only for very thin V films of a few nm-thick. Although the analysis volume obtained from these samples is quite limited, it is possible to discuss on the distribution of D quantitatively to certain extent. Contrary to the case of 22 K

(Fig. 5.4.9), where homogeneous distribution of D was observed, peculiar distribution of D was observed in these two cases at 20 K.

Concerning this feature, impact of other elements like Pd, Fe and O on the D distribution will be discussed with respect to both depth and lateral directions in the following sections.

5.4.3.1 Impact of Pd and O atoms at the W substrate

In Fig. 5.4.13 the reconstruction of V single layer taken at 20 K is presented. The purple spheres shown together stand for O atoms. This sample was loaded with D at 0.01 Pa, where c_D of only 0.07 D/Me is expected, i.e. the sample is in the α -solid solution phase. But, according to the result of Fig. 5.4.13, the solute D atoms are distributed not homogeneously, but accumulating at the V/W interface where many O atoms are also accommodated.

In order to look closer, the depth profile of the V/W region is shown in Fig.5.4.14. As it can be clearly seen, the W surface is decorated with Pd and O and the D atoms' distribution partly overlaps with that of O. The increased Pd concentration at the W surface is, therefore, caused by dif-

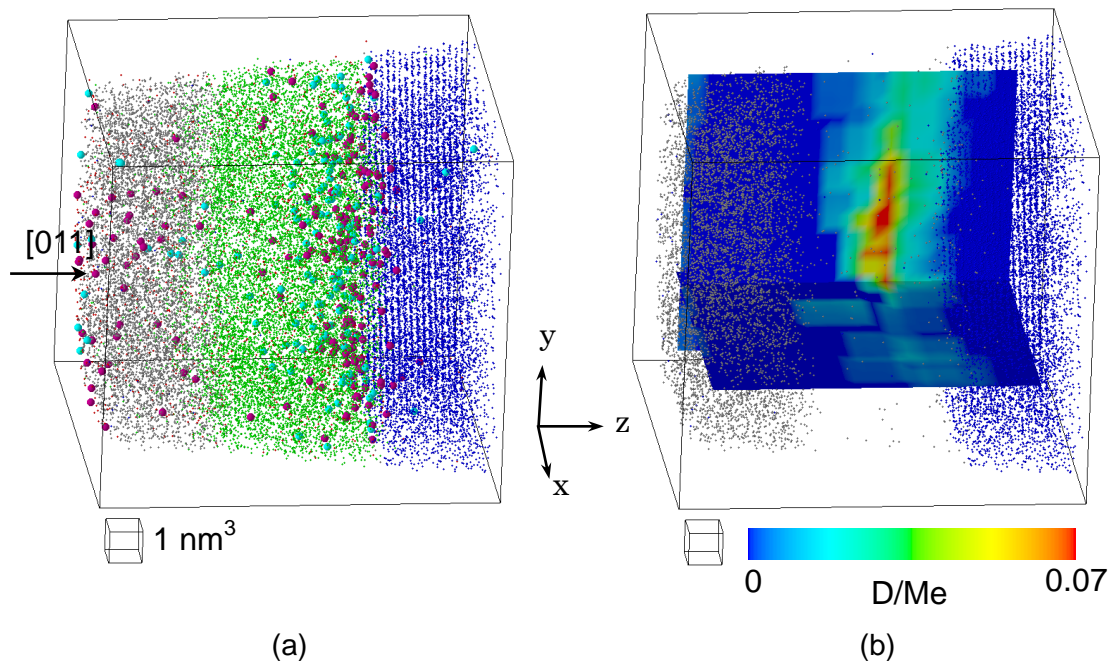


Fig. 5.4.13 The reconstructed volume from the analysis at 20 K (11 nm x 11 nm x 12 nm), loaded with D₂ at 0.01 Pa. (a) The whole volume of reconstruction (grey: Pd, green: V, red: Fe, blue: W, light blue: D, purple: O). (b) Iso-concentration map of D.

diffusive transport of Pd during target cleaning prior to deposition of the V layer.

The V/W can be considered as discontinuous interface in view of deposition scheme, not likely to Fe/V interface, because the W used as substrate was once exposed to air before it was introduced into the sputter chamber. Therefore, adsorbed O atoms are always present on W. The presence of O atoms at the V/W interface can induce an enrichment of D atoms, due to large negative formation enthalpy of $D_2O(g)$ (249 kJ/mol at 298 K [Kedda89]). However, if D_2O were present, both peaks have to appear at the same sample depth, which was not the case. Therefore, it is suggested that O was present as adsorbent and V is deposited on top of this. The thickness of natural W-oxide is about 3 monolayers [King71] and the oxide does not grow at room temperature unless electronic field is applied [Nowak10].

It is likely that at certain positions at the V/W interface, nonstoichiometric V-oxide is formed due to larger affinity of O with V than W or Pd.

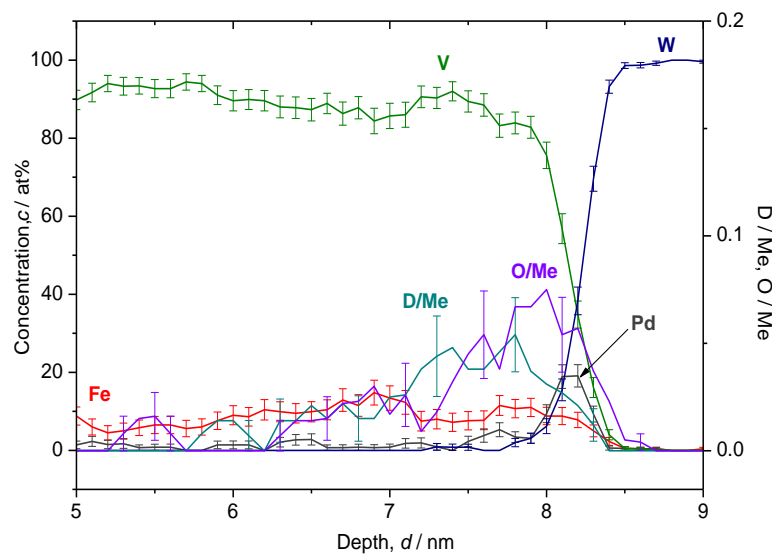


Fig.5.4.14 Depth concentration profile taken from the V/W interface in Fig. 5.4.13 (20 K). The W surface is decorated with Pd and O atoms. D atoms are attracted towards the interface.

5.4.3.2 Artificial interface mixing : analysis problem

A similar D enrichment at the V/W interface was also observed in the case of the sample with high D concentration. The result, shown in

Fig.5.4.15, is of the sample loaded at 1 Pa D_2 pressure, where $c_D = 0.38$ D/Me is expected. The analysis temperature was 20 K and therefore no artificial surface segregation is expected.

In this case, a lateral spread of the D profile like in the case of 30 K (Fig. 5.4.6 (b)) is found as indicated in the figure. The average D concentration

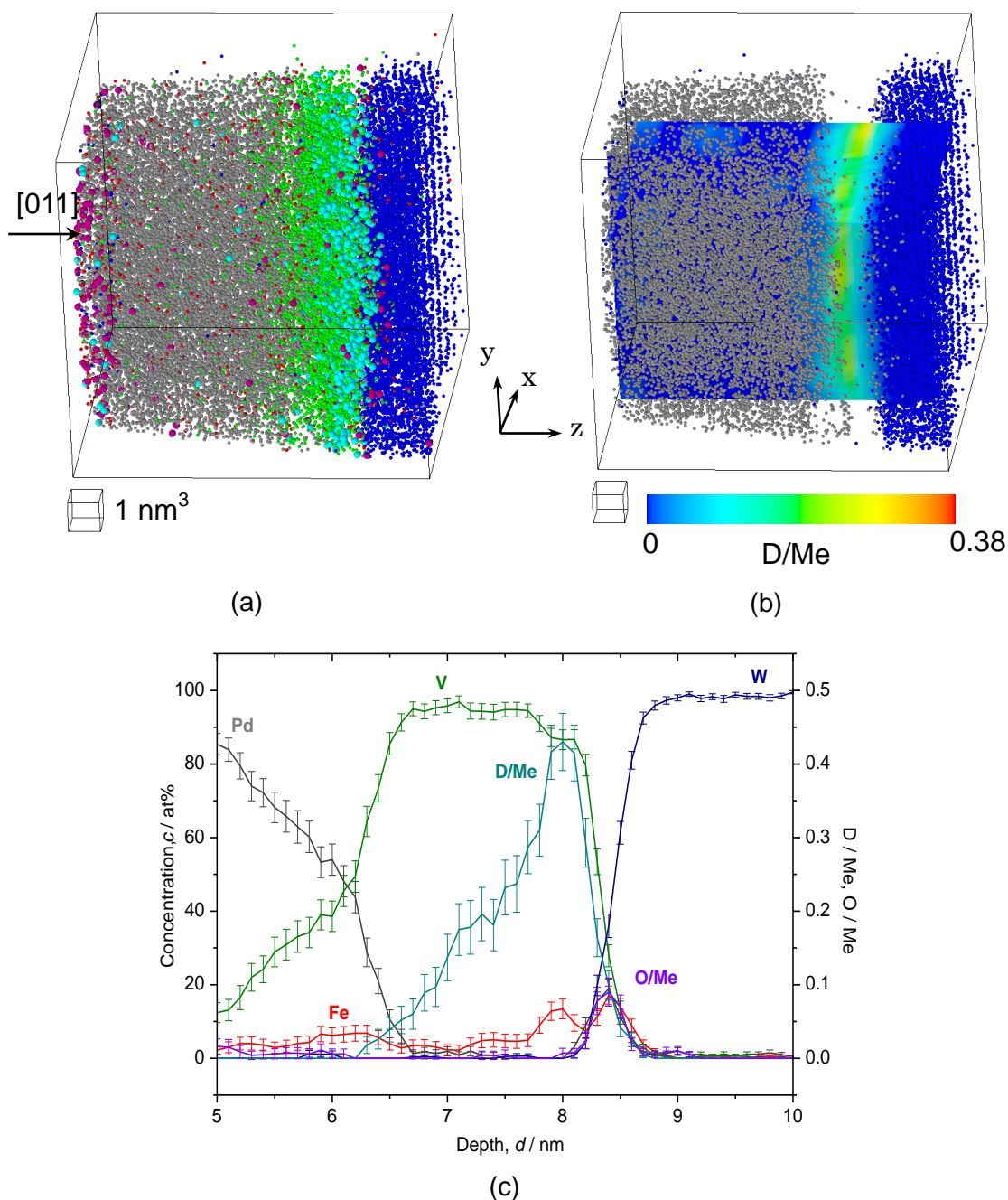


Fig.5.4.15 The reconstructed volume from the analysis at 20 K (11 nm x 11 nm x 11 nm), loaded with D_2 at 1 Pa. (a) The whole volume of reconstruction (grey: Pd, green: V, red: Fe, blue: W, light blue: D, purple: O). (b) Iso-concentration map of D (c) Depth concentration profile at the V/W interface. Note high c_{Fe} and c_D at V/W.

in the V layer was $c_D = 0.17(8)$ D/Me, while the maximum concentration is reaching around 0.4 D/Me near the V/W interface, hinting on a preferred hydride growth. Additionally, the Pd/V interface shows considerable unsharpness.

From the depth profile, the following observations concerning this film should be noticed.

- (i) The D concentration profile shows inhomogeneous feature in the depth i.e. high c_D at the V/W interface.
- (ii) Pd and V seems to be intermixed significantly into the depth of 6.5 nm, and the V layer is alloyed with Pd up to several % into the depth of ca. 7.5 nm.
- (iii) The D concentration profile and that of Fe in V layer show similar trends.
- (iv) O atoms are accumulated at the V/W interface.

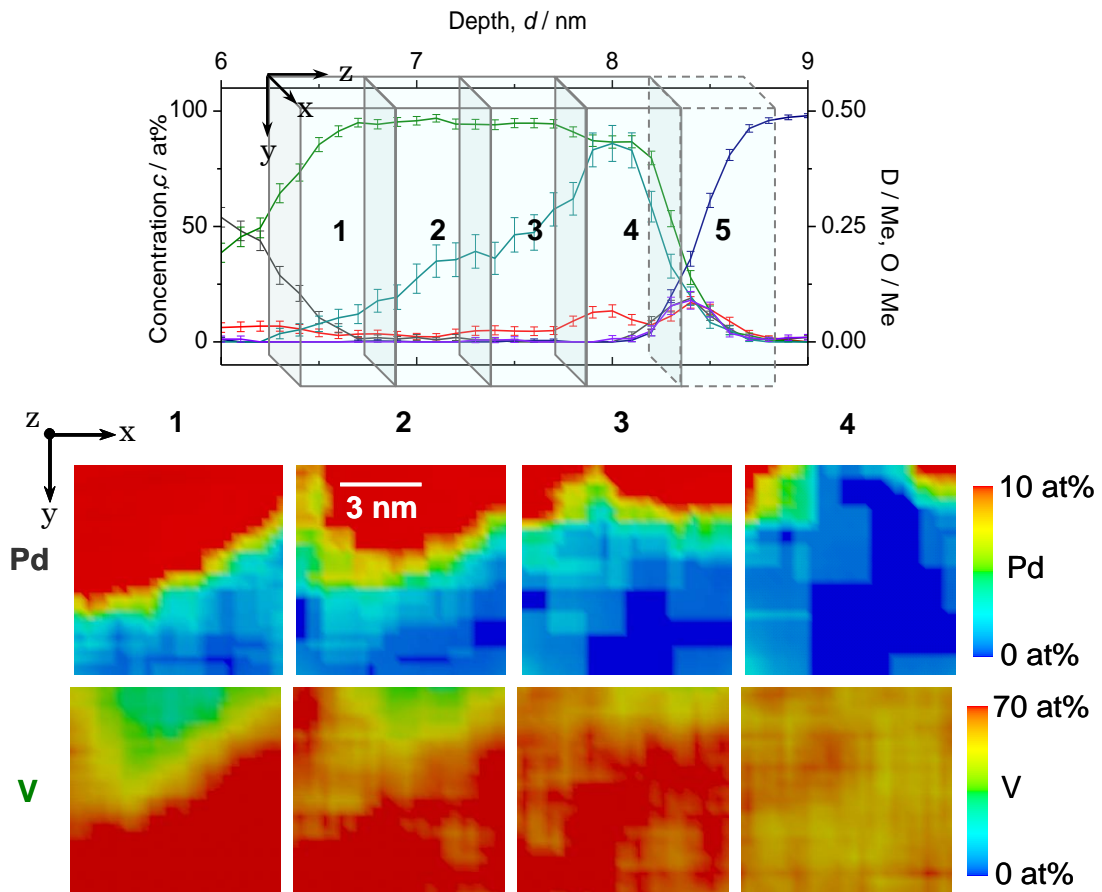


Fig. 5.4.16 2D iso-concentration maps of Pd and V at each cross section (1 ~ 4). Sampling volume (3 nm x 3 nm x 0.5 nm) contains about 100 atoms in total. Clearly, the Pd/V interface is tilted against the depth direction.

To confirm the correlation of the lateral distribution between the elements, 2D iso-concentration maps of Pd and V at each cross section of the depth profile are shown together in Fig. 5.4.16. We should now pay attention that the 2D iso-concentration map was calculated for the whole area of the analysis, not like the 1D concentration profile, which was taken for a selected cylinder volume. Thus, a curved geometry of the sample tip would give a different picture from that of depth profile. In fact, in Fig. 5.4.16 rich Pd can be seen at the upper edge of the 2D map even in the cross section 3. Judging from this consideration, significantly high concentration of Pd in the pictures is because the Pd/V interface was tilted against the analysis direction. The clear inverse correlation between the distribution of D and that of Pd can be understood from this point of view. That is, artificial alloying of Pd with V apparently found in the depth profile was caused by this interface tilt. The real Pd/V interface is in fact as sharp as shown for 1D analysis.

5.4.3.3 Impact of Fe and O atoms at the W substrate

The correlation between D and Fe is not that straightforward as suggested in the depth profile, though there are some overlaps especially at the cross sections 3 and 4 in Fig. 5.4.17. One should now focus on the column 4, where a small dense region of Fe can be confirmed at the right-bottom. Similar condensation of Fe in cross sections 1 ~ 3 must be ignored as they belong to the Pd layer (compare with Fig. 5.4.16). If the solubility limit of Fe in V layer at room temperature is 12 at% likely to that of bulk V (Fig. 2.6), even the Fe concentrated region in the column 4 can be considered as solid solution phase. In fact, no cluster or platelet of Fe was found in this case. If the interface energy is reduced at the Fe-concentrated region, inhomogeneous nucleation [Beck38] of hydride may occur at this nucleation center. However, any mass peak arising from vanadium hydride was not detected.

Concerning the D enrichment at the V/W interface, O distribution is compared with that of D in Fig. 5.4.18. A high D concentration is found just above the V/W interface, where O atoms are accumulated on W. The accumulation of O atoms on W is caused by exposure of W substrate to air atmosphere prior to film deposition. There, the O atoms are adsorbed on the W substrate. Upon the deposition of V onto this O-layer, it is reasonable to assume that nonstoichiometric V-oxide is formed, as discussed already in Chap. 5.4.2.1.

This enrichment of O atoms on W is true for all cases in this study, but considerably inhomogeneous distribution of D at V/W interface was found

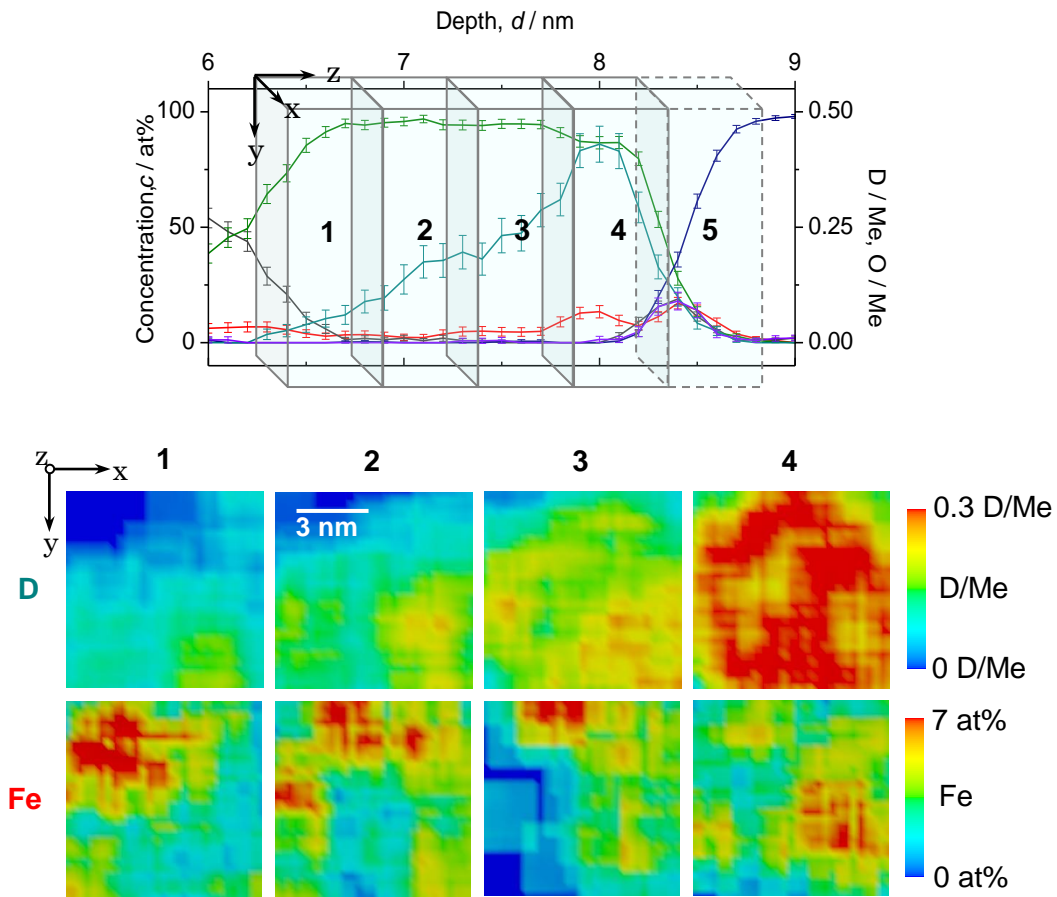


Fig. 5.4.17 2D iso-concentration maps of D and Fe at each cross section (1 ~ 4). Sampling volume (3 nm x 3 nm x 0.5 nm) contains about 100 atoms in total. No correlation of lateral distribution between D and Fe is found.

only in this case at 20 K. Similar picture (condensation of D near the V/W interface) was found also at 30 K (see Fig. 5.4.6 (b)). In both cases the c_D was high, reaching over 0.3 D/Me. This point will be addressed in the discussion.

The results of this chapter are summarized as follows.

- (i) Reliable D distribution was demonstrated for the analysis temperatures below 30 K.
- (ii) Accordingly, a high D concentration was successfully detected.
- (iii) Thereby, interface effects at the V/W interface due to O segregation was commonly observed.
- (iv) This effect was observed at several nm away from the V/W interface.

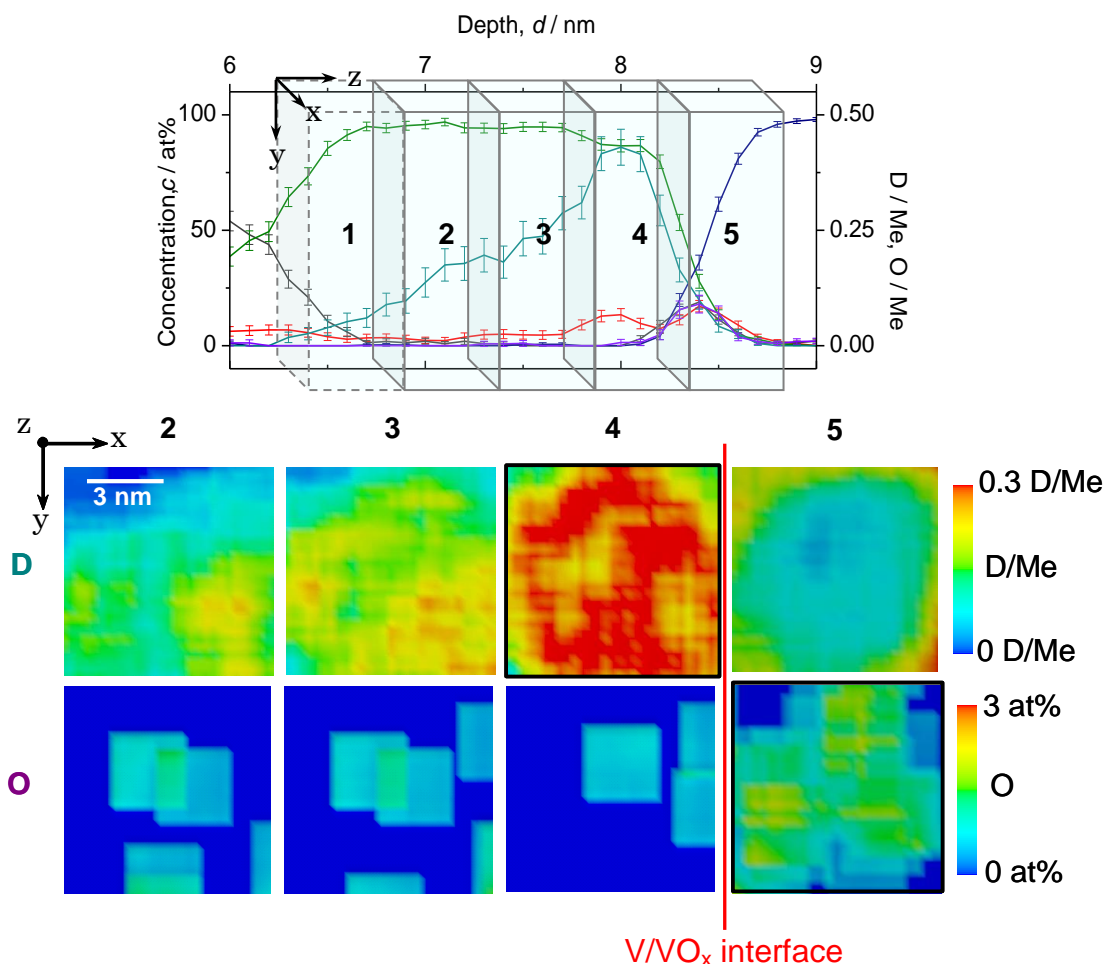


Fig. 5.4.18 2D iso-concentration maps of D and O at each cross section (2 ~ 5). Note high O concentration on the W substrate.

5.4.4 Fe/V-Fe multi-layered film

In this section, the D atoms distribution in Fe/V multi-layered films will be studied. In order to investigate the influence of the D_2 pressure on the local D concentration, the applied D_2 pressure was changed from 0.05 Pa to 1000 Pa. The general analysis temperature was 30 K. But, only for the sample loaded with D_2 at 0.2 Pa, an additional analysis at 60 K was performed in order to study the surface segregation behavior.

An EMF curve i.e. pressure-composition isotherm (p - c - T) of similarly structured film, Pd 20 nm / [(Fe 5 nm / V 5 nm) x 8], was measured ahead for comparison. From this EMF curve, it is possible to derive the expected hydrogen concentration at a certain hydrogen pressure.

The result of EMF measurement is shown in Fig. 5.4.19. As discussed already in the section of stress measurement, the inflection points shown here agree well with deflection points of the stress development curve (Fig. 5.1.16). The red lines crossing the curve in the figure indicate applied D_2

pressures and corresponding c_D for APT. However, the phase boundaries of such thin multi-layered system are still unknown.

Based on this curve, therefore, the expected concentrations c_0 are simply taken from the cross points shown in Fig. 5.4.19. The corresponding c_D and D_2 loading pressures for the APT examination are summarized in Table 5.9.

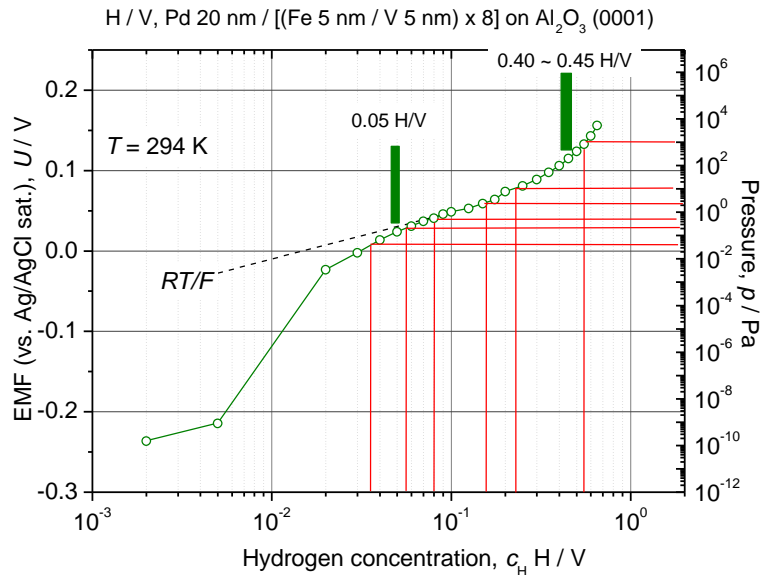


Fig. 5.4.19 EMF curve of Pd 20 nm / [(Fe 5 nm / V 5 nm) x 8] deposited on Al_2O_3 (0001) substrate at room temperature. Green lines indicate the inflection points observed in the stress curve. The black dot line RT/F shows the ideal solubility known as Sieverts' law. The red lines show applied D_2 pressures and corresponding c_D for APT analyses. The values are summarized in Table 5.9.

Table 5.9 Expected mean deuterium concentrations, c_0 (D/Me) in Fe/V at different applied D_2 pressures, derived from Fig. 5.4.19. (The phase boundaries are unknown in this case. Therefore, mean concentrations are given here.)

D_2 pressure / Pa	Analysis temperature, T / K	
	60	30
0.05	-	0.035
0.2	0.053	0.053
0.5	-	0.08
2	-	0.15
10	-	0.22
1000	-	0.55

5.4.4.1 Impact of analysis temperature

- Analysis at 30 K, D₂ 0.2 Pa

Even though the reference data of diffusion coefficient of D in V and actual APT results of D loaded V film implied that 30 K is not low enough to freeze D-mobility (2 nm/hour) [Qi83], reasonable D-distribution and concentration were observed (Fig. 5.4.7).

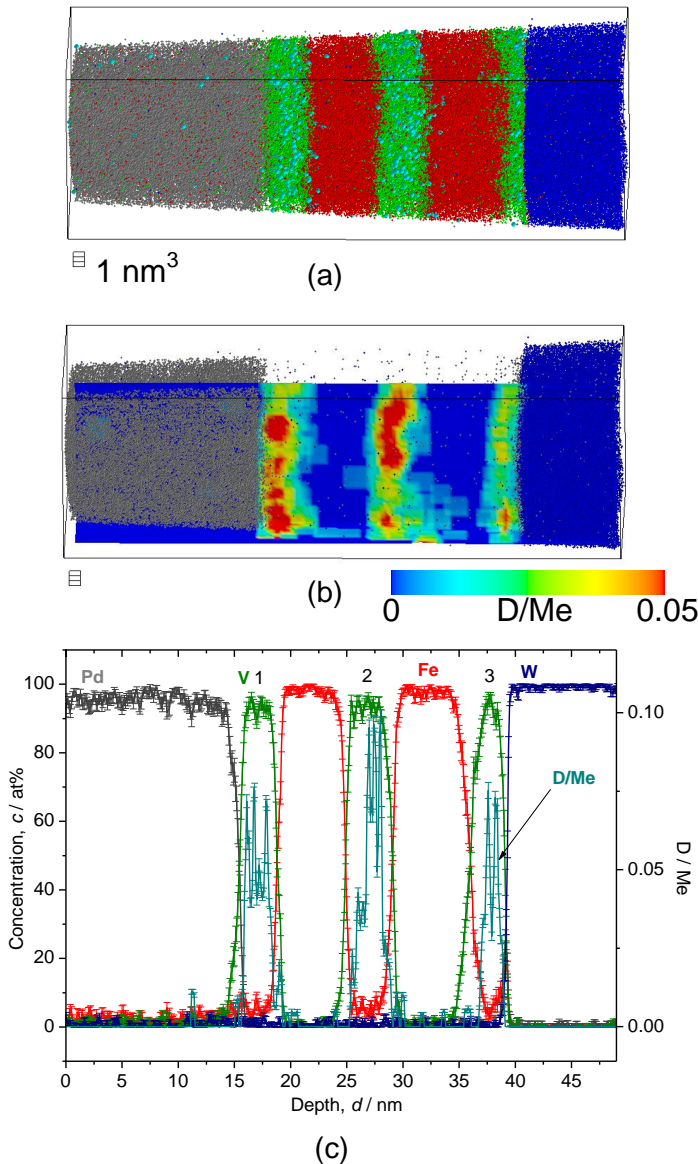


Fig. 5.4.20 The reconstructed volume of Fe/V multi-layer (16 nm x 16 nm x 50 nm), loaded with D₂ 0.2 Pa., analyzed at 30 K. (a) The whole volume of reconstruction (grey: Pd, green: V, red: Fe, blue: W, light blue: D). (b) Iso-concentration map of D concentration ($c_D = 0.05$ D/Me) from the same reconstruction in (a). (c) Depth concentration profile from a 5ϕ nm cylinder.

From the results given in Chap. 5.4.2, the following two conditions as the touchstones of reliable analysis were pointed out as long as the α -phase is concerned.

- (i) Lack of sloped D profile in V layer
- (ii) Lack of D atoms at Pd/V interface

In Fig. 5.4.20 the 3D reconstruction, the iso-concentration map and its depth profile of Fe/V multi-layer that was loaded at 0.2 Pa D_2 , analyzed at 30 K are shown. The conditions above (i) and (ii) are fulfilled and the iso-concentration map indicates that the lateral homogeneity of D distribution is satisfactory.

The average concentration in the 2nd V layer was checked by a histogram (Fig. 5.4.21). The result showed a $c_D = 0.05(2)$ D/Me (the number in the bracket indicates the standard deviation), which is in excellent agreement with the expected concentration, $c_0 = 0.053$ D/Me determined by the corresponding p - c - T curve (Fig. 5.4.19).

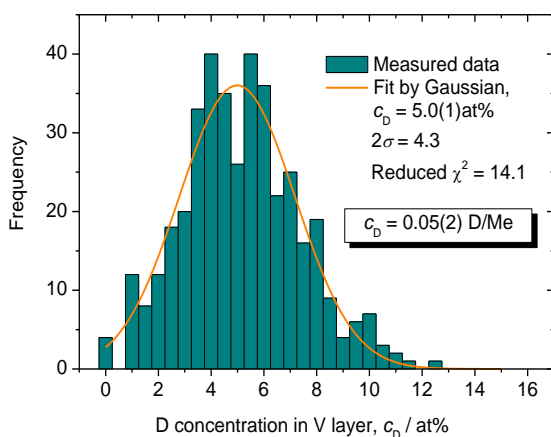


Fig. 5.4.21 D concentration histogram summed up from individual 4 cylinders of 5 nm ϕ placed at the 2nd V layer. 400 data points were included. The number 2 in the bracket indicates the standard deviation.

- Analysis at 60 K, D_2 0.2 Pa

As expected from the results on the influence of analysis temperature discussed in the last section (Chap. 5.4.1.1), peculiar D distribution associated with surface segregation appears at 60 K. The system D-Fe/V was not an exception, either. This confirms that the observed D-segregation at high analysis temperatures (> 30 K) is truly caused by the diffusion of D in the V layer.

In Fig. 5.4.22, the reconstructed volume and corresponding depth profile from a cylinder volume with 5 nm diameters are shown together. Clearly, the D concentration profile (b) shows surface segregation of D (light blue spheres) towards the Fe/V interfaces, indicating an asymmetric D-distribution.

The existence of D within the Pd/V interface also proves the occur-

rence of surface segregation and subsequent loss of D, which is the same as the results of V-Fe single layered films (see e.g. Fig. 5.4.3 and Fig. 5.4.5) However, the loss of D is not as significant as in the case of the V single

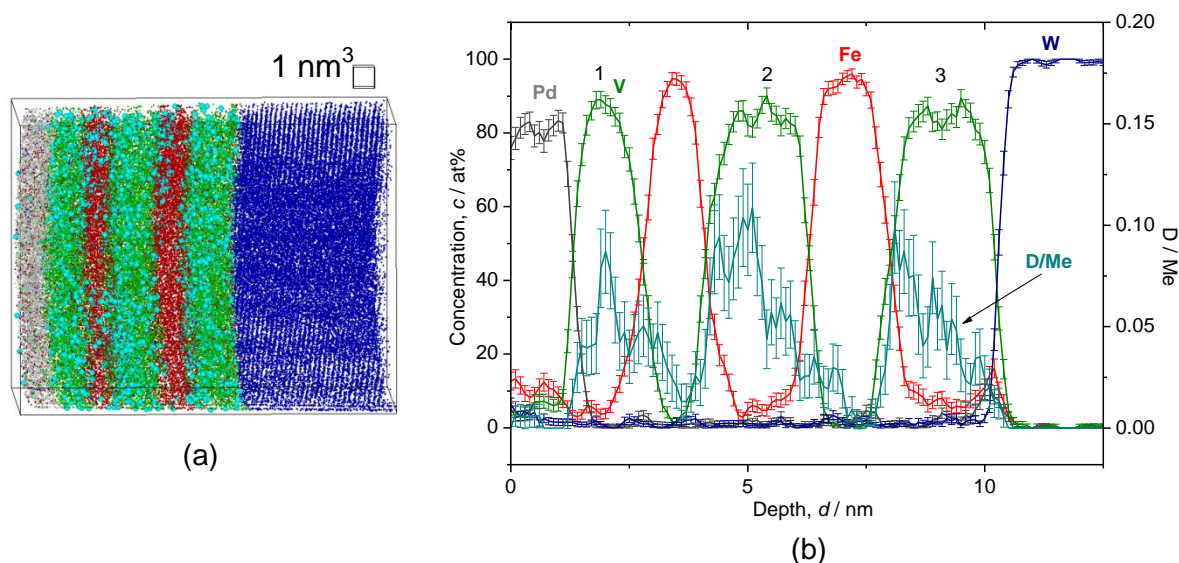


Fig. 5.4.22 The reconstructed volume of Fe/V multi-layer (12 nm x 12 nm x 16 nm), loaded with D_2 0.2 Pa., analyzed at 60 K. (a) The whole volume of reconstruction (grey: Pd, green: V, red: Fe, blue: W, light blue: D). (b) Corresponding depth profile taken from a 5 nm ϕ cylinder.

layered film at 60 K (Fig. 5.4.3), since the observed mean c_D in the 2nd V layer is about 0.05 D/Me, which is same content as the expected c_D .

Comparing the results of 60 K with that of 30 K, the influence of surface segregation is quite pronounced. Therefore, further analyses at different D_2 loading pressure have been carried out at 30 K also because the risk of sample rupture is lower than that at 20 K.

5.4.4.2 Impact of D_2 pressure, at 30 K

- D_2 0.05 Pa

At the D_2 pressure of 0.05 Pa, the sample is in the α -phase and $c_0 = 0.035$ D/Me is expected according to the p - c - T curve. The result of the 3D reconstruction, the iso-concentration map and the depth profile are shown in Fig. 5.4.23.

The average c_D of 0.013(4) D/Me was found in the 2nd V layer. This value is, however, only 1/3 of the expected value. The expected concentra-

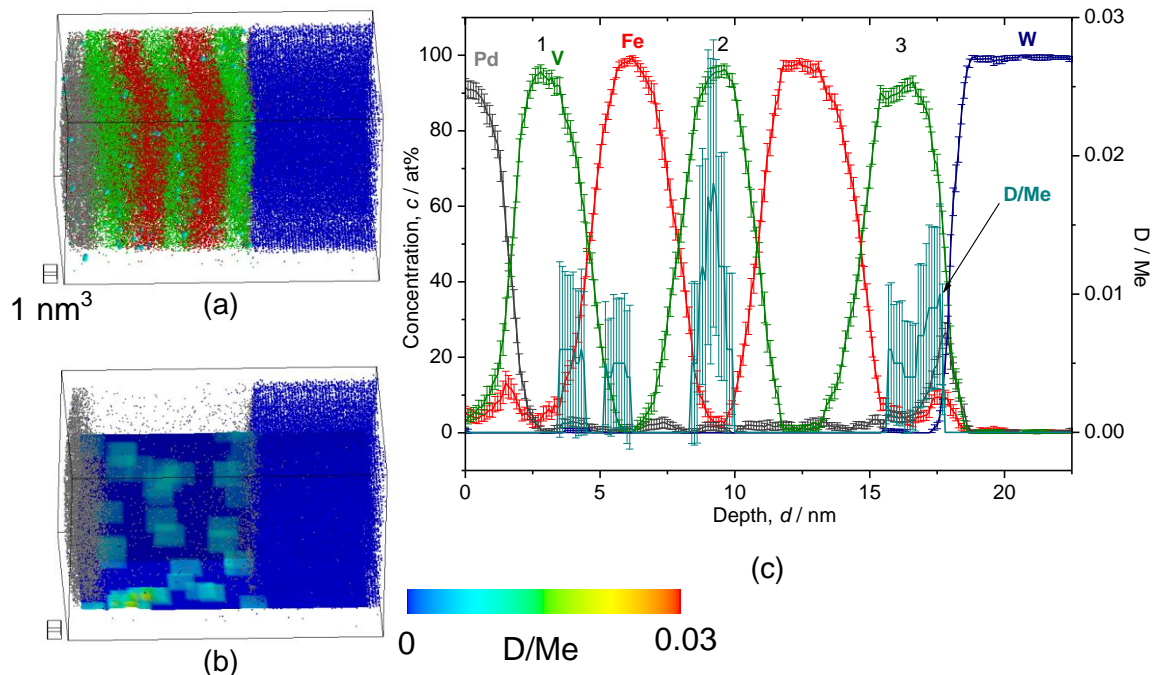


Fig. 5.4.23 Reconstructed volume of Fe/V multi-layer (14 nm x 14 nm x 27 nm), loaded with D_2 0.05 Pa., analyzed at 30 K. (a) The whole volume of reconstruction (grey: Pd, green: V, red: Fe, blue: W, light blue: D). (b) Iso-concentration map of D concentration ($c_D = 0.035$ D/Me) from the same reconstruction in (a). (c) Depth concentration profile from 5 nm- ϕ cylinder volume.

tion c_0 is 0.035 D/Me if significant H-trapping effect is taken into account. If no dislocation exists in the analyzed volume and thus no considerable trapping effect is expected, the c_D at 0.05 Pa should almost follow the linear line indicated as RT/F in Fig. 5.4.19. This would give $c_D = 0.02$ D/Me. Plotting the observed concentration of $c_D = 0.013(4)$ D/Me in Fig. 5.4.19 agrees with this consideration if slight deviation is allowed.

- D_2 0.5 Pa

The sample is considered to be in $\alpha+\beta$ phase with $c_D = 0.08$ D/Me at this pressure, though it is close to the presumable solubility limit of $c_D = 0.10$ D/Me.

In Fig. 5.4.24, the analysis results are shown. Unfortunately the film structure itself was not well deposited and the 2nd V layer is forming sloped interface with respect to the 1st Fe layer. Nevertheless, it clearly reveals laterally homogeneous D distribution in the V layers with even

high c_D of 0.12(5) D/Me. If compared with the presumable solubility limit of bulk V, the V layers can be considered to be in the $\alpha+\beta$ phase. More inter-

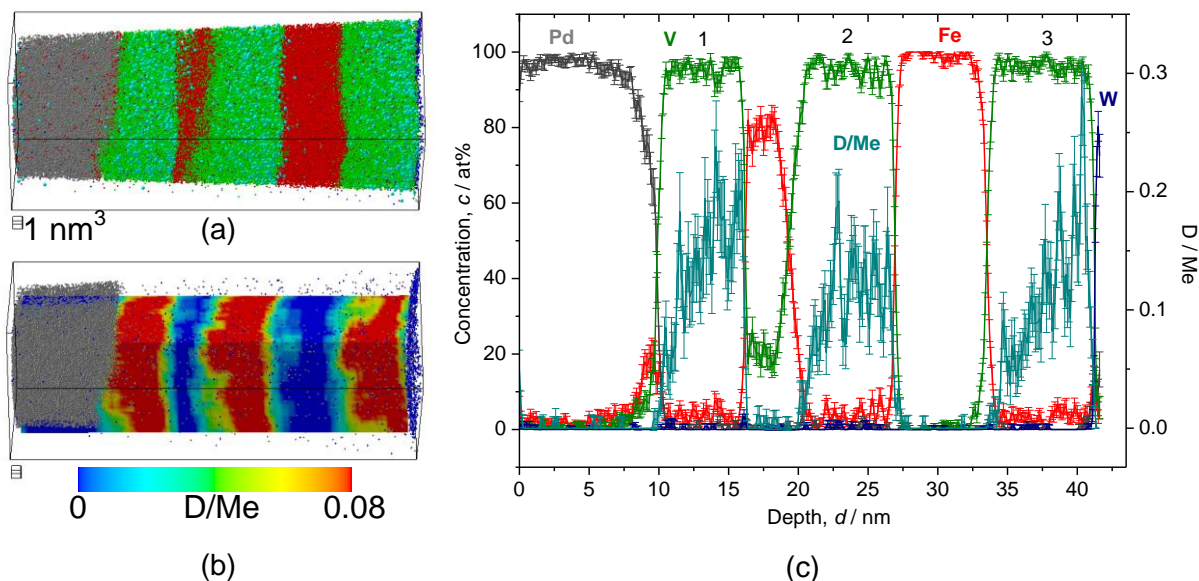


Fig. 5.4.24 Reconstructed volume of Fe/V multi-layer (15 nm x 15 nm x 42 nm), loaded with D_2 0.5 Pa., analyzed at 30 K. (a) The whole volume of reconstruction (grey: Pd, green: V, red: Fe, blue: W, light blue: D). (b) Iso-concentration map of c_D of (a). (c) Depth concentration profile from a 5 nm- ϕ cylinder. The 1st Fe/V interface is tilted.

estingly, the D depth distribution in the 3rd V layer shows relatively high c_D at the V/W interface. This may seem to be analogous to the case of hydride phase in the V single layer discussed in the last section. But, there was no influence of Pd distribution found in this case. One should also note that the slightly sloped c_D profile in all of the V layers towards W, which was not observed in the analysis results of α -phase.

- D_2 2 Pa

At this pressure the sample is supposed to be in the β -phase region for bulk V and the observed $c_D = 0.13(5)$ D/Me reached expected average concentration, $c_D = 0.15$ D/Me within the error bar. Here, one should note that distinctively high c_D is again found in the 3rd V layer just on W, which is almost twice a large than in the other two V layers (Fig. 5.4.25).

Moreover, c_D profile in the 2nd V layer is asymmetric and the concentration maximum of c_D does not accord with the concentration minimum of c_{Fe} . As a general trend, the peak of c_D is slightly shifted towards W substrate.

One should note that the c_D is high at the 3rd V layer (on W substrate). Such enrichment of D was observed also in case of VFe single layered film.

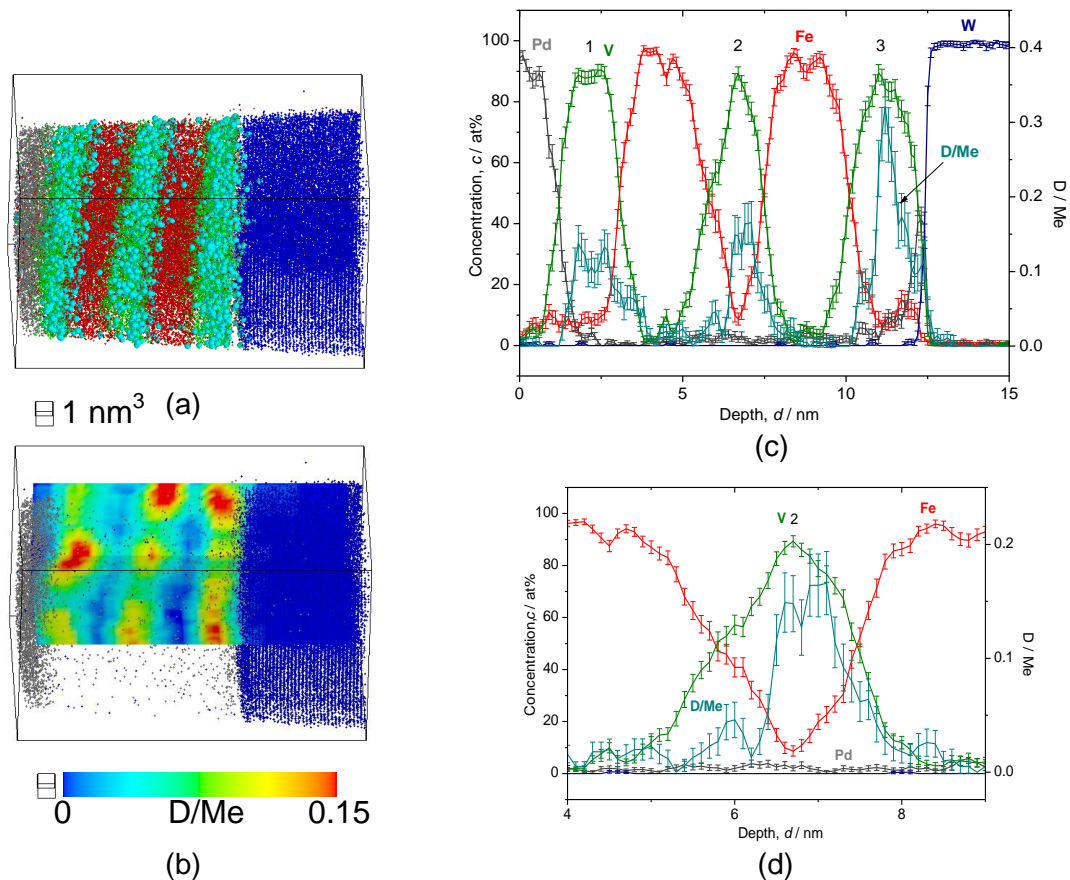


Fig. 5.4.25 The reconstructed volume of Fe/V multi-layer (12 nm x 12 nm x 20 nm), loaded with D_2 2 Pa., analyzed at 30 K. (a) The whole volume of reconstruction (grey: Pd, green: V, red: Fe, blue: W, light blue: D). (b) Iso-concentration map of c_D of (a). (c) Depth concentration profile from a 5-nm ϕ cylinder. Notably high c_D in the 3rd V layer is observed. (d) Magnified plot of the 2nd V layer. The c_D shows an asymmetric profile.

- D_2 10 Pa

The already observed high c_D in the 3rd V layer and the shift of the c_D peak towards W substrate is more pronounced and becomes clear at this pressure (Fig. 5.4.26). The stacking order of Fe/V seems to have a marked impact on the D distribution concerning the high c_D region.

The observed mean concentration $c_D = 0.22(9)$ D/Me was in excellent agreement with the expected $c_D = 0.22$ D/Me.

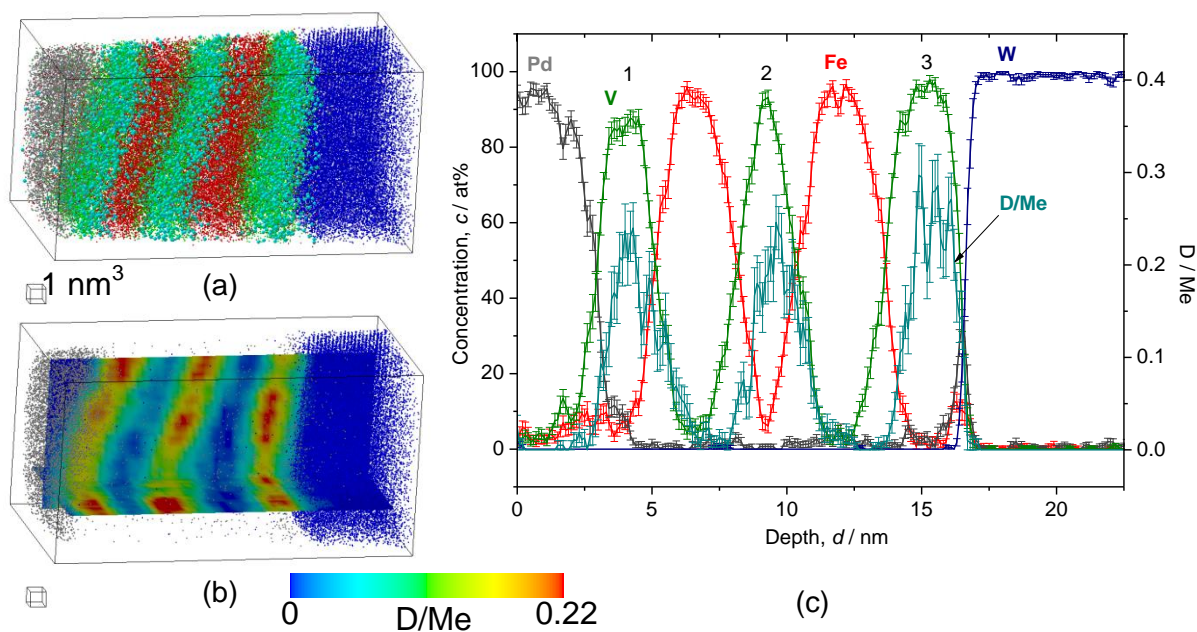


Fig. 5.4.26 The reconstructed volume of Fe/V multi-layer (12 nm x 12 nm x 23 nm), loaded with D₂ 10 Pa., analyzed at 30 K. (a) The whole volume of reconstruction (grey: Pd, green: V, red: Fe, blue: W, light blue: D). (b) Iso-concentration map of c_D of (a). (c) Depth concentration profile from a 5 nm- ϕ cylinder. The c_D in the 3rd V is higher than in the other 2 V layers.

- D₂ 1000 Pa

Fig. 5.4.27 shows the analysis results of the sample with 1000 Pa D₂ loading pressure. Similar distribution of c_D to the results of 10 Pa is observed also at 1000 Pa with more intensive degree, indicating that these curious observations of (i) depth shift of c_D and (ii) high c_D in the 3rd V layer, which might be universally related with hydride formation behavior.

The c_D was 0.28 D/Me, which is nearly a half of the expected concentration. The isotope effect alone cannot explain such a huge difference between c_D and c_H as the phase boundaries of both are nearly the same. Since any loss of D atoms can be disregarded at this analysis temperature, other factors like the difference of the V layer thickness from that of the sample taken for p - c - T or different lattice strain state and the resulting stress contribution may be ascribed to the narrowed miscibility gap and the deviation of terminal concentration in the β -phase.

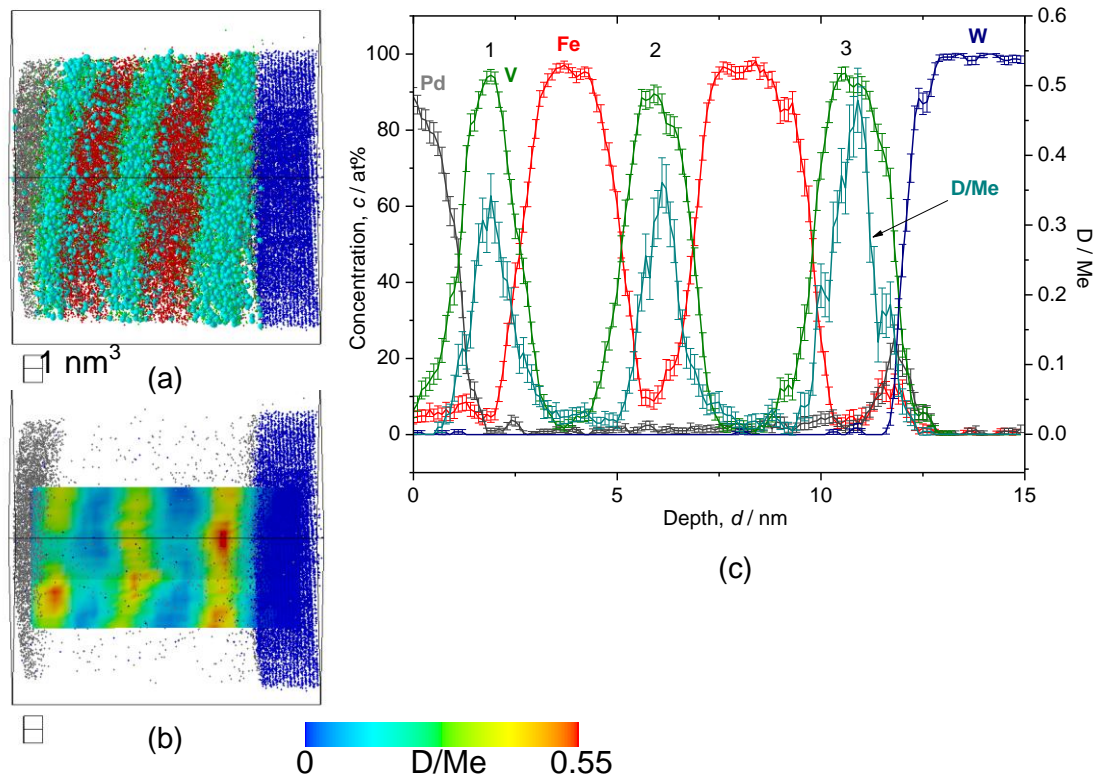


Fig. 5.4.27 The reconstructed volume of Fe/V multi-layer (12 nm x 12 nm x 16 nm), loaded with D₂ 1000 Pa., analyzed at 30 K. (a) The whole volume of reconstruction (grey: Pd, green: V, red: Fe, blue: W, light blue: D). (b) Iso-concentration map of c_D of (a). (c) Depth concentration profile from a 5 nm- ϕ cylinder.

5.4.4.3 Comparison with EMF curve (pressure-composition isotherm)

It is now worth to compare those mean deuterium concentrations c_D at different D₂ pressures obtained by APT with the corresponding p - c - T curve. The results are plotted together in Fig. 5.4.28. All data points were recorded at the analysis temperature of 30 K. The data points of APT results were taken from the c_D in the 2nd V layer, which is put into two Fe layers.

Altogether, the agreement is quite well within the error bar. In case of 1000 Pa, the deviation from the corresponding EMF curve is rather large, which could be due to the difference of the thickness. For APT analyses, the thickness of 2 nm is sometimes necessary due to increased brittleness at low analysis temperatures. Such reduction of the thickness often reduces the terminal hydrogen concentration [Dornh02].

Conclusively, the APT analysis of deuterium in Fe/V can be carried out with enough reliability even at 30 K.

Details on D-distribution at interfaces are discussed in the next section.

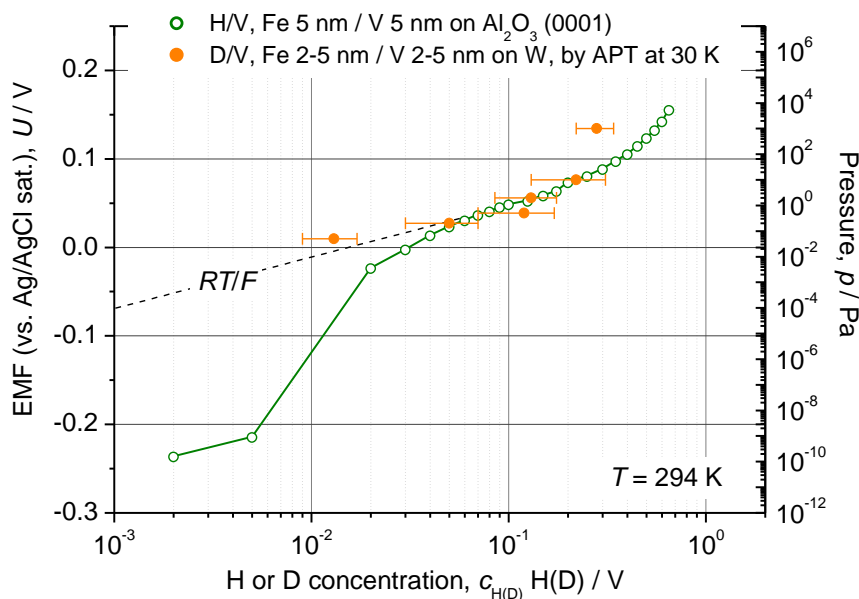


Fig. 5.4.28 EMF curve of Pd 20 nm / [(Fe 5 nm / V 5 nm) x 8] deposited on Al_2O_3 (0001) substrate at room temperature and individual c_{D} determined by APT on the [Fe 2-5 nm / V 2-5 nm / Fe 2-5 nm] stack loaded at different p_{D_2} . The black dotted line RT/F shows the ideal solubility known as Sieverts' law.

5.4.4.4 Local chemistry at Fe/V interface

As it has been shown in the case of V single layered films, all of the W substrate used was covered with O atoms, but not shown to avoid over-loading of figures.

For the samples with low c_{D} , the D distribution shows some deficit at around Fe/V and V/Fe interface of the 2nd V layer, as shown in the ladder diagrams in Fig. 5.4.29. The red arrows show decrease of c_{D} (= lower slope for D) even though these points are in the V layer and are 0.4 ~ 1 nm away from the interfaces. Such profile is reasonably expected from the concept of “dead layer” proposed by Hjörvarsson [Hjörv97]. Furthermore, the Fe/V interface layers contain almost no D atoms. This effect results from alloying. The thick intermixing layer at the 1st Fe/V interface (4.1 nm) is due to tilting of the interface against the sampling cylinder (Fig. 5.4.24).

But, when the pressure is increased, i.e. at high c_{D} , we have observed asymmetric D profile in the 2nd V layer (see Fig. 5.4.25 - Fig. 5.4.27). This

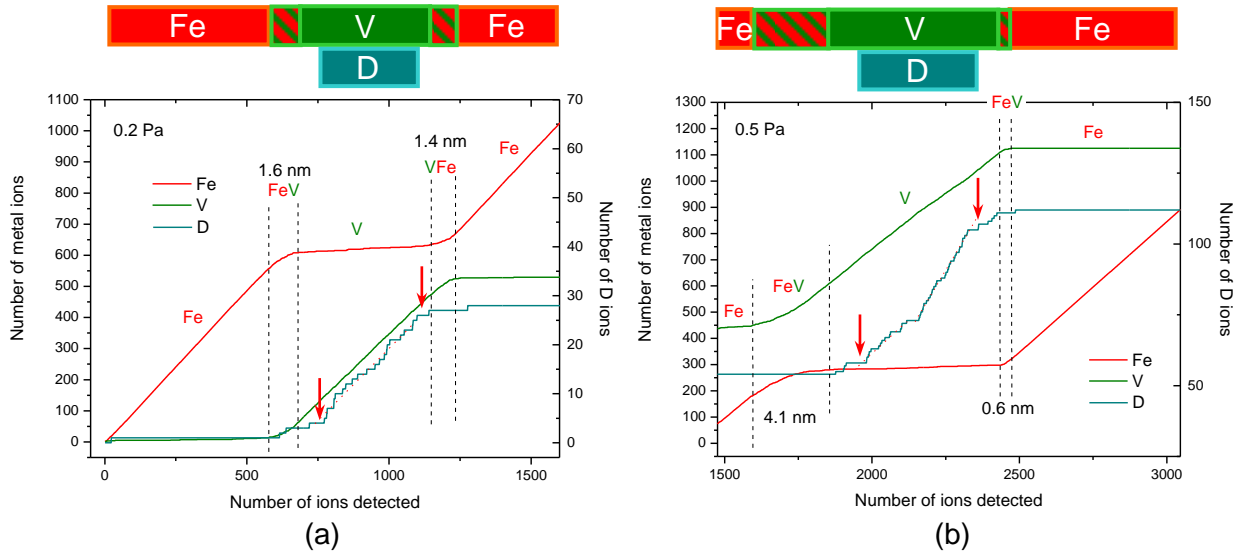


Fig. 5.4.29 Ladder diagrams at Fe/V/Fe (a) the sample with 0.2 Pa D_2 , (b) the sample with 0.5 Pa D_2 . The red arrows indicate D deficiency, which is 0.4 - 1 nm away from the Fe/V and V/Fe interfaces, indicative of the dead-layer. In (b), the Fe/V interface has rather thick intermixing (4.1 nm). But, this is due to tilted interface (see Fig. 5.4.24).

feature is visible also in ladder diagrams (Fig. 5.4.30). The interface layers in these cases absorb rather high amount of D, and this trend is more pronounced at the V/Fe interface than at the Fe/V interface. Thus, no dead-layer effect is visible at $p_{D_2} \geq 2$ Pa. It is worth to note that the Fe/V and the V/Fe interfaces behave different at higher pressures.

By taking the c_D at Fe/V interface and plot against Fe concentration from the sequence of Fe/V and V/Fe for comparison, the difference in c_D will become more clearly visible. In Fig. 5.4.31 (a) and (b), the plots of c_D against c_{Fe} taken from c_D at the Fe/V and V/Fe interfaces are shown, respectively. Corresponding interface is schematically illustrated as well. In the inset the concentration region around 15% Fe and 65% Fe is magnified. The red lines in the inset are drawn to guide eyes.

In both of (a) and (b), it is commonly observed that the c_D decreases as c_{Fe} increases, such that the two-phase region is narrowed. However, the slope of the curves are different. In (a), there is a clear discontinuity in the change of c_D against c_{Fe} at the c_{Fe} of 35 at%, and the onset of slope change at around 60 at% Fe. In (b), there can also be seen the change of slope at $c_{Fe} = 35$ at%, for 2 and 1000 Pa. The mean concentration is higher for the V/Fe interface when compared to the Fe/V interface. This cannot be related to an increased defect concentration, since this is expected to be higher at the Fe/V interface (compare with Chap. 4.3.3). We suggest that different lattice strain is responsible for this effect. Electronic effect and

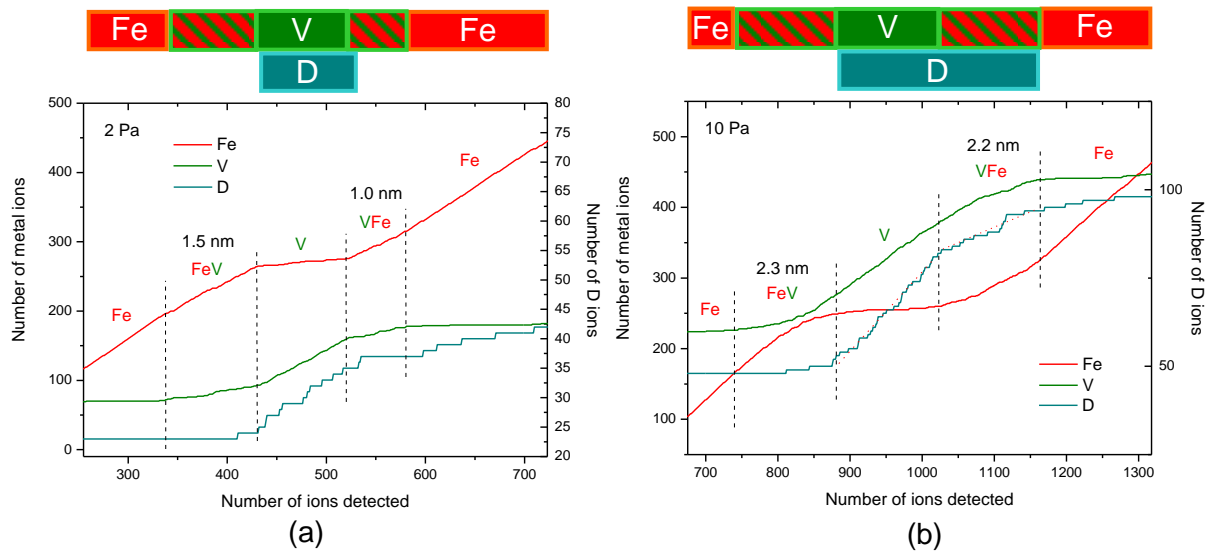


Fig. 5.4.30 Ladder diagram at Fe/V/Fe (a) the sample with 2 Pa D_2 , (b) the sample with 10 Pa D_2 . Note high c_D at V/Fe interface. The dead-layers are not visible anymore.

stress effect should also be considered. For example, the SRIM simulation (Fig.4.23) suggested that the implantation impact of Fe into V and V into Fe is not identical. This might cause difference of initial stress state between the Fe/V and V/Fe interfaces. Hydrogen prefers less compressive region. In this sense, it is inferred that the V/Fe interface could be less compressive than at Fe/V interface.

In case of (b), it can be seen that the c_D at lowest c_{Fe} is even smaller than that at higher c_{Fe} (see 2, 10 and 1000 Pa at around 10 and 20 at% Fe). This peculiarity is caused by the shift of c_D at this interface, which was observed already in Fig. 5.4.25, Fig. 5.4.26 and Fig. 5.4.27.

The change of the slope seen at around 35at% Fe in Fig. 5.4.31 (a) and (b) is exactly at the concentration where Fe-V phase diagram shows the σ -phase formation [Land08].

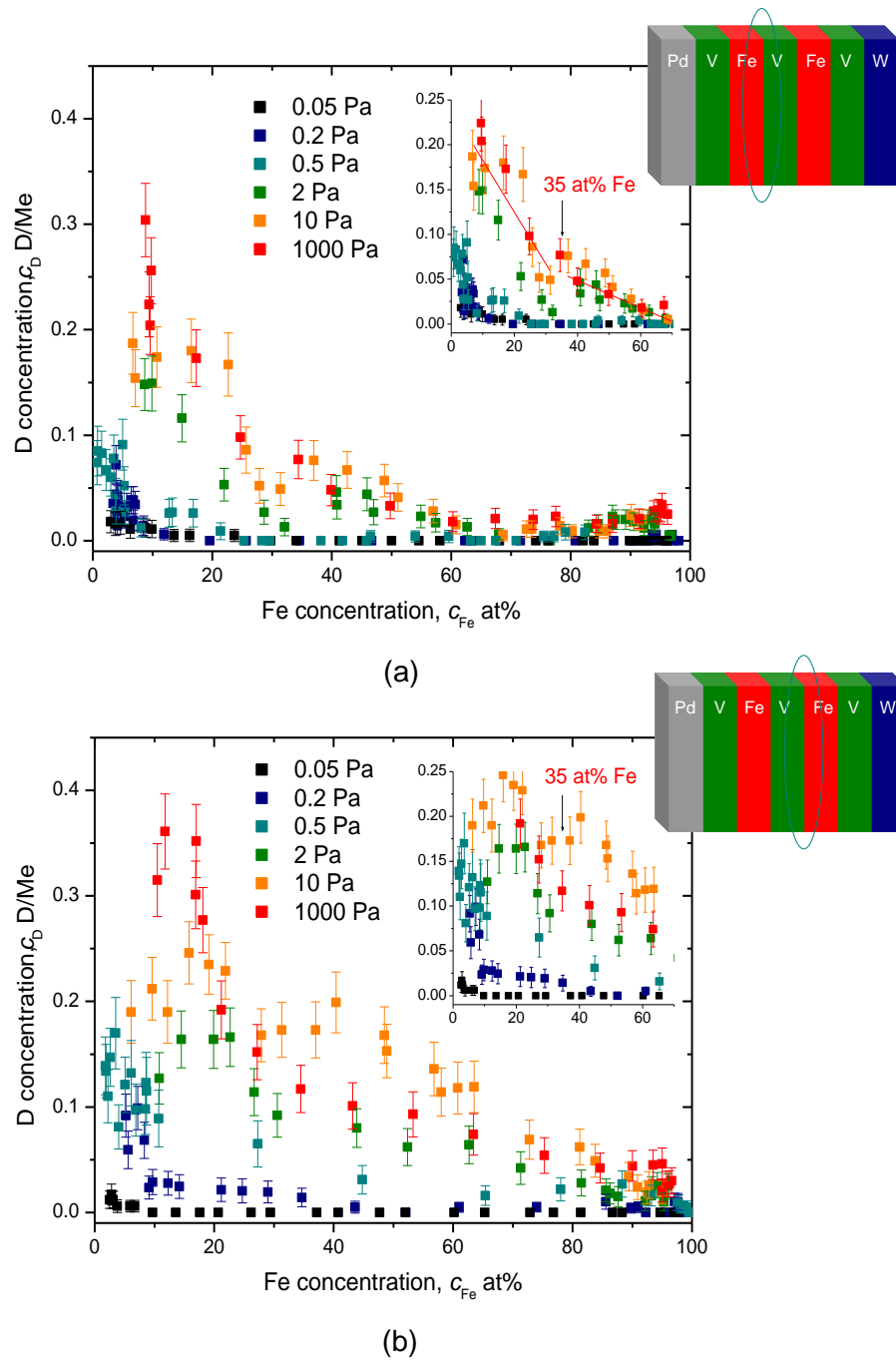


Fig. 5.4.31 D concentration c_D as a function of interface composition taken from the interface (a) Fe/V and (b) V/Fe (circled in the illustration). In (a), change of the slope with Fe concentration c_{Fe} can be seen at 60 at% Fe and 35 at% Fe in the plots of 2, 10 and 1000 Pa. In (b), the same trend is observed except for the case of 10 Pa.

6. Global discussion

In this chapter, the results obtained in different measurements (stress, *in-situ* XRD, acoustic emission and atom probe tomography) are synthesized and discussed. First, H-related mechanical response of VFe thin films is interpreted at different H concentrations (c_H), typically at $c_H = 0 - 0.005$ H/V, at $c_H = 0.005 - 0.1$ H/V, at $c_H \sim 0.1$ H/V and at $c_H = 0.1 - 0.4$ H/V because different mechanisms should be taken into account separately.

Later, peculiar stress response of Fe/V films is discussed in terms of preferential site occupation. The local chemistry of similar films with deuterium, elucidated by atom probe tomography is discussed further from a view point of trapping effects.

6.1 At $0 < c_H \leq 0.005$ H/V - Interaction of H with vacancy in VFe thin films

In the results obtained by *in-situ* stress measurements, the films deposited at high temperatures (773 K and 1073 K) showed, at low c_H (0.002 and 0.005 H/V), remarkable tensile stress (Fig. 5.1.2). The results of

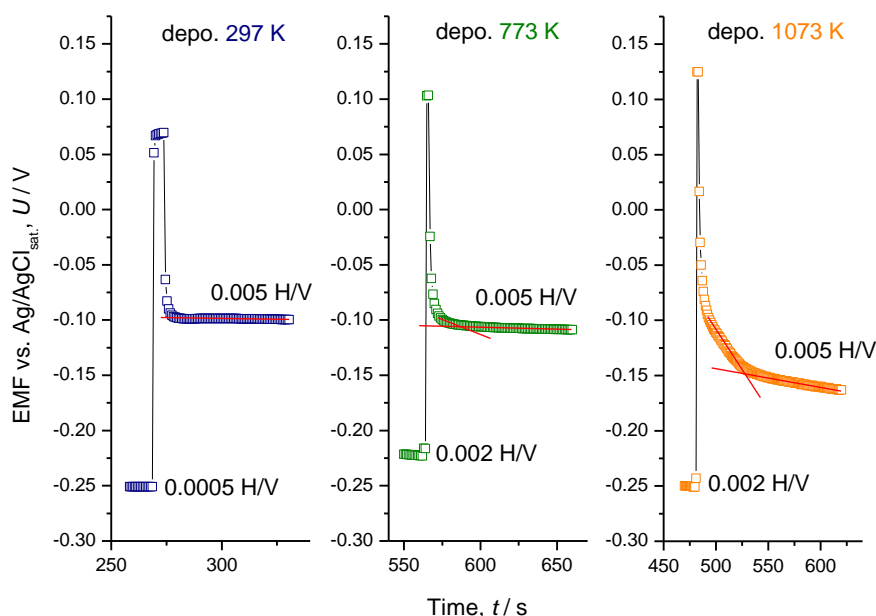


Fig. 6.1 Example of H loading curve of 100 nm V-Fe8at% film deposited at different temperatures. Note that the kinetics of the film deposited at 1073 K is obviously slower than that of the other 2 films, at $c_H = 0.005$ H/V.

in-situ XRD on the film deposited at 1073 K implied that there was no lattice parameter change up to the same concentration ($c_H = 0.005$ H/V) apparently because of mechanical restriction (Fig. 5.2.3 and Fig. 5.2.4). Furthermore, the transition of EMF of this film showed slower kinetics than those of films deposited lower temperatures, as exemplary shown in Fig. 6.1 by the extended time scale for reaching the equilibrium EMF-value.

These findings might hint on the preferential H occupation of sites, which is suggested by Hjorvarsson *et al.* In case of tetragonally strained lattice, H atoms prefer less compressive sites and thus O_z sites can be possessed in an extreme case e.g. Fe/V superlattice [Olsson03]. However, the V-Fe film deposited at 1073 K did not indicate such an initial lattice distortion (see Fig. 5.2.3 (a)), and the whole lattice volume was contracted -2% compared to that of bulk. Therefore, the preferential site occupation is not consistent.

Another possibility is the trapping of H atoms at defects like dislocations and/or vacancies. A contribution of H-trapping at pre-existing dislocations is also possible. Due to the difference of thermal expansion coefficient α_{th} between the film and the substrate, the dislocation density might be higher for the film deposited at higher temperatures. Hence the EMF potential should be lower for the films deposited at higher temperatures. This is supported by the results (Fig. 6.1).

However, the critical stress $\sigma_{\alpha,lim}$ (stress at the initial bending point) was smaller for the films sputtered at higher temperatures (Fig. 5.1.2) and the dislocation rearrangement effect was not visible there. Both effects hint on a lower dislocation density for the films deposited at higher temperatures. It is reasonable to assume that films deposited at higher temperatures contain a higher amount of vacancies, regarding the equilibrium concentrations.

The equilibrium concentration of vacancies c_v depends exponentially on the formation energy of vacancy E_f and the temperature T [Haas78++].

$$c_v \propto \exp\left(\frac{E_f}{RT}\right) \quad (6.1)$$

In V, E_f of a monovacancy is 2.2 eV [Jano82]. By applying this value as E_f and $T = 1073$ K as the maximum limit, the monovacancy (Vac) concentration c_v in the V layer is approximately $c_v \approx 5 \times 10^{-11}$ Vac/V.

Vacancies are known to trap H with strong affinity [Fukai05]. In case of V, the binding energy of H atoms to vacancies is 0.23 eV [Danie84] which is smaller than that of e.g. Nb, 0.55 eV [Haut85]. In Nb, one monovacancy is believed to trap up to four H atoms, forming a Vac-4H complex

[Cizek04]. If we assume this number also for V, the trapped hydrogen concentration in the film deposited at 1073 K would give $4H \times 5 \times 10^{-11}$ Vac/V, thus $\sim 2 \times 10^{-10}$ Vac-H/V at maximum limit. This value is, however, 7 orders of magnitude smaller than 0.005 Vac-H/V, which is the expected value of $4H \times 0.00125$ Vac/V. Therefore, it is not reasonable to explain the observed tensile stress seen in Fig. 5.1.2 by the trapping of H atoms at intrinsic thermal vacancies.

Fukai has reported on the formation of superabundant vacancy (SAV) under the presence of H and found evidence of Vac-H clusters with anomalously high concentrations of 1 to 10 at% in various metals [Fukai05]. Fukai *et al.* firstly observed SAV under high temperature and high H_2 pressure conditions. Later, however, the existence of Vac-H clusters was confirmed in various electrodeposited [Fukai03+, Fukai03++] and electrochemically charged metals [Cizek04, Cizek07], as well as in thin surface films after plasma-based ion implantation [Semi80]. In summary these experiments showed that high hydrogen pressure and high temperature conditions are not thermodynamically necessary for SAV formation.

If the degree of lattice contraction is known e.g. by XRD, the Vac-H concentration can be estimated via Eq. (6.2), with applying the relaxation volume of Vac-H, ν_{cl}^R/Ω , as ~ 0.30 , which is known to be a good approximation for various metals [Fukai01].

$$c_{cl} = \frac{3 \cdot \frac{\Delta a}{a}}{\frac{\nu_{cl}^R}{\Omega}} \quad (6.2)$$

By assuming Vac-4H complex formation and thus introducing $c_{cl} = 0.00125$ Vac/V in Eq. (6.2), the required relative contraction of the lattice parameter $\Delta a/a$ can inversely be estimated and, yields 1×10^{-4} . For bulk metals, quantitative monitoring of tiny lattice parameter variation by careful XRD measurements enables to assess the vacancy concentration [Simmo60]. But, in case of a preferentially oriented thin film it is often difficult because the number of reflections is limited. Therefore, alternative methods like e.g. positron annihilation spectroscopy (PAS) should be applied to estimate c_{cl} at low concentrations. In total, the introduction of SAV can explain the observed behavior of films that were deposited at 1073 K.

Tensile stress components were also observed for some other films of 200, 100 and 50 nm thickness which were deposited at room temperature. Even though some tensile stress components might be regarded as negli-

gibly small (see Fig. 5.1.5, and Fig. 5.1.7), the initial slope of all of these stress curves commonly showed smaller values than that expected from linear elastic theory (compare with Chap. 2). As this is a trend similar to that of the films which were deposited at 773 K or 1073 K, it can be assumed that this generally hints on the incorporation of a vacancy-H interaction in VFe-thin films.

Concerning the other films that did not directly show the vacancy-H interaction, other reasons must be considered, e.g. different contribution of micro-structural defects in the initial state which might work as a sink for vacancies. This would, however, also modify the elastic response of films from the linear elastic model. This was not observed in this study. Instead, the agreement with the linear elastic behavior was established in most cases. Here, another interest arises i.e. to conduct the same measurement at higher temperatures. Such investigation would give more insight about the question above.

6.2 At $0.005 < c_H \leq 0.1$ H/V - Quasiplastic response in the elastic regime of VFe thin films upon H uptake

For thinner films less of than 200 nm thickness, small stress-releasing departures of the stress development (denoted as σ_1 or σ_2 in Fig.5.1.4 - Fig. 5.1.9) were observed even in the elastic regime of the stress curve. This effect is surprising and needs special discussion because at this low stress state, dislocation generation is not reasonable. This is supported by the AE-signals of minor and localized intensity. But, considering the H introduction and corresponding volume expansion, it is plausible to interpret this relaxation as that caused by propagation of pre-existing dislocations. This interpretation is supported by the results of AE measurements, for example on the 120-nm thick film (Fig. 5.3.1) that actually revealed a local increase of the AE-signal at the same concentration where the stress relaxation occurred in 100-nm thick film ($c_H = 0.04$ H/V in the stress curve, $c_H = 0.039$ H/V in the cumulative AE curve). This concentration corresponds to that value where the EMF curve finally follows Sieverts' law. Below this concentration, the EMF curve suggests significant H-trapping at defects. Here, also the AE-signals were negligible. Also, above this value AE-signals were negligible.

The onset of Sieverts' type behavior, meaning the concentration above which hydrogen is predominately solved on interstitial sites in the V-lattice, the first AE-signal increase is initiated (compare Fig. 5.3.1 - Fig.

5.3.3). This can be interpreted by a rearrangement of pre-existing dislocations in the lattice, which is initiated by hydrogen-induced stress. According to the orientation relationship between the film and the substrate, large misfit ($\sim 10\%$) is expected (see Fig. 4.4 and Fig. 4.11). Thus, the pre-existing misfit dislocation density in the film is considered to be large, too. Additionally to the effect of H on the deformation behavior of thin films, the impact of “deformation rate” should be addressed, since the yield stress depends on the deformation rate. With the H-loading technique employed in this study the deformation rate cannot be controlled. It depends on the thin film microstructure and stress state and thus the apparent diffusion coefficient of H in the film. The yield stress of polycrystalline bulk V at 298 K ranges around 0.2 - 0.55 GPa, significantly depending on the strain rate [Lennon97].

This is graphically shown in Fig. 6.2. The diffusion coefficient of H in pure V at 298 K is $5 \times 10^{-5} \text{ cm}^2 \text{ s}^{-1}$ [Qi83], which corresponds to the deformation rate of $7 \times 10^{-3} \text{ s}^{-1}$ as the upper limit. The actual diffusion coefficient

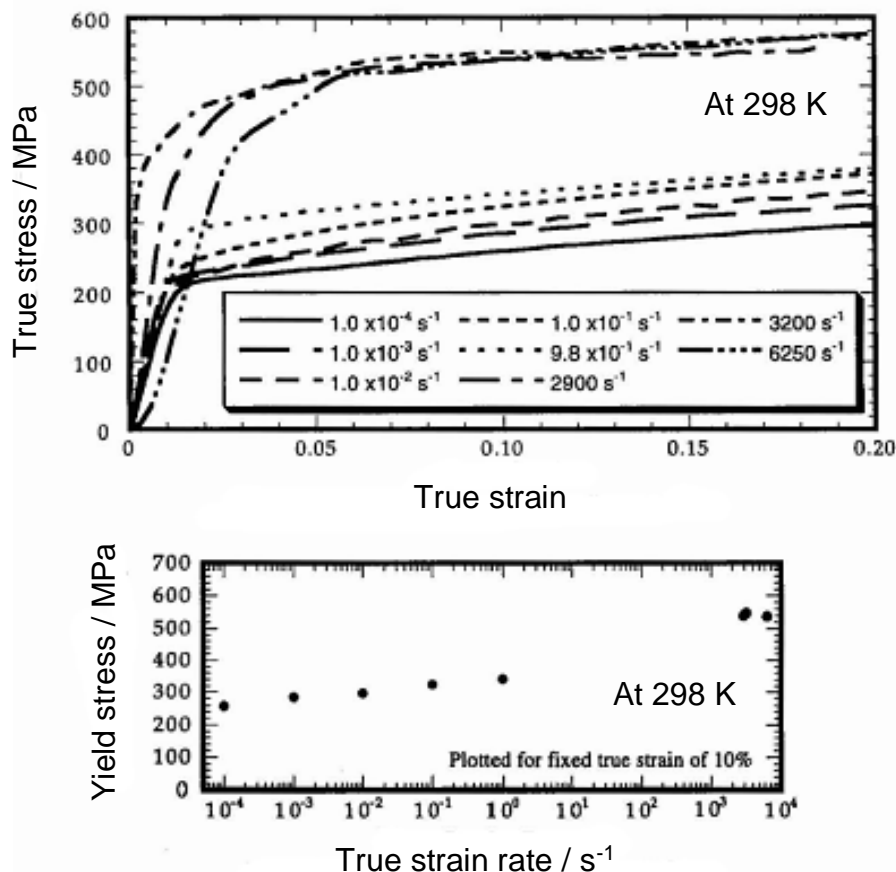


Fig. 6.2 (a) True stresses / true strain curve of pure V (polycrystalline) at 298 K recorded at different deformation rates [Lennon97]. (b) Yield stress at different strain rates. Strong dependence of true stress on the strain rate was observed.

cient of H in V-films can be smaller due to trapping effects. As first approximation, the true stress σ_t of the film studied corresponds to 0.27 GPa according to Fig. 6.2.

In the Sieverts' regime, the first AE-signals were observed at concentrations of $c_H = 0.039$ H/V, $c_H = 0.018$ H/V and $c_H = 0.018$ H/V for 120 nm, 210 nm and 400-nm thick films, respectively (Fig. 5.3.1 - Fig. 5.3.3). The corresponding stress at each concentration recorded in the stress measurements for 100 nm, 200 nm and 400-nm thick films was, -0.21 GPa, -0.18 GPa and -0.22 GPa, respectively (Fig. 5.1.4 - Fig. 5.1.6). These values are in remarkable agreement with the true stress-values of polycrystalline V, shown in Fig. 6.2, that range from 0.27 GPa to 0.35 GPa [Lennon97]. These values are slightly higher than those found for hydrogen loaded VFe-films, indicating an easier initiation of pre-existing dislocation's motion under the presence hydrogen. This is in good agreement with results of H. Barnoush *et al.* [Barn09] who have reported that, under presence of H, the nucleation of a new dislocation loop occurs at lower mechanical load than in samples without H. Barnoush recorded this phenomenon using nano-indentation, as a departure (called often "pop-in") from the elastic behavior of the load-displacement curve. Tal-Gutelmacher *et al.* [Tal-G10+] have detected the same effect in V (100) single crystals. This effect is currently understood well by using the defect-acting-agent (*defactant*) model, proposed by R. Kirchheim [Kirch07]. Thereby, the reduction of the dislocation line energy by H-segregation is ascribed for the observed reduction of "pop-in" load.

One should note, however, that the nano-indentation is carried out on large single grains with an extremely low initial dislocation density. Thus, the observed "pop-ins" are generated by newly created dislocation loops. Therefore, a direct agreement of the stress obtained by nano-indentation with that of stress measurement of the films used in this study is not expected.

Up to now, the discussion does not take twinning deformation into account. But, it has been reported recently by Yu *et al.* [Yu10], that the twinning process is suppressed as the dimension of specimen is decreased and plastic deformation by dislocations becomes dominant. In this sense, detailed microscopic observations are necessary by paying attention also on the reduction of the stacking fault energy under the presence of hydrogen [Ferre96].

The onset of the above mentioned rearrangement might also be linked to the initial stress state of the film. It was shown that the initial in-plane compressive stress was larger for thinner films than that of thicker films, as shown in Table 5.4. By H atom introduction the elastic response is ex-

pected to be larger in an in-plane-compressed lattice than that in a non-stressed lattice. Thus, the final H-induced in-plane compressive stress is also expected to be larger for thinner films [Lauda98]. Such larger stress as a driving force for dislocation motion, would initiate the above mentioned rearrangement more significantly. In fact, the observed “first” small relaxation (either at concentration c_1 or at c_2) became more visible (distinct) as the thickness decreases. This trend suggests that the dislocation rearrangement tends to occur altogether for thinner films, while the thicker films (with multiple domains) deform more moderately. The same trend by the reduction of the film thickness is supported by the results of AE measurements, as it is discussed below.

Further H uptake yields large departures from the Sieverts’ law at 0.10 H/V. At this concentration the V-H films are at the concentration of the solid solution limit. Here, the stress curve starts to deviate from the linear elastic behavior due to more significant hydrogen-induced plastic deformation, and the AE curve shows a remarkable increase, too. This behavior suggests that the “avalanche” of misfit dislocation formation by hydride precipitation marking the onset for misfit generation. At this concentration all of the films showed large stress relaxation of $\Delta\sigma_{\text{lim}} = -0.3 \sim -1$ GPa. When considering the Peierls stress of V, being $\tau_p \sim 0.03G$ (which is reasonable for bcc crystals [Wang01]), the τ_p would result in 1.4 GPa using the shear modulus $G = 46.7$ GPa for V [Bolef61]. The observed values of $\Delta\sigma_{\text{lim}}$ are smaller than this theoretical strength. But it is qualitatively consistent taking contributions of internal defects and hydrogen into account.

Hydrogen segregation at dislocations is expected to lower the yield strength [Kirch07]. Other factors like cross slip are also of importance for bcc crystals. But, as a first approximation, the upper limit of dislocation density ρ of the film can be estimated by taking the σ_{lim} as the yield stress of the film (= the onset of dislocation multiplication). Following Barrett, the boundary condition for multiplication of dislocations is [Barrett73], for bulk material,

$$\tau = \frac{2Gb}{l} \quad (6.3).$$

Here, G is the shear modulus $(C_{11} - C_{12} + C_{44})/3$, l is the length of the dislocation, and b is the Burger’s vector. Since l is defined as $1/\sqrt{\rho}$, the dislocation density ρ can be approximated by the following relationship [Barrett73].

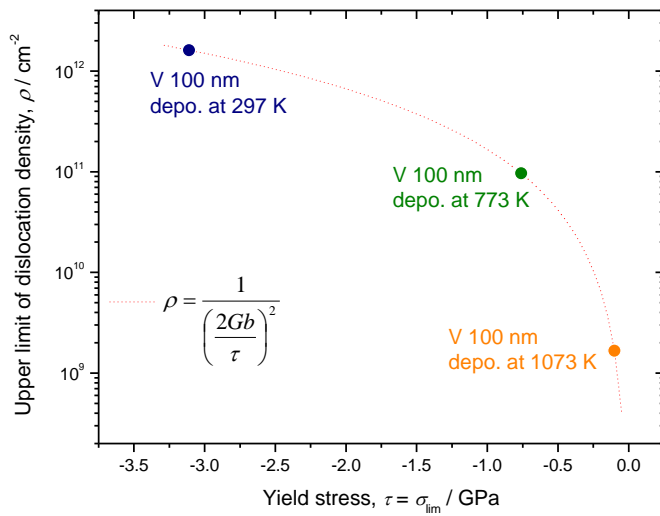


Fig. 6.3 Estimated upper limit of dislocation density in the film given by Eq. (6.4). The critical stress σ_{lim} of each VFe (110) single-layered 100-nm thick film deposited at different temperature was considered and corresponding ρ of these films are implemented. Initial stress for each film is taken into consideration.

$$\rho = \frac{1}{\left(\frac{2Gb}{\tau}\right)^2} \quad (6.4)$$

By taking $b = 0.2624$ nm ($1/2 \langle 111 \rangle$), $G = 46.7$ GPa [Bolef61], and $\sigma_{\text{lim}} \approx \tau$ into consideration, the relationship between the upper limit of ρ and τ is shown in Fig. 6.3. Corresponding ρ for VFe films deposited at different temperatures on Al_2O_3 (11-20) are implemented together. As indicated, ρ is smaller for the films deposited at higher temperatures. The estimated ρ for the film deposited at 1073 K ($\rho = 1 \times 10^9$ cm $^{-2}$) is somewhat smaller than the result obtained for epitaxial Nb 100-nm thick film on Al_2O_3 (11-20) through STM study revealing $\rho = 7 \times 10^{10}$ cm $^{-2}$ [Nörth06], but in a reasonable order, even though Eq. (6.4) is not directly addressing for thin films.

It is known classically by the Hall-Petch relationship, that the dislocation pile-up at grain boundaries induces a high yield strength of solid [Haas78+]. Laudahn *et al.* showed that thin Nb-films composed of nano-grains show larger in-plane stress upon H uptake than epitaxial films [Lauda98]. This was also found to be valid for VFe films (see Fig. 5.1.2, Fig. 5.1.3, and also Fig. 5.1.10). The observed dependence of hydrogen induced stress on the reciprocal of square root thickness was found to be linear, which qualitatively supports this consideration in the thickness range from 10 nm - 400 nm (compare Fig. 5.1.10).

If the adhesion between the film and the substrate is weak, hydride formation is accompanied with the onset of film delamination due to high in-plane compressive stress. However, in this study, it should be reminded again that delamination of the film was not observed until c_{H} exceeds $0.3 \sim$

0.4 H/V, depending on the film thickness. For the films thinner than 100 nm no buckling was observed even after full loading, while the films of 100-nm - 400-nm thick showed significant delamination.

Nikitin [Nikit05] has successfully reported the influence of adhesion energy on delamination phenomenon through “buckle” formation (linear detachment of film from substrate). In case of Nb film on sapphire, the adhesion energy is very large and no buckling was observed even with Nb thickness of 1.95 μm , while on polycarbonate (PC) the buckling was always present when the c_H exceeds the solubility limit. This study, using the combination of V and sapphire, is in accordance with the findings by Nikitin. Moreover, the buckled region is under less compressive stress and H atoms tend to diffuse to this relaxed region (Gorsky effect). This is known to discontinuously lower the plateau pressure [Wagn08]. In this study, any EMF drop in the plateau region was not observed. Thus, the observed AE behavior at $c_H = 0.10$ H/V can reasonably be ascribed to misfit dislocation formation.

The AE technique is a non-quantitative method to investigate the mechanical response. But, according to the results obtained, one can extract a notable behavior of the thickest films (V-Fe5at% 400 nm and [Fe 20 nm / V 42 nm] x 2). It shows a continuous increase of AE signal, increasing with the sample thickness as shown in Fig. 5.3.3 and Fig. 5.3.6. Vice versa, the thinner films show distinct change of the AE slope as if elastic energy release in the film “bursts” at certain hydrogen concentrations i.e. at certain stress states (Fig. 5.3.1, Fig. 5.3.2, Fig. 5.3.4, Fig. 5.3.5). This trend, again, implies an analogy to the Hall-Petch relationship [Haas78+], which qualitatively explains the results of stress measurements on VFe single-layered films. The onset of the relaxation (presumably the first motion of the pre-existing dislocations) in the elastic regime tends to shift from large σ to small σ as the thickness increases (see e.g. Table 5.3). For the films with thicknesses above 100 nm this small relaxation disappears and the AE increases constantly, implying that the dislocation motion in thicker films ($l > 100$ nm) happens one after the other, but not all at the same time.

Additionally, one should consider the possibility for dislocation movement at multiple slip systems. In bcc systems, Schmidt’s law often is not valid [Barrett73]. The probability of multiple slip is expected to increase with the domain number in the film. If only one slip system in the film is activated, the total response of the stress relaxation becomes more visible in the stress measurement. But, the films deposited at room temperature commonly showed multiple domain structure. To conclude, occurrence multiple slip would be of minor importance.

Conclusively, the applied AE technique was found to be more sensitive than the stress measurement to detect initial dislocation operation, when limited to the film thickness of > 100 nm.

6.3 At $c_H \sim 0.1$ H/V

At around $c_H \sim 0.1$ H/V, strong relaxation of film stress was observed. The EMF curves also showed deviation from the Sieverts' type behavior (see Fig.5.1.4 - Fig. 5.1.9). These behaviors are generally interpreted as the onset of hydride precipitation [Lauda99], which is accompanied with misfit dislocation emission due to coherency stress between the hydride and the matrix [Schob73, Make80]. Certainly, the AE signal showed a remarkable increase at around 0.1 H/V, too (Fig. 5.3.1 and Fig. 5.3.2).

However, the XRD scans did not reveal clear development of hydride peak until $c_H = 0.4$ H/V (Fig. 5.2.1 and Fig. 5.2.2). Instead, the slope of the relative change of $d(110)$ showed a slight deviation from its linearity at above $c_H = 0.15$ H/V (Fig. 5.2.3). This is possibly explained by that, a small or coherent precipitate cannot be explicitly monitored by XRD [Micha95].

Therefore, in case of VFe-thin film used in this study, any deviation from linear elastic behavior i.e. mechanical relaxation does not immediately account for incoherent hydride precipitation. Recently, through *in-situ* XRD measurement on Pd/sapphire, Pundt and Wagner have suggested a coherent Pd-hydride phase which is coherent with the matrix and incoherent to sapphire substrate [PW10]. Similar interpretation might be valid also for this film according to the results given here, though it calls further investigation in the future.

6.4 At 0.1 H/V $< c_H < 0.3 \sim 0.4$ H/V - Hydride formation in V-Fe thin films

As described above, hydride formation in the 100-nm thick epitaxial V-Fe film has been monitored by *in-situ* XRD, and was observed at above $c_H = 0.40$ H/V (Fig. 5.2.2). By this, it is also suggested that films thicker than 100 nm went through the formation of incoherent hydride phase when H was fully loaded through the plateau region. This is supported by the result of the H-unloading EMF-curve of a 200 nm film showing large stress hysteresis (Fig. 5.1.12 (a)). When c_H in 100-nm thick films reaches $0.36 \sim 0.42$ H/V, both, AE and EMF, as well as the compressive stress increases further. There are two possibilities to interpret the increase of the AE signal at this stage. One possibility is buckle formation. Another pos-

sibility is due to further precipitation and/or growth of hydride phase and resulting dislocation emission [Make80], which accordingly relaxes compressive biaxial stress in thin films [Lauda98]. The plateau region in the EMF curves of the films is flattened by this relaxation, which is assigned as film delamination [Wagn08]. The AE measurement of 100 nm-thick film showed that the EMF curve starts to increase at the concentration of 0.4(3) H/V, while AE signal increased already at 0.36 H/V (Fig. 5.3.1). Thus, the beginning of the AE signal-increase at 0.36 H/V is attributed to acoustic emission by delamination of the film. Commonly, the buckling also was visible at above this concentration for the films thicker than 100 nm, one cannot explicitly distinguish the influence from these two factors on AE at concentrations higher than 0.4 H/V.

The mechanical irreversibility was actually observed by comparing the unloading EMF-curve with the loading EMF-curve of a 200-nm thick film (Fig. 5.1.12 (a)): Both curves differ strongly opening a hysteresis loop. Contrary to this, the unloading curve of a 20-nm thick film reversibly traced the H-loading curve almost identically (compare Fig. 5.1.12 (b)), and the in-plane stress after unloading was still compressive as in the initial state (Fig. 5.1.12 (b)). No hysteresis loop is detected for this case. This difference may call to consider the formation of a coherent phase and a lowering of the critical temperature.

Nörthemann *et al.* [Nörth08] have recently given experimental proofs on the existence of a coherent and, for larger hydrides, semi-coherent hydride phase in epitaxial Nb (110) thin films grown on Al₂O₃ (11-20) substrate. They concluded that the semi-coherent hydride phase should possess cylindrical shape. By considering the formation energy of a dislocation loop in these films with various thicknesses, it was suggested that the creation of dislocation loops is not possible when the thickness of Nb is reduced to less than 26 nm. There, semi-coherent or incoherent hydride cylinder cannot be formed. Their experimental results suggest, however, a significant hysteresis at the plateau region because large strain energy in the films remain almost unreleased and the thermodynamics of the open coherent system operates [Pundt10, Schw06]. This was not observed for the V-Fe films, regarded in this work, even for a film thickness of 20 nm.

Concerning the reduction of the critical temperature T_c , that temperature where the miscibility gap vanishes, p - c - T curves taken at different temperatures are necessary to discuss. It has been generally suggested for thin films of Pd-H [Weiss99, Feens83], Nb-H [Song96] and Fe/V-H systems [Olsson01], that the T_c is considerably lowered (~ 100 K) as the film thickness decreases to several tens of nm. This can be explained by increased repulsive H-H interaction [Gries99, Olsson01]. This consideration is quali-

tatively true when the site occupation of H is random and the H-H interaction is isotropic. For the bulk V-H system, the T_c of $\text{VH}_{0.5}$ is at 423 K (150 °C). Olsson *et al.* [Olsson01] have reported for Fe/V (001) superlattices that the transition between the lattice gas to the anisotropic liquid ($c_H = 0.35$ H/V) shows no hysteresis and that T_c reduces to 316 K (43 °C). This temperature is close to the experimental condition in this study, 294 K. This model assumes lattice coherency and does not include the formation of dislocations.

Thus, in order to explain the lack of a hysteresis for 20-nm thick VFe films, the repulsive H-H interaction of this V-Fe film should be larger than those of Fe/V films by Olsson *et al.*, thereby reducing the critical temperature T_c below 294 K. Then, the film would remain in a single phase region and a hysteresis would not be expected anymore.

This assumption of T_c lowering is, however, not consistent with the results of the stress measurements shown in Chap. 5.1.2 (Fig. 5.1.8 and Fig. 5.1.9) because the H-loading stress curve shows relaxation (deviation from linearity), which is usually interpreted as hydride formation and thus dislocation emission. This might be due to equilibrium pressure increase by Fe content. If any other film-stress relaxation process is addressed, for such thin films, the T_c lowering and the missing hysteresis loop observed in Fig. 5.1.12 (b) can be understood. The microstructural origin of this stress relaxation is, however, yet known. Assuming that the in-plane stress is released below the hydrided volume and the vertical stress to the matrix is not relaxed, there is no concrete description given yet whether this situation causes a lowering of the critical temperature, or not.

Therefore, to answer this question, further EMF measurements taken at different temperatures need to be carried out in a future work. Additionally, it will be of particular interest to investigate such thin V films especially with thicknesses below 50 nm by acoustic emission (AE). For this purpose, an improvement of the sensitivity of the AE set-up is needed and should be of major future interest.

6.5 Fe/V multi-layered films

In case of Fe/V multi-layered films, further boundary condition is added due to adjacent Fe layers. Both electronic and elastic contributions of these Fe layers have a marked impact on the H-related behavior of V or vice versa. For example, the magnetic coupling between 2 Fe layers can be altered from ferromagnetic to antiferromagnetic by H insertion into the V layer [Hjörv97++]. Andersson *et al.* [Ander97+] have reported that the V

lattice between Fe layers is compressed in in-plane, and that the O_z site occupation is initiated. Thereby, within the range of $c_H = 0 - 0.1$ H/V, attractive H-H interaction in the in-plane, and repulsive one in out-of-plane directions are suggested, respectively. Such an anisotropic interaction is equivalent to induce elastic dipole formation [Olsson01] and, thus causes deviation from the linear elastic model.

The experimental results of stress measurements on single layered films were in agreement with the Hall-Petch relation (Fig. 5.1.10). The initial stress state was found to have an impact on the H-induced stress, too (Fig. 5.1.11). Concerning the H-induced stress at 0.4 H/V, three of four Fe/V multi-layered film samples also show a dependence similar to the single-layered films (Fig. 5.1.17). An exception to this is the thinnest one, the Fe 5.95 nm / V 6.04 nm film. Surprisingly, this film showed tensile stress in the course of H loading (Fig. 5.1.17). This is contrary to the theoretical prediction and can also not be attributed to the SAV, only.

There are several considerations needed to interpret the observed tensile stress. The first one is the possibility of film detachment from the substrate right at the beginning of the measurement. But, since no film detachment was observed until 0.3 H/V, this possibility can be immediately dropped. Second, the H trapping effect at defects should be addressed as it is discussed in Chap. 6.1. This effect is usually significant at low concentrations, because the occupation of H at such energetically favorable sites as defects is terminated as soon as these sites are fully occupied. The maximum hydrogen concentration addressed by this effect, is in the range of 10^{-4} H/V. Therefore, only the tensile stress at the very beginning of the stress curve may be explained by this trapping idea. That is, the tensile stress in the whole concentration range is not consistent with this consideration.

The third possibility that needs to be considered is the idea of preferential site occupation, as suggested by Hjörvarsson *et al.* (see e.g. Ref [Olsson03] or Chapter 2.1.5). The in-plane compressive stress in thin films that builds up upon H-loading as predicted by linear elasticity theory (see Chapter 2.2) is expected only when the site occupation of H is assumed to be random. But, if the H atoms are preferentially distributed at specific sites, this assumption fails. Hjörvarsson *et al.* found preferential O_z site occupation in Fe/V superlattice, and he also found that the host V lattice tries to expand in z direction i.e. perpendicular to the film plane of (100)-oriented film more than that expected by linear elasticity theory. At the same time, the lattice in in-plane direction tends to shrink rather to expand. It is therefore expected that the film, at this state, shows tensile stress. Since the films in this study are (110)-oriented, a direct correlation

with this idea is not possible. But, similar interpretation is possible as discussed below.

In an unstrained lattice e.g. a well-annealed massive V single crystal, H atoms usually occupy T-sites at low c_H below the solubility limit. Above the solubility limit, further H loading induces then O-site occupation as a result of H induced lattice expansion. V_2H phase has this O-site occupation, as shown in Chapter 2.1.5.

In Fig. 6.4, the difference of the lattice orientation and the corresponding O-site configuration between (100)- and (110)-oriented lattices is schematically illustrated. Concerning an (100) film, if the film is initially in tetragonal distortion as in the case of the Fe/V superlattice of Hjörvarsson, the O_z -sites are energetically preferential for H atoms, since O_x - and O_y -sites are contracted (see Fig. 6.4 (a)). This initially expanded lattice can induce preferential O_z occupation even at c_H below the H solubility limit and, thus giant lattice expansion in the film out-of-plane direction should be observed for V-films, as reported by Andersson *et al.* [Ander97].

For the films with (110) out-of-plane orientation, the situation is different because the $\langle 001 \rangle$ direction of the lattice is not parallel to the out-of-plane direction of the film. According to the results of XRD (Fig. 5.2.7), the initial lattice distortion of Fe/V films prepared in this study could be close to a rhombohedral distortion and can be drawn as shown in Fig. 6.4 (b). This drawing is rather exaggerated and simplified to emphasize the loss of cubic symmetry. A rhombohedral phase of bulk vanadium metal is established only under ultra high pressure of around ~ 0.15 TPa, which was expected by theoretical calculation [Landa06] and recently also found by experiment [Ding07] (for details, see e.g Ref. [Lee08]). The distortion of this phase is reported to be along the $\langle 111 \rangle$ axis and, thus, it is not identical with that illustrated in the figure. Nevertheless, it is obviously seen that not only O_z , but also O_y occupation is possible, if the distortion shown in Fig. 6.4 (b) is assumed. Additionally, the axis strain field of each O-site is not aligned with that of the film. Due to these geometrical differences between (100) and (110), it is inferred that the H-induced out-of-plane lattice expansion of a (110)-oriented film can be smaller than that of a (100)-oriented film. This is in good agreement with results reported for Mo/V superlattices [Hjörv97]. It is suggested here that the same situation should be true also for the Fe/V system, which shows attractive H-H interaction in in-plane direction.

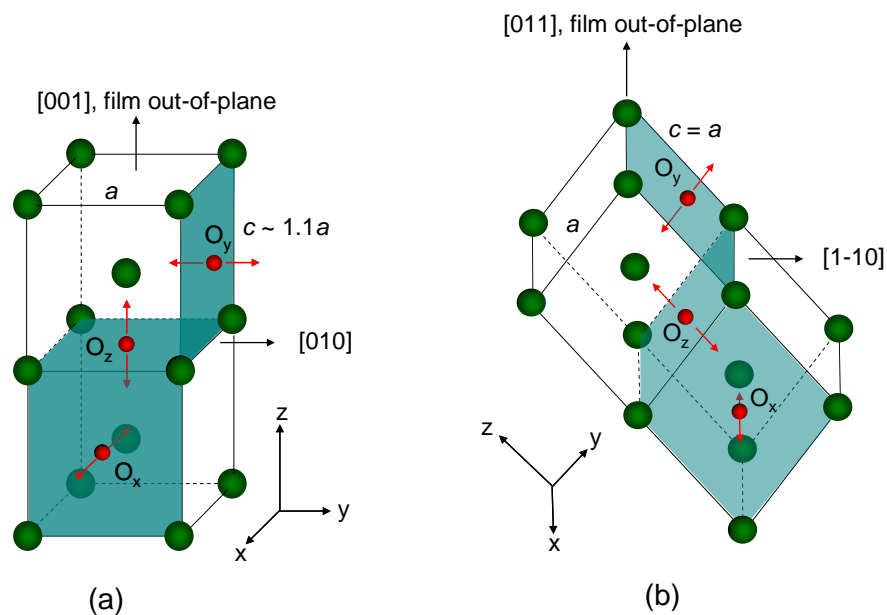


Fig. 6.4 Schematic illustration of O sites in (a) a tetragonally distorted V (100)-oriented film and in (b) a rhombohedrally distorted V (110)-oriented film. Note the difference of the strain field contributions of O sites against the film out-of-plane, as indicated by red arrows.

In order to explain the observed in-plane tensile stress, a similar attractive H-H interaction found in Fe/V (100) superlattices should be present also for (110)-oriented films with an out-of-plane strained lattice. In this study, the tensile stress upon hydrogen loading was found only in case of the thinnest Fe 5.95 nm / V 6.04 nm (110) layered stack. Other thicker films showed compressive stress. But the shape of the curve loses its compressive trend with decreasing the double layer thickness (Fig. 5.1.13 - Fig. 5.1.15), regardless how the initial out-of-plane expansion of V layer is large. These results indirectly support the interpretation concerning the dominant influence of thickness reduction on the observed tensile stress development.

Andersson *et al.* [Ander02] have also investigated hydrogen absorption behavior of thick single layered V film with thicknesses of 50 nm and 100 nm. Contrary to the case of Fe/V, the O_z site occupation is not suggested, possibly due to deterioration of lattice coherency and relaxation of biaxial stress by misfit dislocation implementation. Therefore, the impact of thickness reduction and biaxial stress cannot be distinguished.

One should note that, the thinnest Fe/V was deposited directly on sapphire substrate, while the others were on 21.4-nm thick V buffer layer. It has been shown that 20-nm thick single VFe-film indicates highly compressive biaxial stress upon H-loading (Fig. 5.1.8). The 10-nm thick VFe single layered film showed significant high compressive stress, too (Fig.

5.1.9). Therefore, the expected tensile stress development might be cancelled out due to the presence of the buffer layer.

To conclude, the thinnest multi-layered stack showed the H-induced tensile stress development which is probably related attractive in-plane H-H interaction. As suggested by Alefeld [Alefeld72], the H-H interaction is linked to elastic dipole interaction. Thus, the mechanical boundary condition such as in-plane strained situation of V lattice between Fe layers would play a role on the H-H interaction in the V layer. The stress measurement of Fe 5.95 nm / V 6.04 nm (110) multi-layered film seems to follow this prediction, also implying excess lattice expansion from the linear elastic prediction. Unfortunately, *in-situ* XRD data of this film was not available in this thesis. Therefore, further *in-situ* XRD as well as stress investigations on the same system without V buffer layer would be rather important for future studies.

6.6 Investigation of local chemistry by APT

In Chap. 5.4.1 the influence of the APT measurement temperature on the detected chemistry was studied, yielding realistic concentrations for temperatures below 45 K. Further, it was shown that (011) pole regions apparently showed high c_D , which was caused by low relative density of V atoms, due to an aberration effect. The results discussed below are, therefore, obtained at low temperatures and mostly not at pole regions to reasonably evaluate the D-distribution.

6.6.1 Impact of oxygen adsorbates on the local D distribution in V-Fe single-layer and Fe/V multi-layered films

In V-Fe films deposited on W substrates, a D-enrichment was commonly observed (Fig. 5.4.13 - Fig.5.4.15).

The dead-layer effect as suggested previously in Refs. [Hjörv91, Ander97+] resulting from electron transfer at the interfaces of Fe/V and Mo/V system, cannot explain the observed D-enrichment at this V/W interface. The Fermi-level of electrons in W is much higher than in V [Watson78] (But, isomer shift of V in ^{182}W in Mössbauer measurements did not reveal clear difference [Watson77]), thereby resulting in an electron transfer towards the V layer. This electron transfer should decrease of the local solubility of hydrogen at the V-side of the interface, which is

opposite to the experimental finding. Recently, Meded *et al.* [Mede05] have shown that elastic contribution from the adjacent Fe layers would affect the solubility of hydrogen in the V layer, i.e. larger shear modulus of Fe hinders H absorption in the V layer nearby. But, the shear modulus of W ($G = E/2(1+\nu) = G = 411/2(1+0.28) = 160.5$ GPa [Hear84]) is much larger than that of V ($G = 46.7$ GPa [Bolef61]). Thus, the elastic contribution cannot explain either.

Considering the impact of mechanical stress occurring at the interface of V and W, a (110)-plane matching of V-Fe8at% (with $a = 0.3006$ nm) onto W (with $a = 0.3165$ nm) results in 5.28% lattice mismatch. According to this, the V lattice is in a tensile strain state. Regarding the high stress sensitivity of the hydrogen site occupation in V [Koike81, Sugi84], preferential formation of a D concentrated region caused by stress-induced site change at the V/W interface might explain the observed discontinuous D distribution. But, according to the model of Matthews and Blakeslee [Matth74], formulated as in Eq. (6.3), the corresponding critical thickness for the implementation of misfit dislocations is 0.7 nm, for an ideal film. The result of calculation is shown in Fig. 6.5.

$$h_c = \frac{b}{2\pi f} \left[\frac{(1-\nu \cos^2 \alpha)}{(1+\nu) \cos^2 \lambda} \right] \left(\ln \frac{h_c}{b} + 1 \right) \quad (6.3)$$

For the calculation of critical thickness, Burger's vector b (typically $a/2 <111>$ for a bcc structure), Poisson's ratio $\nu = 0.37$, angle between the dislocation line and the Burger's vector $\alpha = 35.7^\circ$, angle between the slip direction and the direction which is perpendicular to the line of intersection of the slip plane and the interface $\lambda = 35.7^\circ$ and lattice mismatch f between the film and the substrate, are applied.

Both analyzed films have thicknesses above the critical value and, thus the presence of misfit dislocations is very likely. Since the V lattice

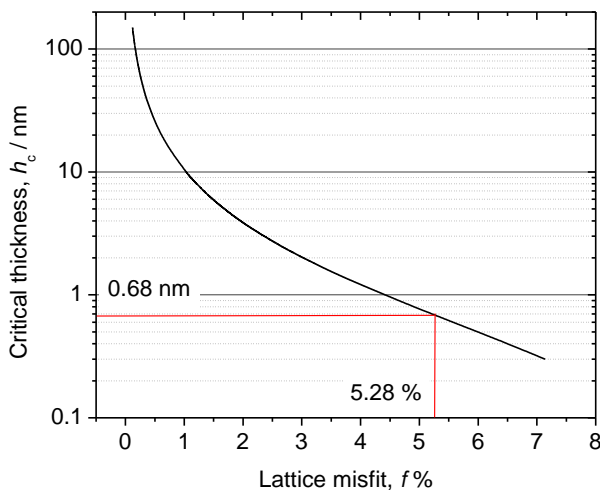


Fig. 6.5 Calculated critical thickness h_c for implementation of misfit dislocation in V as a function of lattice misfit f by Eq. (6.3). Parameters are described in the text.

constant is smaller than the W one, extra half planes are implemented in the V lattice. If the dislocation lines were located right at the interface (to accommodate maximum stress) compressive stress fields are expected above the V/W interface. D does not favor such regions. If the dislocation lines were located above the interface, D could be trapped there. This could, then, explain a deuterium segregation. But, the deuterium peak is located further away from the interface for the 2-nm thick V-Fe5at% film. There, the c_D maximum is about 0.4 nm away from V/W interface. Taking a trapping region of 1-2 nm below the dislocation line into account [Maxel01] this would result in a further displacement of the dislocation line from the V/W interface.

However, the W substrate used in this study was exposed to air prior to deposition. The result of APT analysis revealed some O atoms adsorbed on the W substrate. On top of this O-adsorbed layer, in the V-Fe films, the D-enrichment was observed (Fig. 5.4.13 - Fig.5.4.15). Therefore, it is likely that at certain positions at the V/W interface, nonstoichiometric V-oxide is formed as islands (see Fig. 5.4.18). This precipitate does not absorb hydrogen, but due to its larger lattice constant than that of the V-Fe layer, misfit dislocations could be present above these precipitates. In the tensile strain field of these dislocations, deuterium could accumulate resulting in the observed c_D enrichments, simply also explaining the position of high c_D region for both films. This situation is schematically drawn in Fig. 6.6.

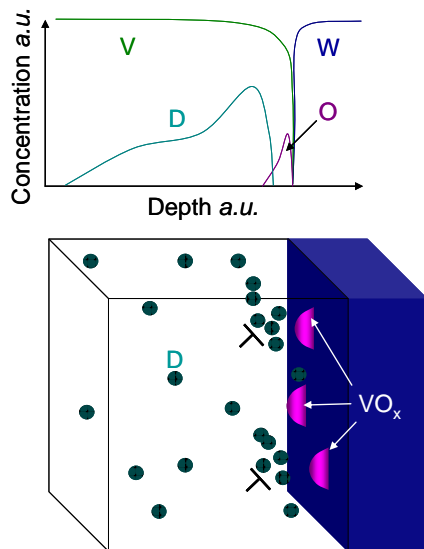


Fig. 6.6 A schematic drawing of VO_x islands formed on W substrate and misfit dislocations implemented above. D atoms are accumulated under the dislocations, resulting in high D concentration.

Additionally, the structural vacancies at the metal/metal-oxide interface induce irreversible hydrogen trapping [Kirch03]. The above mentioned microstructural aspects can be considered for the D enrichment at V/W interface. One should also keep in mind a possible influence of mechanical stress induced by high electric field, which can reach as high as

several GPa [Mill96], on the D distribution. The applied voltage, thus the surface stress changes with increasing the tip radius during analysis. In this study, the tip radius of the sample demonstrated in Fig. 5.4.13 and Fig.5.4.15 was estimated to be 41 nm and 31 nm, respectively. Although nearly common feature for both of these samples have been observed, more detailed study focusing on such essential aspect should be one of the future subjects concerning analysis of deuterium in materials.

To summarize, single adsorbate atoms of oxygen can have a tremendous effect on the local deuterium distribution.

6.6.2 D distribution in V-layer affected by the presence of the Fe-interface

The investigation of the local chemistry of D at the Fe/V interface some interesting features have been found as summarized in chapter 5. At low p_{D_2} (0.2 and 0.5 Pa), as demonstrated in Fig. 5.4.29, lack of D at above the Fe/V intermixing layer which indicates the “dead-layer” effect (refer Chap. 1). From this measurement, the thickness of the “dead-layer” was estimated to be of 0.45 nm according to Hjörvarsson [Hjörv89]. The results of APT analyses on different interfaces showed the dead-layer thickness ranging about 0.4 ~ 1 nm (Fig. 5.4.29), which are in agreement with Hjörvarssons results.

In the Fe/V intermixing layer at low p_{D_2} (0.2 and 0.5 Pa) (Fig. 5.4.29), no D-atoms were observed. This indicates the impact of local alloying on the hydrogen solubility when the number of energetically favorable sites is reduced. In FeV alloy systems the H-solubility is known to decrease [Egu74].

At high pressures $p_{D_2} = 2 - 1000$ Pa ($= c_D > 0.1$ D/Me), however, this “dead-layer” region disappeared. This is exemplarily shown in Fig. 5.4.30. This is contrary to the actual picture of the “dead-layer” effect which is reported to exist independent of c_D . However, it is reported that the “dead-layer” thickness slightly decreases from 0.45 nm approximately to 0.28 nm as the c_D increases [Hjörv93]. In our APT results this thickness reduction was not confirmed.

The origin of this dead-layer effect was, in their early investigations, explained by charge transfer. But, recently, Meded *et al.* [Mede05] have concluded that the electronic effect is not responsible for the dead-layer. Instead, the H-induced volume expansion and associated screening length to be of 2 -3 ML was suggested via computer simulation. Simply, the dead-layer appears because Fe and Mo have higher shear moduli than

that of V

Even more interestingly, there was a strong influence of stacking sequence on D distribution was inferred at high $c_D > 0.1$ D/Me (Fig. 5.4.25 - Fig. 5.4.27, and Fig. 5.4.31). Fig. 5.4.31 showed asymmetric D profiles at the Fe/V and at the V/Fe interface (i.e. higher c_D at the V/Fe interface), also at high p_{D_2} (2 - 1000 Pa). A monotonic decrease of c_D with increasing c_{Fe} was generally observed for both interfaces (compare Fig. 5.4.31), following the lattice parameter change of the FeV alloy, as demonstrated in Fig. 2.7. This results in narrowing of the plateau region. Corresponding shrinkage of lattice size due to alloying of V with Fe (Fig. 2.7) would support this result. But, the V/Fe interface tends to absorb more D than in the Fe/V interface (Fig. 5.4.31). This difference might be attributed to a different strain state at the Fe/V and V/Fe interfaces. We note that the mechanical stress may also influence the critical behavior and thus modifies the phase diagram.

7. Summary and outlook

The intension of this thesis is to study the local hydrogen distribution in thin films with focus on the impact of interfaces and the related defects. This topic is addressed by studying the hydrogen (H)-related mechanical response of $V_{1-x}Fe_x$ ($x = 0.02 \sim 0.08$) single layered (SL) films and Fe/V multi-layered (ML) films in combination with different substrates. The H(D)-distribution was determined using different experimental maneuvers. In particular, *in-situ* acoustic emission (AE) and atom probe tomography (APT) analysis have been successfully developed and applied for such purposes. In combination with *in-situ* stress and *in-situ* XRD measurements, these methods supply important physical insights on metallic thin film-hydrogen systems, present at different mean hydrogen concentrations.

Generally, H-insertion in the lattice of metallic thin films induces large in-plane compressive stress as predicted by linear elasticity theory. Contrary to this, some of the epitaxially grown $V_{0.92}Fe_{0.08}$ single layered (SL) films on sapphire substrates, which were sputtered at high temperatures, showed biaxial tensile stress in the beginning of stress-hydrogen concentration curve. This phenomenon is explained by trapping of H at vacancies differentiating between those induced by hydrogen (superabundant vacancies, SAV) and those at thermal equilibrium (thermal vacancies). The effect was judged to occur by trapping at SAVs. The impact of H-trapping at misfit dislocations at film/substrate interface cannot be avoided either. But, estimated dislocation density by stress measurement was suggested to be lower for the films deposited at higher temperatures.

After saturation of H-trapping at vacancies, the stress curve finally shows the expected linear increase of compressive stress. In most cases, linear increase of the slope following the linear elastic model has been established. But, this linearity is intermittently broken, especially for thinner films than 200-nm thick. This behavior is attributed to rearrangement of pre-existing dislocations in the films under high compressive biaxial stress and by the presence of hydrogen. Especially, AE results of 100-nm thick SL film support this interpretation.

Above the Sieverts' solubility limit, all of the SL films showed considerable departure from the trend of linear compressive stress development. For the films with a good adhesion on the substrates, this is regarded as the onset of hydride formation. *In-situ* XRD measurements did not trace this hydride formation, while AE measurements detected a remarkable increase of the AE-signal at the very same concentration, confirming dislocation nucleation. This could be interpreted by the formation of coherent

hydride phase with matrix, but incoherent with respect to the substrate due to large misfit to the substrate. Such a behavior has recently also been found for Pd-thin films.

Thereafter, an incoherent hydride phase develops, at $c_H = 0.4$ H/V detectable by *in-situ* XRD, which is accompanied often by film delamination. At this stage, a strong AE signal due to film delamination could not be avoided.

For Fe/V multi-layered (ML) films, thicker layered-stack grown on V 21 nm buffer layer showed similar stress development and AE characters as those of SL films. However, the thinnest one grown directly on sapphire had huge tensile stress component (+2 ~ +3 GPa) in the whole concentration range investigated. In this case, only preferential O_z - or O_y - site occupation of H can explain the experimental result. Clearly, the V buffer layer shows compressive stress component upon H uptake. In order to address this preferential site occupation effect more clearly, the ML films should be grown on H-inactive buffer layer or directly on the sapphire substrates, as suggested for future studies. Also, the improvement of AE sensitivity is necessary to investigate films thinner than 100 nm.

The determination of the local hydrogen (using its isotope deuterium D) distribution was addressed by exerting the highly sensitive atom probe tomography. But, reliable analysis of D in metals has been a hard task since long time, because of hydrogen embrittlement raising tip rupture and loss of the light H or D atoms during the destructive measurement. In this thesis it was shown that (i) avoiding any air exposure of D containing films and (ii) avoiding surface segregation of D are the key factors for a correct analysis. Thus, a new experimental set up and new procedures have been designed. For VFe-D and Fe/V-D systems, reliable analysis could be obtained at analysis temperatures below 30 K, at which temperature the possibility of tip rupture is also reduced when compared to that at 20 K. All of the analysis results given below this temperature agreed well with expected D concentration. Equipped with this knowledge the local atomic arrangement in films as influenced by interfaces could be successfully addressed.

A large impact of O interface adsorbates on the local D-distribution was revealed. In this study, a W substrate was exposed to air prior to the deposition, resulting in surface adsorbates. After deposition of a V layer, strong D-segregations are found at the interface. These segregations could be interpreted by the formation of VO_x present at the W substrate and misfit dislocations are created in the V layer. The D atoms are trapped below these dislocations and, thus high local D concentration results. ML samples grown on W substrate showed similarly high D concentration

near the W substrate, confirming this effect well.

At interfaces of Fe and V layer, interface mixing (alloying) of about 1.4 nm thickness was detected, even by deposition at room temperature. This is in accordance with the large solubility of Fe in V and vice versa. This local concentration affects the D-distribution at the interface. But, a more far-reaching impact of Fe layers on the D-solubility in V-layers was observed. The measurements confirm the existence of dead-layers, where the D is depleted at the adjacent Fe layers. This dead-layer was not observed by local measurements before. The thickness of this dead-layer was found to be of 0.4 - 1 nm. This layer, however, disappears as the concentration increases above $c_H = 0.1$ D/V. Moreover, at above $c_H = 0.1$ D/V, the D distribution in the Fe/V/Fe stack was found to be not symmetric anymore. The V/Fe interface showed a higher D-concentration compared to the Fe/V interface. This is interpreted to result from local mechanical stress, which differs for a Fe film growing on V compared to a V film growing on Fe, as suggested by SRIM-simulations. An impact of the high voltage applied during the analysis cannot be excluded. Furthermore, the influence of mechanical stress on the local D distribution is still unclear and, thus is one of important future topics in the APT investigation.

To summarize, hydrogen-absorption in thin films results in different kinds of defects (namely SAV and dislocations) that modify the local hydrogen distribution and mechanical stress. Impurities at interfaces like oxides lead to local hydrogen enrichments. For V films the local stress development is also influenced by a change of the O-site occupation that, for very thin ML-films, results even in tensile stress up to high concentrations.

Appendix

Characterization of hydrogen distribution in Fe/V multi-layered films by using Glow Discharge Optical Emission Spectroscopy (GDOES)

H-segregation behavior at room temperature

In this chapter, the observed surface segregation of hydrogen observed in the atom probe tomography (APT) analysis is confirmed by using different technique, namely “sputter-assisted” analysis called Glow Discharge Optical Emission Spectroscopy (GDOES), which is different in phenomenology from that of the APT.

GDOES analysis [Payle97] was carried out in cooperation with Mr. Marcus Wilke and Prof. Dr. Peter Schaaf in Technische Universität Ilmenau, as an alternative method for hydrogen depth-profiling. This spectroscopy is in principle composed of a Grimm-type glow discharge source [Grimm68] and a spectrometer designed by Rowland [Rowl82]. Based on its multi-element capability, GDOES has become a widely used technique for depth profile analysis of coatings and thin films with a depth resolution of ~ 10 nm. Yet, this technique has not been applied to analyze hydrogen in thin films.

As it is schematically shown in Fig. A1, cathodic sputtering is used for

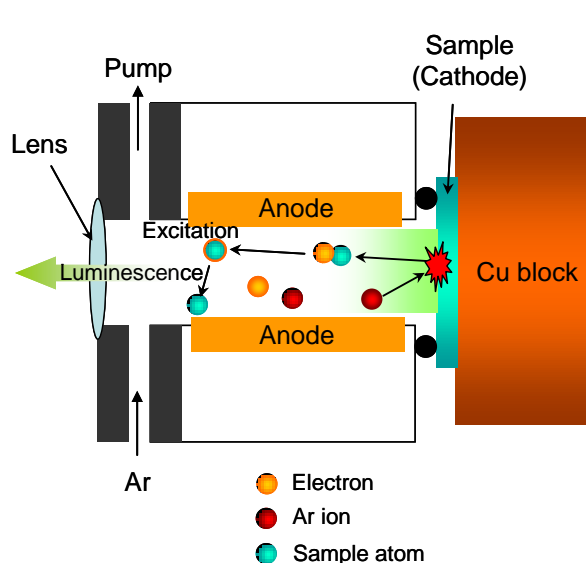


Fig. A1 A schematic illustration of GDOES at analysis chamber. The sample as cathode is sputtered by Ar ion. Sputtered atom then impacts with electron, thereby the atom is excited. Corresponding luminescence is then recorded by a spectrometer placed after the lens shown in the figure.

this analysis, to remove material layer by layer from the sample surface. The atoms removed migrate into the plasma, where they are excited through collisions with electrons. Through the lens, the characteristic spectrum emitted by each excited atom is monitored by the spectrometer. The total analysis time is equal to the sputtering time of the sample, which is typically within several minutes for thin films. The back side of the film is cooled by a Cu block, which is water cooled only. Hence, the heating of the sample by the discharge cannot be completely avoided. This is expected to cause strong surface segregation of H and, thus to influence the depth profile of H.

The Fe/V multi-layered film with [Fe 20 nm / V 42 nm] stacking sequence was prepared ahead in the same manner as described in Chap. 3.1. The surface was thus capped with 20-nm thick Pd layer. The substrate geometry for this sample was 7 mm x 30 mm x 0.2 mm. Before the analysis, hydrogen was loaded electrochemically up to $c_H = 0.05$ H/V (Chap. 3.3). After removing the residual electrolyte on the film sample with water, the film surface was intentionally contaminated by immersing the sample into Xylene (C_8H_{10}) to avoid any hydrogen desorption from the sample before the analysis was carried out.

The GDOES system used in this study was GDA 750 spectrometer (Spectrums Analytik GmbH) equipped with a Grimm-type glow discharge source of 2.5 mm in diameter and a Paschen-Runge type polychromator. The depth profiles were measured in DC excitation mode with optimized parameters 1200 V, 13 mA (constant voltage, constant current mode). After reaching vacuum of ~ 1 Pa, the discharge was initiated.

Before the analysis, the intensity of H was calibrated by using a reference sample of TiH.

In Fig. A2, the results of 3 subsequent analyses (H1, H2, H3) on 3 different analysis points (2.5 mm ϕ) along the longitudinal direction of the sample are shown. These measurements were carried out 60 s (H1), 240 s (H2) and 320 s (H3) after the hydrogen loading.

In the analysis H1, the hydrogen depth profile traces that of vanadium layer to certain extent. The 1st V layer, however, showed extremely sloped profile towards the surface. Moreover, considerable amount of H ($c_H = 0.005$ H/Me) is observed even in the Fe layers. The observed hydrogen concentration in the 2nd V layer was $c_H = 0.010$ H/V (Me) for the profile H1, which is certainly higher than that in the Fe layers. But, it amounts to only 20 % of the expected H concentration, $c_H = 0.05$ H/V. The 2nd Fe layer and the 3rd V layers show slightly higher c_H than those in the 1st Fe layer and in the 2nd V layers. It should be noted that the H-depth profile in the 2nd V layer and in the 3rd V layer shows “tail”, which is already ascribed as

a trace of H-segregation in the results of atom probe analysis (see Fig. 5.4.3 and Fig. 5.4.22).

Further, the next analysis results, H2 and H3, showed even lower c_H . This is globally observed in every V layers. It is thus reasonable to consider that the H atoms in the sample are lost against the time elapsed.

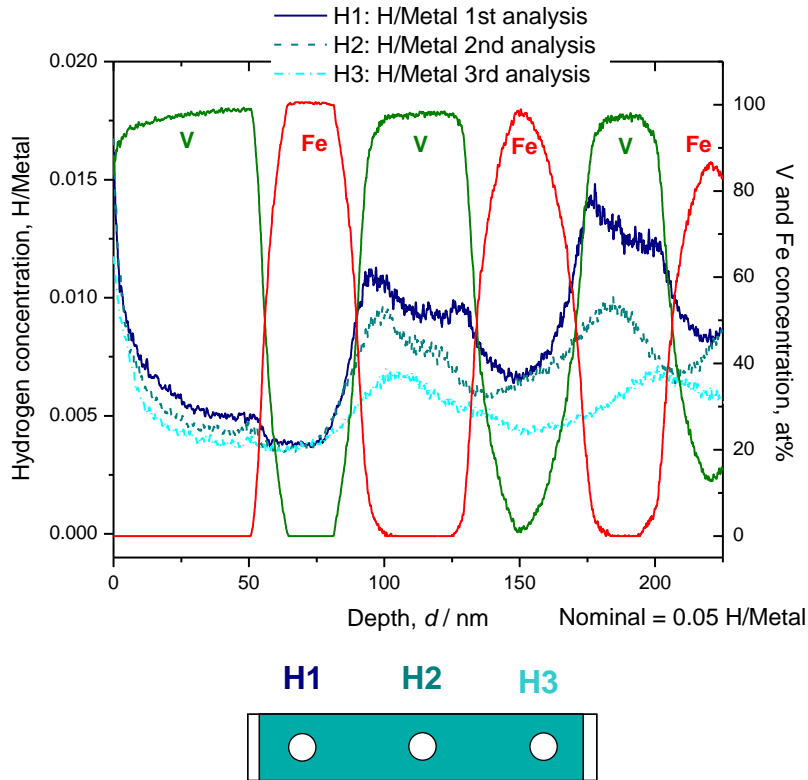


Fig. A2 GDOES results of H-loaded Fe 20 nm / V 42 nm multi-layered film, with nominal c_H of 0.05 H/V. Three measurements were carried out in the sequence after 60 s (H1), 240 s (H2) and 320 s (H3) after H-loading. These measured points on the sample are illustrated on the right hand side of the figure.

In the V layer, which is close to the surface (i.e. the 1st V layer), the difference of H concentration among the 3 measurements is small, when compared to those in the 2nd and in the 3rd V layer. This indirectly suggests that the H-loss behavior occurs mainly at the surface of the film, namely the Pd capping layer. Thus the deeper V layers conserve more H atoms than those layers near the surface. The Pd layer is practically not seen in the figure because of pre-sputtering just before the recording of analysis is initiated, which is only a technical problem.

It is also noticeable that the intermixing thickness of Fe and V increases as the depth increases. This is caused by sputter-induced intermixing and increased interface roughness, which is always present in a

sputter-assisted depth-profiling.

To conclude, the results obtained by GDOES confirm the experimental findings in the XRD study (Fig. 3.12) and atom probe tomography analysis (Fig. 5.4.3 and Fig. 5.4.22) concerning the following points.

- (i) Hydrogen can segregate towards the film surface unless “freezing” condition for H is established.
- (ii) In the course of such segregation, hydrogen can be lost by recombination and H₂O formation under the presence of Pd at the surface.
- (iii) To avoid this H-loss, O₂-free condition is absolutely necessary.

Bibliography

- [Alefeld72] G. Alefeld, *Ber. Bunsenges. Phys. Chem.* 76 (1976) 746.
- [Al-K03] Al-Kassab, T., H. Wollenberger, G. Schmitz, R. Kirchheim, *High resolution imaging and spectrometry of materials, Chap. Tomography by Atom Probe Field Ion Microscopy*, Springer Verlag, Berlin (2003).
- [Ander97] G. Andersson, B. Hjörvarsson, H. Zabel, *Phys. Rev. B* 55 (1997) 15905.
- [Ander97+] G. Andersson, B. Hjörvarsson, P. Isberg, *Phys. Rev. B* 55 (1997) 1774.
- [Ander02] G. Andersson, K. Aits, B. Hjörvarsson, *J. Alloys Comp.* 334 (2002) 14-19.
- [Artman76] D. Artman, J.F. Lynch, T.B. Flanagan, *J. Less-Common Met.* 45 (1976) 215–228.
- [Asano76] H. Asano, Y. Abe, M. Hirabayashi, *Acta Met.* 24 (1976) 95.
- [Atkins82] P.W. Atkins, M.J. Clugston, *Principles of physical chemistry*, Pitman Books (1982).
- [AVS] <http://www.avs.com>
- [Barn09] A. Barnoush, C. Bies, H. Vehoff, *J. Mater. Res.* 24 (2009) 1105-1113.
- [Barrett73] C.R. Barrett, W.D. Nix, A.S. Telelman, *The principles of engineering materials*, Prentice-Hall, Inc., Englewood Cliffs, New Jersey (1973).
- [Beck38] R. Becker, *Ann. Phys.* 32 (1938) 128.
- [Benni94] A. Benninghoven, *Angewandte Chemie International* 33 (1994) 1023-1043.
- [Birch90] J. Birch, Y. Yamamoto, L. Hultman, G. Radnoczi, J.-E. Sundgren, L.R. Wallenberg, *Vacuum* 41 (1990) 1231.

- [Blei87] H. Bleichert, H. Wenzl, Phys. Stat. Sol. B 144 (1987) 361.
- [Bolef61] D.I. Bolef, J. Appl. Phys. 32 (1961) 100.
- [Camb74] M. Cambini, R. Serneels, R. Gevers, Phys. Stat. Sol. (a) 21 (1974) K57.
- [Chris88] K. Christmann, Surf. Sci. Rep. 9 (1988) 1-163.
- [Chris89] K. Christmann, Mol. Phys 66 (1989) 1-50.
- [Cizek04] J. Čížek, I. Procházka, F. Bečvář, R. Kužel, M. Cieslar, G. Brauer, W. Anwand, R. Kirchheim, A. Pundt, Phys. Rev. B 69 (2004) 224106.
- [Cizek07] J. Čížek, I. Procházka, S. Danis, M. Cieslar, G. Brauer, W. Anwand, R. Kirchheim, A. Pundt. J. Alloys Comp. 446-447 (2007) 479-483.
- [Culli78] B.D. Cullity, Elements of X-ray diffraction 2nd ed., Addison-Wesley publishing company, (1978).
- [Danie84] R. Danielou, J. Fontenille, E. Ligeon, Y. Fukai, J. Appl. Phys. 55 (1984) 871.
- [Ding07] Y. Ding, R. Ahuja, J. Shu, P. Chow, W. Luo, and H.-K. Mao, Phys. Rev. Lett. 98 (2007) 085502.
- [DOE] US Department of Energy, USA, <http://www.energy.gov/>
- [Dornh02] M. Dornheim, Spannungen, Dehnungen und Lage der Phasengrenzen in dünnen Nb- und Y-Schichten bei Wasserstoff be- und entladung, Ph.D thesis, Universität Göttingen, (2002).
- [Dornh07] M. Dornheim, S. Doppiu, G. Barkhordarian, U. Boesenberg, T. Klassen, O. Gutfleisch, R. Bormann, Scr. Mat. 56 (2007) 841-846.
- [Egu74] T. Eguchi, S. Morozumi, J. Japan Inst. Metals 38. (1974) 1025-1030.
- [Feens83] R. Feenstra, J. Phys. F: Metal Physics 15 (1983) L13.

[Ferre96] P.J. Ferreira, Ian M. Robertson, H.K. Birnbaum, *Mat. Sci. Forum* 93 (1996) 207-209.

[FG76] E. Fromm, E. Gebhardt, *Gase und Kohlenstoff in Metallen*, Bd. 26 of *Reine und angewandte Metallkunde in Einzeldarstellungen*. Springer-Verlag, Berlin Heidelberg New York, (1976).

[Fries73] H. Frieske, E. Wicke, *Ber. Bunsenges. Phys. Chem* 77 (1973) 48.

[Fukai75] Y. Fukai, S. Kazama, *Scripta Met.* 9 (1975) 1073.

[Fukai01] Y. Fukai, Y. Shimizu, Y. Kurokawa, *J. Alloys. Comp* 329 (2001) 195-201.

[Fukai03⁺] Y. Fukai, *J. Alloys. Comp.* 356-357 (2003) 263–269.

[Fukai03⁺⁺] Y. Fukai, M. Mizutani, S. Yokota, M. Kanazawa, Y. Miura, Y. T. Watanabe, *J. Alloys. Comp.* 356-357 (2003) 270-273.

[Fukai05] Y. Fukai, *The Metal-Hydrogen System*, 2nd ed. Springer-Verlag, Berlin Heidelberg New York, (2005).

[Full92] E.E. Fullerton, I.K. Schuller, H. Vanderstraeten, Y. Bruynseraede, *Phys. Rev. B*, 45 (1992) 9292.

[Gemma09] R. Gemma, T. Al-Kassab, R. Kirchheim and A. Pundt, *Ultra-microscopy* 109 (2009) 631-636.

[Gray72] D.E. Gray, *American Institute of Physics Handbook*, McGraw-Hill Book Company, New York, (1972).

[Gries88] R. Griessen, T. Riesterer, *Hydrogen in Intermetallic Compounds I*, Bd. 63 of *Topics in Applied Physics.*, Ed. L. Schlapbach, Springer-Verlag, Berlin Heidelberg New York, (1988)

[Gries99] R. Griessen, *The Physics of Hydrogen in Metals*, Amsterdam, Vrije Universiteit (1999).

[Grimm68] W. Grimm, *Spectrochim. Acta. Part B* 23 (1968) 443.

[Haas78] P. Haasen, *Physical Metallurgy*, Cambridge University Press,

Cambridge, London, New York, Melbourne, (1978) pp. 230.

[Haas78+] P. Haasen, *Physical Metallurgy*, Cambridge University Press, Cambridge, London, New York, Melbourne, (1978) pp. 254, 282.

[Haas78++] P. Haasen, *Physical Metallurgy*, Cambridge University Press, Cambridge, London, New York, Melbourne, (1978) pp. 220.

[Haut85] P. Hautojärvi, H. Huomo, M. Puska, A. Vehanen, *Phys. Rev. B* 32 (1985) 4236.

[Hear84] R.F.S. Hearmon, *The elastic constants of crystals and other anisotropic materials: Numerical data and functional relationships in science and technology*, Landolt-Börnstein Group III/18, Springer, Berlin (1984).

[HinMeI] G. Alefeld und J. Völkl, Hrsg. *Hydrogen in Metals II*, Bd. 28 der *Topics in Applied Physics*. Springer-Verlag, Berlin, Heidelberg, New York, (1978).

[HinMeII] G. Alefeld und J. Völkl, Hrsg. *Hydrogen in Metals II*, Bd. 29 der *Topics in Applied Physics*. Springer-Verlag, Berlin, Heidelberg, New York, (1978).

[Hirth68] J.P. Hirth, J. Lothe, *Theory of Dislocations*, McGraw-Hill Book Company, New York, (1968).

[Hjörv89] B. Hjörvarsson, J. Rydén, T. Ericsson, E. Karlsson, *Nucl. Instrum. Meth. Phys. B* 42 (1989) 257-263.

[Hjörv91] B. Hjörvarsson, J. Ryden, E. Karlsson, J. Birch and J.-E. Sundgren, *Phys. Rev. B*, 43 (1991) 6440.

[Hjörv93] B. Hjørvarsson, S. Olafsson, F. Stillesjö and E. Karlsson, *Z. Phys. Chem.* 181 (1993) 903.

[Hjörv97] B. Hjörvarsson, G. Andersson, E. Karlsson, *J. Alloys Comp.* 253-254 (1997) 51-57.

[Hjörv97+] B. Hjörvarsson, J. Birch, F. Stillesjö, S. Ólafsson, J-E. Sudgren, E.B. Karlsson, *J. Phys.: Condens. Matter* 9 (1997) 73-85.

[Hjörv97++] B. Hjörvarsson, J.A. Dura, P. Isberg, T. Watanabe, T. Udovic, G. Andersson, C.F. Majkrzak, Phys. Rev. Lett. 79 (1997) 901.

[Hono98] K. Hono and M. Murayama, High Temperature Materials and Processes, 17 (1998) 69.

[Hono99] K. Hono, Atom probe field ion microscopy, Ferrum 4 (1999) 474-481 (*in Japanese*).

[Ikuha98] Y. Ikuhara, Microscopy Res. Tech. 40 (1998) 206-241.

[Isbe98] P. Isberg, P. Granberg, E.B. Svedberg, B. Hjörvarsson, R. Wäppling, P. Nordblad, Phys. Rev. B 57 (1998) 3531.

[Iwas03] W. Iwasaki, Int. J. Hydrogen Energy 28 (2003) 1325-1332.

[Izumi05] F. Izumi, Rigaku J., 36(1) (2005) 18-27. The VICS package is available under <http://homepage.mac.com/fujioizumi/visualization/VENUS.html>

[Jano82] C. Janot, B. George, P. Delcroix, J. Phys. F 12 (1982) 47.

[Kedda89] M. Keddam, Electrochim. Acta 34 (1989) 995.

[Kelly07] T. F. Kelly, D. J. Larson, K. Thompson, R. L. Alvis, J. H. Bunton, J. D. Olson, and B. P. Gorman, Ann. Rev. Mat. Res. 37 (2000) 681-727.

[Kest02] P. Kesten, A. Pundt, G. Schmitz, M. Weisheit, H.U. Krebs, R. Kirchheim, J. Alloys. Comp. 330-332 (2002) 225-228.

[King71] D.A. King, T.E. Maday, J.T. Yates Jr., J. Chem. Phys. 55 (1971) 3236.

[Kirch88] R. Kirchheim, Prg. Mat. Sci. 32 (1988) 262.

[Kirch03] R. Kirchheim, A. Pundt, T. Al-Kassab, F. Wang, C. Kluthe, Z. Metallkunde 94 (2003) 3.

[Kirch07] R. Kirchheim, Acta Mater. 55 (2007) 5129-5148.

- [Koike81] S. Koike, T. Suzuki, *Acta Metall.* 29 (1981) 553–565.
- [Koike93] S. Koike, H. Kojima, *Z. Phys. Chem.* 179 (1993) 383.
- [Landa06] A. Landa, J. Klepeis, P. Söderlind, I. Naumov, L. Vitos, A. Ruban, *J. Phys.: Condens. Matter* 18 (2006) 5079-5086.
- [Land08] V. Ivanchenko, *Iron systems: Phase diagrams, crystallographic and thermodynamic data*, Landolt-Börnstein, Group IV/5 Springer, Berlin (2008).
- [Lauda98] U. Laudahn, *Spannungen und Dehnungen von mit Wasserstoff beladenen Nb-Einfach- und Pd-Nb-Vielfachschichten*, Ph.D thesis, Universität Göttingen, (1998).
- [Lauda99] U. Laudahn, S. Fähler, H.U. Krebs, A. Pundt, M. Bicker, U.v. Hülsen, U. Geyer, R. Kirchheim, *Appl. Phys. Lett.* 74 (1999) 647-649.
- [Läss84] R. Lässer, *Phys. Rev. B*, 29 (1984) 4765.
- [Lebon10] A. Lebon, A. Vega, A. Mokrani, *Phys. Rev. B* 81 (2010) 094110.
- [Lee08] B. Lee, R.E. Rudd, J.E. Klepeis, R. Becker, *Phys. Rev. B* 77 (2008) 134105.
- [Lennon97] A.M. Lennon, K.T. Ramesh, *J. Phys IV FRANCE* 7 (1997) C3-559-C3-564.
- [Luo90] W. Luo, J.D. Clewly, T.B. Flanagan, *J. Chem. Phys.* 93 (1990) 6910-6922.
- [Mael64] A.J. Maeland, *J. Phys. Chem.* 68 (1964) 2197.
- [Mage76] A. Magerl, B. Berre, G. Alefeld, *Phys. Stat. Sol. (a)* 36 (1976) 161.
- [Make80] B.J. Makenas, H.K. Birnbaum, *Acta Metallurgica* 28 (1980) 979-988.
- [Marsh87] R.E. Marsh, *Acta Cryst., Sec. B: Structural science* 43 (1987) 415.

- [Matth74] J.W. Matthews, A.E. Blakeslee, *J. Cryst. Growth* 27 (1974) 118-125.
- [Maxel01] M. Maxelon, A. Pundt, W. Pyckhout-Hintzen, J. Barker, R. Kirchheim, *Acta Mater.* 49 (2001) 2625–2634.
- [McWhan83] D.B. McWhan, M. Gurvitch, J.M. Rowell, L.R. Walker, *J. Appl. Phys.* 54 (1983) 3886.
- [Mede05] V. Meded, S. Mirbt, *Phys. Rev. B* 71 (2005) 024207.
- [Miceli91] P.F. Miceli, H. Zabel, J.A. Dura, C.P. Flynn, *J. Mater. Res.* 6 (1991) 964-968.
- [Micha95] C. Michaelsen, *Philos. Mag. A* 72 (1995) 813-828.
- [Mill87] R.K. Miller, P. McIntire, *Nondestructive Testing Handbook* 2nd ed., Vol. 5 Acoustic Emission Testing, American Society for Nondestructive Testing, (1987).
- [Mill96] M.K. Miller, A. Cerezo, M.G. Hetherington, G.D.W. Smith, *Atom probe field ion microscopy*, Oxford Univ Press, (1996).
- [Mill00] M.K. Miller, *Atom probe tomography: analysis at the atomic level*, Kluwer Academic/Plenum Publishers, New York, Boston, Dordrecht, London, Moscow (2000).
- [Nagen95] D. Nagengast, J. Erxmeyer, F. Klose, Ch. Rehm, P. Kuschnerus, G. Dortmann, A. Weidinger, *J. Alloys Comp.* 231 (1995) 307-309.
- [Nase69] A.P. Nasekovskii, *Russ. Phys. Journal* 12 (1969) 45-48.
- [Nikit08] E. Nikitin, *Controlled delamination of metal films by hydrogen loading*, Ph.D thesis, Universität Göttingen, (2008).
- [Noda86] Y. Noda, T. Kajitani, M. Hirabayashi, S. Sato, *Acta Cryst.* B42 (1986) 529-533.
- [Nörth06] K. Nörthemann, *Wasserstoffabsorption in epitaktischen Niob-schichten: eine STM-Studie*, Ph.D thesis, Universität Göttingen, (2006).

- [Nörth08] K. Nörthemann, A. Pundt, Phys. Rev. B 78 (2008) 014105.
- [Nowak10] C. Nowak, G. Schmitz, R. Kirchheim, Surf. Sci. 604 (2010) 641–648.
- [Olsson01] S. Olsson, P. Blomquist, B. Hjörvarsson, J. Phys.: Condens. Matter 13 (2001) 1685–1698.
- [Olsson03] S. Olsson, Phase transition and phase transformation of hydrogen in quasi-2D lattices, Ph.D. thesis, Uppsala University (2003).
- [Orimo07] S. Orimo, Y. Nakamori, J.R. Eliseo, A. Züttel, C.M. Jensen, Chem. Rev. 107 (2007) 4111-4132.
- [Papat82] K. Papathanassopoulos, H. Wenzl, J. Phys. F 12 (1982) 1369-1381.
- [Parra54] L.G. Parratt, Phys. Rev. 95 (1954) 359-369.
- [Payle97] R. Payling, D. Jones, A. Bengtson (Ed.), Glow Discharge Optical Emission Spectrometry, J. Wiley, New York (1997).
- [Pesc81] W. Pesch, Strukturen und Phasenumwandlungen im Vanadium-Wasserstoff und Vanadium-Deuterium-System, Ph.D thesis, Rheinisch-Westfälische Technische Hochschule Aachen, (1982).
- [Popov68] E.P. Popov, Introduction to mechanics of solids, Prentice-Hall, Inc., Englewood Cliffs, New Jersey, U.S.A. (1968) pp. 112 (Japanese ed.)
- [Pundt04] A. Pundt, Adv. Eng. Mater. 6 (2004) 11-21.
- [Pundt06] A. Pundt, R. Kirchheim, Annu. Rev. Mater. Res. 36 (2006) 555-608.
- [Pundt10] *private communication*
- [PW10] *private communication*
- [Qi83] Zh. Qi, J. Völkl, R. Lässer, H. Wenzl, J. Phys. F 13 (1983) 2053.

- [Rowl82] H.A. Rowland, *Phil. Mag.*, 13 (1882) 469.
- [Röder09] J. Röder, *Analyse der Glättung rauher Oberflächen durch Dünnschichtdeposition*, Ph.D thesis, Universität Göttingen (2009).
- [Saka89] Y. Sakamoto, K. Kajihara, E. Ono, K. Baba, *Z. Phys. Chem. neue folge* 165 (1989) 67-81.
- [Sand99] *Rep. Prog. Phys.* 62 (1999) 809–858.
- [Schm01] G. Schmitz, *Habilitation thesis*, Universität Göttingen (2001).
- [Schob73] T. Schober, *Scripta Met.* 7 (1973) 1119.
- [Schob77] T. Schober, A. Carl, *Phys. Stat. Sol. (a)* 43 (1977) 443.
- [Schob78] T. Schober, *Scripta. Met.* 12 (1978) 549.
- [Schw06] R.B. Schwarz, A.G. Khachaturyan, *Acta Mat.* 54 (2006) 313-323.
- [Semi80] S. Semiletov, R. Baranova, Y. Khodyrev, R. Imamov, *Kristallografiya* 25 (1980) 1162–1168.
- [Shiga78] M. Shiga, Y. Nakamura, *J. Phys. F: Met. Phys.* 8 (1978) 177.
- [Siev29] A. Sieverts, *Z. Metall.* 21 (1929) 37-46.
- [Simmo60] R.O. Simmons, R.W. Balluffi, *Phys. Rev.* 117 (1960) 52-61.
- [Slaug02] W.S. Slaughter, *The linearized theory of elasticity*, Springer (2002).
- [Smith93] J.F. Smith, in: "Phase Diagrams of Binary Iron Alloys", H. Okamoto (ed.), *Materials Information Soc., Materials Park, Ohio*, (1993).
- [Song96] G. Song, M. Geitz, A. Abromeit, H. Zabel, *Phys. Rev. B* 54 (1996) 14093.
- [Stear98] D.G. Stearns, D. P. Gaines, D. W. Sweeney, *J. Appl. Phys.* 84 (1998) 1003.

- [Ston09] G.G. Stoney, Proc. R. Soc. London, Ser. A 82 (1909) 172.
- [Sugi84] H. Sugimoto, J. Phys. Soc. Jpn. 53 (1984) 2592–2599.
- [Takano74] S. Takano, T. Suzuki, Acta Met. 22 (1974) 265.
- [Tal-G10] E. Tal-Gutelmacher, R. Gemma, A. Pundt, R. Kirchheim, Acta Mat. 58 (2010) 3042-3049.
- [Tal-G10+] E. Tal-Gutelmacher, R. Gemma, C.A. Volkert, R. Kirchheim, Scr. Mat. 63 (2010) 1032-1035.
- [Thok95] R. Thokala, J. Chaudhuri, Thin Solid Films 266 (1995) 189-191.
- [Tolan99] M. Tolan, X-ray Scattering from Soft-Matter Thin Films, Springer-Verlag, (1999).
- [Uchi04] H. Uchida, Refrigeration, 79 (2004) 837-840.
- [Velec69] E. Veleckis, R.K. Edwards, J. Phys. Chem. 73 (1969) 683.
- [Vught70] J.H.N. van Vught, F.A. Kuijpers, and H.C.A.M. Bruning, Philips Res. Reports 25 (1970) 133.
- [Wagn08] S. Wagner, A. Pundt, Appl. Phys. Lett. 92 (2008) 051914-051918.
- [Walla95] W.E. Wallace, W.L. Wu, Appl. Phys. Lett., 67 (1995) 1203-1205.
- [Wana72] J. Wanagel, S.L. Sass, B.W. Batterman, Phys. Stat. Sol. (a) 11 (1972) 767.
- [Wang01] G. F. Wang, A. Strachan, T. Cagin, W. A. Goddard, Mat. Sci. Eng. A 309 (2001) 133.
- [Watson77] R.E. Watson, L.H. Bennett, Phys. Rev. B 15 (1977) 5136.
- [Watson78] R.E. Watson, L.H. Bennett, Phys. Rev. B 18 (1978) 6439.
- [Waugh76] A.R. Waugh, E.D. Boyes, M.J. Southon, Surf. Sci. 61 (1976) 109-142.

- [Weiss99] J. Weissmüller, C. Lemier, *Phys. Rev. Lett.* 82 (1999) 213.
- [West83] D.G. Westlake, *J. Less-Common Met.* 91 (1983) 275.
- [Wick64] E. Wicke, G. Nernst, *Ber. Bunsenges. Phys. Chem* 68 (1964) 224.
- [Wild01] A.R. Wildes, J. Mayer, K. Theis-Bröhl, *Thin Solid Films* 401 (2001) 7-34.
- [Windt98] D. Windt, IMD-Software for modeling the optical properties of multilayerfilms, in *Computers in Physics* 12 (1998).
- [Yagi86] E. Yagi, S. Nakamura, F. Kano, K. Watanabe, Y. Fukai, S. Koike, *Phys. Rev. B* 33, (1986) 5121.
- [Yamam95] S. Yamamoto, P. Goppelt-Langer, H. Naramoto, Y. Aoki, H. Takeshita, *J. Alloys Comp.* 231 (1995) 310-314.
- [Yim74] W.M. Yim, R.J. Paff, *J. Appl. Phys.* 45 (1974) 1456-1457.
- [Yu10] Q. Yu, Z-W. Shan, J. Li, X. Huang, L. Xiao, J. Sun, E. Ma, *Nature* 463 (2010) 335-338.
- [Yuka03] H. Yukawa, D. Yamashita, S. Ito, M. Morinaga, S. Yamaguchi, *J. Alloys Comp.* 356-357 (2003) 45-49.
- [Zhan07] Jian-Min Zhang, Yan Zhang, Ke-Wei Xu, Vincent Ji, *J. Phys. Chem. Sol.* 68 (2007) 503-510.
- [Zieg85] J.F. Ziegler, J.P. Biersack, U. Littmark, *The Stopping and Range of Ions in Solids*. Pergamon Press, New York (1985).
- [Zütt00] A. Züttel, C. Nützenagel, G. Schmid, C. Emmenegger, L. Schlapbach, *Appl. Surf. Sci.* 162 (2000) 571-575.

List of publications

- [1] R. Gemma, N. Okada, Y. Nishi and HH. Uchida, *J. Jpn. Inst. Metals* 67 (2003) 440-443.
- [2] R. Gemma, HH. Uchida, N. Okada and Y. Nishi, *J. Alloys Comp.* 356 (2003) 358-362.
- [3] N. Okada, R. Gemma, Y. Nishi and HH. Uchida, *J. Jpn. Inst. Metals* 68 (2004) 223-227.
- [4] N. Okada, R. Gemma, Y. Nishi and HH. Uchida, *J. Mater. Sci.* 39 (2004) 5503-5506.
- [4] R. Gemma, N. Okada, T. Sobue and HH. Uchida, *Int. J. Hydrogen Energy* 31 (2006) 309-311.
- [5] R. Gemma, T. Al-Kassab, R. Kirchheim and A. Pundt, *J. Alloys Comp.* 446-447 (2007) 534-538.
- [6] J. Cizek, I. Prochazka, S. Danis, O. Melikhova, M. Vlach, N. Zaludova, G. Brauer, W. Anwand, A. Mücklich, R. Gemma, E. Nikitin, R. Kirchheim and A. Pundt, *J. Alloys Comp.* 446-447 (2007) 484-488.
- [7] J. Čížek, N. Žaludová, M. Vlach, S. Daniš, J. Kuriplach, I. Procházka, G. Brauer², W. Anwand, D. Grambole, W. Skorupa, R. Gemma, R. Kirchheim, and A. Pundt, *J. Appl. Phys.* 103 (2008) 053508.
- [8] J. Čížek, I. Procházka, S. Daniš, G. Brauer, W. Anwand, R. Gemma, E. Nikitin, R. Kirchheim, A. Pundt and R.K. Islamgaliev, *Phys. Rev. B* 79 (2008) 054108.
- [9] J. Čížek, I. Procházka, M. Vlach, N. Žaludová, S. Daniš, P. Dobroň, F. Chmelík, G. Brauer, W. Anwand, A. Mücklich, E. Nikitin, R. Gemma, R. Kirchheim and A. Pundt, *App. Surf. Sci.* 255 (2008) 241-244.
- [10] J. Cizek, I. Prochazka, M. Vlach, N. Zaludova, S. Danis, G. Brauer, W. Anwand, A. Mücklich, R. Gemma, R. Kirchheim and A. Pundt, *Appl. Surf. Sci.* 255 (2008) 251-253.

- [11] J. Čížek, I. Procházka, G. Brauer, W. Anwand, R. Gemma, E. Nikitin, R. Kirchheim and A. Pundt, *Acta Physica Polonica A* 113(2008) 1293-1299.
- [12] J. Čížek, I. Procházka, M. Vlach, N. Žaludová, P. Dobroň, F. Chmelík, G. Brauer, W. Anwand, A. Mücklich, E. Nikitin, R. Gemma, A. Pundt and R. Kirchheim, *Procedia Engineering* 1, (2009) 99-103.
- [13] J. Čížek, I. Procházka, O. Melikhova, M. Vlach, N. Žaludová, G. Brauer, W. Anwand, W. Egger, P. Sperr, Ch. Hugenschmidt, R. Gemma, A. Pundt and R. Kirchheim, *Phys. Stat. Sol. C*, 6 (2009) 2364-2366.
- [14] R. Gemma, T. Al-Kassab, R. Kirchheim and A. Pundt, *Ultra-microscopy* 109 (2009) 631-636.
- [15] S. Semboshi, T. Al-Kassab, R. Gemma and R. Kirchheim, *Ultra-microscopy* 109 (2009) 593-598.
- [16] E. Tal-Gutelmacher, R. Gemma, A. Pundt and R. Kirchheim, *Acta Mater.* 58 (2010) 3042-3049.
- [17] E. Tal-Gutelmacher, R. Gemma, A. Pundt, R. Kirchheim, *Diffusion in Solids and Liquids IV* 283-286 (2009) 662-668.
- [18] E. Tal-Gutelmacher, R. Gemma, C.A. Volkert and R. Kirchheim, *Scr. Mat.* 63 (2010) 1032-1035.
- [19] R. Gemma, T. Al-Kassab, R. Kirchheim and A. Pundt, *J. Alloys Comp.* 509 Supplement 2, (2011) S872-S876.
- [20] M. Wilke, G. Teichert, R. Gemma, A. Pundt, R. Kirchheim, H. Romanus and P. Schaaf, *Thin Solid Films* *in printing*

Danksagung

An erster stelle möchte ich Frau Prof. Dr. Astrid Pundt ganz herzlich danken für die hervorragende Betreuung meiner Arbeit und ihre unver-schütterliche Zuversicht, und die Geduld für diese lange Arbeit. Ohne ihre Unterstützung konnte diese Arbeit nicht erfolgen. Für meine große Freude und Dankbarkeit auf mit ihr begegnet zu sein und zusammen ge-arbeitet zu haben sind die Worte hier nicht ausreichend.

Auch danke ich herzlich Herrn Prof. Dr. Reiner Kirchheim für seine freundliche Unterstützung und seinen Ratschlag. Mein Dank und meinen Respekt kann ich nicht genug ausdrücken. Nicht nur über die Physik, auch nach seine Menschlichkeit, habe ich viel gelernt wie Man als ein Mensch leben soll.

Für die Atomsondeuntersuchung möchte ich Herrn Prof. Dr. Talaat Al-Kassab herzlich danken, insbesondere für seine ständige Ansprechbe-reitschaft und sein Einsatz für den Aufbau und den reibungslosen Betrieb der tomographischen Atomsonde.

Den anderen Mitgliedern der Wasserstoff-in-Metallen-Gruppe, auch den ehemaligen, Dr. K. Nörthemann, S. Wagner, Dr. E. Nikitin, H.T. Uchida, Dr. D. Marcano, F. Schlenkrich, Dr. M. Suleiman, S. Schmidt, V. Burlaka, C. Izawa und den FIM-Gruppe Dr. C. Ene, Dr. A. Shariq, Dr. C. Nowak, Dr. C. Wille, Dr. T. Boll, M. Sobol, T. Rademacher, T. Kresse danke ich für die sehr gute Arbeitsatmosphäre und die vielen Anregungen und Hilfestel-lungen.

D. Plischke, F. Köhler, T. Nägel, T. Schulz, D. Wagner, M. Tetzlaff, M. Hey danke ich auch für ihre technische Unterstützung beim Reparatur und ihre ständige Freundlichkeit seitdem ich kein Deutch konnte.

M. Hahn, K. Ahlbohn, K. Born, A. Lehmberg danke ich für ihre sofortige Hilfe bei Vakuump Problemen.

Für TEM-Einweisung und Konservativismus des Anlages danke ich Dr. P. Wilbrandt.

T. Liese und A. Meschede danke ich für die Beihilfe bei der XRR-Messung.

Für GDOES-Analyse danke ich Herrn. Marcus Wilke and Prof. Dr. Peter

Schaaf in Technische Universität Ilmenau.

Für die gute Zusammenarbeit bei der AE-Messung danke ich ganz Assoc. Prof. Dr. J. Čížek und Dr. P. Dobron in Chales Universität in der Tschechische Republik.

Beim Rechnerproblem, Messungsproblem, oder beim Problem mit meinem Auto, bei der Bestellung usw. und auch am Alltagsleben hilften M. (Micha) Malcow und Cornelia (Connie) Mewes immer. Ihre Unterstützung wird außerordentlich anerkannt. Tausend Dank!

Für den angenehme Alltag im Institut danke ich alle Leute, insbesondere Dr. E. Tal-Gutelmacher und Dr. Y. Chen danke ich für ihre Nettigkeit und ermutigende Worte auch während unsere Zusammenarbeit.

Ein spezieller Dank geht an Frau C. Kuba, Frau I. Saalfeld, Frau K. Haake und Frau Ph. Quan fuer ihre freudliche, ständige und vorsichtige Unterstützung bei meinem Leben im Institut und im Deutschland.

Zusätzlich, Deutsche Akademische Austausch Dienst (DAAD) danke ich herzlich für die finanzielle Unterstützung dieser Arbeit.

Nicht nur im Rahmen des Austauschprogram zwischen Göttingen und Prag, sondern auch persönlich danke ich Dr. M. Vlach und N. Zaludova für ihre nette Freundschaft.

Jedoch geht nochmal mein herzlicher Dank an C. Izawa, ohne deren Unterstützung diese Arbeit nicht möglich gewesen wäre.

Nicht zuletzt danke ich ganz herzlich meiner Mutter im Himmel, und meinem Vater und meinem Bruder in Japan.

Lebenslauf

Personliche Daten

Name: Ryota Gemma
Geburtsdatum: 25.09.1978
Geburtort: Kanagawa
Familienstand: ledig
Staatsangehörigkeit: japanisch

Ausbildung

Schule	4/94-3/97	Hadano Oberschule, Hadano, Kanagawa, Japan
Studium	4/97-3/01	Human Development, Humanities and Culture, Tokai University, Japan
	3/01	Bachelor of Arts
	4/01-3/03	Metallurgical Engineering, Engineering, Tokai University, Japan
	3/03	Master of Engineering
	seit 6/04-	Ph.D Student in der Arbeitsgruppe von Prof. Dr. Astrid Pundt im Institut für Materialphysik der Universität Göttingen

Aufbaustudium

	4/03-6/04	Mitarbeiter in der Arbeitsgruppe von Prof. Dr. Haruhisa Uchida, Department of Human Development, Tokai University, Japan
	6/04-9/06	Mitarbeiter in der Arbeitsgruppe von Prof. Dr. Astrid Pundt
	10/06-12/10	DAAD Stipendiat für Ph.D Studium
	seit 01/10-	Mitarbeiter in der Arbeitsgruppe von Prof. Dr. Reiner Kirchheim